Modelling and Investigation of Nanoparticle Synthesis from the Gas-Phase

Von der Fakultät für Ingenieurwissenschaften, Abteilung Maschinenbau und Verfahrenstechnik der

Universität Duisburg-Essen

zur Erlangung des akademischen Grades

eines

Doktors der Ingenieurwissenschaften

Dr.-Ing.

genehmigte Dissertation

von

Johannes Sellmann
aus
Lippstadt

Gutachter: Univ.-Prof. Dr.-Ing. Andreas Kempf
Prof. Dr. Igor Rahinov
Tag der mündlichen Prüfung: 01.06.2023

Zusammenfassung

In dieser Arbeit wurde die Herstellung von Nanopartikeln in zwei verschiedenen Prozessen der Gasphasen-Synthese durch numerische Simulationen untersucht. Komplementär wurden die verwendeten Modellansätze anhand experimenteller Daten validiert und neue Modellansätze untersucht. In beiden untersuchten Syntheseprozessen waren Eisenoxidpartikel (Fe_2O_3) das gewünschte Produkt. Bei der Flammensynthese wurden diese aus dem gasförmigen Präkursor Eisenpentacarbonyl ($FeCO_5$) produziert und bei der Sprayflammen-Pyrolyse aus dem flüssigen Präkursor Eisen(III)-nitrat ($Fe(NO_3)_3$). Neben den unterschiedlichen Präkursoren lassen sich die hier untersuchten Reaktoren auch in ihren Strömungszuständen unterscheiden. Der Flammenreaktor weist eine laminare Strömung auf, während im Sprayflammenreaktor eine turbulente Strömung auftritt.

Im ersten Teil der Arbeit wurden hochaufgelöste Simulationen von zwei laminaren Eisenoxidpartikel -bildenden Wasserstoff/Sauerstoff-Flammen in einer Unterdruck-Umgebung untersucht. Die Flammen charakterisieren sich durch ihre unterschiedliche Ausrichtung. Während die eine von oben nach unten brennt (down-firing flame, DFF), brennt die andere Flamme (wie allgemein üblich) von unten nach oben (up-firing flame, UFF). Als Ergebnis dieser Studie konnten starke Variationen im Temperatur-Zeit-Profil der DFF und UFF, sowie eine gute Übereinstimmung zwischen modellierten und experimentell gemessenen Partikelgrößen gefunden werden. Darüber hinaus wurde in den Experimenten eine zweite Partikelbildungszone gefunden. Das entsprechende Reaktionskinetikmodell aus den Simulationen reproduzierte diese Beobachtung für die Bildung von Eisenclustern. Abschießend konnte mithilfe von Simulationen eine systematische Verschiebung der Ergebnisse auf den Einfluss des Probenahmesystems im Experiment zurückgeführt werden.

In einer nachfolgenden Studie wurde der Einfluss des Probenahmesystems auf die Flammenstruktur genauer untersucht. Eine bei Unterdruck betriebene Methan-Sauerstoff-Flamme wurde sowohl experimentell (durch eine andere Arbeitsgruppe) als auch numerisch untersucht. Im Experiment wurden Messungen mit zwei verschiedenen Düsen durchgeführt, die sich in ihrem Material (Quarz/Metall) und in ihrem Öffnungsdurchmesser (90 μm/550 μm) unterschieden. Der Vergleich zwischen Experimenten und Simulationen zeigte eine zufriedenstellende Übereinstimmung. Weiterhin konnten verschiedene Faktoren abgeleitet werden (z.B. Probentemperatur und Saugeffekte), die bei der Bewertung des Probeneffekts zu berücksichtigen sind.

Für den zweiten Teil der Arbeit wurde die Nanopartikel-Synthese in einer turbulenten Strömung untersucht und dafür die turbulente Sprayflamme 'SpraySyn' mittels Grobstruktursimulationen (LES) berechnet. Die Ergebnisse konnten im Kontext der Forschungsgruppe SPP1980 erstmalig mit experimentell gemessenen Partikelgrößenverteilungen validiert werden. Darauf aufbauend wurde ein Sub-Filter Modell für den Koagulationsquellterm implementiert und getestet. Das Sub-Filter-Modell zeigte keinen großen Einfluss auf die Ergebnisse. Im letzten Teil dieser Arbeit wurde die Methode der Lagrange-transportierten gefilterten Wahrscheinlichkeitsdichtefunktion (FDF) zur Beschreibung des Partikel-Wachstums in den LES-Code implementiert und an einem generischen Testfall validiert. In ersten Simulationen der 'SpraySyn' Flamme mit der FDF-Methode wurde kein signifikanter Einfluss im Vergleich zur herkömmlichen Partikelwachstumsbeschreibung beobachtet. Die Ursache dafür ist noch unklar und erfordert weitere Untersuchungen. Es ist zu Beachten, dass diese Beobachtung auf einem nicht ausreichend validierten Prototypen basiert.

Summary

In this work, the production of nanoparticles in two different gas-phase synthesis processes was studied by means of numerical simulations. Complementarily, the applied modelling approaches were validated against experimental data, and new modelling approaches were investigated. The desired products in both examined processes were iron oxide (Fe_2O_3) particles, produced either from the gaseous precursor iron pentacarbonyl ($FeCO_5$) in flame synthesis or from the liquid precursor iron (III) nitrate ($Fe(NO_3)_3$) in spray flame pyrolysis. Besides their different precursors, the processes can be distinguished by their flow type: laminar flow in the flame reactor and turbulent flow in the spray flame reactor.

In the first part of the work, highly-resolved simulations of two laminar, iron-oxide particle forming, hydrogen/oxygen flames in a low-pressure environment were performed. The flames were characterized by their different orientations, one burning from the top down (down-firing flame, DFF) and the other, as is commonly done, from the bottom up (up-firing flame, UFF). Substantial variations between the temperature-time profile of the DFF and UFF and a good agreement between modeled and experimentally measured particle sizes were found. Moreover, a early particle formation zone was detected in the experiments, and the corresponding reaction kinetics model from simulations reproduced this observation for iron clusters. Finally, simulations reproduced a systematic shift of the results. This shift could be attributed to the influence of the probing system in the experiment

The influence of the probing system on the flame structure was further investigated in the subsequent study. A methane-oxygen flame, operated at low pressure, was investigated experimentally (by another working group) and numerically. The measurements were performed with two different probing nozzles, which differed in their material (quartz/metal) and their orifice diameter (90 μm/550 μm). Experiments and simulations showed good agreement, and several factors, that should be considered when evaluating the sample effect, could be derived (e.g., sample temperature and suction effects).

The second part of the work investigated nanoparticle synthesis in a turbulent flow. For this purpose, the turbulent spray flame 'SpraySyn' was simulated using large eddy simulations (LES). In the scope of the research group SPP1980, the resulting particle size distribution could be validated with experimentally measured data for the first time and agreed well. A sub-filter model for the coagulation source term was implemented and tested based on the validated data. The sub-filter model did not show a significant influence on the results. As the final part of this work, a Lagrangian-transported filtered probability density function (FDF) method with a sectional particle model was implemented in the LES code and validated against a generic test case. Initial simulations of the "SpraySyn" flame were carried out using the FDF method, in which a significant impact could not be observed compared to the conventional description of particle growth. It is important to note that the reason for the lack of influence at this stage remains unclear. Further investigation is required to gain a deeper understanding of the underlying factors. It is important to emphasize that this observation is based on preliminary results that still require more extensive validation.

Preface

The work presented in this thesis was done during my time as a research assistant at the Chair of Fluid Dynamics at the University of Duisburg-Essen. First, I would like to express my gratitude to Prof. Dr.-Ing. Andreas Kempf for giving me the opportunity to do my doctoral studies in his group. He was not only a supervisor, but he also gave support in difficult times and has been a source of inspiration. He also provided me the opportunity to present my work at many leading international conferences, which has given me unforgettable moments for which I will always be grateful. Further, I want to thank Dr.-Ing. Irenaeus Wlokas for his ongoing scientific support, motivation and the good times we spent together at many conferences.

I want to thank my colleagues at the Department of Fluid Dynamics. In particular, I would like to mention our secretary and good soul of the chair Sylvia Helwig, who has always been there for me, even for problems unrelated to work. But of course, I would also like to thank all the rest of my colleagues who accompanied me during my time at the department: Sheeba Babuswamy, Seung-Jin Baik, Luis Cifuentes, Lei Deng, Jonas Eigemann, Linus Engelmann, Pascal Gruhlke, Olaf Hasemann, Eray Inanc, Peter Janas, Hossein Janbazi, Timo Lipkowicz, Dominik Meller, Khadijeh Mohri, Monika Nanjaiah, Thuong Nguyen, Fabian Proch, Martin Rieth, Andreas Rittler, Nejra Sikalo, Vahid Shari, Andreas Unterberger, Michael Vetter, Claudia Weise, Patrick Wollny. There were only a few days during my PhD, when I was not content going to work, because my colleagues were there to cheer me up, to have inspirational conversations in the kitchen, to have a leisurely meal in the cafeteria and to enjoy the occasional beer after work. Special thanks once again to Pascal, Patrick, Timo, Dominik, Linus, Monika, Seung-Jin, Marcel and Linus for proof-reading this work.

During my doctoral period, I worked in two separate research groups, which allowed me to meet many researchers. I want to thank all the people I met and worked with during this time. Special thanks go to Prof. Christof Schulz, Hartmut Wiggers, Prof. Igor Rahinov, Prof. Tina Kasper, Yasin Karakaya, Adrian Münzer, Samer Suleiman, Thore Rosenberger and Florian Schneider.

I want to thank my friends for always giving me a good time besides work: Thilo Wietzke, Ali Rodegro, Maxi Siech, Justin Schieven, Joshua Sänger, Jan Tepper, Matthis Börner, David Müller, Tobias Päsler, Hady Khalifa, Janik Hohmann mit Familie, Christian Saupe, Marcel Reefman and Christoph Simke.

Finally, I want to thank my parents, Anette and Hans-Jürgen and my siblings, Thomas, Markus, and Judith, for who I am and for always believing in me while providing unwavering support. I am deeply grateful to Catrin for her love and support and for making life so great.

PhD history and supplemental work

Due to the author's unusual journey through his PhD, this section is intended to give an overview of the chronology of the doctoral period. The PhD started in September 2015, along with the newly formed DFG research group FOR2284. Within this project, the authors objectives included the analysis, improvement and interpretation of different laboratory flow reactors (plasma, hot-wall and flame) by numerical simulations. Experimentally, the reactors were investigated by colleagues of the research group. The project in its first funding period from 2015-2018 has been outstandingly successful for the author with the publication of one first-author publication, four co-author publications, and one co-author review. He thus layed the foundation for follow-up proposals, whereby the FOR project is now in the third funding period. During the same period, data from the master's thesis were also continuously analyzed and led to a first-author publication in the first year of the PhD.

In the year 2018, the author agreed to take over a project within the research group SPP1980 due to a (unexpectedly) departing colleague. The work included support of the partner project, which aimed to simulate the research group's main target flame: 'SpraySyn'. Based on the simulation results, the author further investigated sub-filter contributions of the coagulation kernel in the 'SpraySyn' flame. This work resulted in two first-author publications (one journal and one proceeding). Among the mentioned publications, the following publications were within the scope of the thesis and are included in their entirety in the following chapters:

- J. Sellmann, I. Rahinov, S. Kluge, H. Jünger, A. Fomin, S. Cheskis, C. Schulz, H. Wiggers, A. Kempf, I. Wlokas, Detailed simulation of iron oxide nanoparticle forming flames: Buoyancy and probe effects [206]
- Yasin Karakaya, Johannes Sellmann, Irenäus Wlokas, Tina Kasper, Influence of the sampling probe on flame temperature, species, residence times and on the interpretation of ion signals of methane/oxygen flames in molecular beam mass spectrometry measurements [96]
- J. Sellmann, P. Wollny, S.-J. Baik, S. Suleiman, F. Schneider, C. Schulz, H. Wiggers, I. Wlokas, A. M. Kempf, LES of nanoparticle synthesis in the SpraySyn burner: a comparison against experiments [208]
- J. Sellmann, P. Wollny, S.-J. Baik, S. Suleiman, H. Wiggers, I. Wlokas, A. Kempf, Hybrid LES/Lagrange-FDF approach for the sub-grid modelling of nanoparticle synthesis in the SpraySyn burner [207]

The following survey shows the co- and first-author contributions of the author that are beyond the scope of this thesis. The publication information will be given below, while the abstract and a brief summary of the author's contribution in each publication can be found in the Appendix C.1-C.6.

- A. Münzer, J. Sellmann, P. Fortugno, A. Kempf, C. Schulz, H. Wiggers, Inline coating of silicon nanoparticles in a plasma reactor: Reactor design, simulation and experiment [148]
- P. Wollny, J. Menser, L. Engelmann, J. Sellmann, C. Schulz, H. Wiggers, A. Kempf, I. Wlokas, The role of phase transition by nucleation, condensation, and evaporation for the

synthesis of silicon nanoparticles in a microwave plasma reactor — Simulation and experiment [250]

- T. Rosenberger, I. Skenderovi, J. Sellmann, P. Wollny, A. Levish, I. Wlokas, A. Kempf, M. Winterer, and F. E. Kruis, Determining the sintering kinetics of Fe and FexOy-Nanoparticles in a well-defined model flow reactor [194]

- I. Rahinov, J. Sellmann, M. R. Lalanne, M. Nanjaiah, T. Dreier, S. Cheskis, and I. Wlokas, Insights into the Mechanism of Combustion Synthesis of Iron Oxide Nanoparticles Gained by Laser Diagnostics, Mass Spectrometry, and Numerical Simulations: A Mini-Review

- L. Cifuentes, J. Sellmann, I. Wlokas, and A. Kempf, Direct numerical simulations of nanoparticle formation in premixed and non-premixed flame–vortex interactions [29]

- J. Sellmann, Jiawei Lai, A. Kempf, N. Chakraborty, Flame surface density based modelling of head-on quenching of turbulent premixed flames [205]

Contents

List of Figures

List of Tables

Nomenclature

Abbreviations

1D	one dimensional
2D	two dimensional
3D	three dimensional
ATF	artificial thickened flame
CDS	central differencing scheme
CFD	computational fluid dynamics
CMC	conditional moment closure
DNS	direct numercal simulation
DTF	dynamic thickened flame
FDF	filtered density function
FMDF	filtered mass density function
FPI	flame prolongation
FSD	flame surface density
GDE	general dynamics equation
HMOM	hybrid method of moments
IEM	interaction-by-exchange-with-the-mean
ILDM	intrinsic low-dimensional manifolds
LES	large eddy simulation
LHS	left hand side
max	maximum
min	minimum
MPI	message passing interface
PBE	population balance equation
PDF	probability density function
PFGM	premixed flamelet-generated manifolds
PSD	particle size distribution
RANS	Reynolds averaged Navier-Stokes
RHS	right hand side
SGS	sub-grid scale
TVD	total variation diminishing
UDS	upwind differencing scheme

Lower case latin symbols

a	surface area	m^2
a_s	surface area of completely fused particle	m^2
a_i	(components) of the droplet acceleration vector	$\mathrm{m/s}^2$
a_m	Runge-Kutta coefficient for the sub-step m	–
b_m	Runge-Kutta coefficient for the sub-step m	–
c	normalized combustion progress variable	–
c_p	heat capacity at constant pressure	$\mathrm{J/(kg \cdot K)}$
c_v	heat capacity at constant volume	$\mathrm{J/(kg \cdot K)}$
c_α	molar concentration	$\mathrm{mol/m}^3$
d_av	average particle diameter	m
d_c	collision particle diameter	m

d_m	mass averaged particle diameter	m
d_p	primary particle diameter	m
dx, dy, dz	differential operator	m
f_F	fine-grained PDF	–
f_1	Stokes drag coefficient	–
g_i	(components) of the gravitational acceleration vector	$\mathrm{m/s^2}$
g_P	particle transition parameter	m
h	enthalpy	J/kg
h_c	standard enthalpy of formation	J/kg
h_s	sensible enthalpy	J/kg
k	turbulent kinetic energy	$\mathrm{m^2/s}$
l_I	integral lenght	m
l_P	particle mean free path	m
m	mass	kg
n	partikel number concentration in PBE	–
n_p	primary partikel number	–
p	pressure	Pa
q	reaction rate	$\mathrm{mol/(m^3 \cdot s)}$
r_c^*	critical cluster radius	m
s_D	displacement speed	m/s
s_L	laminar burning velocity	m/s
t	time	s
t_I	eddy turn-over time	s
u_i	(components) of the velocity vector	m/s
v	particle volume	$\mathrm{m^3}$
v'_α	stoichiometric coefficients	–
v_K	Kolmogorov velocity scale	m/s
v_P	particle velocity	m/s
w	interpolation weight	m
w_m	Runge-Kutta coefficient for the sub-step m	–
x_i	(components) of the spatial coordinate vector	m

Upper case latin symbols

A	particle surface area concentration	$\mathrm{m^2/m^3}$
C_B	ratio between v_1 and v_2 in Bimodal model	–
C_c	Cunningham slip correction factor	–
C_K	Kolmogorov constant	–
C_m	model constant in Sigma/Smagorinsky turbulence model	–
D_t	turbulent diffusion coefficient	$\mathrm{m^2/s}$
D_f	fractal dimension	–
$D_{\alpha,\beta}$	binary diffusion coefficient	$\mathrm{m^2/s}$
$D_{\alpha,\beta}$	particle diffusion coefficient	$\mathrm{m^2/s}$
E	efficency function in ATF approach	–
E_a	activation energy	J/mol
F	flow direction in UDS	–
F_F	filtered density function	–
F_t	thickening factor in ATF approach	–
G	filter operator	1/m
I	nucleation source term	$\mathrm{\#/(m^2 \cdot s)}$
J_i	components of diffusive flux vector	$\mathrm{m^2/(s \cdot m)}$
L	length	m

L_v	latent heat	J/kg
M_k	kth moment of the PSD	–
N	particle number concentration	$\#/m^3$
N_s	number of species	–
N_t	total number of computational cells	–
P	probability density function	–
$\dot{Q}$	heat source term	$J/(kg \cdot s)$
Q_c	conditioned quantity	–
RR	reaction rate	$mol/(m^3 \cdot s)$
RR_b	backward reaction rate	$mol/(m^3 \cdot s)$
RR_f	forward reaction rate	$mol/(m^3 \cdot s)$
S	saturation state	–
S_M	area source term in momentum equation	$kg/(m^2 \cdot s^2)$
S_{ij}	strain rate	1/s
T	temperature	K
V	control volume	m^3
V	particle volume concentration	m^3/m^3
V_m	molecule cluster volume	m^3
V_i^c	(components) of the external corection velocity	m/s
W	molecular weights	kg/kmol
W_i	(components) of the Wiener term	s
X	molar fraction	–
Y_α	mass fraction of species alpha	–
Z	Bilger mixture fraction	–
Z_j	element mass fraction	–

Lower case greek symbols

β	coagulation frequency / kernel	m^3/s
δ_{th}	thermal flame thickness	m
δ_{ij}	Kronecker delta	–
ϵ	dissipation rate	m^2/s^3
η_K	Kolmogorov length scale	m
λ	mean free path	m
μ	dynamic viscosity	$Pa \cdot s$
ν	kinematic viscosity	m/s^2
θ	limiter function for the TVD schemes	
ρ	density	kg/m^3
σ	standard deviation	–
σ	surface tension	J/m^2
$\sigma_{\alpha,\beta}$	average collision diameter	Å
τ_d	droplet relaxation time	s
τ_K	Kolmogorov time scale	s
τ_{ij}	viscous stress tensor	N/m^2
τ_{ij}^{SGS}	unresolved fluxes in LES	s
τ_{ij}^{test}	unresolved fluxes of test filter in dynamic Germano procedure	$kg/(m \cdot s^2)$
χ_α	chemical symbol	–
$\chi_{i,j,k}$	interpolation factor	–
ϕ	equivalence ratio	–
$\phi(\boldsymbol{x}, t)$	scalar array in FDF-method	–
ψ	composition domain of scalar array in FDF-method	–
$\dot{\omega}_E$	evaporation source term for species α	$kg/(m^3 \cdot s)$

$\dot{\omega}_\alpha$	chemical source term for species α	$\mathrm{kg}/(\mathrm{m}^3 \cdot \mathrm{s})$
ω_I	intermittency factor	–

Upper case greek symbols

$\dot{\Gamma}_\rho$	mass source term due to evaporation	$\mathrm{kg}/(\mathrm{m}^3 \cdot \mathrm{s})$
Σ	flame surface density	
Ξ	flame wrinkling factor	–
Ω	flame sensor	–
Ω_m	mixing frequency in IEM-model	1/s
$\Omega_{\alpha,\beta}$	collision integral	–

Subscripts to an arbitrary quantity ϕ

ϕ_α	species
ϕ_Δ	sub-grid
ϕ_b	boiling
ϕ_d	droplet
$\phi_\mathrm{E}, \phi_\mathrm{e}$	eastern cell center, eastern surface
ϕ_F	fuel
ϕ_f	cell surface
ϕ_g	gas
$\phi_\mathrm{N}, \phi_\mathrm{n}$	northern cell center, northern surface
ϕ_O	oxygen
ϕ_P	particle
ϕ_p	progress
$\phi_\mathrm{S}, \phi_\mathrm{s}$	southern cell center, southern surface
ϕ_t	turbulent
ϕ_u	unburned
$\phi_\mathrm{W}, \phi_\mathrm{w}$	western cell center, western surface

Superscripts to an arbitrary quantity ϕ

ϕ'	fluctuation
ϕ^SGS	sub-grid scale
ϕ^0	reference condition
ϕ^n	time step

Mathematical symbols and operators to an arbitrary quantity ϕ

$\mathrm{d}\phi$	total derivative
$\overline{\phi}$	filtering in LES
$\overline{\phi}$	temporal averaging in RANS
$\partial\phi$	partial derivative
$\widehat{\phi}$	test-filtering for dynamic models
$\widetilde{\phi}$	mass weighted Favre temporal averaging in RANS
$\widetilde{\phi}$	mass weighted Favre-filtering in LES

Dimensionsless numbers

Le	Lewis number: ratio of thermal to mass diffusivity
Re_crit	critical Reynolds number
Re_d	droplet Reynolds number
Re	Reynolds number: ratio of inertial to viscous forces
Re_t	turbulent Reynolds number

Sc_t	turbulent Schmidt number
Sc	Schmidt number: ratio of momentum to mass diffusivity
Sh	Sherwood number: ratio of convective to diffusive mass transfer
CFL	Courant Friedrichs Lewy number: ratio of physical to numerical velocity
B_h	Spalding heat transfer number
B_m	Spalding mass transfer number
Kn	Knudsen number: the ratio of the molecular mean free path to a representative length scale
Nu	Nusselt number: ratio of convective to conductive heat transfer
Pr	Prandtl number: ratio of momentum to thermal diffusivity

Physico-chemical constants

k_b	Boltzmann constant	$1.380 \cdot 10^{-23}\,\mathrm{J/K}$
N_A	Avogadro constant	$6.022 \cdot 10^{23}\,1/\mathrm{mol}$
R_u	universal gas constant	$8.314\,\mathrm{J/(mol \cdot K)}$

Chapter 1
Introduction

1.1 Background

The term nanoparticle is a combination of the word particle, which refers to the presence of a solid that is small compared to its surroundings, and the term nano (Greek word for dwarf), a prefix for units of measurement, in this case, a measure of length, and corresponds to one billionth (10^{-9}). The term nanoparticle thus describes all particles with a characteristic size of 100 nm and below [13]. Particles of this size are found in everyday life, for example, in candle flames, where they are better known as soot, but they are also produced in industry. An example of an industrial product is the material carbon black, which is used in the production of car tires or as a colourant [81]. In its early use, however, the nanoscale nature of carbon black was not deliberately and consciously realized.

Nanoscale nature means that many materials have remarkably different chemical, mechanical and optical properties compared to the bulk material, once they exist in nano size. For example, the melting point, fluorescence, electrical conductivity, magnetic permeability, and chemical reactivity can be altered and fine-tuned as a function of size. For instance, depending on its size, silicon changes luminescence colour when dissolved in water [16]. Many of these effects can be attributed to two main factors. First, particles in the nanometer range move in a frame where quantum effects[1] dominate [81]. Second, the particles have a sizeable surface-to-volume ratio, leading to increased reactivity. For example, a solid cube with a side length of 1 cm has a surface area of 6 cm^2, while cubic nanoparticles with a side length of 1 nm and the same total volume have a surface area of 6000 m^2, slightly less than a football ground (7140 m^2).

In the 4th century AD, the Romans took early advantage of optical properties by (presumably) inadvertently forming nanoparticles through their unique glassmaking technique. This method, which was used to make the Lycurgus cup [49], causes the cup to show different colors depending on the angle at which it is viewed. It is worth noting that the Romans probably could not fully understand or control this process. Today, new production and analysis capabilities at the nanoscale, as well as development in theoretical understanding of the behaviour, have extended the field of applications. Due to their large surface area, they are particularly suitable for increasing the efficiency of electrodes or catalysts for fuel cells and heavy oil recovery [36]. Likewise, the optical properties allow for an increase in efficiency in solar modules [155]. In biomedicine, magnetic nanoparticles are transported to specific body locations, such as tumours, to destroy cancerous tissues via magnetic hyperthermia [66]. In the strongly related field of nanobiotechnology, work is being done on producing artificial proteins or blood bodies [91].

The demands on particle size, shape, and composition for each application are precisely defined and must be controlled throughout the production process, which is categorized into two methods. In the case of top-down methods, particles are split off from existing bulk material, while in the bottom-up approach, particles synthesize from a fluid phase. Examples of the top-down method are classical milling processes or laser beam lithography used to create nanostructures for semiconductors. However, this work only handles the bottom-up method, e.g., the sol-gel method [27], where the precursor is dissolved in a solution and builds, through reactions, particles in the nanoscale, or the synthesis of nanoparticles from the vapour phase. Gas-phase synthesis allows

[1] The quantum size effect describes the physics of electron properties in solids with significant reductions in particle size. This effect does not come into play from macro to micro dimensions but when reaching the nanometer size range.

the production of large particle quantities of high purity with a narrow size distribution [93] and is the focus of the present work. Reactors for the synthesis are usually distinguished by the way in which heat is provided. For example, there are hot wall reactors [193, 194], plasma reactors [148], and flame reactors [96, 206, 208]. The hot wall and plasma reactors allow the synthesis of non-oxide nanomaterials while being used primarily in research. These two types of reactors have been investigated in the context of these doctoral studies but are not the subject of the thesis. Flame reactors, on the other hand, have the highest relevance for synthesizing oxidic particles due to their efficiency and the robustness of the process. Carbon black, fused silica, iron oxide, and titania pigments, for example, can be synthesized on an industrial scale in flame reactors [228]. Compared to the hot wall and the plasma reactor, the heat is not introduced externally but rather in situ by combustion.

Since both processes, combustion and particle formation, run partly in parallel, flame reactors are highly complex and challenging to control. Moreover, in most technical flames, the flow even becomes turbulent due to reactor size and high gas velocities, further increasing the complexity due to interactions with both processes. In order to remove at least this fluid mechanical complexity from the process, laminar laboratory flames were developed. A widely used setup is the laminar flat flame [40, 75], which is stationary and stabilized on a cooled burner matrix (burner stabilized flames). The reactants cross a sintered matrix, which damps the turbulent motions and leads to a laminar, well-defined flow field behind this sintered matrix with temperature and gas composition profiles that are spatially uniform, i.e., the same in the radial direction. These flames are usually operated at low pressure, which leads to an expansion of their flame zone [97], increases the spatial resolution in the axial direction, and enables measurements. The primary motivation for this kind of lab-scale reactor is the lack of a comprehensive understanding of the reaction kinetics in the process of flame-based synthesis of nanoparticles [97]. Thus, laminar premixed flames doped with a precursor offer excellent conditions to investigate further, understand and improve the process of nanoparticle synthesis.

These types of flames are usually analyzed in a complementary way by simulations and experiments. Due to the uniform spatial distribution, the flame can be treated as one-dimensional. As a result, the effort to simulate these flames is drastically reduced and allows the use of detailed reaction mechanisms, which can then be validated against experimental data and developed further if necessary. Experimental measurements can be made using two different techniques: optical methods and probing techniques. Optical measurement techniques are non-intrusive, have a high spatial resolution, and can measure simultaneously at multiple locations. Classical optical methods for measuring the flow field are laser Doppler and particle imaging velocimetry (PIV) [245], while temperature and species profiles can be measured with laser-induced fluorescence [43]. However, these approaches are typically complex, expensive, and elaborate to carry out.

Among the probing techniques, the molecular beam sampling (MBS) technique [97], in particular, is widely used in combustion research. The MBS is invasive and takes gas samples along the flame centerline. The sample is sucked through an orifice, expands into a chamber at low pressure, and forms a beam, which transports the particles (atoms, free radicals, molecules, or ions) to the measuring instrument. In the beam, the particles move at a similar speed and with minor collisions. Hence, the growth of particles and all reactions are quenched and frozen. The probe is usually conically shaped with an orifice at its tip and is manufactured from quartz or metal [96]. For the measurement, the probe tip is moved to the measuring point and sucks the sample inside the probe. Unfortunately, both the mere presence of the probe and the suction of the gas sample inevitably disturb the flame structure. As a result, the measured data often deviates significantly from the ideal 1D model calculations. As a result, to be complementary with 1D simulations, this deviation is in need of special investigation and must be corrected. In addition to this disturbance of the 1D assumption by the probing device, fluid mechanical effects such as buoyancy can result in deviations from 1D assumptions. A promising approach to determine this disturbance is the calculation by means of 2D or 3D simulations [40], which can

represent and interpret these effects.

While the classic flame synthesis is limited to gaseous precursors, flame spray pyrolysis enables the use of liquid (or even solid) precursors [133]. The liquid precursor is dissolved in a liquid fuel such as ethanol and injected into the hot reactor, where it atomizes and forms a spray. The spray then evaporates and burns due to the presence of a pilot flame. After evaporation, classical flame synthesis occurs, and particles are formed by nucleation, coagulation, and sintering. However, these flows are typically turbulent, making the spray flame synthesis a very complex physical system, which is currently under investigation by several research groups in the scope of the SPP1980 [203]. Each group investigates a part of the spray flame according to its field of expertise, starting from precursor chemistry [103], spray droplet distributions [202], and particle distributions [224] up to finished particles [8]. As part of this work, the flame was simulated and validated with experiments to subsequently make the first steps to investigate the interaction between turbulence and particle growth in flame synthesis.

1.2 Objectives and scope of the thesis

This work aims at simulating the gas-phase synthesis of iron oxide particles in laminar and turbulent flames. The simulations were carried out in the scope of two research groups, where other researchers examined these flames through experiments. The following objectives were pursued by the simulations:

- Validation of the simulations with experimental data, with a focus on particle sizes.
- The interpretation of simulated flow and thermochemistry data.
- Evaluation of uncertainties induced by the invasive measurement technique in experiments. The simulations are complementary and enable to either correct the measured data or interpret it correctly.
- The investigation of the particle model predictions in terms of subfilter modelling. Applying two subfilter modelling approaches, i.e. an intermittency model and an FDF-method.
- Aim to provide benchmark data for other simulation groups and their codes.

In summary, the simulation results were validated and used to interpret the flow physics, investigate the impact of invasive measurement devices, studied in terms of subgrid modelling, and finally served as benchmark data for other simulation groups. First, laminar particle-forming flames were investigated, applying a straightforward Bi-modal particle model. The results were compared with experiments, and the impact of the invasive measurement technique was examined. In the second step, the suitability of particle modelling in a turbulent spray flame were studied via large-eddy simulations. Accordingly, the data was compared with experimental in situ data, which is done for the first time to the best of the author's knowledge.

Finally, the influence of unresolved terms in particle modelling was examined. Two approaches were pursued: a related model from the field of soot modelling and a transported Lagrangian FDF method. Both models were implemented and applied as a closure approach.

1.3 Thesis outline

This thesis is structured as follows. In the second Chapter 2 the relevant basic background is presented i.e. the basic mathematical equations describing flow, combustion and multiphase flow. Chapter 3 introduces models that are necessary to solve the fundamental equations in the CFD simulation. Chapter 4 presents the required numerical solution methods to solve the equations. Subsequently, the results of the work on laminar flames are presented in Chapter 5 and include a

discussion of probing and buoyancy effects in a down-firing flat flame configuration, as well as an investigation of the probing effect in a regular upward burning methane flame. Chapter 6 then contains the results of work on turbulent flames. This includes the simulation of the SpraySyn flame with the intermittency model as a subfilter model and the first study with a hybrid LES-FDF method for the simulation of particle growth. In Chapter 7, the work is summarized and in Chapter 8, a conclusion is drawn with an outlook. In addition Appendix A shows supplemental material mentioned in Chapter 5, B shows a validation study of the implemented FDF method, and Appendix, C.1-C.6 shows the co-author and further first-author publications of the author, which are not part of this thesis.

Chapter 2
Theoretical background

This chapter introduces the governing equations and processes, describing the gas-phase synthesis of nanoparticles in reacting flows, i.e. gas- and spray-flames. First, the conservation equations are presented. These equations are valid for non-reacting and reacting flows, while the latter additionally accounts for the chemical conversion of educts to products. Therefore, the second section addresses combustion processes. The last section presents the basic equations for describing multiphase flows, i.e. spray and nanoparticle laden flows.

2.1 Fluid flow

The movement of any fluid can be mathematically described. In order to consider the fluid on a scale that is relevant to most technical applications, it is feasible to assume the fluid to be a continuum and to neglect the molecular structure of the observed fluid so that it can be described in terms of partial differential equations.

2.1.1 Conservation equations

Conservation of mass

The mass of a single-phase flow in a control volume $\mathrm{d}V = \mathrm{d}x \cdot \mathrm{d}y \cdot \mathrm{d}z$ changes only by the inflow or outflow of mass beyond the limits of the control volume. The conservation of mass states that mass can neither be produced nor destroyed and reads:

$$\frac{\partial \rho}{\partial t} + \frac{\partial \rho u_i}{\partial x_i} = 0 \tag{2.1}$$

Here, ρ is the density of the fluid, u the velocity, t and x_i are time and the spatial coordinate in i direction, respectively. For a multiphase flow as present in spray flames, the evaporation of droplets results in an additional source term $\dot{\Gamma}_\rho$ on the right-hand-side (RHS) of the equation as follows:

$$\frac{\partial \rho}{\partial t} + \frac{\partial \rho u_i}{\partial x_i} = \dot{\Gamma}_\rho \tag{2.2}$$

Conservation of momentum

The conservation equations for momentum describe the effect of forces acting on the fluid. By assuming a Newtonian fluid[1], the conservation equations of momentum become the Navier-Stokes equations which read:

$$\frac{\partial \rho u}{\partial t} + \frac{\partial \rho u_i u_j}{\partial x_j} = -\frac{\partial p}{\partial x_j} + \frac{\partial \tau_{ij}}{\partial x_j} + \rho g_i + \dot{S}_\mathrm{M} \tag{2.3}$$

The two terms on the left-hand side (LHS) of Eq. (2.3) are the accumulation and the convection term, respectively. The right-hand side presents the forces acting on the fluid. These forces are related to pressure p, viscous stresses τ_{ij}, gravitation ρg_i, and $\dot{S}_\mathrm{M}$ which accounts for additional forces, i.e. a source term for the exchange of moments between liquid and gas phase, Coriolis or

[1] Newtonian Fluid: the viscous stresses are proportional to the strain rate of the flow

centrifugal forces. The stress tensor depends on fluid properties and is calculated, for a Newtonian fluid, from the dynamic viscosity μ as follows:

$$\tau_{ij} = \mu \left(\frac{\partial u_i}{\partial x_j} + \frac{\partial u_j}{\partial x_i} \right) - \mu \frac{2}{3} \frac{\partial u_k}{\partial x_k} \delta_{ij} \tag{2.4}$$

where δ_{ij} is the Kronecker delta which equals 1 for $i = j$ and 0 for $i \neq j$, and μ describes the dynamic viscosity.

Conservation of species

A mixture composition of a fluid can be described by means of its mass fractions Y_α, where the subscript α represents the species in the mixture. The mass fraction is defined as the mass of the respective species m_α related to the total mass of the mixture m_t:

$$Y_\alpha = \frac{m_\alpha}{m_t} = \frac{m_\alpha}{\sum_{i=1}^{N_\mathrm{s}} m_i} \tag{2.5}$$

In this equation, N_s is the number of species. The conservation equation for species mass fractions reads:

$$\frac{\partial \rho Y_\alpha}{\partial t} + \frac{\partial \rho Y_\alpha u_j}{\partial x_j} = \frac{\partial J_{\alpha,j}}{\partial x_j} + \dot{\omega}_\alpha + \dot{\omega}_\mathrm{E} \tag{2.6}$$

The two terms on the LHS describe the accumulation and convective transport of Y_α. The terms on the RHS present the species diffusion flux $J_{\alpha,j}$, the chemical source term $\dot{\omega}_\alpha$, which will be introduced in the following section, and the evaporation term $\dot{\omega}_\mathrm{E}$. The diffusion flux can be approximated by Fick's law:

$$J_{\alpha,j} = \rho D_{\alpha,\beta} \frac{\partial Y_\alpha}{\partial x_j} \tag{2.7}$$

The binary diffusion coefficient $D_{\alpha,\beta}$ considers the diffusion of species α into the surrounding species β. The computation of this coefficient is based on kinetic gas theory and utilises the Chapman-Enskog theorem:

$$D_{\alpha,\beta} = \frac{1.863 \cdot 10^{-3} \sqrt{T^3 (W_\alpha + W_\beta)}}{p \sigma_{\alpha,\beta}^2 \Omega_{\alpha,\beta}} \tag{2.8}$$

Here W is the molecular mass, $\sigma_{\alpha,\beta}$ is the collision diameter, and Ω is the collision integral. The latter two are temperature-dependent, change with species combinations, and are determined by experiments or kinetic theory.
The definition above is applicable to a mixture of two species, α and β. For a mixture consisting of multiple species, two different approaches are used in the thesis. First, for simulations of laminar flows in which the conservation equations were solved directly and the diffusion of the individual species plays an important role, the mixture diffusion coefficient was calculated for each species using the Hirschfelder and Curtiss [79] approximation:

$$D_{\mathrm{m},\alpha} = \frac{1 - Y_\alpha}{\sum_{\alpha \neq \beta} X_\beta / D_{\alpha,\beta}} \tag{2.9}$$

Here $D_{\mathrm{m},\alpha}$ is not a binary diffusion coefficient but an equivalent diffusion coefficient of species α within the mixture. In order to maintain global conservation of mass, a common approach is to calculate the correction velocity V_i^c, which can be derived from the requirement that the diffusion fluxes of the species must sum up to zero. It is defined as:

$$V_i^c = \sum_{\alpha=1}^{N} D_{\mathrm{m},\alpha} \frac{\partial Y_\alpha}{\partial x_i} \tag{2.10}$$

The velocity is added to Eq. (2.7) and results in:

$$J_{\alpha,j} = \rho D_{\alpha,\beta} \frac{\partial Y_\alpha}{\partial x_j} - Y_\alpha V_c \tag{2.11}$$

Substituting Eq. (2.11) in Eq. (2.6), the final transport equation for species results:

$$\frac{\partial \rho Y_\alpha}{\partial t} + \frac{\partial \rho Y_\alpha u_j}{\partial x_j} = \frac{\partial}{\partial x_j}\left(\rho D_{m,\alpha} \frac{\partial Y_\alpha}{\partial x_j} - \rho Y_\alpha V_c\right) + \dot{\omega}_\alpha + \dot{\omega}_E \tag{2.12}$$

As a second approach to describe the diffusion coefficient in turbulent flows, the non-dimensional Schmidt number approach was used in this thesis. The Schmidt number relates the species diffusivities to the mixture viscosity:

$$S_{c\alpha} = \frac{\mu}{\rho D_{\mathrm{m},\alpha}} \tag{2.13}$$

By substituting Eq. (2.13) into Eq. (2.6), the species mass fraction conservation equation takes the form:

$$\frac{\partial \rho Y_\alpha}{\partial t} + \frac{\partial \rho Y_\alpha u_j}{\partial x_j} = \frac{\partial}{\partial x_j}\left(\frac{\mu}{S_{c\alpha}} \frac{\partial Y_\alpha}{\partial x_j}\right) + \dot{\omega}_\alpha + \dot{\omega}_E \tag{2.14}$$

Conservation of energy

The energy in a fluid flow can be expressed in terms of different energy forms [166], where the mean enthalpy of the mixture was chosen in this work. The mean enthalpy h is the sum of the sensible enthalpy h_s and the standard enthalpy of formation h_c. The sensible enthalpy is calculated as follows:

$$h_\mathrm{s} = \sum_{\alpha=1}^{N_\mathrm{s}} \int_{T_0}^{T} Y_\alpha c_{p,\alpha} dT \tag{2.15}$$

In this equation, $c_{p,\alpha}$ is the specific heat capacity at constant pressure for species α. The formation enthalpy is determined from the sum of the formation enthalpies $h^\circ_{\mathrm{f},\alpha}$ of the individual species:

$$h_\mathrm{c} = \sum_{\alpha=1}^{N_\mathrm{s}} Y_\alpha \Delta h^\circ_{\mathrm{f},\alpha} \tag{2.16}$$

The conservation equation of the mean enthalpy reads:

$$\frac{\partial \rho h}{\partial t} + \frac{\partial \rho h u_j}{\partial x_j} = \frac{Dp}{Dt} - \frac{\partial q_j}{\partial x_j} + \tau_{ij} \frac{\partial u_i}{\partial x_j} + \dot{Q} + \rho \sum_{\alpha=1}^{N_\mathrm{s}} Y_{\alpha,j} f_{\alpha,j} J_{\alpha,j} \tag{2.17}$$

The two terms on the LHS represent the temporal change and the change by convective transport of the enthalpy. The first term on the RHS presents the temporal change of pressure and was neglected in this work assuming flames at low Mach number conditions. The second and third term present the heat/enthalpy flow and the change by viscous heating, which is also small compared to the other terms, and hence is neglected.

2.1.2 Turbulent flows

In general, the prevailing flow condition can be distinguished by differentiating between laminar and turbulent flows. Laminar flows have smooth, regular profiles, whereas turbulent flows fluctuate chaotically. Both types of flow have their benefits and drawbacks, although in most technical applications the flow is turbulent [172], since technical systems are usually "large", leading to high Reynolds numbers. The Reynolds number is a dimensionless quantity that can be used to

predict or characterise flow patterns in different situations. It is calculated from the ratio of inertial forces to viscous forces:

$$Re = \frac{\rho u L}{\mu} \tag{2.18}$$

Here L is the characteristic length (e.g. a pipe diameter or the length of a plate). Depending on the flow situation, critical Reynolds numbers are specified, which mark the transition from laminar to turbulent flows. As an example, for a flow-over a plate, the value is $Re_{\text{crit}} = 10^5$ and for a pipe flow $Re_{\text{crit}} = 2,300$.

Even though turbulent flows tend to behave in a chaotic, unpredictable manner, assumptions can be made about its characteristics. These assumptions are based on the concept of the 'energy cascade' first introduced by Richardson [185]. Accordingly, a turbulent flow can be described as an accumulation of an indefinite number of turbulent eddies of different sizes. The size of the largest eddy is proportional to the dimension of the geometry, for example, the combustion chamber of an engine. The large eddies break down into smaller eddies and transfer their kinetic energy to the smaller ones. This process repeats itself until the eddies reach their smallest possible size, the Kolmogorov scale η_{K}. At this scale, they dissipate by the action of viscosity, and their energy dissipates into heat through molecular friction. This concept was further developed by Kolmogorov [111], and the following conclusion was drawn: if the smallest eddies are dissipated only by viscosity, then the dissipation ϵ must be equal to the rate of kinetic energy k supplied to the largest vortices. Based on this assumption, the smallest turbulent scales can be derived which are also known as Kolmogorov microscales:

$$\eta_{\text{K}} = (\nu^3/\epsilon)^{1/4} \quad \tau_{\text{K}} = (\nu/\epsilon)^{1/2} \quad v_{\text{K}} = (\nu\epsilon)^{1/4} \tag{2.19}$$

In this equation τ_{K} and v_{K} represent the Kolmogorov time and velocity scales, respectively. The

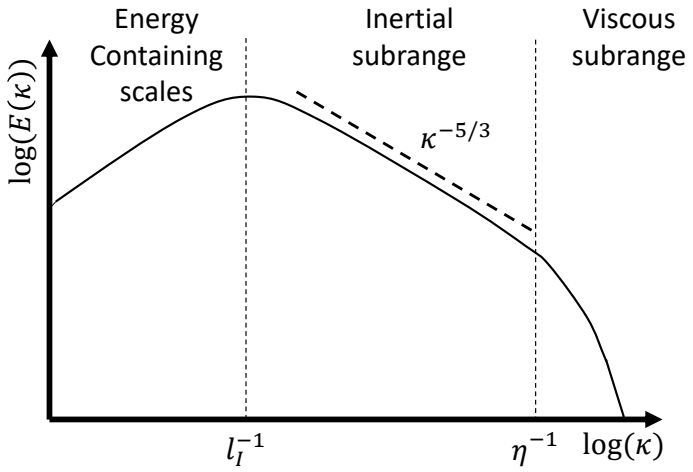

Figure 2.1: Illustration of the turbulent energy spectrum (as presented by Peters [164])

largest eddy size is defined by its integral length l_{I}. The kinetic energy is proportional to u'^2, where u' describes the turbulent velocity fluctuations. The dissipation rate ϵ is then defined from the ratio of the kinetic energy and one turn-over time of this eddy $t_{\text{I}} = l_{\text{I}}/u'$ as:

$$\epsilon \sim \frac{u'^3}{l_{\text{I}}} \tag{2.20}$$

Based on his findings and the idea of an energy cascade, Kolmogorov derived the theoretical form of the energy spectrum of the different scales in a turbulent flow. A sketch of the resulting energy spectrum and its shape is shown in Fig. 2.1. The turbulent kinetic energy reaches its maximum

when the wavenumber corresponds to the inverse integral length scale L. For wavenumbers larger than the inverse integral length scale, the turbulent kinetic energy decreases with an exponent of -5/3. This region is called the 'inertial subrange' and ends when it reaches the inverse Kolmogorov scale.

2.2 Combustion

In the previous section, the conservation equations for mass, momentum, energy and species were introduced. But the chemical conversion of educts to products through exo- or endothermic reactions was only briefly mentioned by introducing the species source term Eq. (2.6). In the reactive flows investigated in this work, the source term results mainly from reactions that occur through combustion. The term combustion is defined as the exothermic reaction of oxygen with a combustible substance (fuel). This substance can be gaseous, liquid, or solid, whereby only liquid and gaseous fuels are used in this thesis. The reaction of oxidiser and fuel as reactants to the resulting products can be exemplarily shown in a global one-step reaction of methane (CH_4) and oxygen (O_2):

$$CH_4 + 2 \cdot O_2 \longrightarrow CO_2 + 2 \cdot H_2O \tag{2.21}$$

This reaction is a simplified description, while in reality, the conversion of fuel and oxidiser to the combustion products, water (H_2O) and carbon dioxide (CO_2), occurs through numerous elementary reactions with the formation of many intermediate species. Many of these reactions have already been studied and combined in detailed reaction mechanisms. The kinetics behind these reaction steps will be discussed in the following section. Further, the different modes of combustion will be introduced.

2.2.1 Reaction kinetics

Each chemical reaction during the combustion process takes place at a defined rate, which depends on the conditions of the system: the concentration of the chemical compounds, pressure, temperature, radiative effects or the presence of a catalyst. The forward or backward reaction of species A and B to AB can be written as:

$$A + B \rightleftharpoons AB \tag{2.22}$$

For a chemical one-step reaction of any complexity, the following stoichiometric equation represents a reaction in a more general way:

$$\sum_{\alpha=1}^{N_s} v'_\alpha \chi_\alpha \rightleftharpoons \sum_{\alpha=1}^{N_s} v''_\alpha \chi_\alpha \tag{2.23}$$

In this equation, v'_α and v''_α represent the stoichiometric coefficients of the educts and the products, respectively. χ is the arbitrary specification of all chemical species, and N_s is the total number of compounds involved. The reaction rate from reactants to products, and reverse, is based on the law of mass action [117]. The law states that the rate at which a chemical species disappears is proportional to the products of the reacting chemical species concentration $c_\alpha = \rho Y_\alpha / W_\alpha$ when each concentration is raised by a power equal to the corresponding stoichiometric coefficient. The net reaction rate RR_k for a reaction k is the difference between the forward ($RR_{k,\mathrm{f}}$) and backward rates ($RR_{k,\mathrm{b}}$) and is given as:

$$RR_k = RR_{k,\mathrm{f}} - RR_{k,\mathrm{b}} = q_{k,\mathrm{f}} \prod_{\alpha=1}^{N_s} (c_\alpha)^{v'_{k,\alpha}} - q_{k,\mathrm{b}} \prod_{\alpha=1}^{N_s} (c_\alpha)^{v''_{k,\alpha}} \tag{2.24}$$

here $q_{k,f}$ and $q_{k,b}$ are the specific forward and backward reaction-rate constants for reaction k. These reaction rates are temperature-dependent and can be calculated based on an Arrhenius equation as outlined in Eq. (2.25):

$$q = BT^n \exp\left(-\frac{E_\mathrm{a}}{R_\mathrm{u}T}\right) \tag{2.25}$$

Here B, E_a and R_u are the pre-exponential factor, activation energy, and the universal gas constant, respectively. The first term BT^n represents the collision frequency while the exponential function is the Boltzmann factor. The chemical source term $\dot{\omega}_\alpha$ for species α from Eq. (2.6) can then be determined as:

$$\dot{\omega}_\alpha = \sum_{k=1}^{N_r} \dot{\omega}_{k,\alpha} = W_\alpha \sum_{k=1}^{N_r} (v''_{k,\alpha} - v'_{k,\alpha}) R R_k \tag{2.26}$$

In this equation, N_r is the number of reactions. The source term couples the combustion chemistry with the flow solver and completes (closes) the transport equation of species mass fraction. Reactive flows can then be examined by solving the transport equations for mass (Eq. (2.2)), momentum (Eq. (2.4)), species (Eq. (2.6)) and energy (Eq. (2.17)). The thermodynamic variables are related by the ideal gas law, which is expressed by Eq. (2.27):

$$\frac{p}{\rho} = T\frac{R}{W} \tag{2.27}$$

2.2.2 Modes of combustion

The combustion community classically distinguishes two modes of combustion: non-premixed and premixed combustion. They differ in terms of the mixing of fuel and oxidiser. In premixed combustion, a combustible fuel-oxidiser mixture is generated before combustion, while separated fuel and oxidiser streams enter the flame zone in non-premixed combustion. Both situations were investigated in the present work and will be discussed in the following.

Premixed combustion

Possibly the oldest premixed laboratory flame was developed and studied by Bunsen in 1888 [117]. Gas turbines or internal combustion engines are technical combustion devices where the premixed combustion mode prevails. One of the most important quantities to characterize a premixed flame is the laminar flame speed s_L with which the flame propagates towards the unburnt (fresh) gas. The other important quantity is the laminar thermal flame thickness δ_L which determines the required mesh grid resolution to compute the flame and resolve the flame front. Both quantities depend on the fuel (methane, ethane, etc.), pressure, the mixture's temperature, and the equivalence ratio ϕ. The latter defines the ratio between the local oxygen (O) and fuel (F) mass fractions to its stoichiometric ratio and can be defined as [166]:

$$\phi = \left(\frac{Y_\mathrm{F}}{Y_\mathrm{O}}\right) / \left(\frac{Y_\mathrm{F}}{Y_\mathrm{O}}\right)_\mathrm{s} \tag{2.28}$$

The laminar flame speed can be determined according to Eq. (2.29) and can be calculated from a one-dimensional flame using a chemistry library, e.g. Cantera [62] with a detailed reaction mechanism. In this calculation, a steady-state flame characterized by an unburned gas mixture at $-\infty$ and a burned gas mixture at $+\infty$ is analyzed. By integrating the continuity equations, it is observed that the mass flow through the flame remains constant. Accordingly, the flame speed can be defined as follows:

$$(\rho s^0_\mathrm{L})_\mathrm{u} = (\rho u)_{-\infty} \tag{2.29}$$

The flame speed indicates how fast a flame propagates through a resting fuel gas mixture. There are various definitions for the laminar flame thickness, some of which require a calculation of a 1D flame, others can be determined from scaling laws. However, according to Poinsot [166], the most suitable estimation is the thermal flame thickness determined by using a one-dimensional temperature profile:

$$\delta_{\mathrm{th}} = \frac{T_{\mathrm{b}} - T_{\mathrm{u}}}{\max|\frac{\partial T}{\partial x}|} \tag{2.30}$$

The comparison of the flame thickness of a premixed flame with a non-premixed flame through their temperature profile is shown in Fig. 2.2. The premixed flame has typically a significantly

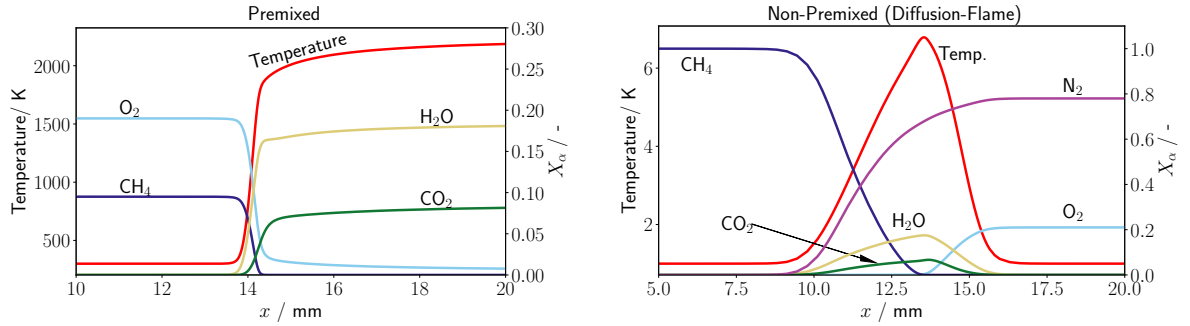

Figure 2.2: Spatial profiles of temperature, methane, oxygen, carbon dioxide and water mole fractions from a 1D simulation of a premixed (left) and a non-premixed (right) stoichiometric methane flame.

thinner flame front as a result of the reactants being both located in the fresh gases in a mixed state. The combustion process from unburnt reactants to burnt products can be quantified for a premixed flame by the combustion progress variable Y_p. The definition of this variable is not unique and can be chosen individually for every configuration while maintaining monotonicity over the entire combustion process. For methane combustion, for example, the products H_2O and CO_2 are suitable so that the progress can be defined as:

$$Y_{\mathrm{p}} = Y_{\mathrm{CO_2}} + Y_{\mathrm{H_2O}} \tag{2.31}$$

This definition of the combustion progress was found to be suitable for describing the reaction zone. In some cases, however, it may be of interest to include species that are of relevance downstream of the flame front, such as pollutants ($\mathrm{CO}, \mathrm{NO_x}$) or target products (nanoparticles, Fe_2O_3). In order to include these in the combustion progress, the following formulation was found suitable [83]:

$$Y_{\mathrm{p}} = \sum a_\alpha Y_\alpha + \sum b_\alpha (Y_{\mathrm{f},\alpha} - Y_\alpha) \tag{2.32}$$

The first term on the RHS is the sum of all product species to be considered for the progress description. The factor a is a weighting factor that allows species with a low concentration (nanoparticle precursor, pollutants) to have greater impact in the total combustion progress. This formulation also allows fuels to be used as progress species. The second term on the RHS describes the fuel species with a weighting factor b. From the combustion progress variable Y_{P}, the better known normalised combustion progress variable c can be calculated, which is $c = 0$ in the unburnt and $c = 1$ in the burnt gases:

$$c = \frac{Y_{\mathrm{p}} - Y_{\mathrm{p}}^{\mathrm{u}}}{Y_{\mathrm{p}}^{\mathrm{b}} - Y_{\mathrm{p}}^{\mathrm{u}}} \tag{2.33}$$

Here the superscript u indicates the unburnt state and b the burnt state.

Non-Premixed combustion

In a non-premixed flame configuration, oxygen and fuel are fed separately into the burning zone. Both streams mix in this region, and the reactants diffuse into the reaction zone before they react with each other. The process of mixing is slower than the reaction itself, and the combustion becomes controlled by mixing. Figure 2.2 (right) shows a non-premixed configuration. Instead of one inlet as in the premixed flame, there are two inlet streams: fuel from the left and air from the right. The advantage of non-premixed combustion is that mixtures exist that are either too rich or too lean to burn. In consequence, it is less dangerous than a premixed flame, as there is no flashback[2]. Another benefit is that there is no complex premixing required. The disadvantages of non-premixed combustion compared to premixed combustion are higher pollutant levels caused by higher temperatures and lower efficiency as there may not be enough oxidant to complete the reaction. In contrast to the premixed flame, the non-premixed flame is not characterized by a flame speed, as it does not propagate by itself. Furthermore, non-premixed flames have no characteristic flame thickness as this varies mainly with stretch and strain and not the fluid properties

An important quantity to describe non-premixed combustion is the mixture fraction Z, which characterizes the mixing between pure fuel ($Z = 1$) and oxidizer ($Z = 0$). Various definitions of the mixture fraction exist. In the general case, wherein there is an absence of oxygen in the fuel stream and no presence of fuel in the oxygen stream, the variable Z can be mathematically expressed as follows [166]:

$$Z = \frac{sY_\mathrm{F} - Y_\mathrm{O} + Y_\mathrm{O}^0}{sY_\mathrm{F}^0 + Y_\mathrm{O}^0} \tag{2.34}$$

In this expression, $s = (Y_\mathrm{O}/Y_\mathrm{F})_\mathrm{ST}$ represents the mass stoichiometric ratio, Y_F signifies the mass fraction of the fuel, Y_O denotes the mass fraction of the oxidizer, while Y_F^0 and Y_O^0 are the mass fractions of the fuel and oxidizer streams, respectively. In this definition of the mixture fraction, it should be noted that the mass of the species change during the reaction and is difficult to determine. Another definition of the mixture fraction can be derived by relating it to the chemical elements since their mass is conserved. Denoting m_j as the mass of all atoms j in the system, a_{ij} as the number of atoms of an element j in a molecule of species i, and W the molecular mass, one can define the mass fraction of element j as [164]:

$$Z_j = \frac{m_j}{m} = \sum_\alpha^{N_s} \frac{a_{\alpha j} W_j}{W_\alpha} Y_\alpha \tag{2.35}$$

For hydro-carbon fuels Bilger [11] proposed a mass fraction, which is based on the elemental mass fractions of carbon Z_C, hydrogen Z_H and oxygen Z_O as shown in Eq. (2.36).

$$Z = \frac{Z_\mathrm{C}/(mW_\mathrm{C}) + Z_\mathrm{H}/(nW_\mathrm{H}) + 2(Y_{\mathrm{O}_2,2} - Z_\mathrm{O})/(\nu'_{\mathrm{O}_2})}{Z_{\mathrm{C},1}/(mW_\mathrm{C}) + Z_{\mathrm{H},1}/(nW_\mathrm{H}) + 2Y_{\mathrm{O}_2,2}/(\nu'_{\mathrm{O}_2} W_{\mathrm{O}_2})} \tag{2.36}$$

In this formula, the variables m and n stand for the components of the hydrocarbon fuel, namely $\mathrm{C_mH_n}$. The variable $Y_{O_2,u}$ represents the mass fraction of unburned oxygen. The superscript numbers "1" and "2" denote the fuel and oxidant flow, respectively. The formula can be determined from numerical or experimental data of mass fractions. Often, instead of solving the equation directly, a transport equation for Z is solved, which describes the mixing in a system:

$$\frac{\partial \rho Z}{\partial t} + \frac{\partial \rho u_j Z}{\partial x_j} = \frac{\partial}{\partial x_j}\left(\rho D \frac{\partial Z}{\partial x_j}\right) \tag{2.37}$$

[2]Flashback: an uncontrolled upstream propagation of the flame

2.3 Multiphase flow

So far, only the calculation of a single gaseous phase has been discussed. For the gas phase synthesis of nanoparticles, however, the system under consideration is extended to account for the solid phase of the nanoparticles, resulting in a two-phase flow. This two-phase system may be further extended by a third liquid phase of spray droplets (occurs with spray flame pyrolysis). By considering three phases, the flow is denoted as multiphase flow. The distinction between the individual phases is made between dispersed or continuous. In the continuous phase, the assumption is made that the movement from one point to another can be made without leaving the medium [34], while the disperse phase is materially not connected. The additional phases are treated separately, and their case specific modelling is discussed below.

2.3.1 Spray

A spray is a two-phase flow with liquid droplets dispersed in a gas. Naturally occurring sprays can be sea sprays from crashing ocean waves or strong winds, but clouds or mist are also examples of naturally occurring sprays. In industry, various spraying processes are found for surface treatment, rocket propulsion, gas turbines [117], or the synthesis of nanoparticles from the spray flame [132], which is investigated in this thesis.

The process of spray formation from the liquid phase is called atomization and can be realized by the application of spray nozzles. Atomization includes the primary break up of the liquid flow and the secondary break up of the droplets. The break-up of the continuous liquid phase is triggered by small disturbances, such as the deformation of the liquid-gas interface or velocity fluctuations [5, 18]. There are theories for the analytical solution of atomisation, but they mostly apply just to laminar cases. Moreover, for most applications, an analytical calculation is not possible due to the various parameters that influence jet break-up, such as turbulence, nozzle influence, the thermodynamic state of the gas and liquid phases and the velocity profile. However, the resulting droplet size and velocity distributions are essential as boundary conditions for numerical modelling and simulations. The size and velocity distributions can be determined numerically by calculating the primary break up with a volume of fluid method (VOF) [80] or by measurements. In the present work, measurement data could be used as a boundary condition and primary and secondary break up was not computed. However, with the spray statistics, from measurements at a certain height above the burner, the spray droplets' evolution can be described using a Lagrangian particle method and is introduced in the following.

Liquid phase transport and evaporation

The Lagrangian particle method is used here to describe the transport and evaporation of the dispersed spray phase. The procedure was applied after primary and secondary break-up, with only the spray droplets distributed in the gas stream. In this method, each numerical Lagrangian particle represents a set of material particle that is subject to Newtown's law of motion. In contrast to the Eulerian approach, where a fixed control volume is observed, each individual spray droplet moves through time and space in its own coorinate system. For the droplets, the following simplifications were made:

- The gas density is much lower than that of the liquid.
- Spherical droplets.
- No internal flows in the droplets.

For the Lagrangian method, particle size and velocity distribution are needed initially, and an distinct droplet size and velocity is assigned to each particle from this distribution. Depending on the number of droplets and the computational capacity, it is also common that a Lagrangian

particle represents a parcel with several droplets. In this work, however, each particle was resolved. The position of individual particles changes due to the movement of the droplet and can be described by its velocity $u_{\mathrm{d},i}$ as follows:

$$\frac{\mathrm{d}x_{\mathrm{d},i}}{\mathrm{d}t} = u_{\mathrm{d},i} \tag{2.38}$$

The velocity of the droplet is computed from its acceleration, which in turn results from the drag and buoyancy or gravitational forces acting on the droplet:

$$\frac{\mathrm{d}u_{\mathrm{d},i}}{\mathrm{d}t} = a_{\mathrm{d},i} = \frac{f_1}{\tau_{\mathrm{d}}}(\tilde{u}_i - u_{\mathrm{d},i}) + (1 - \frac{\bar{\rho}}{\rho_{\mathrm{d}}})g_i \tag{2.39}$$

here, f_1, τ_{d}, u_i, $u_{\mathrm{d},i}$, ρ, ρ_{d}, and g_i denote the Stokes drag coefficient, the droplet relaxation time, the gas phase and droplet velocity, the gas phase and liquid density and the gravitational acceleration, respectively. The Stokes drag coefficient can be determined through a Schiller Neumann correlation [127]:

$$f_1 = \begin{cases} 1 + \frac{3}{20} Re_{\mathrm{d}}^{0.687} & Re_{\mathrm{d}} \leq 1000 \\ 0.44 \cdot Re_{\mathrm{d}} & Re_{\mathrm{d}} > 1000 \end{cases} \tag{2.40}$$

The droplet Reynolds number Re_{d} is calculated as:

$$Re_d = \frac{\rho |u_i - u_{d,i}| d_d}{\mu_m} \tag{2.41}$$

The droplet relaxation time τ_{d} for a Stokes flow results from the density of the liquid ρ_{d}, the droplet diameter, d_{d} and the viscosity of the surrounding fluid:

$$\tau_{\mathrm{d}} = \frac{\rho_{\mathrm{d}} d_{\mathrm{d}}^2}{18 \mu_{\mathrm{g}}} \tag{2.42}$$

As the droplets are assumed to be spherical, their change in size is evaluated due to the change in droplet mass $\dot{m}_{\mathrm{d}}$, which is calculated with an expression given by Baumgartner [7]. Dependent on the Schmidt number Sc, the Sherwood number Sh, the Spalding number B_m for the mass transfer, and the current mass of the droplet m_{d} according to the Eq. (2.43):

$$\frac{\mathrm{d}m_{\mathrm{d}}}{\mathrm{d}t} = - \frac{Sh \; m_{\mathrm{d}}}{3Sc \; \tau_{\mathrm{d}}} \ln(1 + B_m) \tag{2.43}$$

The Spalding number is calculated as following:

$$B_m = \frac{Y_{\mathrm{F}}^{\mathrm{S}} - Y_{\mathrm{F}}^{\infty}}{1 - Y_{\mathrm{F}}^{\mathrm{S}}} \tag{2.44}$$

This expression depends on the mass fraction at the surface Y_F^S and the mass fraction in the droplet surrounding distant field Y_{F}^{∞}. The surface fuel mass fraction can be determined using Raoult's law, assuming that the mole fraction at the surface $X_{\mathrm{F}}^{\mathrm{S}}$ is equal to the ratio of the partial pressure of the fuel vapour to the total pressure of the gas. Raoult's law reads:

$$Y_{\mathrm{F}}^{\mathrm{S}} = \frac{X_{\mathrm{F}}^{\mathrm{S}}}{X_{\mathrm{F}}^{\mathrm{S}} + (1 - X_{\mathrm{F}}^{\mathrm{S}}) \frac{W}{W_{\mathrm{F}}}} \tag{2.45}$$

with W_{F} being the molar mass of the surrounding fuel and W the molar mass of the droplet. The mole fraction may be determined using the Clausius-Clapeyron equation according to Eq. :

$$X_{\mathrm{F}}^{\mathrm{S}} = \exp\left[\frac{L_v}{R_m/W}\left(\frac{1}{T_{\mathrm{b}}} - \frac{1}{T_{\mathrm{S}}}\right)\right] \tag{2.46}$$

with the latent heat L_v (here $L_v = 846,000\,\mathrm{J/kg}$), the boiling temperature T_b (here $T_\mathrm{b} = 351,55\,\mathrm{K}$) and the local temperature of the droplet T_d. The change in temperature is calculated using the widely used infinite conductivity model [34, 38, 190], which is popular due to its computational efficiency and simple implementation:

$$\frac{\mathrm{d}T_\mathrm{d}}{\mathrm{d}t} = \frac{\mathrm{Nu}\ c_p}{3Pr\ c_{p,\mathrm{d}}} \frac{T - T_\mathrm{d}}{\tau_\mathrm{d}} \frac{\ln(1+B_h)}{B_h} + \frac{\dot{m}_\mathrm{d} L_v}{m_\mathrm{d} c_{p,\mathrm{d}}} \tag{2.47}$$

In this equation $c_{p,\mathrm{d}}$ (here $c_{p,\mathrm{d}} = 2440\,\mathrm{J/kg/K}$) denotes the specific heat of the liquid in the droplet. The Prandtl number is noted here as Pr, the Nusselt number as Nu, the gas temperature as T_g and the Spalding number for heat transfer as B_h, which is defined as:

$$B_h = \frac{c_p}{L_v}(T_\mathrm{g} - T_\mathrm{d}) \tag{2.48}$$

The influence of the convective flow around the droplets is taken into account by the Nusselt and the Sherwood number, which both are calculated from the Ranz-Marshall correlation [183] as follows:

$$Sh = 2 + 0.552 Re^{1/2} Sc^{1/3} \tag{2.49}$$

$$Nu = 2 + 0.552 Re^{1/2} Pr^{1/3} \tag{2.50}$$

2.3.2 Nanoparticle synthesis[3]

Two methods can characterize the production of nanoparticles. The top-down method, in which particles are split off from existing bulk material. Or the bottom-up approach, in which particles synthesize from a fluid phase. Examples of the top-down method are classical milling processes or laser beam lithography used to create nanostructures for semiconductors. However, this work only handles the bottom-up method. Examples include the sol-gel method, in which the precursor is dissolved in a solution and forms nanoscale particles through reactions, or the synthesis of nanoparticles from a vapour phase. The method of interest in this work is the gas phase synthesis, using precursors[4] in liquid or gaseous form. The process of gas phase synthesis is shown in Fig. 2.3 and can be described in simplified manner as follows: the precursor is injected into the reactor chamber and heated by a secondary heat source. This secondary heat sources might be microwave

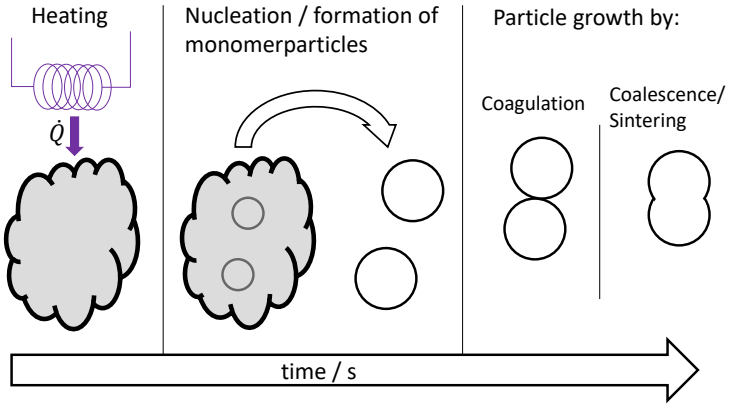

Figure 2.3: Illustrates the detailed internal processes during particle synthesis from the gas phase, i.e., from a gaseous precursor to aggregates.

plasma, heated walls, or flames. After injection, the precursor decomposes due to the heat and subsequently the first nanoparticles, the monomer particles, form from the gas phase. Once

[3]Synthesis: Conversion of two or more elements into a new unit
[4]Precursor: Starting material for chemical reactions

monomer particles have formed, further growth is characterized by three processes: coagulation, surface growth and sintering/coalescence. Coagulation corresponds to the collision of two solid particles, creating a larger particle, while coalescence or sintering corresponds to the melting of the two particles. Surface growth refers to the formation of particles on the surface of an existing particle.
In the following section, the relevant growth processes of particle formation and coagulation are presented as well as the derivation of the general equation for the dynamics with which particle growth can be determined over time and space.

Particle formation

The particle formation process may be split into homogeneous nucleation and heterogeneous condensation. The first subprocess represents the generation of new particles, while the second process represents the condensation on existing particles, i.e. surface growth. Both can happen either sequentially or simultaneously in the same volume package. In the following, the overall process may be illustrated by a laminar fame utilised for the production of nanoparticles. The starting point is mixing the precursor with the fresh fuel gas and feeding it into the combustion chamber. In the combustion chamber, the gas ignites, and the flame heats the mixture, which leads to a precursor decomposition and its reaction with intermediates. As a result, condensable products are formed, leading to a supersaturated[5] state that is not at equilibrium. From this state, the gas tends back to equilibrium either by homogeneous nucleation or heterogeneous condensation.

The processes happen spontaneously, on small scales, and the exact process is very complex and uncertain. Still, for simulations of nanoparticle growth, it is crucial to understand the process to determine the formation rate, i.e., the number of particles per time and the distribution of the condensed material for the particle size.

For **homogenous nucleation**, the saturation state of the gas plays an important role and is stated by the saturation ratio S as:

$$S = p_1/p_e \tag{2.51}$$

with p_1 being the partial pressure of the species and p_e being the vapour pressure along a flat surface [110]. The gas is saturated for $S = 1$ and supersaturated for $S > 1$. A snapshot of a diluted saturated vapour would show single molecules or atoms and small collections of molecules, and extremely rare, larger clusters. These clusters can exist on any scale and at different temperatures or pressures. However, their lifetime is very short, and they dissolve again when atoms leave them. These clusters' overall concentration remains constant while the gas is at a saturation equilibrium, and no nucleation of a stable phase occurs. For $S > 1$, more molecules bombard the clusters, and a higher number of larger clusters is formed than at $S = 1$ and may reach a size (radius) at which they are thermodynamically stable. The radius is called the critical radius and is referred to here as r_c^*. The higher the saturation ratio, the smaller the cluster radius that can serve as a stable nucleus for condensation [51]. The critical cluster radius may be determined by its relation with the free energy change:

$$\Delta G = \underbrace{-\frac{4}{3}\pi\frac{r^3}{V_m}k_B T \ln(S)}_{\text{volume free energy}} + \underbrace{4\pi r^2\sigma}_{\text{surface free energy}} \tag{2.52}$$

Here V_m is the cluster volume, k_b is the Boltzmann's constant, and σ is the surface tension. For a spherical cluster with the radius r, ΔG is composed of the energy released for the creation of the volume (first term RHS) and the energy consumed to maintain an interface between the gas and the solid interface (second term RHS) [147]. If the energy required to create the nucleus surface is greater than the energy released from the creation of the volume, it remains unstable. Figure

[5]Supersaturation: the concentration of a solute exceeds the concentration determined by the equilibrium solubility value

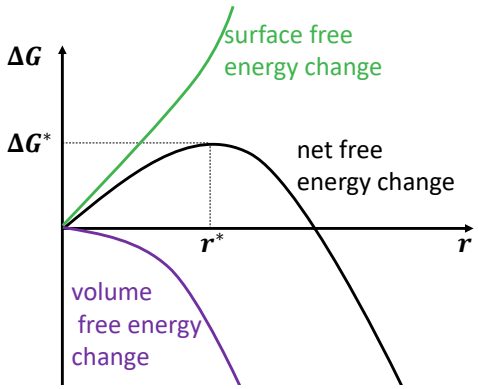

Figure 2.4: Change in free energy during the particle nucleation process.

2.4 shows the change of free energy along the particle radius. This maximum is the energy barrier that a cluster needs to pass to achieve a stable state and is calculated according to equation:

$$\frac{\partial \Delta G}{\partial r} = -4\pi \frac{r^2}{V_m} k_B \ln(S) + 8\pi r\sigma \tag{2.53}$$

Rearranging Eq. (2.53) leads to the Kelvin relation for the critical cluster radius at which a cluster becomes stable:

$$r_c^* = \frac{2\sigma V_m}{k_B T \ln(S)} \tag{2.54}$$

Equation (2.54) implies that the higher the saturation ratio, the smaller the cluster radius that can serve as a stable nucleus for homogeneous nucleation [51, 98, 238].

During **heterogeneous condensation**, clusters are condensate on the surface of existing particles [110] and the process is therefore often called surface growth. The supersaturation in this process does not have to be as high as for homogeneous nucleation since the presence of the foreign substrate reduces the surface energy due to a smaller surface area. Since the contact area between the foreign substrate and the newly formed particle has no impact on the surface energy of the particle. Due to the lower surface energy, the energy barrier that has to be overcome for nucleation also becomes smaller. At the same supersaturation, the critical particle radius for heterogeneous condensation is smaller than homogeneous nucleation. Consequently, the heterogeneous process is dominant when both processes occur simultaneously. The maximum surface energy reduction can be achieved when the existing substrate and the nucleating substrate are the same material. Then the process is called secondary nucleation. However, the parameters necessary to calculate the critical radius are unknown for many of the particles produced in material synthesis. The data is known only for well-studied systems like TiO_2 or SiO_2 and many elements (Ag, Al, etc.).

Besides homogeneous and heterogeneous condensation, there is also **collision controlled nucleation**. This type of nucleation occurs when there is no thermodynamic barrier to nucleation, i.e., when the critical diameter is smaller than the monomer size (in the order of $r = 0.1\,\text{nm}$, i.e., the size of an atom or molecule that nucleates) [110]. Then the process of particle formation proceeds so that the precursor decomposes and reacts with the environment until the particle molecule is formed, which immediately nucleates and passes into the solid phase. In this particular case, the nucleation is equivalent to the reaction, in the sense that any reactant molecule that forms a product monomer, in essence, forms a thermodynamically stable particle. In general, this is the case for most metal oxide particles such as TiO_2, Al_2O_3 or Fe_2O_3, and the reaction is indistinguishable from classical nucleation. However, it is important to note that this should take place under moderate temperatures at up to about $T = 1800\,\text{K}$ [110] due to unstable oxygen bindings. The particles considered in this work are all Fe_2O_3, and the nucleation and subsequent growth

are mainly collision or coagulation and coalescence controlled, which are discussed and presented in the following sections.

Coagulation

Coagulation describes the irreversible process when particles collide, stick to each other, and form an irregular new cluster called (soft) agglomerate. During the coagulation process, the mean particle size increases, and the particle number concentration[6] decreases while the total particle volume and -mass concentrations are conserved. The primary driving mechanism for the collision of individual particles is Brownian molecular motion, but electrical, gravitational, shear and other forces can also act as drivers. A vital quantity to describe coagulation is the coagulation frequency β_{ik}, which describes the rate of collisions between two-particle classes i and k. In the following, the basic equations for calculating β_{ik} are first presented only for spherical particles. Based on these, two modified variants are discussed, which allow calculating the coagulation frequency for particle aggregates with a fractal dimension and further overcome deficiencies of the basic equations.

The calculation depends on the prevailing regime distinguished by the Knudsen number ($Kn = \lambda/r$), i.e., the continuum regime ($Kn < 0.1$) and the free molecular regime ($Kn > 10$). In the continuum regime, the radius of a particle is larger than the mean free path of the surrounding gas, while in the free molecular regime, a particle is smaller than the mean free path. Based on this classification, the coagulation frequency in the continuum region can be calculated using the Stokes-Einstein relation as follows [204]:

$$\beta_{ik} = \frac{2k_\mathrm{B}T}{3\mu}\left(\frac{1}{v_i^{1/3}} + \frac{1}{v_k^{1/3}}\right)\left(v_i^{1/3} + v_k^{1/3}\right) \tag{2.55}$$

Here μ is the viscosity of the surrounding gas, and v is particle volume. In the free molecular range, the coagulation frequency is derived from an equation of the kinetic theory of gases, which describes collisions between aggregate particles that behave like rigid elastic spheres [51, 204]:

$$\beta_{ik} = \left(\frac{3}{4\pi}\right)^{1/6}\left(\frac{6k_\mathrm{B}T}{\rho_\mathrm{p}}\right)^{1/2}\left(\frac{1}{v_i} + \frac{1}{v_k}\right)^{1/2}\left(v_i^{1/3} + v_k^{1/3}\right) \tag{2.56}$$

here ρ_p is the bulk material density. Interested readers can find a detailed derivation of both equations in the book of Seinfeld et al. [204].
When applying these equations in simulations, the following problems might arise:

- Neither of the two equations (Eq. (2.55) and Eq. (2.56)) correctly describes the coagulation frequency in the transition range $0.1 < Kn < 10$
- The particle size in an aerosol may vary over at least two orders of magnitude, resulting in a smooth transition from free molecules to the continuum range in this aerosol
- Size distribution dynamics depend strongly on the agglomerate structure, and the behaviour differs significantly from that of spherical particles [51]

The influence of the agglomerate structure can be taken into account following Kruis et al. [115], who used the collision diameter d_c instead of the spherical particle diameter or volume. This diameter is equivalent to a round particle diameter with the same aggregate collision characteristics and is calculated as:

$$d_\mathrm{c} = d_\mathrm{p} \cdot n_\mathrm{p}^{1/D_\mathrm{f}} = d_\mathrm{p} \cdot \left(\frac{v}{v_\mathrm{p}}\right)^{1/D_\mathrm{f}} \tag{2.57}$$

[6] Particle number concentration is the total number of particles per unit volume of a gas

It is calculated from a mean primary particle diameter $d_\mathrm{p} = 6v/a$ (here a is the surface of an aggregate and v the volume), number of primary particles n_p in an aggregate, and the fractal dimension D_f of the aggregate, which is $D_\mathrm{f} = 3$ if it is spherical and $D_\mathrm{f} = 1.8$ if it has a long chain structure. The difference between primary particle diameter, collision diameter, and aggregate or averaged diameter is sketched in Fig. 2.5. In order to take into account the free molecular

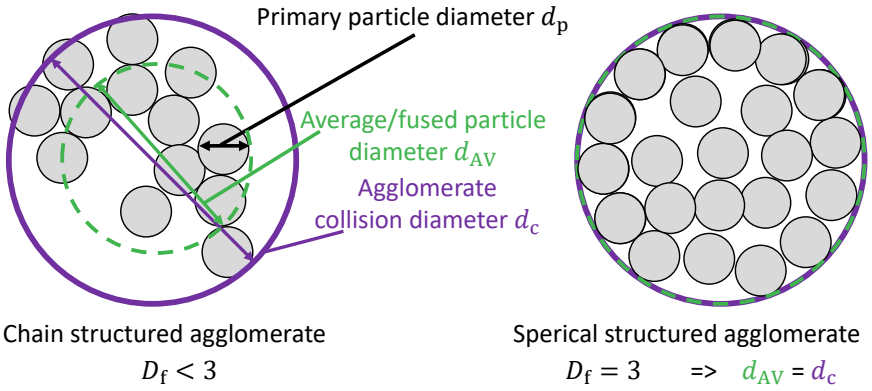

Figure 2.5: Schematic illustration of different diameter definitions Kruis et al. [115] for a long chained particle ($D_\mathrm{f} = 1.7$) and a spherical/fused particle ($D_\mathrm{f} = 3$).

($Kn > 10$), the continuum ($Kn < 0.1$) and the transition region ($0.1 < Kn < 10$) in an aerosol cloud, two different methods for calculating the coagulation rate were used in the present work. **The first approach** uses an interpolation method covering the entire range from free molecular to continuum regime and was first introduced by Fuchs [52]:

$$\beta_{ik} = 2\pi(D_{\mathrm{P},i} + D_{\mathrm{P},k})(d_{\mathrm{c},i} + d_{\mathrm{c},k}) \left(\frac{d_{\mathrm{c},i} + d_{\mathrm{c},k}}{d_{\mathrm{c},i} + d_{\mathrm{c},k} + 2\sqrt{g_{\mathrm{P},i}^2 + g_{\mathrm{P},k}^2}} + \frac{8(D_{\mathrm{P},i} + D_{\mathrm{P},k})}{(d_{\mathrm{c},i} + d_{\mathrm{c},k})\sqrt{v_{\mathrm{P},i}^2 + v_{\mathrm{P},k}^2}} \right)^{-1} \tag{2.58}$$

where D_P is the particle diffusion coefficient, g_P is the transition parameter, and c_P is the particle velocity. The particle diffusion coefficient D_P is calculated according to the Einstein-Smoluchowski relation [125] as outlined below:

$$D_\mathrm{P} = \frac{k_\mathrm{B} T}{3\pi\mu d_\mathrm{c}} C_\mathrm{c} \tag{2.59}$$

Here C_c is the Cunningham slip correction factor [204]. For $Kn << 1$, the correction is unity, and Eq. (2.59) becomes the Stokes-Einstein relationship based on a no-slip assumption applicable for the continuum regime. While for $Kn >> 1$, the correction factor transforms the expression and allows to calculate the free molecular regime ([204]). There are various definitions of the factor [100, 115, 204], but the results differ only slightly. In this work the definition from Kruis et al.[115] was used in Eq. (2.60):

$$C_\mathrm{c} = \frac{5 + 4Kn + 6Kn^2 + 18Kn^3}{5 - Kn + (8 + \pi)Kn^2} \tag{2.60}$$

The average particle velocity c_P in Eq. (2.58) is determined from the density of the particulate matter ρ_P and the particle volume v, according to Eq. (2.61).

$$v_\mathrm{P} = \sqrt{\left(\frac{8 k_\mathrm{B} T}{\pi \rho_\mathrm{p} v} \right)} \tag{2.61}$$

The transition parameter g_P in Eq. (2.58) accounts for the transition from the continuum to the free molecule regime and is determined from the particle mean free path l_P and the particle collision diameter d_c.

$$g_\mathrm{P} = \frac{(d_\mathrm{c} + l_\mathrm{P})^3 - (d_\mathrm{c}^2 + l_\mathrm{P}^2)^{3/2}}{3 d_\mathrm{c} l_\mathrm{P}} \tag{2.62}$$

The equation for the mean free path of the particles is then:

$$l_\mathrm{P} = \frac{8 D_\mathrm{P}}{\pi v_\mathrm{P}} \tag{2.63}$$

The Fuchs interpolation method is somewhat complex and, in this work, only applied to a bi-modal size distribution model. **The second approach** is a global collision frequency based on the harmonic mean. The definition is considered to be more straightforward and can, therefore, be better optimised. The approach was first introduced by Pratsinis et al. [173] for a monodisperse particle size distribution function (PSDF) and further developed and tested for a broader range of PSDF by Kazakov et al. [100]. Instead of the semiempirical formula by Fuchs (Eq. (2.58)), they approximated the whole regime from free molecular to continuum with the harmonic mean of each limit value.

$$\beta_{ik} = \frac{\beta_{ik}^c \beta_{ik}^\mathrm{f}}{\beta_{ik}^\mathrm{f} + \beta_{ik}^\mathrm{c}} \tag{2.64}$$

Here the superscripts c and f refer to the continuum and free molecular regime, respectively. For the free molecular regime, the coagulation frequency is defined as:

$$\beta_{ik}^\mathrm{f} = J \left(\frac{\pi k_\mathrm{B} T}{2} \right)^{1/2} \left[\frac{1}{m_i} + \frac{1}{m_k} \right]^{1/2} (d_{\mathrm{c},i} + d_{\mathrm{c},k})^2 \tag{2.65}$$

In the present work, $J = 1$ was set. In the context of soot [100], and for oxidizing nanoparticles like silica [140, 210], $J = 2.2$ is used in the literature to mimic the increase in coagulation frequency due to van der Waals forces. For iron particles, there was good agreement by using the Fuchs interpolation kernel without the factor J. The collision frequency in the continuum regime is:

$$\beta_{ik}^\mathrm{c} = \frac{2 k_\mathrm{B} T}{3 \mu} \left[\frac{C_{\mathrm{c},i}}{d_{\mathrm{c},i}} + \frac{C_{\mathrm{c},k}}{D_{\mathrm{c},k}} \right] (d_{\mathrm{c},i} + d_{\mathrm{c},k}) \tag{2.66}$$

In Kazakov's work, the Cunningham slip correction factor C_c was suggested as:

$$C_\mathrm{c} = 1 + 1.257 \cdot \frac{2\lambda}{d_\mathrm{c}} \tag{2.67}$$

In summary, the calculation of coagulation can be divided into two regimes: the free molecular and the continuum regime. Both regimes can occur in a particle cloud with a broad PSD and can be calculated together either with the Fuchs interpolation method or the harmonic means approach. We found the harmonic mean better to optimise and hence less computationally costly for the sectional model, while the computational costs with both methods are moderate for the monodisperse and bi-modal model. Both have been introduced and applied in this work.

Coalescence / sintering

Sintering occurs after an agglomerate of at least two particles has formed. It describes the fusion of these particles. During the process, a material transport occurs at the interfaces between them, and their surfaces area reduces although their mass is conserved. The dominating transport mechanism for liquids (e.g., silica) is viscous flow, and for solids (e.g., crystallites) diffusion.

With liquids, the sintering process is complete when the agglomerate has reached its equilibrium when the thermodynamic potential of the agglomerate has reached a minimum value, and

forms a sphere. This condition implies that the agglomerate has reached a state of maximum stability with the lowest energy input. To illustrate this principle, it is important to consider the role of thermodynamic forces at the interfaces of the individual particles within the agglomerate.

The free enthalpy associated with these particle interfaces is primarily influenced by two factors: surface tension and the extent of the boundary layer surrounding the agglomerate. In this context, surface tension can be considered a constant property that remains relatively unchanged throughout the process. Therefore, in order to minimize the free enthalpy of the particle interfaces, the surface area of the individual particles and grain boundaries must be reduced until equilibrium form (sphere) is reached.

The equilibrium form of solids is presumable determined by a Wulff construction[7], but exact calculations have not been made [51]. A common assumption to determine the sintering process is that two spheres are in contact, equidistant to the liquid droplets in contact, and the particles sinter through grain boundary diffusion. The process starts with the fast growth of a sinter neck (shown in Fig. 2.6) driven by lattice diffusion and reduces after a short time, and the particles will not merge further. However, the sintering for solids and liquids can be characterized by

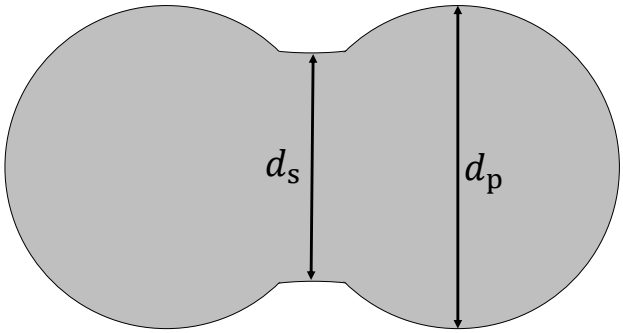

Figure 2.6: Schematic of two particles during the sintering process.

the characteristic sintering time τ, which is also an indicator for the particle morphology [115]. Expressions for τ are based on so-called early-stage sintering models that describe the neck growth between the two particles. Therefore the height of the neck is described by a characteristic diameter d_s, which is indicated in Fig. 2.6, that grows until the equilibrium particle shape is formed. In its early stage ($d_\mathrm{s}/d_\mathrm{p} < 0.3$) the growth can be:

$$\left(\frac{d_\mathrm{s}}{d_\mathrm{p}}\right)^n = C\frac{t}{d_\mathrm{p}^m} \tag{2.68}$$

The power-law exponents, m and n depend on the sintering mechanism, t is the sintering time, and C is the material and temperature-dependent coefficient. With the according material-dependent coefficients, Eq. (2.68) allows the determination of the characteristic sintering time, as demonstrated for silica by Kruis et al. [115]. For the use in particle models, however, the change of the aggregate surface a is still meaningful and can be calculated from the following relaxation approach using the characteristic sintering time:

$$\frac{\partial a}{\partial t} = \frac{1}{\tau}(a - a_\mathrm{s}) \tag{2.69}$$

Here, a_s is the surface area of a completely fused aggregate. The sintering time and temperature required to fuse towards equilibrium shape depend on the aggregate's size, shape, and material, which are often unknown. In general, it can be stated that high temperatures lead to almost immediate sintering after contact, resulting in large individual particles, while lower temperatures lead to slower sintering, producing fractal-like agglomerates.

[7]Wulff construction method determines the equilibrium shape of a droplet or crystal with a fixed volume inside a separate phase.

Particle transport equation

The individual processes of formation and growth of single particles during the gas-phase synthesis have been discussed in the previous section. In the following, the description of the overall process, including particle transport, is presented. For this purpose, the individual particle is not considered any more, instead a particle size distribution n is examined. This distribution can take two forms, a discrete[8] or a continuous[9] form [51], and the change in both distributions due to gas-phase synthesis can be accounted for in time and space by the general dynamic equation (GDE), often referred to as the population balance equation. The discrete form is only chosen for small particles ($d_\mathrm{p} < 50\,\mathrm{nm}$) when the individual particles consist of only a few thousand molecules [51]. The GDE for the discrete particle size is outlined in Eq. (2.70):

$$\frac{\partial n_k}{\partial t} + (u_j + u_j^\mathrm{e})\frac{\partial n_k}{\partial x_j} = \frac{\partial}{\partial x_j}\left(D_{\mathrm{p},k}\frac{\partial n_k}{\partial x_j}\right) + \left[\frac{\partial n_k}{\partial t}\right]_\mathrm{growth} + \left[\frac{\partial n_k}{\partial t}\right]_\mathrm{coagulation} \tag{2.70}$$

Here k represents the number of molecules in a particle, u is the gas velocity, u^e is a superficial velocity caused by external forces such as gravitation or thermophoresis, and D_p is the diffusion coefficient Eq. (2.59). For a defined volume, diffusion and convection terms describe the change of n by the means of transport out off or into the control volume. The growth term represents the processes of nucleation, condensation and evaporation, while the coagulation term represents the change of n by coagulation. The coagulation source term may be determined for the discrete size distribution n, using the coagulation frequency β_{ik} as shown in Eq. (2.71).

$$\left[\frac{\partial n_k}{\partial t}\right]_\mathrm{coagulation} = \begin{cases} -\sum_{i=1}^{k_\mathrm{max}} \beta_{ik} n_i n_k & \text{for} \quad k = 1 \\ \frac{1}{2}\sum_{l=1}^{k_\mathrm{max}} \beta_{il} n_i n_l - \sum_{i=1}^{k_\mathrm{max}} \beta_{ik} n_i n_k & \text{for} \quad k > 1 \end{cases} \tag{2.71}$$

It is common to change from the discrete size distribution to the continuous form when the particles become larger than the respective maximum discrete size [51]. However, this transition requires care. Not only does the distribution function n_k change to n, but the coagulation term becomes:

$$\left[\frac{\partial n}{\partial t}\right]_\mathrm{coagulation} = \frac{1}{2}\int_0^v \beta(\tilde{v}, v-\tilde{v}) n(\tilde{v}) n(v-\tilde{v})\mathrm{d}\tilde{v} - \int_0^\infty \beta(\tilde{v}, v) n(v) n(\tilde{v})\mathrm{d}\tilde{v} \tag{2.72}$$

If then Eq. (2.72) is substituted into Eq. (2.70) and n_k is replaced by n, the subsequent GDE for a continuous distribution is obtained:

$$\begin{aligned} &\frac{\partial n}{\partial t} + (u_j + u_j^\mathrm{e})\frac{\partial n}{\partial x_j} = \frac{\partial}{\partial x_j}\left(D_\mathrm{p}\frac{\partial n}{\partial x_j}\right) + \left[\frac{\partial n}{\partial t}\right]_\mathrm{nucleation} + \\ &\frac{1}{2}\int_0^v \beta(\tilde{v}, v-\tilde{v}) n(\tilde{v}) n(v-\tilde{v})\mathrm{d}\tilde{v} - \int_0^\infty \beta(\tilde{v}, v) n(v) n(\tilde{v})\mathrm{d}\tilde{v} \end{aligned} \tag{2.73}$$

The presented discrete and continuous GDE's can only be solved directly for very simplified and exceptional cases. Usually, they are transferred into a more straightforward form and then solved numerically. Common simplified models of the GDE are discrete, sectional, or moment methods [110]. The sectional, the monodisperse model, and the modified monodisperse model (bi-modal model) will be introduced in the next chapter, while for all other PBE models, the fundamentals and model principles are explained by Ramkrishna [182], and Friedlander [51].

[8] The number of particles at a location and time is counted and plotted for a fixed particle diameter.
[9] Draws a continuous function through the maxima of the discrete distribution.

Chapter 3
Modelling of reactive particle laden flows

The governing equations of fluid flow presented in Chapter 2 can directly be used to describe any non-reacting or reacting flow and particle synthesis. But the cost of computation is a limiting factor for most relevant flows in technical applications or in nature, and only very small and abstract flow problems can be described without any modelling assumptions. Over the years, many models have been developed to investigate reactive flow problems from laboratory to industrial scale such as the Smagorinsky Modell [214] or the flamelet generate manifolds approach (FGM) [231]. In the following, the models used in this work are introduced, distinguishing between models used to describe turbulent flows, combustion, and nanoparticle synthesis from the gas phase.

3.1 Turbulent flow modelling

The smallest scale that occurs in a turbulent flow is the Kolmogorov microscale η_K (Eq. (2.19), and in order to describe a flow and its features correctly, the computational grid spacing must be smaller than η_K. This statement might be visualised by Fig. 3.1, assuming the smallest turbulent structure to be a vortex of diameter η_K. The Navier-Stokes equations calculate an averaged

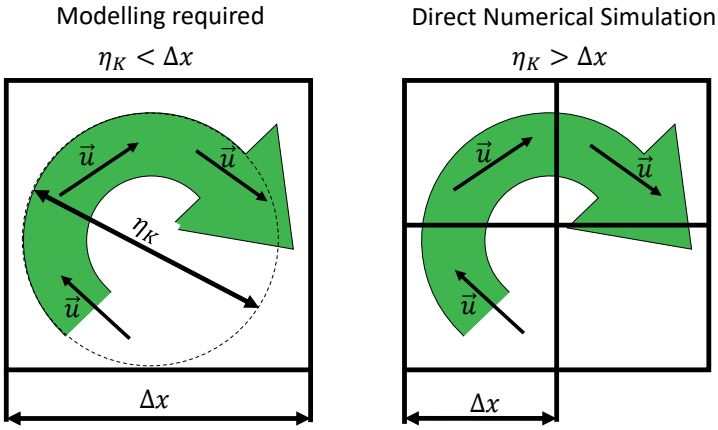

Figure 3.1: Sketch of the smallest possible vortex in a turbulent flow and its resolution on a computational grid.

momentum over the present cell (here with the size Δx) using the finite volume method, hence, the vortex can only be resolved by computational grids smaller than the vortex. Calculations with such a high resolution are referred to as Direct Numerical Simulation (DNS), in which the Navier Stokes equations are fully solved spatially and temporally by resolving the energy-dissipating scales of the turbulent spectrum, without any model assumptions. Unfortunately, typical Kolmogorov scales range in the micrometre size for medium and high Reynolds number flows, and the required resolution often exceeds the available computer resources. Therefore, there are two paradigms to model turbulence and mimic the influence on the main flow. The first paradigm is known as Large Eddy Simulation (LES) which aims for the resolution of the energy carrying structures within the energy spectrum and expresses the influence of the dissipative structures - which are assumed to behave universal - in a model. The method allows for the observation of temporal changes and fluctuations. The second paradigm is the Reynolds Averaged

Navier Stokes (RANS) equation simulation approach. As the name implies, the time-averaged conservation equation is solved and the artificial viscosity models the turbulence and its effects on the flow field. All three approaches are presented and explained below.

3.1.1 Direct numerical simulations

In Direct Numerical Simulation, the transport equations Eq. (2.2), (2.3), and (2.17) are solved directly without any modelling. The temporal and spatial resolution must be high enough to resolve all relevant scales. Spatially, the smallest scale in most cases is the Kolmogorov scale, and thus the required grid resolution is given as:

$$\Delta_{\mathrm{m}} \sim \eta_{\mathrm{K}} \tag{3.1}$$

With the smallest scale η_{K} and the largest scale, the integral length scale l_{I}, the approximate number of cells n_{t} to solve the flow problem can be determined for one dimension and related to the Reynolds number as follows [172]:

$$n_{\mathrm{t}} \approx \frac{L}{\Delta} \approx \left(\frac{Lu'}{\nu}\right)^{3/4} = Re_{\mathrm{t}}^{3/4} \tag{3.2}$$

Assuming an isotropic equidistant mesh results in a total number of cells of $N_{\mathrm{t}} = n_{\mathrm{t}}^3$, which leads to the following relationship with the turbulent Reynolds number:

$$N_{\mathrm{t}} \propto Re_{\mathrm{t}}^{9/4} \tag{3.3}$$

While these are the limiting factors in spatial dimensions, the only limiting factor in time is the maximum time step width Δt. It can therefore be determined for an explicit time integration scheme from the Courant-Friedrichs-Lewy condition (CFL), which is defined as follows:

$$\mathrm{CFL} = \frac{\Delta \mathrm{t} \cdot \mathrm{u}}{\Delta \mathrm{x}} \tag{3.4}$$

While for explicit schemes, the CFL number is a limiting factor and can not be larger than CFL=1, implicit schemes allow CFL numbers higher than CFL>1. The time and spatial dependence of the CFL number leads to the following cubic correlation between the computational effort and the turbulent Reynolds number:

$$\left(Re_{\mathrm{t}}^{3/4}\right)^4 = Re_{\mathrm{t}}^3 \tag{3.5}$$

These high computational costs currently limit DNS application to small Reynolds numbers and basic research and will not be possible for simulations of technically relevant plants in the near future.

3.1.2 Reynolds averaged simulations

In contrast to DNS, the Reynolds Averaged Navier Stokes computation enables the simulation of flows with higher Reynolds numbers, and with the scale of industrial, technical and scientific applications. However, unlike DNS, the Navier stokes equations (Eq. (2.2), (2.3), (2.17)) are not directly solved, but the time-averaged equations are solved, making the RANS approach a statistical method. For better understanding, some further information and mathematical techniques are therefore introduced before the equations are presented. During the averaging process, the respective quantities, i.e. the velocity vector u_i, the pressure p, the species mass fraction Y_α and the enthalpy h, are not directly averaged but first substituted with their Reynolds decomposition. For the Reynolds decomposition, the respective quantity is decomposed into its

expectation value (average) and its fluctuation around the expectation value. For example, for an arbitrary quantity ϕ, the decomposition would be as follows:

$$\phi(t) = \bar{\phi} + \phi'(t) \tag{3.6}$$

Here $\bar{\phi}$ represents the time-averaged portion and ϕ' the fluctuating portion of ϕ. Thus, the time average can be defined as follows:

$$\overline{\phi}(\vec{x}, t_1) = \frac{1}{t_1 - t_0} \int_{t=t_0}^{t=t_1} \phi(\vec{x}, t_1) \tag{3.7}$$

The time interval is chosen as infinite for stationary mean flows in a conventional RANS simulation or large enough to represent several integral time scales for an unsteady/periodic flow in an unsteady RANS (URANS) simulation. While URANS are only an option if the process time scale is much larger than the turbulent time scale. Only then will the turbulent spectrum and the process spectrum separate. As a result, the time-averaged fluctuating component becomes zero:

$$\overline{\phi'}(\vec{x}, t_1) = \frac{1}{t_1 - t_0} \int_{t=t_0}^{t=t_1} \phi'(\vec{x}, t_1) = 0 \tag{3.8}$$

It is essential to point out that this does not apply to $\overline{u'^2}$. While u' fluctuates between positive and negative values and adds up to zero on average, by its definition, u'^2 can only be positive and does not become zero on average. Consequently the Reynolds decomposition and averaging of the conservation equations results in an unclosed term that does not vanish, as shown here for the stress tensor $\overline{u_i' u_j'}$:

$$\overline{u_i u_j} = \overline{(\overline{u_i} + u_i')(\overline{u_j} + u_j')} = \overline{\overline{u}_i \overline{u}_j} + \cancel{\overline{\overline{u}_i u_j'}} + \cancel{\overline{u_i' \overline{u}_j}} + \overline{u_i' u_j'} = \overline{u}_i \overline{u}_j + \overline{u_i' u_j'} \tag{3.9}$$

As flows with variable density are considered in this work, a Favre averaging was also applied for products of ϕ and the density ρ. For these products the Favre averaging has the advantage that additional non-closed terms are avoided, which arise as follows:

$$\overline{\rho\phi} = \overline{(\overline{\rho} + \rho')(\overline{\phi} + \phi')} = \overline{\rho}\overline{\phi} + \overline{\rho'\phi'} \tag{3.10}$$

Favre averaging is a density-weighted averaging method and is defined as follows:

$$\widetilde{\phi} = \frac{\overline{\rho\phi}}{\overline{\rho}} \tag{3.11}$$

With the considerations made so far, the conservation equations for the Favre weighted and Reynolds averaged mass, momentum and enthalpy can be derived as (spray evaporation source terms are neglected):

$$\frac{\partial \overline{\rho}}{\partial t} + \frac{\partial \overline{\rho} \widetilde{u}_j}{\partial x_j} = 0 \tag{3.12}$$

$$\frac{\partial \overline{\rho} \widetilde{u}_i}{\partial t} + \frac{\partial \overline{\rho} \widetilde{u}_i \widetilde{u}_j}{\partial x_j} = -\frac{\partial \overline{p}}{\partial x_i} + \frac{\partial \overline{\tau}_{i,j}}{\partial x_j} - \frac{\partial \overline{\rho} \widetilde{u_i'' u_j''}}{\partial x_j} \tag{3.13}$$

$$\frac{\partial \overline{\rho} \widetilde{Y}_\alpha}{\partial t} + \frac{\partial \overline{\rho} \widetilde{u}_j \widetilde{Y}_\alpha}{\partial x_j} = \frac{\partial}{\partial x_j} \left(\overline{\rho} D_\alpha \frac{\partial \widetilde{Y_\alpha}}{\partial x_i} \right) + \overline{\dot{\omega}}_\alpha - \frac{\partial \overline{\rho} \widetilde{u_j'' Y_\alpha''}}{\partial x_j} \tag{3.14}$$

$$\frac{\partial \overline{\rho} \widetilde{h}}{\partial t} + \frac{\partial \overline{\rho} \widetilde{u}_j \widetilde{h}}{\partial x_j} = \frac{\partial}{\partial x_j} \left(\overline{\frac{\lambda}{c_p} \frac{\partial h}{\partial x_j}} \right) - \frac{\partial \overline{\rho} \widetilde{u_j'' h''}}{\partial x_j} \tag{3.15}$$

In Eq. (3.13) - (3.15), RHS is the last term consisting of turbulent fluctuating components. These terms mimic the interaction between the mean flow and the turbulent fluctuations, i.e.

how the mean flow drives the fluctuations and how the fluctuations affect the mean flow. The biggest challenge is to model this constant energy trade between turbulent kinetic and mean flow energy using only mean flow variables. The most prominent approach is the turbulent viscosity model proposed by Boussinesq [17, 201], which assumes that the turbulent fluctuations act on the transport equations like the molecular viscosity. Hence the last term in Eq. (3.13), the Reynolds stress tensor, can be modelled by an artificial turbulent dynamic viscosity μ_t and the turbulent kinetic energy k using the expression in Eq. (3.16).

$$\overline{\rho u_i'' u_j''} = \overline{\rho}\widetilde{u_i'' u_j''} = -\mu_t \left(\frac{\partial \widetilde{u}_i}{\partial x_j} + \frac{\partial \widetilde{u}_j}{\partial x_i} - \frac{2}{3}\delta_{ij}\frac{\partial \widetilde{u}_k}{\partial x_k} \right) + \frac{2}{3}\overline{\rho}k \tag{3.16}$$

The unresolved species ($\overline{\rho}\widetilde{u_j'' Y_\alpha''}$) and enthalpy ($\overline{\rho}\widetilde{u_j'' h''}$) turbulent fluxes can be generally closed using a classical gradient assumption:.

$$\overline{\rho}\widetilde{u_j'' Y_\alpha''} = -\frac{\mu_\mathrm{t}}{Sc_\mathrm{t}}\frac{\partial \widetilde{Y_\alpha}}{\partial x_i} \tag{3.17}$$

$$\overline{\rho}\widetilde{u_j'' h''} = -\frac{\mu_\mathrm{t}}{Pr_\mathrm{t}}\frac{\partial \widetilde{h}}{\partial x_i} \tag{3.18}$$

where Sc_t and Pr_t are the turbulent Schmidt number and Prandtl number respectively. The main challenge is to obtain the turbulent viscosity in the equation (3.13) - (3.15). Therefore three main approaches have been proposed over the years:

1. Algebraic models, which does not require additional transport equations, e.g. Prandtl's mixing length model [244]
2. One-equation closure, e.g. the k-equation or Spalart-Allmaras model [217, 244], which is widely used in aerospace applications
3. Two equation models, e.g. the k-epsilon (k-ϵ) model or SST [92, 139] for which two additional transport equations are solved for the turbulent kinetic energy and its dissipation

All these models have their advantages and disadvantages, and none is universally applicable. However, all of them have the advantage to be computationally cheap and allow to predict the mean behaviour of turbulent flows, and therefore the most prominent one, the k-epsilon, will be introduced here. In this approach, the turbulent viscosity is estimated from the turbulent kinetic energy k and its dissipation rate ϵ as:

$$\mu_\mathrm{t} = \overline{\rho} C_\mu \frac{k^2}{\epsilon} \tag{3.19}$$

where C_μ is a model constant, while two balance equations describe the turbulent kinetic energy and dissipation rate:

$$\frac{\partial \rho k}{\partial t} + \frac{\partial \overline{\rho}\widetilde{u}_i}{\partial k} = \frac{\partial}{\partial x_i}\left[\left(\mu + \frac{\mu_\mathrm{t}}{\sigma_k} \right) \frac{\partial k}{\partial x_j} \right] + 2\mu_\mathrm{t}\tilde{S}_{ij}\tilde{S}_{ij} - \overline{\rho}\epsilon, \tag{3.20}$$

$$\frac{\partial \rho \epsilon}{\partial t} + \frac{\partial \overline{\rho}\widetilde{u}_i}{\partial \epsilon} = \frac{\partial}{\partial x_i}\left[\left(\mu + \frac{\mu_t}{\sigma_\epsilon} \right) \frac{\partial \epsilon}{\partial x_j} \right] + \frac{\epsilon}{k}(C_{\epsilon,1}\mu_\mathrm{t}\tilde{S}_{ij}\tilde{S}_{ij} - C_{\epsilon,2}\overline{\rho}\epsilon). \tag{3.21}$$

Here $\tilde{S}_{ij}$ is the rate of strain which can be defined as:

$$S_{ij} = \frac{1}{2}\left(\frac{\partial \tilde{u}_i}{\partial x_j} + \frac{\partial \tilde{u}_j}{\partial x_i} \right) \tag{3.22}$$

The model constants in Eq. (3.20), and Eq. (3.21) are case dependent, but the commonly used values are [166]: $C_\mu = 0.09$, $\sigma_k = 1.0$, $\sigma_\epsilon = 1.3$, $C_{\epsilon,1} = 1.44$, $C_{\epsilon,2} = 1.92$. Its simplicity and

cost-effectiveness make the k-ϵ model very popular, while it also has the benefit of providing turbulent time scales for the integral length k/ϵ and the Kolmogorov length scales $\sqrt{k/\epsilon}$, both used in turbulent combustion models [166]. However, there are some well-known drawbacks. For example, the unclosed terms, which arise in the transport equations for k and ϵ, and require additional modelling. Furthermore, the k-ϵ shows poor results for important flow cases such as unconfined flows or rotating flows. To overcome this poor performance, a variety of modified k-ϵ models exist. For instance, the RNG k-epsilon proposed by Yakhot et al. [252], and the realizable k-epsilon model proposed by Shih et al. [211]. These models allow an improved performance for flows involving boundary layers or vortices, but they still show weaknesses in the vicinity of walls. These weaknesses were compensated, by the k-omega model first proposed by Wilcox et al. [243] Here, a transport equation is solved for the specific dissipation rate instead of an equation for ϵ. However, it shows deficiencies in the free flow. To overcome these drawbacks, Menter et al. [139] proposed a combination of the advantages of the k-epsilon and the k-omega in the shear stress model (SST). Still, it shows deficiencies for free shear flows and for rotating flows. In summary, the RANS method offers a simple, cost-efficient method for simulating turbulent flows. However, it requires a certain amount of experience, especially in choosing the suitable turbulence model according to the flow problem and interpreting the simulation results.

3.1.3 Large eddy simulations

The concept of the Large Eddy Simulation (LES) approach is illustrated in Fig. 3.2. While the

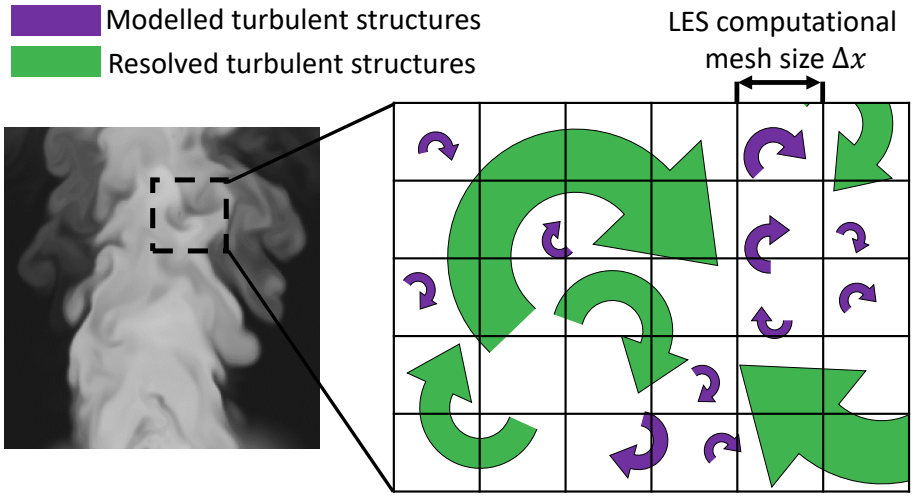

Figure 3.2: The schematic representation of the basic principle of the LES concept.

large scales of turbulent motions (illustrated by green vortices) are resolved, the small (purple) scales are modelled. The approach assumes that the large scales contain most of the energy, and as the information of the flow governing geometry is lost successively with the eddies traversing through the energy cascade, the small scales show a universal character. This allows for a more general description of their influence in the form of models and thus, it is possible to calculate with a lower grid resolution at moderate computing costs, allowing more complex flows to be calculated compared to a DNS. In contrast to RANS simulations, the LES delivers time-resolved results, which are significantly more accurate due to a lower model error. However, the turbulent flow separation into small and large scales is achieved by spatially filtering the governing equations. For example, for an arbitrary quantity ϕ, the filtering operation can be generally expressed by the following operator:

$$\overline{\phi}(\boldsymbol{x}) = \int_D \phi(\boldsymbol{x}) G(\boldsymbol{x} - \boldsymbol{x'}) d\boldsymbol{x'} \tag{3.23}$$

Here D is the domain size over which the integration was performed, and G is the LES filter applied, where the filter width corresponds to the smallest filtered scale. Common filters in physical space are the *box filter*:

$$G(x'-x) = \begin{cases} 1/\Delta^3 & \text{if} \quad |x'-x| \leq \Delta/2 \\ 0 & \text{otherwise} \end{cases} \tag{3.24}$$

or the *Gaussian* filter:

$$G(x'-x) = \left(\frac{6}{\pi\Delta^2}\right)^{3/2} \exp\left[-\frac{6|x'-x|}{\Delta^2}\right] \tag{3.25}$$

Here, Δ denotes the filter width (in implicitly filtered LES Δ is equal to the grid resolution). Similar to the RANS equations (Eq.(3.11)), Favre filtering is applied to quantities multiplied by density to reduce the number of unclosed terms (Eq. (3.10)) in the conservation equations. Thus, the Favre filter corresponds to density-weighted filtering:

$$\widetilde{\phi} = \frac{\overline{\rho\phi}}{\overline{\rho}} \tag{3.26}$$

The separation of filtered resolved scales $\overline{\phi}$ and the unresolved subgrid scales ϕ' can be expressed for Reynolds filtering as (similar to Reynolds decomposition [172]):

$$\phi = \overline{\phi} + \phi' \tag{3.27}$$

and for Favre filtering as:

$$\phi = \widetilde{\phi} + \phi' \tag{3.28}$$

The filter operation applied to the transport equations Eq. (2.2), (2.3), (2.12), (2.17) gives the Favre filtered transport equations. These are presented below, first for mass and momentum, and their closure is discussed. Subsequently, the transport equations for scalars are presented and discussed.

Filtered mass and momentum transport

Applying the filter operation to the continuity equation, with a source term for spray droplets, as well as exchanging filtered terms multiplied by ρ with their Favre filter, gives the following transport equation:

$$\frac{\partial\overline{\rho}}{\partial t} + \frac{\partial\overline{\rho}\widetilde{u}_j}{\partial x_j} = \overline{\dot{\Gamma}}_\rho \tag{3.29}$$

For the transport equation of the momentum, the following non-closed equation results:

$$\frac{\partial\overline{\rho}\widetilde{u}_i}{\partial t} + \frac{\partial\overline{\rho}\widetilde{u}_i\widetilde{u}_j}{\partial x_j} = -\frac{\partial\overline{p}}{\partial x_i} + \frac{\partial}{\partial x_j}\left(\overline{\tau}_{ij} - \overline{\rho}(\widetilde{u_i u_j} - \widetilde{u}_i\widetilde{u}_j)\right) + \overline{\dot{S}}_\mathrm{M} \tag{3.30}$$

This transport equation contains an unclosed term: the unresolved subgrid stress term $\tau_{ij}^\mathrm{sgs} = \widetilde{u_i u_j} - \widetilde{u}_i\widetilde{u}_j$, whose modelling is one of the main challenges in LES. Similar to the RANS modelling, the Boussinesq approximation [17] is used here, where the unresolved scales are treated as additional viscosity. In analogy to the Reynolds stress tensor for Newtonian fluids, the deviatoric part of the subgrid stress tensor $\tau_{ij}^\mathrm{sgs,D}$ is described with the eddy viscosity ν_t as follows:

$$\tau_{ij}^\mathrm{sgs,D} = \tau_{ij}^\mathrm{sgs} - \frac{1}{3}\tau_{kk}^\mathrm{sgs} = -\overline{\rho}\nu_\mathrm{t}\left(\frac{\partial\widetilde{u}_i}{\partial x_j} + \frac{\partial\widetilde{u}_j}{\partial x_i} - \frac{2}{3}\delta_{ij}\frac{\partial\widetilde{u}_k}{\partial x_k}\right) \tag{3.31}$$

The isotropic part of the subgrid stress is not solved explicitly and is instead added to the filtered pressure and solved implicitly:

$$\overline{p}_\mathrm{mod} = \overline{p} + \frac{1}{3}\tau_{kk}^\mathrm{sgs} \tag{3.32}$$

This assumption can be made for low Mach number flows since the pressure Poisson equation is solved to satisfy continuity (this assumption is no longer valid for compressible flows, and additional modelling is required).

Eddy viscosity modelling

The turbulent viscosity can be described either with an additional transport equation, e.g. for the turbulent kinetic energy [138] or an algebraic model. In the present work, the latter approach was used. The basic Smagorinsky model [214] is the most popular model due to its simple formulation, robustness, and satisfying performance and is presented below. Based on the Smagorinsky model, many modifications have been developed, of which the Sigma model [151] and the dynamic Germano model [56] will be presented in the following.
The **Smagorinsky** model reads as follows:

$$\mu_\mathrm{t} = \nu_\mathrm{t}\overline{\rho} = \overline{\rho}(C_\mathrm{m}\Delta)^2 D_\mathrm{m}(\widetilde{u}_i) \tag{3.33}$$

Here, D_m is a differential operator depending on the filtered velocity field, and C_m is a modelling constant. The model constant is usually set to values between 0.05 and 0.2, and the differential operator is derived from the magnitude of the filtered strain rate as follows:

$$D_\mathrm{m} = \sqrt{2\widetilde{S}_{ij}\widetilde{S}_{ij}} \quad \text{while} \quad \widetilde{S}_{ij} = \frac{1}{2}\left(\frac{\partial \widetilde{u}_i}{\partial x_j} + \frac{\partial \widetilde{u}_j}{\partial x_i}\right) \tag{3.34}$$

The disadvantage of using this model is an overprediction of the turbulent flux near walls and in shear flows, which leads to artificial damping of the flow in these regions. Several models have been proposed to overcome this disadvantage, such as the Vreman [236], the WALE [150] or the Sigma model which was applied in this work.
The **Sigma model** was developed by Nicoud et al. [151] and uses a different differential operator based on singular values of the velocity gradient:

$$D_\mathrm{D} = \frac{\sigma_3(\sigma_1 - \sigma_2)(\sigma_2 - \sigma_3)}{\sigma_1^2} \quad \text{with} \quad \sigma_1 \geq \sigma_2 \geq \sigma_3 \tag{3.35}$$

Here σ_i are the singular values, formed by the square root of the eigenvalues of the following tensor G:

$$G_{i,j} = \frac{\partial \tilde{u}_k}{\partial x_i}\frac{\partial \tilde{u}_k}{\partial x_i} \tag{3.36}$$

In his work, Nicoud [152] found $C_\mathrm{m} = 1.5$ to be a suitable value for various test cases. In conclusion, the model is known to be well suited for combustion applications as it does not predict turbulent viscosity for solid body rotations and thermal expansion.
To overcome the shortcoming of the constant model parameter C_m, Germano et al. [56] proposed a dynamic procedure, for which $C_\mathrm{m}(x,t)$ is determined dynamically, varying in space and time. For this purpose, a test filter $\widehat{Q}$ is introduced with the size $\widehat{\Delta}$, which is usually chosen to be twice the LES filter width Δ. The unresolved subgrid momentum fluxes of the regular LES are:

$$\tau_{ij}^\mathrm{sgs} = \overline{\rho u_i u_j} - \frac{\overline{\rho u_i \rho u_j}}{\overline{\rho}} \tag{3.37}$$

The unresolved subgrid momentum fluxes of the test filter are:

$$\tau_{ij}^\mathrm{test} = \widehat{\overline{\rho u_i} u_j} - \frac{\widehat{\overline{\rho u}}_i \widehat{\overline{\rho u}}_j}{\widehat{\overline{\rho}}} \tag{3.38}$$

According to Germano [56], the two expressions above can be combined and linked to the Leonard stresses (in the variable density formulation defined by Moin et al. [143]) as:

$$L_{ij} = \tau_{ij}^\mathrm{test} - \widehat{\tau_{ij}^\mathrm{sgs}} = \widehat{\overline{\rho}\widetilde{u}_i\widetilde{u}_j} - \frac{\widehat{\overline{\rho}\widetilde{u}}_i \widehat{\overline{\rho}\widetilde{u}}_j}{\widehat{\overline{\rho}}} \tag{3.39}$$

While Eq. (3.37) and Eq. (3.38) still contain the trace part of the filtered and test-filtered unresolved stresses, the model for the traceless part can be written as follows:

$$\tau_{ij}^{\text{test}} - \frac{\delta_{ij}}{3}\tau_{kk}^{\text{test}} = \alpha_{ij}/C_{\text{m}}^2 = \widehat{\overline{\rho}}/C_{\text{m}}^2 = \widehat{\overline{\rho}}\widehat{\Delta}^2 D_{\text{m}}\left(\widehat{\widetilde{u}_i}\right)\left[\frac{2}{3}\frac{\partial\widehat{\widetilde{u}}_k}{\partial x_k}\delta_{ij} - \left(\frac{\partial\widehat{\widetilde{u}}_i}{\partial x_j} + \frac{\partial\widehat{\widetilde{u}}_j}{\partial x_i}\right)\right] \tag{3.40}$$

$$\tau_{ij}^{\text{sgs}} - \frac{\delta_{ij}}{3}\tau_{kk}^{\text{sgs}} = \beta_{ij}/C_{\text{m}}^2 = \overline{\rho}/C_{\text{m}}^2 = \overline{\rho}\Delta^2 D_{\text{m}}\left(\widetilde{u}_i\right)\left[\frac{2}{3}\frac{\partial\widetilde{u}_k}{\partial x_k}\delta_{ij} - \left(\frac{\partial\widetilde{u}_i}{\partial x_j} + \frac{\partial\widetilde{u}_j}{\partial x_i}\right)\right] \tag{3.41}$$

Substituting Eq. (3.40) and (3.41) into the traceless part of Eq. (3.39) leads to an overdetermined system of six independent equations (five for constant density), from which C_m can be determined.

$$L_{ij} - \frac{\delta_{ij}}{3}L_{kk} = \widehat{C_{\text{m}}^2\beta_{ij}} - C_{\text{m}}^2\alpha_{ij} = M_{ij} \tag{3.42}$$

In their work, Lilly et al. [124] proposed determining C_{m} based on a least square error estimate and assuming C_{m} to be independent of the filtering, which leads to the following expression for C_{m}^2:

$$C_{\text{m}}^2 = \frac{M_{ij}\left(L_{ij} - \frac{\delta_{ij}}{3}L_{kk}\right)}{M_{kl}M_{kl}} \tag{3.43}$$

As an alternative to Lilly's approach, there is also the solution approach of Piomelli and Liu et al. [165] , in which the value of C_m is calculated based on the value of the model constant from the previous iteration step $C_m^{*,2}$:

$$C_{\text{m}}^2 = \frac{-\alpha_{ij}\left(L_{ij} - \frac{\delta_{ij}}{3}L_{kk} - \widehat{C_{\text{m}}^{*,2}\beta_{ij}}\right)}{\alpha_{kl}\alpha_{kl}} \tag{3.44}$$

It is claimed that this method is more robust than the Lilly method because the model constant remains in the filter operation, and no assumption has to be made about (partially) spatial homogeneous C_{m} fields.

Summarised, eddy viscosity models are the most popular approaches because they are robust and relatively accurate. However, it is often noted that they cannot capture backscattering. The Smagorinsky and Sigma model are not parameter-free, while the Germano model is costly due to filtering. It should not remain unmentioned that there are other philosophies like Scale-Similarity Type models [30].

Filtered scalar transport equations

Within the framework of the LES approach, the filtered transport equations for scalar quantities such as the species mass fraction Y_α or the enthalpy h result in further unclosed terms. The Favre filtered transport equation for an arbitary scalar quantity ϕ can be written as follows:

$$\frac{\partial\overline{\rho}\widetilde{\phi}}{\partial t} + \frac{\partial\overline{\rho}\widetilde{\phi}\widetilde{u}_j}{\partial x_j} = \frac{\partial}{\partial x_j}\left(\overline{\rho}D_\phi\frac{\partial\widetilde{\phi}}{\partial x_j} - \overline{\rho}\left(\widetilde{\phi u_j} - \widetilde{\phi}\widetilde{u}_j\right)\right) + \overline{\dot{\omega}}_\phi \tag{3.45}$$

In this filtered transport equation, two unclosed terms appear, the turbulent scalar flux $\overline{\rho}\widetilde{\phi u_j} - \overline{\rho}\widetilde{\phi}\widetilde{u}_j$ and the reaction source term $\overline{\dot{\omega}}_\phi$. The latter requires an individual description since, besides unresolved turbulent fluxes, its interaction with the chemical reactions needs to be considered. The modelling of the source term is therefore discussed separately in the next section about turbulent combustion modelling. However the scalar fluxes are often described similar to RANS simulations [166] using a gradient assumption:

$$\rho\tau_\phi^{\text{sgs}} = \overline{\rho}\widetilde{\phi u_j} - \overline{\rho}\widetilde{\phi}\widetilde{u}_j = \overline{\rho}D_{\text{t}}\frac{\partial\widetilde{\phi}}{\partial x_j} \tag{3.46}$$

Here D_t represents the turbulent diffusivity, which results from the turbulent kinematic viscosity ν_t and, depending on the investigated scalar, from the turbulent Schmidt number Sc_t or the turbulent Prandtl number Pr_t, which are close to unity for the gas-phase:

$$D_\mathrm{t} = \frac{\nu_\mathrm{t}}{Sc_\mathrm{t}} \quad \text{or} \quad D_\mathrm{t} = \frac{\nu_\mathrm{t}}{Pr_\mathrm{t}} \tag{3.47}$$

3.2 Turbulent combustion modelling

So far, the modelling of non-reactive turbulent flows has been discussed. However, as soon as combustion occurs, the situation becomes even more complex. Depending on the number of species and reactions in the applied reaction mechanism:

- The evaluation of chemistry might become very time consuming.
- Additional transport equations need to be solved for each species.
- The interaction of turbulence and chemistry in the sub-grid requires modelling.

The flow solver is coupled to the chemistry by the filtered reaction rate $\widetilde{\dot{\omega}}$, which was introduced in its unfiltered form in Section 2.2. As already mentioned, the description of $\widetilde{\dot{\omega}}$ is typically the bottleneck of reactive flow simulations in terms of computational costs, and its modelling will be addressed in the following.

3.2.1 Chemistry modelling

The reaction rate or species source term is calculated from a reaction mechanism that represents a thermochemical database in which a sequence of elementary reactions describes the conversion from fuel and oxidiser to the combustion products. The development of reaction mechanisms is an inverse problem in which neither the structure of the individual reactions nor their reaction rates are known. Consequently, they are created from an elaborate combination of experiments and detailed molecular simulations. Most of these mechanisms are purpose-built for specific fuels and operating conditions, outside of which they may lead to unsatisfactory results. For standard fuels such as methane or hydrogen, numerous reaction mechanisms are available in the literature. These reaction kinetics are solved directly during simulation run-time in the finite rate chemistry combustion model. Alternatively, the mechanism is used for 1D pre-processing simulations in the tabulated chemistry approach. However, both approaches can be pursued in varying degrees of detail and are discussed below.

Finite rate chemistry

Direct solution of the finite rate chemistry is standard in laminar simulations but is rarely used for turbulent simulations due to high computational costs and stiffness. In the approach, the reaction rate is calculated locally dependent on the species mixture composition, temperature, and pressure. Since additional transport equations are solved for each species, the computational effort is strongly dependent on the number of species. Detailed mechanisms with several hundred species and over 1000 reactions, such as the Polimi CRECK mechanism [184] (300 species and 5000 reaction steps), can only be used for 0D or 1D simulations. However, detailed mechanisms with a lower degree of detail exist, such as the GRI-Mech 3.0 [215] (53 species and 325 reactions) or the hydrogen mechanism by Li et al. [121] (8 species and 25 reactions). The latter can even be used for the DNS of turbulent flames. For example, in the context of numerical spray flame investigations, Gutheil and Sirignano [68] studied an n-heptane / O_2 counterflow flame by DNS. Kong and Reitz [112] used a detailed mechanism to simulate spray injection into a homogeneously charged compression ignition engine. An alternative to a detailed mechanism

is the reduced mechanism. Reduced mechanisms can be developed from a detailed reference mechanism, for example by using a genetic algorithm reduction and optimisation approach [212]. In this procedure, unnecessary reactions and species are identified and discarded while maintaining the prediction accuracy of predefined objective functions, such as the temperature profile or flame speed. These reduced mechanisms can then be used even for the LES of gas turbine combustion chambers with direct chemistry, as recently shown by Gruhlke et al. [65].

Tabulated chemistry

The tabulated chemistry approach is a computationally very efficient and, hence, popular method. This model assumes that the 3D turbulent flame can be described as an ensemble of laminar 1D flames. The principle concept of a flamelet is shown schematically in Fig. 3.3. In the tabulated

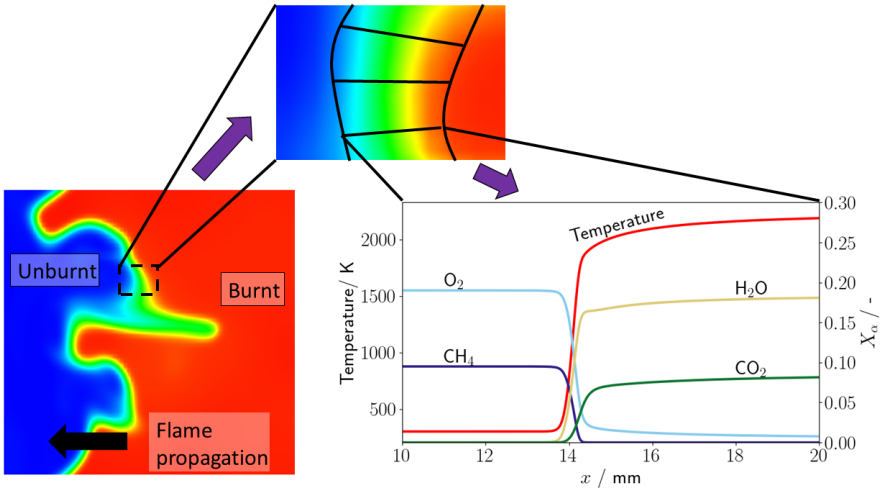

Figure 3.3: The schematic representation of the basic principle of tabulated chemistry.

chemistry approach, 1D flames of different fuel to oxidiser compositions are calculated before the CFD simulation in a pre-processing step. These 1D flames are calculated with kinetic libraries such as Cantera [62], or Chemkin [101] using detailed reaction mechanisms. In contrast to 2D or 3D simulations, these 1D simulations are computationally efficient, enabling the consideration of laminar flames covering a wide range of equivalence ratios. The resulting flame solutions are then transformed from spatial into combustion progress coordinates. Finally, the thermochemical state, including transport coefficients, source terms, and species mass fractions, is stored in chemistry tables. The tables are accessed during simulation run-time in dependency of the local stoichiometry, which is represented by the mixture fraction Z and the combustion progress represented by the normalised combustion progress variable c. The source term of the combustion progress variable is then looked up using Z and c as:

$$\overline{\dot{\omega}} = f(Z, c) \tag{3.48}$$

Different combustion models rely on tabulated chemistry, for example [166]: the intrinsic low-dimensional manifolds (ILDM) approach [130, 131], flame-prolongation of ILDM (FPI) [57] and the premixed flamelet-generated manifolds (PFGM) approach [231, 233] which is also used in the present work.

3.2.2 Sub-grid turbulence-chemistry interaction

The modelling of the turbulence-chemistry interaction in the subgrid is associated with an additional problem: the resolution of the flame thickness. The thickness of a premixed flame may

vary between 0.1 to 1 mm (depending on pressure) and is thus often resolved by only a single LES cell. However, several models are resolving these difficulties in the overall combustion modelling. In Poinsot's work [166], a summary of various models can be found. For combustion modelling in spray flame synthesis, this study employed the artificially thickened flame model (ATF). Additionally, the author previously explored and enhanced the flame surface density model (FSD), which is briefly presented here as well.

The flame surface density approach

The FSD model is typically used to investigate premixed flames. In this approach, a transport equation for the combustion progress variable c is solved, which reads:

$$\frac{\partial \rho \tilde{c}}{\partial t} + \frac{\partial \rho \widetilde{u_j c}}{\partial x_j} = \overline{\frac{\partial}{\partial x_j} \rho D \frac{\partial c}{\partial x_j}} + \overline{\dot{\omega}} \tag{3.49}$$

The two terms on the right-hand side are the filtered molecular diffusion of c and the mean reaction rate, respectively. The closure of these terms is modelled in the FSD approach using the generalized flame surface density Σ. This quantity represents the flame surface area per unit volume contained in the filtered LES volume, and behaves similarly to the sum of the filtered source term and the diffusion term of the progress variable. Thus, the right hand side of Eq. (3.49) can be modelled as [15]:

$$\overline{\frac{\partial}{\partial x_j} \rho D \frac{\partial c}{\partial x_j}} + \overline{\dot{\omega}} = \overline{\rho s_d} \Sigma \approx \rho_u s_L \Xi \left| \frac{\partial \overline{c}}{\partial x_i} \right| \tag{3.50}$$

Here $s_d = (D_c/D_t)/|\nabla c|$ is the flame displacement speed. Assuming a unity Lewis number, this term can be modelled as $\overline{\rho s_d} = \rho_\mathrm{u} s_\mathrm{L}$ [129]. Chakraborty and Cant [23] investigated deviations from the unity Lewis number assumption and proposed the following correlation to model the flame displacement speed: $\overline{\rho s_d} = \rho_\mathrm{u} s_\mathrm{L}/Le$. In this equation, ρ_u is the density of the unburned gas, and Ξ is the flame wrinkling factor. Different approaches exist to model Ξ and Σ, for example algebraic models [15, 24], similarity models [107, 108] or the approach of solving an additional transport equation [15, 205, 241]. In summary, this model presents a computationally efficient combustion model, which, however, only distinguishes between burnt and unburnt gases. Consequently, the prediction of intermediate species is not possible using the FSD model.

Aritficial thickened flame model

The artificial thickened flame (ATF) approach [20] is an efficient method to resolve the thin premixed flame front on a coarse numerical grid. A sketch in Fig. 3.4 illustrates the thickening approach. The concept of this approach is to artificially thicken the flame until it can be resolved on the numerical grid, while maintaining the flame speed. The laminar flame thickness δ_L^0 and flame speed s_L^0 can therefore be related to each other following the classical laminar flame theory [166] by:

$$\delta_\mathrm{L}^0 \propto \frac{D_\mathrm{th}}{s_\mathrm{L}^0} = \sqrt{\frac{D_\mathrm{th}}{\dot{\omega}}} \tag{3.51}$$

The flame thickness is artificially broadened by applying a thickening factor F to the thermal diffusion (FD_th), while maintaining the laminar flame speed by multiplying the reaction rate by $1/F$:

$$s_\mathrm{L}^0 \propto \sqrt{D_\mathrm{th} \cdot \dot{\omega}} = \sqrt{F D_\mathrm{th} \cdot \dot{\omega}/F} \tag{3.52}$$

As a result of the thickening, the flame is less wrinkled, accompanied by a reduced flame surface, resulting in a lower flame speed. These effects are compensated by the introduction of an efficiency

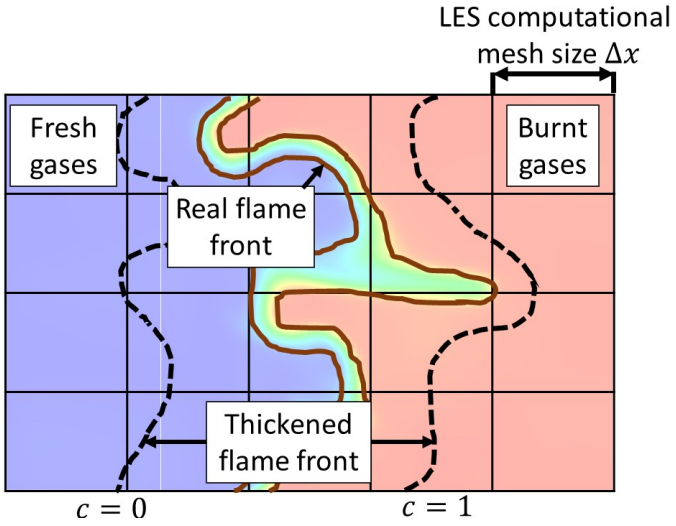

Figure 3.4: Thickened flame approach: the laminar flame is thickened while the flame speed is conserved (abstracted from [166])

function E. Together with the flame thickening factor F, the modified diffusion, and source terms become:

$$D_{\mathrm{th}} \rightarrow EFD_{\mathrm{th}} \quad , \quad \dot{\omega} \rightarrow \frac{E}{F}\dot{\omega} \tag{3.53}$$

By introducing E, the flame thickness remains unchanged, while the flame speed increases:

$$s_{\mathrm{T}}^0 = Es_{\mathrm{L}}^0 \quad \text{and} \quad \delta_T = F\delta_{\mathrm{L}}^0 \tag{3.54}$$

Various approaches exist to model the efficiency function [25, 31]. In the present work, the approach of Charlette et al. [25, 26] is used, which was further modified by Wang et al. [237]. In this approach, the efficiency function is determined from the maximum value of the thickening factor $F_{\mathrm{t,max}}$, the sub-grid velocity fluctuation u'_Δ, the sub-grid Reynolds number Re_Δ and the fitted efficiency function gamma Γ_Δ:

$$E = \left[1 + \min\left(F_{\mathrm{t,max}} - 1, \Gamma_\Delta\left(F_{\mathrm{t,max}}, \frac{u'_\Delta}{s_{\mathrm{l}}^0}, Re_\Delta\right)\frac{u'_\Delta}{s_{\mathrm{l}}^0}\right)\right]^{0.5} \tag{3.55}$$

The sub-grid velocity fluctuation can be approximated according to Colin et al. [31], while Re_Δ is determined as [25]:

$$Re_\Delta = 4F\frac{u'_\Delta}{s_{\mathrm{L}}} \tag{3.56}$$

The fitted efficiency function Γ_Δ is calculated from:

$$\Gamma_\Delta\left(F_{\mathrm{t,max}}, \frac{u'_\Delta}{s_{\mathrm{l}}^0}, Re_\Delta\right) = \left\{\left[f_u^{-a} + f_\Delta^{-a})^{-\frac{1}{a}}\right]^{-b} + f_{Re}^{-b}\right\}^{-\frac{1}{b}} \tag{3.57}$$

The terms f_u, f_Δ, f_{Re}, the constants a and b are expressed as:

$$f_u = 4\left(\frac{27C_{\mathrm{K}}}{110}\right)^{0.5}\left(\frac{18C_{\mathrm{K}}}{55}\right)\left(\frac{u'_\delta}{s_l^0}\right)^2, \tag{3.58}$$

$$f_\Delta = \left[\frac{27C_{\mathrm{K}}\pi^{\frac{4}{3}}}{110}\left(F_{\mathrm{t,max}}^{4/3} - 1\right)\right]^{\frac{1}{2}} Re_\Delta^{1/2} \tag{3.59}$$

$$f_{Re} = \left[\frac{9}{55}\exp\left(-\frac{3}{2}\mathrm{C_K}\pi^{\frac{4}{3}}Re_\Delta^{-1}\right)\right]^{\frac{1}{2}} Re_\Delta^{\frac{1}{2}} \tag{3.60}$$

$$a = 0.6 + 0.2\exp\left(-0.1\frac{u'_\Delta}{s_\mathrm{l}^0}\right) - 0.2\exp\left(-0.01F_{\max}\right) \tag{3.61}$$

$$b = 1.4 \tag{3.62}$$

These equations depend on the Kolmogorov constant $C_\mathrm{K} = 1.5$. The calculation of the efficiency function is computationally expensive compared to the remaining CFD solver and adds up to 25 % of the computation time [176]. This deficiency can be overcome by calculating the efficiency function in Eq. (3.55) at the beginning of the simulation in a pre-processing step and tabulating the resulting values as a function of the local thickening factor and the velocity ratio.

The application of flame thickening leads to non-physical diffusion outside the flame, which influences pure mixing processes. Therefore, Legier et. al [119] proposed the dynamic thickened flame model (DTF). In this model, the flame region is detected using a flame sensor Ω which applies thickening only to the flame ($F > 1$). Outside of the flame region, F reduces to unity. The flame thickening factor is then calculated as:

$$F = 1 + (F_{max} - 1)\Omega \tag{3.63}$$

With a maximum flame thickness $F_{t,max}$ defined as:

$$F_{\mathrm{t,max}} = \max\left(\frac{n\Delta}{\delta_t h}, 1.0\right) \tag{3.64}$$

In this equation, n is the number of cells that resolve the flame (typically $n = 5 - 10$). The flame sensor function is calculated as proposed by Proch and Kempf [176]:

$$\Omega = \frac{\frac{dY_\mathrm{p}}{dx}}{\max\left(\frac{dY_\mathrm{p}}{dx}\right)} \tag{3.65}$$

The DTF model applied to the Favre filtered conservation equations for species Eq. (3.45) yields:

$$\frac{\partial\overline{\rho}\widetilde{Y}_\alpha}{\partial t} + \frac{\partial\overline{\rho}\widetilde{Y}_\alpha\widetilde{u}_j}{\partial x_j} = \frac{\partial}{\partial x_j}\left[(\overline{\rho}FED_\alpha + (1-\Omega)D_\mathrm{t})\frac{\partial\widetilde{Y}_\alpha}{\partial x_j}\right] + \frac{E}{F}\overline{\dot{\omega}}_\alpha \tag{3.66}$$

The implementation of the dynamic thickened flame approach is straightforward and can be combined with tabulated or finite rate chemistry approaches to describe spray-flames, as demonstrated by Rittler et al. [190, 191]. Most importantly, this approach allows to resolve the flame structure and, hence, allows for the prediction of particle nucleation. For this reason, the DTF approach is used in combination with the computationally efficient tabulated chemistry in the present work.

Turbulent spray-flame model

The spray-flame chemistry of the SpraySyn burner was modelled with a modified PFGM combustion model combined with the DTF approach. The standard PFGM model was originally developed to describe premixed flames [231, 232] and needs to be modified for SpraySyn flame simulations for two reasons:

1. The structure of the flame consists of at least three different feed streams, namely, in the centre (a) a liquid ethanol/precursor stream surrounded by (b) a dispersion oxygen stream atomising the liquid phase, and outside (c) a CH_4/oxidiser stream for the pilot flame which ignites the evaporated spray mixture downstream. Due to the presence of two different fuel streams, a two mixture fraction approach (Z_1, Z_2) was chosen [191] instead of a one mixture fraction (Z_1) approach as originally proposed.

2. The standard FGM approach was extended to account for spray evaporation. This was achieved by adding an evaporation source term $\dot{\Gamma}_Z$ to the mixture fraction of the spray/fuel gas streams [28, 38, 190]

These modifications enable the prediction of the SpraySyn flame, while further assumptions were made: a) unity Lewis number, i.e., no preferential diffusion, and b) no heat exchange between the individual streams.

The choice of mixture fractions depends on the flow problem. Rittler [189] proposed to use element mass fractions to describe the mixture fractions in his work, but this has proven to be very error-prone due to artifacts in the tables, and inflexible since the result was highly dependent on the choice of element. Therefore, in this work, species mass fractions of the spray components and the pilot were used for Z_1 and Z_2, respectively.

The choice of the combustion progress variable is important to accurately describe the combustion process and predict nanoparticle synthesis. In order to account for the formation processes in the SpraySyn flame, a weighted progress variable is used following Wollny et al. [249]. The progress variable is composed of a weighted linear combination of product and fuel species:

$$Y_\mathrm{p} = \sum \alpha Y_i + \sum \beta (Y_{f,i} - Y_i) \tag{3.67}$$

where the first term represents the product species Y_i with the weighting factor α and the second term the fuel species $Y_{f,i}$ with the weighting factor β. The normalised progress variable c is then used for the tabulation $c = Y_\mathrm{p}/Y_\mathrm{p,max}$ [231]. For Z_1, Z_2 and Y_p, transport equations were solved following Peters [164]:

$$\frac{\partial \bar{\rho}\tilde{Z}_\alpha}{\partial t} + \frac{\partial \bar{\rho}\tilde{u}_i\tilde{Z}_\alpha}{\partial x_i} = \frac{\partial}{\partial x_i}\left(\left[FE\bar{\rho}D_\mathrm{p} + (1-\Omega)\frac{\mu_\mathrm{t}}{Sc_\mathrm{t}}\right]\frac{\partial \tilde{Z}_\alpha}{\partial x_i}\right) + \dot{\Gamma}_{\tilde{Z}_\alpha} \tag{3.68}$$

$$\frac{\partial \bar{\rho}\tilde{Y}_\mathrm{p}}{\partial t} + \frac{\partial \bar{\rho}\tilde{u}_i\tilde{Y}_\mathrm{p}}{\partial x_i} = \frac{E}{F}\overline{\dot{\omega}}_s + \overline{\dot{\omega}}_\mathrm{p,evp} + \frac{\partial}{\partial x_i}\left(\left[FE\bar{\rho}D_\mathrm{p} + (1-\Omega)\frac{\mu_\mathrm{t}}{Sc_\mathrm{t}}\right]\frac{\partial \tilde{Y}_\mathrm{p}}{\partial x_i}\right) \tag{3.69}$$

3.3 Aerosol dynamics modelling

A complete mathematical description of the aerosol dynamics in terms of a particle size distribution (PSD) results from the general dynamics equation (GDE) as presented in Eq. (2.73). Unfortunately, this GDE can not be solved analytically, except for simplified cases. Instead, the GDE is usually transformed into forms that allow a numerical calculation. Among the most popular are the discrete, the sectional, the moment method and the monodisperse model. They will be briefly introduced in the following pages, while more detailed information can be found in the book of Marchisio and Fox [135].

The distribution function of the particle size related to the different models is shown in Fig. 3.5.

In the **discrete modelling** approach, the particle sizes are divided into discrete sizes, corresponding to monomers (single atoms or molecules), dimers, trimers, and so on. In addition, an individual conservation equation is solved for each particle size, which makes this model conceptually very simple. However, due to the high computational demand, it is mainly used to describe particles limited to hundreds or thousands of atoms, while for more extensive size ranges, cheaper models are required. For **sectional modelling**, the particle size distribution is divided into sections. The particle characteristics in each section are calculated from the average particle sizes of this section, and therefore a histogram illustrates the particle size distribution in Fig. 3.5. When selecting the sections, two aspects have to be balanced: the desired accuracy and the available computing resources. The accuracy increases with the number of sections, but the computational

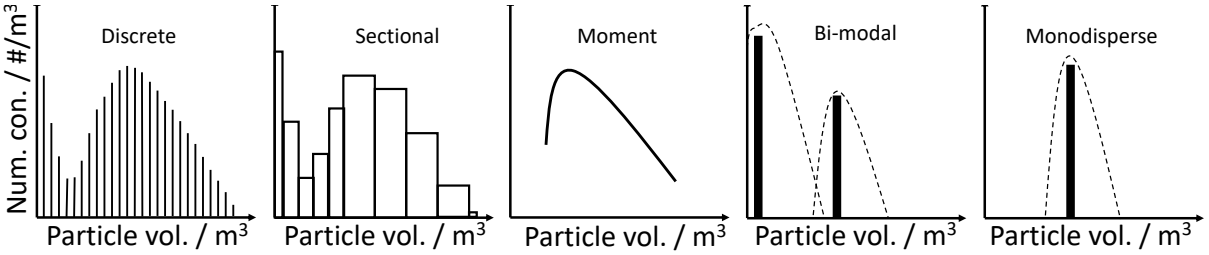

Figure 3.5: The particle size distribution functions for the discrete, the sectional, moment-method, bi-modal and monodisperse model.

effort increases simultaneously since a transport equation is solved for each section. Therefore, both factors must be considered for the individual case to be investigated.

In the **moment method**, the particle size distribution is not directly resolved as in the sectional or discrete method. Instead, the shape of the PSD is assumed, and only one or several integrals of the PSD are calculated. The integral of the PSD corresponds to one of the lower moments, where for example, the 0^{th}, 2^{nd}, and 3^{rd} moment represent the number concentration, the surface area concentration, and the volume concentration, respectively. Thus, the moments ($k = 0, 2, 3....$) are defined as [51]:

$$M_k = \int_0^\infty n(v_\mathrm{p}) v_\mathrm{p}^k \mathrm{d}v_\mathrm{p} \tag{3.70}$$

A standard transport equation approximates the evolution of the moments in time and space. From these moments, the particle size distribution is then modelled based on the assumptions previously made about the shape of the distribution. The standard model is based on the log-normal distribution and can be determined from the 0^{th} moment M_0, the average volume v_g, and the standard deviation σ:

$$n(v_\mathrm{p}) = \frac{M_0}{2\sqrt{2}\ln(\sigma)} \exp\left[-\frac{1}{18}\left(\frac{\ln(v_\mathrm{p})/v_\mathrm{g}}{\ln(\sigma)}\right)^2\right]\frac{1}{v_\mathrm{p}} \tag{3.71}$$

However, there are more advanced models for describing the particle size distribution based on stochastic methods [61]. The advantage of this method is that it considers the main physical mechanisms (collision, coalescence, and particle deposition). The disadvantage is that the distribution function must be presumed (log-normal or normal) and often does not correlate with the natural distribution. Nevertheless, this model was used by Sung et al. [225, 226] to describe Titania formation in non-premixed flames. Furthermore, this model is prevalent in the soot modelling context [144–146].

The **monodisperse model** [115] and the **bimodal model** [90] are particular cases of the moment method.

In summary, there are several model approaches, and depending on the flow problem and the computational resources, it is necessary to decide in advance which model to use. The sectional and the bimodal models were used in the present work and will be presented in the following.

3.3.1 Sectional model

In the sectional model [14, 128, 141], the PSD is divided into a number of sections N_s and thus resolved, as shown in Fig. 3.5. Each section k represents the particle number concentration $N_k[\#/\mathrm{m}^3]$ of particles with a fixed volume $v_k[\mathrm{m}^3]$. The evolution of the particle number concentrations within the individual sections in space, time, and their growth through coagulation and nucleation can be approximated by a transport equation, which can be written as follows:

$$\frac{\partial N_k}{\partial t} + \frac{\partial N_k u_j}{\partial x_j} = \frac{\partial}{\partial x_j}(D_Q)\frac{\partial N_k}{\partial x_j} + \dot{\omega}_k^\mathrm{C} + I\delta_{k1} \tag{3.72}$$

here D_k represents the particle diffusion term and $\dot{\omega}^C$ the coagulation source term. The last term on the right is the nucleation source term I, which is only valid in the first section hence $\delta_{k1} = 1$ for $k = 1$ and $\delta_{k1} = 0$ for $k \neq 1$. The principle of coagulation has already been presented in Section 2.3.2, the growth of particles by collision. Therefore, the coagulation source term of each section consists of a *death*-term describing the coagulation of the respective section with itself or other sections and a *birth*-term for the coagulation of other sections. An exception, however, applies to the first section, where particles can only disappear through coagulation and arise through nucleation. Thus, the source term $\dot{\omega}$ can be written as follows:

$$\dot{\omega} = \begin{cases} \underbrace{-\sum_{i=1}^{N_s} \beta_{i1} N_i N_1}_{\text{Death}} & \text{for} \quad k = 1 \\ \underbrace{\frac{1}{2} \sum_{l=1}^{N_s} \sum_{i=1}^{N_s} \chi_{ilk} \beta_{il} N_i N_l}_{\text{Birth}} - \underbrace{\sum_{i=1}^{N_s} \beta_{ik} N_i N_k}_{\text{Death}} & \text{for} \quad k > 1 \end{cases} \tag{3.73}$$

here $\chi_{i,j,k}$ is an interpolation function, and β represents the coagulation kernel which can be calculated via Fuchs interpolation or the harmonic mean. If the coagulation results in a particle whose size falls between two sections, the contribution is divided between the two sections using the interpolation function $\chi_{i,j,k}$, which is defined as:

$$\chi_{ilk} = \begin{cases} \dfrac{v_{k+1} - (v_i + v_l}{v_{k+1} - v_k} & \text{for} \quad v_k \leq (v_i + v_l) < v_{k+1} \\ \dfrac{(v_i + v_l - v_{k-1})}{v_k - v_{k-1}} & \text{for} \quad v_{k-1} \leq (v_i + v_l) < v_k \\ 0 & \text{otherwise} \end{cases} \tag{3.74}$$

The nucleation source term I indicates the net production rate, i.e., how many monomer particles nucleate per concentration per time. For particles that nucleate or condense homogeneously, this can be determined with the classical nucleation theory. However, in the present work, iron oxide particles were investigated under the assumption that they nucleate directly as monomers from the gas phase after the formation of the monomer species through reactions. Based on this assumption, I is determined by the monomer species mass-fraction change, the Avogadro constant, the density, and the molar mass:

$$I = \frac{\mathrm{d}y_{\mathrm{prec}}}{\mathrm{d}t} \rho \cdot N_{\mathrm{A}} / M_{\mathrm{prec}} \tag{3.75}$$

The resulting PSD distribution is characterised by the diameter of average volume (mass), which can be calculated from the average volume $\overline{v}_m$ as follows:

$$\overline{v}_{\mathrm{m}} = \frac{\sum_{j=1}^{N_{\mathrm{s}}} N_j v_j}{\sum_{j=1}^{N_s} N_j} \qquad \longrightarrow \qquad d_{\mathrm{m}} = \left(\frac{6 \cdot \overline{v}_{\mathrm{m}}}{\pi} \right)^{1/3} \tag{3.76}$$

In order to use the model in LES simulations, Eq. (3.72) has to be Favre filtered, which leads to the following transport equation [128]:

$$\frac{\partial \overline{N}_k}{\partial t} + \frac{\partial \overline{N}_k \widetilde{u}_j}{\partial x_j} = \frac{\partial}{\partial x_j} \left(D_k \frac{\partial \overline{N}_k}{\partial x_j} - \left(\overline{N_k u_j} - \overline{N}_k \widetilde{u}_j \right) \right) + \overline{\dot{\omega}}_k^{\mathrm{C}} + \overline{I} \delta_{k1} \tag{3.77}$$

In this equation, three unclosed terms occur. First the unclosed subfilter flux $\left(\overline{N_k u_j} - \overline{N}_k \widetilde{u}_j \right)$ which is modelled by an eddy diffusivitiy approach, following Loeffler et al. [128] and Rittler et

al. [191]. The second unclosed term is the nucleation source, which is closed by the combustion model. This work investigates the closure of the coagulation rate, which is the third unclosed term introduced in Section 3.3.4. However, considering the closure of the unclosed subfilter flux, Eq. (3.77) can be written as:

$$\frac{\partial \overline{N}_k}{\partial t} + \frac{\partial \overline{N}_k \widetilde{u}_j}{\partial x_j} = \frac{\partial}{\partial x_j}(D_k + \frac{\nu_\mathrm{t}}{Sc_\mathrm{t}})\frac{\partial \overline{N}_k}{\partial x_j} + \overline{\dot{\omega}}_k^\mathrm{C} + \frac{E}{F}\overline{I}\delta_{k1} \tag{3.78}$$

The effect of the subgrid velocity contribution is considered via the turbulent viscosity approach [128, 191] entering the diffusion coeffcient, while the particle motion is assumed to follow the gas phase velocity.

The sectional model allows the PSD to be discretised and requires less computational resources than the discrete model. It also resolves the mixing between PSDs of different time histories, which occurs in turbulent flames. However, it should be noted that instantaneous coalescence, i.e., sintering, is assumed and thus spherical particles are implied. This assumption is valid in hot zones close to the flame, while downstream, aggregates can form.

3.3.2 Monodisperse model

In the monodisperse model, a homogeneous distribution is assumed at each location in the CFD simulation. Particles are characterised by the number concentration N, the particle surface concentration A, and the volume concentration V. The volume averaged diameter d_m can be calculated from the number concentration and volume concentration as follows:

$$d_m = \left(\frac{6V}{\pi N}\right)^{\frac{1}{3}} \tag{3.79}$$

In contrast to the sectional model, the surface concentration in the monodisperse model can be used to represent the sintering process and other agglomerate structures then spherical particles with the collision diameter d_c shown in Eq. (2.57).

The model was first proposed by Kruis et al. [115] and considers particle growth through coagulation and sintering. Panda and Pratsinis [161] extended the model by including a particle nucleation term I. The following conservation equation can determine the evolution of N in space, time, and particle space:

$$\frac{\partial N}{\partial t} + \frac{\partial N u_j}{\partial x_j} = \frac{\partial}{\partial x_j} D_Q \frac{\partial N}{\partial x_j} - \frac{1}{2}\beta N^2 + I \tag{3.80}$$

Here, the coagulation of particles at a coagulation frequency beta leads to a decrease of N. At the same time, the nucleation leads to an increase of N. The Fuchs coagulation kernel from Eq. (2.58) introduced in the precious chapter simplifies, following Kruis et al. [115], in the monodisperse model to:

$$\beta = 4\pi D_\mathrm{p} d_\mathrm{c} \left[\frac{\frac{1}{2}d_\mathrm{c}}{d_\mathrm{c} + \sqrt{2}g} + \frac{\sqrt{2}D}{\frac{1}{2}c d_\mathrm{c}}\right]^{-1} \tag{3.81}$$

The evolution of the surface area concentration is calculated by Eq. (3.82):

$$\frac{\partial A}{\partial t} + \frac{\partial A u_j}{\partial x_j} = \frac{\partial}{\partial x_j} D_Q \frac{\partial A}{\partial x_j} + \frac{1}{\tau}(A - A_\mathrm{s}) + I a_\mathrm{m} \tag{3.82}$$

Here, the second term on the right side represents the sintering as introduced in Eq. (2.69). The sintering time τ of Fe_2O_3 particles was in this thesis calculated following Wlokas et al. [247] as:

$$\tau = A \cdot T d_\mathrm{m}^4 \exp\left(\frac{T_a}{T}\right) \tag{3.83}$$

with the parameter $A = 8 \times 10^{16}$[s/(Km^4)], and $T_\mathrm{a} = 30,000$ [K]. For other material systems, the definition of τ and the parameters of the material systems vary (SiO_2 [105], TiO_2 [109]). While the completely fused particle surface is calculated as follows:

$$A_\mathrm{s} = \left(\frac{V}{N v_\mathrm{m}}\right)^{\frac{2}{3}} N a_\mathrm{m} \tag{3.84}$$

The volume increases through nucleation but is otherwise conserved. The following transport equation describes its evolution:

$$\frac{\partial V}{\partial t} + \frac{\partial V u_j}{\partial x_j} = \frac{\partial}{\partial x_j} D_Q \frac{\partial V}{\partial x_j} + I \tag{3.85}$$

To summarise, the monodisperse model is an easy-to-implement and computationally affordable model. It provides a reasonable estimate of the order of magnitude of the expected particles [82, 174], allows insight into the synthesis process [63, 174] and is a fundamental tool for upscaling [19, 63]. However, it provides no information about the PSD-shape, and due to its inherent monodisperse assumption, the model cannot correctly determine particle dynamics when nucleation and other particle growth processes co-exist. The bi-modal model [90] was applied in this work to overcome this shortcoming and will be discussed below.

3.3.3 Bimodal model

The bimodal model [90] couples one discrete section with a monodisperse model. The discrete part represents the process of nucleation (nucleation mode), while the monodisperse model part represents the processes of coagulation and coalescence (accumulation mode). In the nucleation mode, particles arise through nucleation from the gas phase, vanish after colliding and transfer into the accumulation mode. Therefore the dynamics of the nucleation mode can be described by the following transport equation for the number concentration N_1:

$$\frac{\partial N_1}{\partial t} + \frac{\partial N_1 u_j}{\partial x_j} = \frac{\partial}{\partial x_j} D_{N_1} \frac{\partial N_1}{\partial x_j} - \frac{1}{2} C_{B1} \beta_{11} N_1^2 - \beta_{12} N_1 N_2 + I \tag{3.86}$$

The particles can coagulate either by collision with each other β_{11} (intra-mode coagulation) or by collision with particles from the accumulation mode β_{12} (inter mode coagulation). For intra-mode coagulation, it should be noted that the particles are larger in the accumulation mode, and the variable $C_{B1} = r/(r-1)$ scales the transferred particles to maintain mass [90]. The variable $r = v_1/v_2$ corresponds to the ratio of the particle volume of the first mode $v_1 = v_m$ to the particle volume of the second mode $v_2 = V_2/N_2$. The particle volume V_1 and the surface concentration and A_1 of the nucleation mode result from the number concentration and the monomer volume and the monomer surface.($V_1 = N_1 v_1$; $A_1 = N_1 a_1$).

The accumulation mode is determined by the number concentration N_2, the volume concentration V_2 and the surface concentration A_2. A transport equation is solved for each of those quantities (Eq. (3.87)-(3.88)):

$$\frac{\partial N_2}{\partial t} + \frac{\partial N_2 u_j}{\partial x_j} = \frac{\partial}{\partial x_j} D_{N_2} \frac{\partial N_2}{\partial x_j} + \frac{1}{2} C_{B2} \beta_{11} N_1^2 - \frac{1}{2} \beta_{22} N_2^2 \tag{3.87}$$

Here, β_{22} corresponds to the collision frequency for intramode coagulation in accumulation mode, and $C_{B2} = 1/(r-1)$ is the interpolation variable that ensures mass conservation. The number concentration N_2 is not affected by intermode coagulation with the nucleation phase N_1. In contrast, the volume concentration and the surface concentration increase by intramode coagulation of the first phase and intramode coagulation with the second phase. The transport equations for both are written as follows.

$$\frac{\partial A_2}{\partial t} + \frac{\partial A_2 u_j}{\partial x_j} = \frac{\partial}{\partial x_j} D_{N_2} \frac{\partial A_2}{\partial x_j} + \frac{1}{\tau}(A_2 - N_2 a_{s2}) + a_1 \left(\frac{1}{2} C_{B1} \beta_{11} N_1^2 + \beta_{12} N_1 N_2\right) \tag{3.88}$$

$$\frac{\partial V_2}{\partial t} + \frac{\partial V_2 u_j}{\partial x_j} = \frac{\partial}{\partial x_j} D_{N_2} \frac{\partial V_2}{\partial x_j} + v_1 \left(\frac{1}{2} C_{B1} \beta_{11} N_1^2 + \beta_{12} N_1 N_2 \right) \tag{3.89}$$

The coagulation frequency β is approximated according to Fuchs (Eq. 2.58) following Jeong [90], and the average diameters are calculated according to Eq. (3.76). In summary, the bimodal model improves the monodisperse model when nucleation and coagulation coexist, at moderate computational costs. The disadvantage is the interpolation factor, which is sensitive to large gradients or differences between nucleation and accumulation mode. Nevertheless, the model was applied in the scope of this work to predict particle synthesis in laminar flames, and a good agreement with the experiments was found [206].

3.3.4 Modelling of nanoparticle-turbulence interactions

Prior to this PhD dissertation, the influence of subfilter turbulence in LES had been examined by only a few research groups. Loeffler [128] employed LES and DNS to investigate a nanoparticle jet, focusing on turbulence's impact on the coagulation rate. Discrepancies in mean particle sizes were observed, particularly in the high gradient region, although good agreement was found in the bulk flow. Flow structures resulting from LES and DNS differed, suggesting the effect cannot be solely attributed to subfilter phenomena. Additionally, it is not clear if this study resolved the Batchelor scale. Garrick [54] simulated turbulent mixing between a particle and a non-particle layer via DNS. He investigated a-priori the influence of the small subfilter structures and found an enhancement and a weakening of the coagulation term. Further, Cifuentes [29] studied a particle-forming vortex using DNS and analysed its behaviour in a reacting flow. In an a-priori analysis, a significant error in agglomeration rate was found due to coarse grid resolution in practical RANS or LES simulations.

In this work, the small-scale structures' influence is modelled with a closure from the soot community [144]. Furthermore, the small-scales are resolved using the so-called filtered density function method. These methods will be presented in more detail in the following.

Intermittency model

In the context of soot, Mueller and Pitsch [144] were the first to propose an intermittency model as a closure approach for the coagulation source term. They were using a hybrid method of moments (HMOM) to describe the soot dynamics, while Rodrigues [192] applied this model to the sectional approach. In this work, the model was adopted and applied as a closure approach to the coagulation source term to simulate nanoparticle synthesis.

The model relies on the δ-PDF approach, wherein turbulent fluctuations are neglected, and quantities are represented by their mean value. Therefore the probability density function (PDF) P of a particle scalar σ (for instance: number-, volume or surface area concentration) can be approximated as:

$$P(\sigma) = \delta(\sigma - \overline{\sigma}) \tag{3.90}$$

This PDF assumption blurs particle structures smaller than the LES cell. Thus the model is only valid if the minor structures of the observed scalar are larger than the LES cell. For soot, however, experiments [37, 178] and simulations [144, 145] have shown that this is not the case and that turbulent eddies stretch the fields into thin filaments smaller than the LES cell. The result is a spatially and temporally intermittent soot field. In simulations of nanoparticle synthesis [29, 128], a similar intermittent region was found in the mixing zone between streams with and without nanoparticles. Comparable intermittent zones can be found in turbulent free shear flows [172] where they describe the imprecisely defined boundary layer between the laminar and the turbulent flow. In other words, the probability that the flow is turbulent or laminar at a certain point. Based on the findings of turbulent free shear flows, Mueller and Pitsch proposed the

following expression for a more sophisticated PDF:

$$P(\sigma) = \omega_{\mathrm{I}}\delta(\sigma) + (1-\omega_{\mathrm{I}})\delta(\sigma-\sigma^*) \tag{3.91}$$

This definition of the PDF has two modes: the first delta function describes a non-particle mode, and the second delta function a particle mode. The intermittency ω_{I} here is the probability of finding particles at a random point in the LES cell. ω_{I} becomes unity if the probability is low and the particle layer infinitely thin, or zero for a homogeneous distribution. It should be noted that in contrast to Eq. (3.90), σ has been replaced with σ^*. Therefore, σ^* must be chosen such that the integration of the PDF results in the mean value. This results in the following definition:

$$\overline{\sigma} = \int \sigma P(\sigma) d\sigma = \sigma^*(1-\omega_{\mathrm{I}}) \iff \sigma^* = \overline{\sigma}/(1-\omega_{\mathrm{I}}) \tag{3.92}$$

The subfilter intermittency ω_{I} is defined as:

$$\omega_{\mathrm{I}} = 1 - \frac{\overline{\sigma}^2}{\overline{\sigma^2}} \tag{3.93}$$

where σ^2 is the raw second moment and should not be confused with the second central moment (variance). In their work, Mueller and Pitsch [144] considered different soot scalars (number-, volume- or surface area concentration) to approximate ω but found the total particle number concentration N_{tot} to be the best choice:

$$\omega_{\mathrm{I}} = 1 - \frac{\overline{N_{\mathrm{tot}}}^2}{\overline{N_{\mathrm{tot}}^2}} \tag{3.94}$$

In order to use the introduced PDF approach and to evaluate ω_{I}, two additional transport equations for $\overline{N}_{\mathrm{tot}}$ and $\overline{N_{\mathrm{tot}}^2}$ are solved besides the system of equation for the sectional model. The filtered equation for $\overline{N}_{\mathrm{tot}}$ is given as [144, 192]:

$$\frac{\partial \overline{N}_{\mathrm{tot}}}{\partial t} + \frac{\partial \tilde{u}_i \overline{N}_{\mathrm{tot}}}{\partial x_i} = \overline{\dot{N}}_{part} + \frac{\partial}{\partial x_i}\left(\frac{\nu^{sgs}}{Sc_t}\frac{\partial \overline{N}_{\mathrm{tot}}}{\partial x_i}\right) \tag{3.95}$$

Here the transport equations deviate from [192], and the thermophoretic component was neglected here for simplicity. The transport equation for $\overline{N^2}_{\mathrm{tot}}$ is given as:

$$\frac{\partial \overline{N^2}_{\mathrm{tot}}}{\partial t} + \frac{\partial \tilde{u}_i \overline{N^2}_{\mathrm{tot}}}{\partial x_i} = 2\overline{N}_{\mathrm{tot}}\overline{\dot{N}}_{part} - \overline{N^2}_{\mathrm{tot}}\frac{\partial \tilde{u}_i}{\partial x_i} + \frac{\partial}{\partial x_i}\left(\frac{\nu^{sgs}}{Sc_t}\frac{\partial \overline{N^2}_{\mathrm{tot}}}{\partial x_i}\right) \tag{3.96}$$

In theory, the transport of $\overline{N}_{\mathrm{tot}}$ is not required, and it can be recomputed from the transported values of each section. But $\overline{N}_{\mathrm{tot}}$ is transported to conserve the same numerical treatment between $\overline{N}_{\mathrm{tot}}$ and $\overline{N^2}_{\mathrm{tot}}$ part (certainly for the artificial viscosity).

Lagrangian Monte Carlo FDF methods

While the intermittency model aims to model the subfilter FDF from two moments, the filtered density function (FDF) approach aims to solve a transport equation of the FDF. Therefore, it has the advantage that the FDF shape does not have to be known and evolves during the simulation. The transported FDF approach is based on the transported PDF approach, which was first developed to describe reactive flows, either as a stand-alone method or in combination with RANS simulations by Dopazo & O'Brien [41], Pope [168], Janicka [87]. However, it first became a tractable tool for practical cases by applying a Monte Carlo method to solve the transport equation [170]. For a detailed overview of this topic, please refer to Pope [171].

The first suggestion to use transported PDF's in LES was made by Givi et al. [59], and Pope proposed the concept and notation of transporting a filtered density function [169]. The first closure approach for the transported FDF in LES was then proposed by Gao & O'Brien [53]. Most applications of the transported FDF method were for combustion modelling and as a closure approach for the reaction source term [180, 181, 209], but it can also be applied to any other scalar quantity. Initially, a distinction was made between the FDF for isothermal flow with constant density and the filtered mass density function (FMDF) for flows with variable density and exothermic reactions. In the present work, the transported FDF approach centres around the scalar-FMDF, but for brevity, the FMDF will be referred to as FDF, denoted by F_{F}. For a defined local coordinate $\boldsymbol{x}$, F_{F} describes the scalar fluctuations of the underlying scalars' array $\boldsymbol{\phi}(\boldsymbol{x},t) = [\phi_1, \phi_2 ... \phi_{n_s}]$ [32], with n_s scalars, in the composition domain of the scalar array $\boldsymbol{\psi}$, and is defined by:

$$F_{\mathrm{F}}(\boldsymbol{\psi};\boldsymbol{x},t) = \int_{-\infty}^{+\infty} \rho(\boldsymbol{x'},t) f_{\mathrm{F}}(\boldsymbol{\psi}, \phi(\boldsymbol{x'},t)) G(\boldsymbol{x'}-\boldsymbol{x}) d\boldsymbol{x'} \tag{3.97}$$

In this equation f_{F} is the fine-grained PDF in composition space (i.e., the PDF in one realisation of the flow) [153, 171], and G the filter kernel. Equation (3.97) implies that the FDF is the spatially Favre filtered value of the fine-grained density f_{F}, which is defined as:

$$f_{\mathrm{F}}(\boldsymbol{\psi}, \phi(\boldsymbol{x'},t)) = \delta(\boldsymbol{\psi} - \boldsymbol{\phi}(\boldsymbol{x},t)) = \prod_{\alpha=1}^{n_s} \delta[\psi_\alpha - \phi_\alpha(x,t)] \tag{3.98}$$

here, ϕ_α denotes a point in the sample space of the state space vector ψ_α. The evolution of the FDF in time and space can be described by a transport equation, which is deduced by taking the time derivative of Eq. (3.97) and applying some algebraic manipulations that leads to [32, 53, 181]:

$$\frac{\partial F_{\mathrm{F}}}{\partial t} + \frac{\partial \tilde{u}_i F_{\mathrm{F}}}{\partial x_i} = -\frac{\partial}{\partial x_i}\left(\left[\overline{u_i|\psi} - \tilde{u}_i\right] F_{\mathrm{F}}\right) + \frac{\partial}{\partial \psi_\alpha}\left[\overline{\frac{1}{\rho}\frac{\partial J_i^\alpha}{\partial x_i}\Big|\psi} F_{\mathrm{F}}\right] - \frac{\partial S_\alpha F_{\mathrm{F}}}{\partial \psi_\alpha} \tag{3.99}$$

Equation (3.99) represents the exact solution of the FDF in time and space but contains two unclosed terms (first two terms on the right-hand side). The first term represents the turbulent subfilter velocity fluxes, and the second term the subfilter diffusive fluxes. The subfilter velocity fluxes are commonly closed by a gradient diffusion approach [32]:

$$\frac{\partial}{\partial x_i}\left(\left[\overline{u_i|\psi} - \tilde{u}_i\right] F_{\mathrm{F}}\right) = -\frac{\partial}{\partial x_i}\bar{\rho} D_t \frac{\partial (F_{\mathrm{F}}/\bar{\rho})}{\partial x_i} \tag{3.100}$$

The term of the subfilter diffusion fluxes can be closed by a mixing model, such as the interaction-by-exchange-with-the-mean (IEM) model [235] or Curl's model [35]. Here in this work, the IEM model was applied:

$$\frac{\partial}{\partial \psi_\alpha}\left[\overline{\frac{1}{\rho}\frac{\partial J_i^\alpha}{\partial x_i}\Big|\psi} F_{\mathrm{F}}\right] = \frac{\partial}{\partial x_i}\bar{\rho}\widetilde{D}\frac{\partial (F_{\mathrm{F}}/\bar{\rho})}{\partial x_i} + \frac{\partial}{\partial \psi_\alpha}\left[\Omega(\psi_\alpha - \widetilde{\phi}_\alpha) F_{\mathrm{F}}\right] \tag{3.101}$$

Substituting Eq. (3.101) and Eq. (3.100) into Eq. (3.99), leads to the following closed transport equation:

$$\frac{\partial F_{\mathrm{F}}}{\partial t} + \frac{\partial \tilde{u}_i F_{\mathrm{F}}}{\partial x_i} = \frac{\partial}{\partial x_i}\bar{\rho}(D_t + \widetilde{D})\frac{\partial (F_{\mathrm{F}}/\bar{\rho})}{\partial x_i} + \frac{\partial}{\partial \psi_\alpha}\left[\Omega(\psi_\alpha - \widetilde{\phi}_\alpha) F_{\mathrm{F}}\right] - \frac{\partial S_\alpha F_{\mathrm{F}}}{\partial \psi_\alpha} \tag{3.102}$$

This transport equation is a high-dimensional equation with n_s dimensions for the scalar array, three dimensions in space, and an evolution in time. In total this equation spans n_s+4 dimensions and is for $n_s > 1$ not tractable with conventional finite-different/finite-volume based discretisation schemes [48]. Therefore, the transport is not solved directly but evolves based on a Lagrangian

Monte Carlo procedure [171]. In this procedure, individual Monte Carlo elements (notional particles) develop in physical-, and composition space based on stochastic equations. Each of these particles can be seen as a representation of a singular realisation of the turbulent scalar field. In this study, a total of $n_\mathrm{p} = 20$ particles were initially seeded in accordance with Rieth et al.[187]. Throughout this work, superscript $^+$ is used for particle quantities and Euler fields interpolated at a particle position as opposed to Eulerian field quantities (i.e., $\widetilde{u}$, $\overline{\rho}$). Each particle has a mass m^+, assigned at its initialisation, corresponding to the fluid mass occupied by the particle. The location of each particle is denoted by x^+, while the following equation governs the particle evolution in physical space [169]:

$$dx_i^+ = \left(\tilde{u}_i + \frac{1}{\bar{\rho}} \frac{\partial \bar{\rho} (\tilde{D}^+ + D_\mathrm{t}^+)}{\partial x_i} \right) dt + ((\tilde{D}^+ + D_\mathrm{t}^+))^{1/2} dW_i^+(t) \tag{3.103}$$

The change of particle position depends on the turbulent diffusivity D_t^+ and the molecular diffusivity $\tilde{D}^+$, the filtered velocity $\tilde{u}$ and a three dimensional Wiener process dW_i^+. The turbulent diffusivity is determined under the assumption of a constant turbulent Schmidt number (Sc_t) and the Lewis number. The evolution in composition space is in this work covered by the IEM mixing model [235]:

$$d\psi_\alpha = -\Omega_\mathrm{m}^+ (\psi_\alpha - \bar{\phi}_\alpha) dt + S_\alpha(\psi) dt \tag{3.104}$$

with Ω_m^+ beeing the mixing frequency:

$$\Omega_\mathrm{m}^+ = C_\mathrm{m} \frac{\tilde{D}^+ + D_\mathrm{t}^+}{\Delta^2} \tag{3.105}$$

with a model constant $C_\mathrm{m} = 12$ [188] for all the components, where Δ is the filter width. The Favre averaged quantities $\tilde{q}$ are calculated by averaging over all particles in a LES cell:

$$\tilde{q} = \frac{\sum_{p=1}^{n_\mathrm{p}} m_p^+ q_p^+}{\sum_{p=1}^{n_\mathrm{p}} m_p^+} \tag{3.106}$$

Alternatively, improved mixing frequency models should be developed. At this stage, the observation that the FDF model does not significantly change the results compared to a "primitive" model may well be due to the mixing model tested (i.e., the use of turbulent diffusivity or mixing frequency).

Future proposal

The disputation provided a noteworthy insight for upcoming simulations. While the definition of the mixing term in equation (3.105) agrees with existing literature, this term is predominantly influenced by turbulent diffusion. The diffusion of the nanoparticles is clearly limited due to the high Schmidt numbers ($D_\mathrm{t} > 1000D$), so that their correct mixing behaviour may not be properly represented. Subsequent investigations could benefit from the implementation of a revised mixing term:

$$\Omega_\mathrm{m}^+ = C_\mathrm{m} \frac{\tilde{D}^+}{\Delta^2} \tag{3.107}$$

Alternatively, improved mixing frequency models should be developed. At this stage, the observation that the FDF model does not significantly alter the results compared to a "primitive" model may only be due to the mixing model tested (i.e. use of turbulent diffusivity or mixing frequency).

Chapter 4
Numerical simulation

The conservation equations for mass, momentum, and energy form a non-linear system of equations. As a result, these equations' exact and analytic solutions can only be achieved for simplified flow problems. More complex flow problems require an approximation of the solution via numerical methods[1].

The numerical procedure involves discretizing the equations by decomposing the continuous partial differential equations into discrete differentials. The most well-known methods are the finite difference method (FDM), the finite element method (FEM), and the finite volume method (FVM). While all three methods are present in the scope of CFD simulations, the FVM is most prominent due to its ability to handle complex geometries, conservation properties, and good control over fluxes at the cell boundaries. In the following, the FVM method will be introduced starting from the following conservation equation:

$$\underbrace{\frac{\partial \phi}{\partial t}}_{\text{Accumulation}} + \underbrace{\frac{\partial (\rho \phi u_j)}{\partial x_j}}_{\text{Convection}} = \underbrace{\frac{\partial}{\partial x_j}\left(D_\phi \frac{\partial \phi}{\partial x_j}\right)}_{\text{Diffusion}} + \underbrace{\dot{\omega}_\phi}_{\text{Source}} \tag{4.1}$$

Numerical methods for the spatial and temporal discretisation terms in the FVM, and the pressure-velocity coupling, will be presented. Subsequently, the numerical treatment of Lagrangian particles is presented, followed by a brief introduction to the two CFD software packages used in this thesis: PsiPhi and OpenFOAM.

4.1 Finite volume method

The conservation equation Eq. (4.1) is written in its integral form as a starting point for the finite volume method, i.e., each term is integrated over an arbitrary finite volume, which leads to the following expression:

$$\int_V \frac{\partial \phi}{\partial t} dV + \int_V \frac{\partial (\rho \phi u_j)}{\partial x_j} dV = \int_V \frac{\partial}{\partial x_j}\left(D_\phi \frac{\partial \phi}{\partial x_j}\right) dV + \int_V \dot{\omega}_\phi dV \tag{4.2}$$

Then, the Gaussian theorem $\int_{\Delta V} \nabla \cdot \phi dV = \int_{\Delta A} \nabla \cdot \phi \cdot \boldsymbol{n} dA$ is applied to the transport terms (convection and diffusion), where $\boldsymbol{n}$ is the normal vector, and the volume integrals are replaced by surface integrals:

$$\int_V \frac{\partial \phi}{\partial t} dV + \int_A \frac{\partial (\rho \phi u_j)}{\partial x_j} n_j dA = \int_A \frac{\partial}{\partial x_j}\left(D_\phi \frac{\partial \phi}{\partial x_j}\right) n_j dA + \int_V \dot{\omega}_\phi dV \tag{4.3}$$

This formulation describes the change of ϕ in a single control volume. Many of these control volumes are joined together to form a computational grid and discretise a whole flow problem. Accordingly, the control volume size needs to be smaller than the smallest flow structure (in DNS (Sc $\leq$ 1.0), the Kolmogorov length scale introduced in Section 2.1.2). The control volumes can all be cubic and form a structured grid, or they can take another form (triangles, tetrahedra) and form an unstructured grid. Both types have been used in this thesis, but only the structured one will be discussed below for simplicity. Figure 4.1 shows a cubic control volume in 2D. The

[1] Branch of mathematics dealing with the construction and analysis of algorithms for continuous mathematical problems

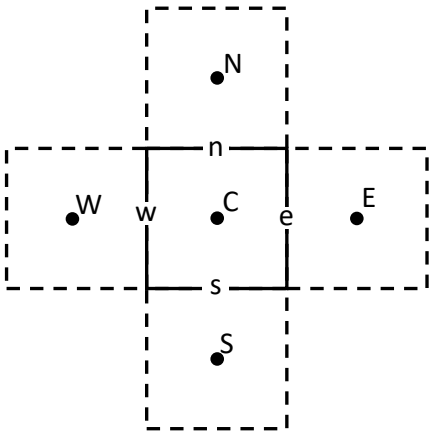

Figure 4.1: Sketch of a Cartesian 2D cell and its neighbours.

discretisation of a single cell with centre C requires values from the neighbouring cell represented by the letter of the respective cardinal direction (i.e., W=west). The boundaries between the individual cells are represented by lower case letters (i.e., w=western boundary of cell C).

4.1.1 Volume integral discretisation

The integral over the cell volume must be calculated to determine the source term and the accumulation term in Eq. (4.3). For this purpose, the general assumption is made that all cell values are equal to the value in the cell centre. This assumption allows the following simple expression for the computation, shown at the example of the source term:

$$\int_{\Delta V} \dot{\omega}_C \approx \dot{\omega}_{\phi,C} \Delta^3 = \dot{\omega}_{\phi,C} \cdot dx \cdot dy \cdot dz \tag{4.4}$$

In this equation, Δ is the cell size.

4.1.2 Convective flux

The convective flux is described by an integral over the cell surfaces. This integral can be approximated for a cubic cell with six sides by adding up the individual fluxes over each cell surface:

$$\int_{\Delta A} \rho \phi u_j n_j dA \approx \sum_f \rho_f \phi_f u_f n_f \Delta A_f \tag{4.5}$$

The subscript f refers to values on the cell surfaces which, unlike the values at the cell centre, are not known. Thus, the difficulty in approximating the convection term is determining these cell surface values from the cell centre values. Over the years, various interpolation methods have been developed, with the trade-off between the method's accuracy, numerical stability, and computational cost. In the following, the most popular interpolation methods are presented and discussed. The direction of flow F from left to right ($F \geq 0$) applies to the discussions in each case.

Central discretisation scheme

The central difference scheme (CDS) is probably the most intuitive and calculates the values on the cell surfaces by linearly interpolating the values from neighbouring cell centres:

$$\phi_{\mathrm{w}} = \frac{1}{2}(\phi_{\mathrm{W}} + \phi_{\mathrm{C}}) \tag{4.6}$$

This method has second-order accuracy[2], but it tends to numerical instabilities for unstructured grids and rapid flow changes.

Upwind discretisation scheme

Besides the central difference scheme, the upwind differencing scheme (UDS) is the second fundamental method. In this method, the cell mean value from the upstream cell is chosen as the cell face value depending on the flow direction F:

$$\phi_e = \begin{cases} \phi_C, & \text{if } F \geq 0 \\ \phi_E, & \text{if } F < 0 \end{cases} \tag{4.7}$$

This method is very robust, but only of first-order accuracy. Furthermore, UDS is not suitable for complex flows due to its high numerical diffusion, which smears the complex structures.

Total variation diminishing scheme

A compromise between the second-order (but unstable) CDS and the first-order (but robust) UDS is offered by the total variation diminishing scheme (TVD). The TVD blends between CDS and UDS and allows CDS where possible (smooth solutions) and UDS when bounded non-oscillating solutions are necessary. The face value is calculated from:

$$\phi_e = \phi_C + \frac{\theta(r)(\phi_C - \phi_E}{2}) \tag{4.8}$$

θ here represents a so-called flux limiter, which regulates the proportion of UDS to dampen oscillations and the application of CDS where possible. Although there exist different limiters [234], in the present work, the Charm Limiter [254] in the PsiPhi framework, and the Sweby Limiter [227] in the context of OpenFOAM were used. The Charm limiter is defined as follows.

$$\theta(r) = \frac{r^*(3r^* + 1)}{(r^* + 1)^2} \tag{4.9}$$

here r^* is defined as $r^* = \max(r, 0)$, and r represents the ratio of successive gradients along the grid and is defined as:

$$r = \frac{\phi_W - \phi_C}{\phi_C - \phi_E} \tag{4.10}$$

The Sweeby limiter is defined as follows:

$$\theta(r) = max\left(max\left(\frac{2r}{k}, 1\right), 0\right) \tag{4.11}$$

Here k is a user-defined quantity between 0 and 1. Thus, for $k = 0$, the limiter tends to a pure CDS scheme and features the highest accuracy and least bounding. While $k = 1$ leads to pure UDS. For both limiters, $\theta = 0$ leads to a pure upwind scheme, and $\theta = r$ leads to a pure CDS scheme.

[2]Order of accuracy quantifies the rate of convergence of a numerical approximation of a differential equation to the exact solution.

4.1.3 Diffusive flux

To approximate the diffusive flux in Eq. (4.3), the derivatives of ϕ at the cell faces are required. In most cases, this is achieved with a central difference method, which is robust and accurate enough for diffusive fluxes. The surface integral is expressed as the sum of the fluxes over the cell surface as a starting point.

$$\int_{\Delta A} \left(\rho D_\phi \frac{\partial \phi}{\partial x_j} \right) n_j dA = \sum_f \left[\rho D_\phi \frac{\partial \phi}{\partial x_j} \right]_f n_f \Delta A_f \tag{4.12}$$

For orthogonal cells, the expression in the bracket can then be determined as follows:

$$\left[\rho D_\phi \frac{\partial \phi}{\partial x_j} \right]_f n_f = |n_f| \frac{\phi_E - \phi_C}{\Delta} \tag{4.13}$$

An orthogonal corrector can be applied for non-orthogonal cells, as is the case with unstructured grids, giving the following equation:

$$\left[\rho D_\phi \frac{\partial \phi}{\partial x_j} \right]_f n_f = \underbrace{\gamma_f d_f \frac{\phi_E - \phi_C}{\boldsymbol{d}}}_{\text{orthogonal}} + \underbrace{(n_f - \gamma_f d_f) \frac{\phi_E - \phi_C}{\boldsymbol{d}}}_{\text{non-orthogonal}} \tag{4.14}$$

γ is a weighting factor chosen depending on the grid orthogonality[3], while d_f represents the projection of n_f and $\boldsymbol{d}$ is a distance vector between the cell centers C and E. The correction is essential for OpenFOAM simulations, and detailed information can be found in Jasak's thesis [89].

4.1.4 Temporal evolution

The accumulation term describes the time evolution of a flow, starting from a given initialisation. As a starting point for the temporal discretisation, the other spatial terms need to be approximated, and these terms will be collectively referred to as the right-hand side:

$$\frac{\partial \rho \phi}{\partial t} = \underbrace{-\frac{\partial (\rho \phi u_j)}{\partial x_j} + dx_j \left(D_\phi \frac{\partial \phi}{\partial x_j} \right) + \dot{\omega}_\phi}_{\text{RHS}(\rho\phi)} \tag{4.15}$$

The discretisation schemes of the accumulation term can be categorized into explicit schemes, implicit schemes, and hybrid explicit-implicit schemes. The explicit and implicit Euler methods' are elementary models for these schemes and will be presented below to clarify the implicit and explicit concepts. On this basis, the higher accurate Runge-Kutta model and the hybrid Crank-Nicholson are presented.

In the following, the nomenclature is n for the current time step at time t and $n+1$ for the time step to be calculated at time $t + \Delta t$.

Euler explicit scheme

In the explicit Euler method, the temporal development of the flow field is calculated based on the values of the current time step. The accumulation term is written as follows:

$$\frac{\partial \rho \phi}{\partial t} \approx \frac{[\rho \phi]^{n+1} - [\rho \phi]^n}{\Delta t} = \text{RHS}([\rho \phi]^n) \tag{4.16}$$

[3] In elementary geometry, two straight lines or planes are called orthogonal (or perpendicular) if they enclose a right angle, i.e., an angle of 90°.

This method is of first-order accuracy and is implemented as the basic method in most CFD solvers. The time step Δt is calculated from the CFL condition named after Courant, Friedrichs, and Lewy [120] and is written as follows:

$$\mathrm{CFL} = \frac{|u_i|\Delta t}{\Delta x} \tag{4.17}$$

For the first-order Euler explicit scheme applies CFL< 1, which is a necessary condition to ensure the stability of the numerical scheme. However, it is important to note that this stability criterion only applies to upwind methods, whereas CDS is unconditionally unstable.

Runge-Kutta scheme

The Runge-Kutta method is a more robust and accurate scheme for LES and DNS as an alternative to explicit Euler. It is an explicit method that calculates the next time step solution based on the current solution but divides a whole time step into three subsequent intermediate time steps $m = 1, 2, 3$:

$$\phi^{n_m} = \phi^{n_{m-1}} + b_m q_m \tag{4.18}$$

$$q_m = a_m q_{m-1} + \mathrm{RHS}(\phi^{n_{m-1}}) \tag{4.19}$$

The resulting equations are:

$$\begin{aligned}
\phi^{n_1} &= \phi^n + b_1\mathrm{RHS}(\phi^n)\Delta t \\
\phi^{n_2} &= \phi^{n_1} + a_2 b_2 \mathrm{RHS}(\phi^n)\Delta t + b_2\mathrm{RHS}(\phi^{n_1})\Delta t \\
\phi^{n_3} &= \phi^{n_2} + a_2 a_3 b_3 \mathrm{RHS}(\phi^n)\Delta t + a_3 b_3 \mathrm{RHS}(\phi^{n_1})\Delta t + b_3\mathrm{RHS}(\phi^{n_2})\Delta t
\end{aligned}$$

The weighting factors can be adopted in different ways, but Williamson [246] found in his work that the following values offer a good compromise between numerical precision and stability:

$$\begin{aligned}
a_1 &= 0; & b_1 &= 1/3; & w_1 &= 1/3 \\
a_2 &= -5/9; & b_2 &= 15/16; & w_2 &= 5/12 \\
a_3 &= -153/128; & b_3 &= 8/15; & w_3 &= 1/4
\end{aligned}$$

Here w_1, w_2 and w_3 represent weighting factors to calculate the time between the sub-steps in the Runge kutta method: $t^m = t^{m-1} + \Delta t \cdot \omega_n$.

Euler implicit scheme

For the implicit Euler scheme, the time evolution is implicitly calculated based on the new time step as follows:

$$\frac{\partial \rho\phi}{\partial t} \approx \frac{[\rho\phi]^{n+1} - [\rho\phi]^n}{\Delta t} = \mathrm{RHS}([\rho\phi]^{n+1}) \tag{4.20}$$

This procedure is of first-order accuracy and is unconditionally stable. It allows for much larger time steps than the explicit Euler scheme, but its implementation is more complicated. Nevertheless, its large time step widths make it an attractive method for flows with only weak transient behaviour or steady-state solutions.

Crank Nicolson

The Crank-Nicolson method [33] is a hybrid between Euler explicit and Euler implicit with a blending scheme. The method has second-order accuracy and reads as:

$$\frac{\partial \rho\phi}{\partial t} \approx \frac{[\rho\phi]^{n+1} - [\rho\phi]^n}{\Delta t} = \left[\gamma_{\mathrm{CN}}\mathrm{RHS}([\rho\phi]^{n+1}) + (1-\gamma_{\mathrm{CN}})\mathrm{RHS}([\rho\phi]^n)\right] \tag{4.21}$$

γ_{CN} is the blending factor and is $\gamma_{CN} = 0.5$ for the classical Crank-Nicolson method. A variation of this value always leads to a solution with lower accuracy. Closer to zero, it tends more to an explicit Euler and closer to unity to an implicit Euler, where it becomes unconditionally stable.

4.1.5 Pressure correction

The flows investigated in this work can be assumed to be incompressible, which is justified by their low Mach numbers (Mach number < 0.3). With this assumption, a constant background pressure, e.g., ambient pressure, prevails in the entire computational domain. The pressure gradient in the momentum equation represents a dynamic pressure, which is necessary for the velocity to satisfy continuity. Therefore the pressure and the density are not coupled via the equation of state, contrary to compressible flow. However, a predictor-corrector scheme is applied in most CFD codes to overcome this issue in incompressible flows and determine the pressure gradient. In this scheme, the momentum equation is solved without exact knowledge of the pressure gradient and then iteratively corrected to satisfy the continuity equation. Two different flow solvers (PsiPhi and OpenFOAM) were used in the present work, and their respective predictor-corrector procedures will be briefly presented here.

The predictor-corrector scheme from the PsiPhi flow solver is based on the work of Kempf [104] and Stein [220]:

- In the predictor step, the RHS of the momentum transport equation is solved without the pressure gradient. The resulting predicted solution contains the unknown pressure gradient.
- The difference between predicted momentum and pressure gradient can be inserted into the continuity equation and allows to write a poison type equation for the pressure.
- Iterative solvers then approximate this equation. In PsiPhi, for example, a Gaus Seidel or a Jacobi solver are applied.
- With the solution from the pressure equation, the moment field is then corrected.

Further information on this pressure correction algorithm can be found in the work by Proch [175].

The OpenFOAM flow solver uses the pressure implicit split operator (PISO) scheme [84]. The procedure of this scheme is as follows:

- The momentum equation is solved in the predictor step, including the pressure gradient using the pressure field from the previous time step.
- A pressure equation can be formulated from the predicted velocities whose solution leads to a correction of the pressure field.
- The velocities are then corrected in a corrector step based on the new pressure.
- This correction is carried out iteratively until the remaining error is below a certain limit.

More information about pressure correction with the Piso scheme can be found in the work of Jassak [89].

4.2 Lagrangian particles

The numerical treatment of the equations describing the temporal evolution of the Lagrangian particles is consistent with the Euler quantities embedded in the Runge-Kutta scheme. However, an essential element for the Euler-Lagrangian method is the interpolation between Euler and Lagrangian quantities, e.g., the projection of Euler quantities onto Lagrange particles or vice

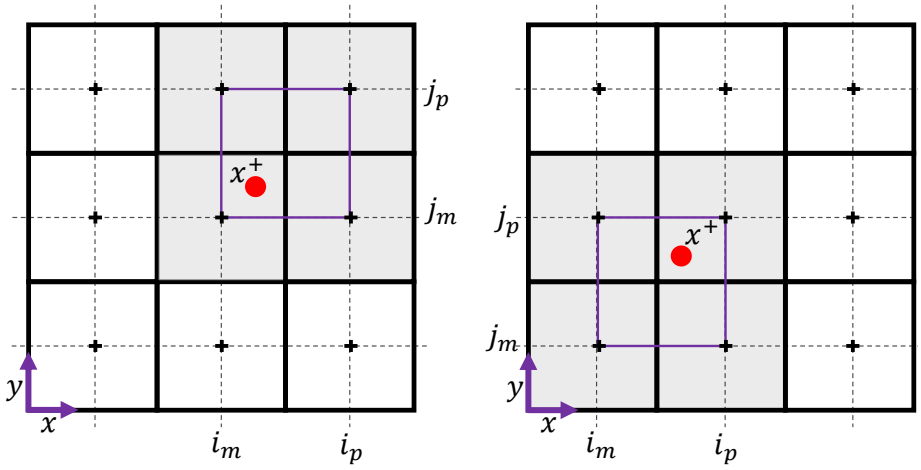

Figure 4.2: Sketch of a Lagrangian particle located in an cartesian 2D grid.

versa. This interpolation method is presented in the following illustrated by a 2D problem, schematically shown in Fig. 4.2. A Lagrange particle, at any point in the Eulerian grid, as long as it is not precisely on a cell centre, will lie between 4 cell centres (8 cell centres in 3D). For the interpolation, first, the position of the individual particle x^+ in Cartesian space is determined, its distance to the nearest cell centre in negative x-direction $x(i_\mathrm{m})$ and to the nearest cell centre in positive x-direction $x(i_\mathrm{p})$. Based on this, a weighting to the respective cell centre can be calculated $w(i_\mathrm{m}) = x(i_\mathrm{m}) - x(i_\mathrm{p})$ and $w(i_\mathrm{p}) = 1 - w(i_\mathrm{m})$. The direction of the y-axis is treated equivalently. The 2D interpolation of an arbitrary quantity ϕ from the eulerian grid to a Lagrangian particle can then be written as follows:

$$\phi_p = \sum_{i\in[i_m,i_p]} \sum_{j\in[j_m,j_p]} w(i)w(j)\phi(i,j) \tag{4.22}$$

The interpolation of ϕ transported on a Lagrangian particle interpolated to the Euler cells is then calculated as follows:

$$\begin{aligned}
\phi(i_\mathrm{m}, j_\mathrm{m}) &= w(i_\mathrm{m})w(j_\mathrm{m})\phi_\mathrm{p}, \\
\phi(i_\mathrm{m}, j_\mathrm{p}) &= w(i_\mathrm{m})w(j_\mathrm{p})\phi_\mathrm{p}, \\
\phi(i_\mathrm{p}, j_\mathrm{m}) &= w(i_\mathrm{p})w(j_\mathrm{m})\phi_\mathrm{p}, \\
\phi(i_\mathrm{p}, j_\mathrm{p}) &= w(i_\mathrm{p})w(j_\mathrm{p})\phi_\mathrm{p}.
\end{aligned} \tag{4.23}$$

The Lagrangian particles are used on an orthogonal equidistant mesh, which allows a straightforward calculation of the particle position and distance towards the cells.

Since all simulations took place in free space without walls, no special treatment for interaction with walls (e.g., no-slip treatment) was needed, and the boundaries had an outflow condition. For the initialisation of the particles and the coupling between the Euler/Lagrange phase, in this work, the Lagrange particles are divided into two subsets of particles: liquid particles for describing liquid spray droplets and stochastic particles for the stochastic solution approach of the FDF method. First, the liquid particles were initialised, by assigning each particle the weight of the liquid droplet it represents. Further, the gaseous Euler phase was coupled with the liquid particles via momentum and mass exchange in both directions. The stochastic particles were initialised at the inflow with the mass of the respective inflowing gas amount it represents. For the coupling it should be noted that the FDF method was used in this work to describe the nanoparticle synthesis and its dynamics. Due to the small amount of nanoparticles, they are transported as a disperse phase, but do not influence the gas phase and its dynamics. For this

reason, the particles are only unilaterally coupled in the calculation and do not give any direct feedback to the gas phase.

4.2.1 Particle number density control in the FDF method

For stochastic Lagrangian solution methods, the statistical error scales with the number of particles ($N_P^{-1/2}$, N_P stands for the number of particles). For meaningful statistics, therefore, it is necessary to have a sufficient number of particles in each computational cell. For this reason, an algorithm splits particles in this work when the particle number density in a computational cell is low. The algorithm determines the heaviest particle in the cell, divides its weight, and clones the particle so that two particles exist in the end. The algorithm carries out this process until a sufficient particle density is present. In order to avoid load balancing elsewhere in the simulation domain, the reverse process is done, i.e., when the particle density exceeds a particular value. The algorithm selects the two lightest particles, deletes one (the lightest), adds up the masses of these two particles, and transfers the mass-averaged properties of the two particles to the second lightest particle. Also, this process is continued until a sufficient particle density is present. This process artificially reduces the subgrid variance and is therefore only applied at very high number densities and not frequently.

4.3 CFD-Solver

Two different CFD codes were used to solve the conservation equation in the present work. The open-source package OpenFOAM was used to simulate *laminar* particle-forming flames and the in-house code PsiPhi to simulate *turbulent* particle-forming flames. Both are presented below.

4.3.1 OpenFOAM

OpenFOAM (*Open Source Field Operation and Manipulation*) is a C++ toolbox (library) that includes numerical solvers for continuum mechanical problems, focusing on computational fluid dynamics (CFD) [241]. The base code was developed in 1998 and is an open-source project licensed under the GNU general public license (GPL)[4]. This library includes basic turbulence solution approaches (RANS/LES/DNS) with the most popular turbulence models (Sigma, K-epsilon...), but it also allows the implementation and development of individual models. Moreover, unstructured grids can be used for discretising the computational domains, allowing grid refinement in specific domains. This has the benefit that flow problems in complex geometries can be approximated. The program is used both in industry and academia, so the models have been validated extensively and further developed. For the laminar flame simulations in this work, a modified version of the flow solver *reactingFoam* was used. While the initial version solves the flame chemistry through finite rate chemistry with a unity lewis assumption, Deng [39] extended the solver for detailed heat and transport diffusion. Unfortunately, this modification is not standard in OpenFOAM, but is particularly important for laminar hydrogen flames, which were the focus of the study.

In the present work, OpenFoam was extended with the monodisperse and bi-modal models and used to simulate nanoparticle synthesis in laminar flames.

4.3.2 PsiPhi

PsiPhi is an in-house code, conceptualized and originally developed by Prof. Kempf at Imperial College London. The primary goal was to create a fast, efficient and accurate flow solver to investigate and develop the LES method and its models for reactive flows.

[4]GPL is a series of widely used free software licenses that guarantee end users the freedom to run, study, share, and modify the software

Since its release, the code has been continuously developed at the Imperial College London, Instituto Superior Tecnico de Lisboa, the University of Leeds, Sheffield, and the University Duisburg-Essen contributed with features with their expertise in high-performance computing, numerical methods, and physics modelling. The code enables LES or DNS simulation of compressible [126] and incompressible [176, 177] flows using detailed or tabulated chemistry models. It further includes approaches for multiphase flows such as nanoparticle synthesis [191] and spray [190] or charcoal [186] combustion.

The code is written in Fortran and uses MPI for massive parallelization. In addition, PsiPhi uses a Cartesian uniform grid to discretise computational domains. Its Cartesian grid preserves the theoretical accuracy of the schemes but has the disadvantage that complex structures can only be resolved with great effort.

In the present work, the code was extended by the intermittency model (Section 3.3.4) and an FDF-method (Section 3.3.4) to resolve the subgrid structures of the coagulation kernel. A simulation setup for the SpraySyn burner was implemented.

Chapter 5
Detailed simulation of laminar flames

5.1 Detailed simulation of iron oxide nanoparticle forming flames: Buoyancy and probe effects [206] (Paper I)

This section of Chapter 5 including all text, figures and tables is published in the Proceedings of the Combustion Institute 'Sellmann, J., Rahinov, I., Kluge, S., Jünger, H., Fomin, A., Cheskis, S., Schulz, C., Wiggers, H., Kempf, A., Wlokas, I. (2019). Detailed simulation of iron oxide nanoparticle forming flames: buoyancy and probe effects. Proceedings of the Combustion Institute, 37(1), 1241-1248.' [206] and is reprinted with permission from Elsevier.
Contributor Roles Taxonomy: J. Sellmann developed the code, ran the simulations and wrote the original manuscript draft. The author I. Rahinov performed the experiments and wrote the original manuscript draft of the paper. The author S. Kluge performed experiments. The authors H. Junger, A. Fomin, S. Cheskis, H. Wiggers provided a discussion of the results. The authors C. Schulz, A. Kempf and I. Wlokas provided a discussion of the results and contributed to the manuscript.

Abstract

Nanoparticle formation in flames is strongly influenced by the residence-time–temperature history inside the flame. We study how the temperature history can be intentionally modified by orienting flames either in an upward-firing or downward-firing configuration. We also investigate the influence of unintended residence-time modifications caused by sampling nozzles. These phenomena are investigated by experiments and simulations for the synthesis of iron oxide nanoparticles from premixed iron-pentacarbonyl-doped hydrogen/oxygen flat flames. The experiments apply molecular-beam sampling with a particle mass spectrometer to measure particle sizes and a quartz microbalance to detect the presence of condensed matter. The simulations rely on a finite-rate chemistry approach with species-specific diffusion, particle dynamics are described by a bi-modal population balance model. It is demonstrated that the downward-burning flame forms a detached stagnation point, causing longer residence times at elevated temperature than an upward- or horizontally firing flame, permitting the growth of larger particles. These iron oxide particles are eventually formed in the recombination zone of the flame, but no condensed matter was found in the reaction zone. The experiments also observed the formation of particles in the preheat zone, but their composition and all aspects of their disappearance remain uncertain. Current models do, however, suggest the formation of iron particles and their subsequent evaporation and combustion.

5.1.1 Introduction

Materials synthesis from gas-phase processes has gained a large significance [102, 122]. From the large variety of materials, the process of forming iron oxide nanoparticles is among the best investigated [46, 58, 106, 158, 167, 219, 242, 247], but it is still difficult to control the iron oxide synthesis process to achieve desired product properties. Iron pentacarbonyl ($Fe(CO)_5$) is frequently used as a precursor. Its high vapour pressure enables the nanoparticle synthesis from premixed gases which also provides well-defined experimental conditions for fundamental investigations in low-pressure flat flames, in flow reactors, and in shock tubes [58, 158]. It is the main precursor for nanosized iron powders from thermal pyrolysis (carbonyl iron, [58, 142,

242]) and it is known for its strong impact on flame chemistry, making it a potential anti-knock agent and a flame inhibitor [196]. Staude et al. [219] presented a good overview of the state of research on $Fe(CO)_5$. Measurements of particle sizes from $Fe(CO)_5$-doped flames [45] lead to a model of particle formation from the flame, but without experimental evidence of Fe_2O_3 particle growth as a gas-phase species [247]. This model was extended by Feroughi et al. [46] to account for the pyrolysis and Fe-cluster formation steps proposed by Wen et al. [242], after metallic deposits were observed on the burner surface during iron oxide synthesis from a non-premixed flame. Measurements by Poliak et al. [167] using the combined PMS-QCMB-technique (particle mass spectrometry, quartz-crystal micro balance) validated Feroughi's model for early formation of condensable matter in the preheat zone of a premixed flame. Further validation, including measurements of FeO formation in the premixed flame, was achieved by Kluge et al. [106]. A closer look at the findings of Poliak [167] and Kluge [106] suggests that the structure of a $Fe(CO)_5$-doped flame features two very distinct particle forming zones: Condensable matter is initially formed in the preheat zone of the flame, but no condensed material is observed in the reaction zone, and iron oxide particles are formed only in the late recombination zone. This was also confirmed by the model that describes the formation and the succeeding decomposition of iron clusters from thermal pyrolysis of $Fe(CO)_5$ and the combustion of the pyrolysis products.

For designing scalable flame-synthesis processes that generate materials with well-defined properties, the individual processes of gas-phase reactions, the effects of intermediate species, particle nucleation, and particle growth must be understood in detail. An ideal experiment for further studies are one-dimensional laminar, premixed, flat flames, which are popular for experiments on nanoparticle formation from the gas phase [42], for the validation and development of reaction mechanisms, and for the prediction of the flame structure. However, particle formation from low-pressure flames is usually observed at large distances from the burner surface (DFB, typically at distances larger than 100 mm at 3000 Pa). At such large distances, the flow is strongly affected by buoyancy and heat losses and the assumption of a one-dimensional flow is no longer valid [239]. The experimental setup used in the present work features both an up-firing flame (UFF) and a down-firing flame (DFF) configuration. Typical arrangements in the past were upward- or horizontally-burning flames [88, 106, 239, 247]. The DFF configuration as a "buoyancy-opposed flame" shown in Fig. 3 allows to generate residence-time–temperature histories inaccessible in other setups. An example of a DFF setup was used for aerogel formation from a gas-phase process by Chakrabarty et al. [22], allowing to avoid complicated reactor modifications that would be otherwise required to achieve a significant increase in particle residence times at high temperatures.

Regardless of the orientation of the burner, the deviation from an ideal one-dimensional flow assumption is not negligible in case of invasive particle probing [40]. Thus, for a decent interpretation of the measurements, complementary 2D or 3D direct numerical simulations are indispensable to "reconstruct" the flow and temperature field to enable quantification of the deviations from an ideal 1D flow. The importance of such simulations was demonstrated for example by Weise et al. [239] and Kluge et al. [106] for molecular-beam (MB) sampling measurements with PMS in a horizontally-oriented [239] and in an upward-burning flame (called up-firing flame, UFF, here) [106]. Deng et al. [40] used MB mass spectrometry from atmospheric flames and Camacho et al. [21] and Saggese et al. [198] probe soot from stagnation-point flames. In these cases, the authors demonstrated the improvement of the interpretability of corresponding measurements by numerical reconstruction of the flow and temperature field that is influenced by the sampling. In the down-firing flame, the flow-field simulations become an essential part of the experiment by calculation of the stagnation point at which the hot flow is deflected. In this work, we present the first attempt of modelling both buoyancy effects and sampling-induced perturbations on the time history of the formed particles, validate the simulations against the experiment, and use the results to improve the interpretation of the measurements on iron oxide nanoparticle formation from laminar, premixed, low-pressure (30 mbar) hydrogen/oxygen/Argon down-firing flames

doped with $Fe(CO)_5$, supported on a porous sintered plate. The results highlight how buoyancy decelerates the flow, causing a detached stagnation point, and how the probing nozzle changes the overall shape of the flame, depending on the distance between the probe and the burner. The corresponding residence times are strongly affected by the probe – an effect previously observed for up-firing flames with a stagnation plate [40].

5.1.2 Experiment

The experimental apparatus used in this work is shown in Fig. 5.1 and has been described before [219], thus only an overview will be presented here. The same flat-flame burner equipped with

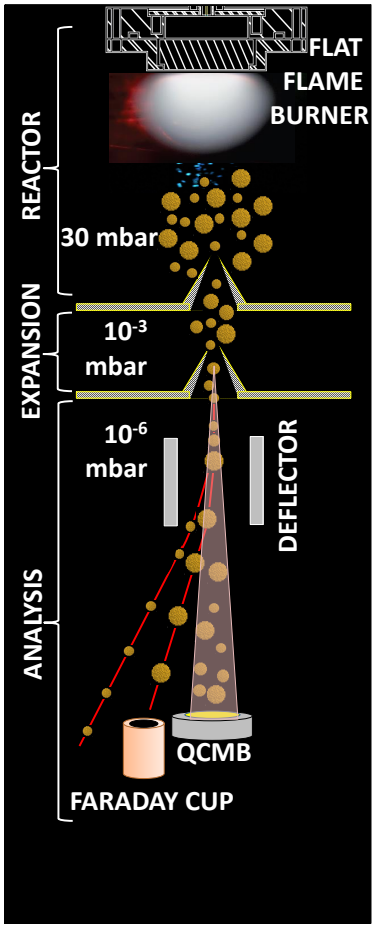

Figure 5.1: Sketch of the experimental setup (not to scale).

a water-cooled 36-mm diameter sintered-metal plate, was operated in two different geometrical setups. First, in the upward firing configuration in Duisburg housed by a reactor with $D = 100\,\text{mm}$, and in the downward firing configuration in Tel Aviv laboratories with a reactor of $D = 256\,\text{mm}$. Two low-pressure (3000 Pa) $H_2/O_2/Ar$ flames doped with $Fe(CO)_5$ were studied with precursor mass flows ranging from 200–300 ppm (table 5.1.2). The properties of the flame-

Table 5.1: Flame conditions used in the present work

Flame	H_2	O_2	Ar	CH_4	$Fe(CO)_5$
	sccm	sccm	sccm	sccm	ppm
A	400	400	600	-	200
B	400	400	600	10	300

made particles, in terms of their size and the total mass loading in the aerosol are determined via molecular-beam sampling shown in Fig. 5.1. At variable distance from the burner, the post-flame gas is sampled via a nozzle/skimmer setup and expanded into the vacuum, forming a particle-laden molecular beam. The decomposition of the precursor and its influence on the flame chemistry can be studied by varying the distance between the burner and the nozzle. Particles within the gas are then either collected on (i) a quartz-crystal microbalance (QCMB) [47] to study the deposition rate and thus the (relative) mass concentration of all condensable matter in the extracted gas, or (ii) in a particle mass spectrometer (PMS) [88] evaluating their size distribution.

5.1.3 Flow, combustion and particle modelling

modelling the reacting flow and particle dynamics

The simulations used the framework described by Deng et al. [106], which was also used in other work [40, 106]. The reaction mechanism was based on the one proposed by Feroughi et al. [46] and was reduced into a skeletal mechanism, using the genetic algorithm based method proposed by Sikalo et al. [212]. Particle dynamics were calculated using the population-balance model proposed by Jeong et al. [90], assuming a bi-modal particle-size distribution. The first mode "1" describes newly generated particles is a size fixed "nucleation mode", the second mode "2" for particles growing by coagulation and coalescence is a moving "accumulation mode". Convection and diffusion of particles were calculated using the flow field (velocity, temperature, and species mass fractions) obtained from the reacting flow simulations. The evolution of the particles by aerosol- and fluid-dynamic processes is described by the particle-number concentration $N_{1/2}[\,\mathrm{m}^{-3}]$, the volume concentration $V_{1/2}[\,-]$, and the surface-area concentration $A_{1/2}[\,\mathrm{m}^2/\mathrm{m}^3]$. The rate of change in time and space, for the particle number concentration in the first mode N_1 can be described as follows:

$$\frac{\partial N_1}{\partial t} + \nabla \cdot (uN_1) = \nabla \cdot (D_p \nabla N_1) - \frac{1}{2}\beta_{11} N_1^2 \left(\frac{r}{r-1}\right) - \beta_{12} N_1 N_2 + I. \tag{5.1}$$

The coagulation kernel β_{ij} covers the free molecular and the continuum regime, given by Fuchs interpolation function [90]. To capture the effect of the aggregate structure, the solid-sphere diameter in the calculation of β_{ij} was replaced by the collision diameter as proposed by Kruis et al. [115]. The particles' fractal dimension was estimated as $D_f = 1.8$ according to Poliak et al. [167], who found iron oxide, formed at similar conditions, branched as chains of soft-agglomerated particles. The ratio between the monomer volume and the volume of particles in the second mode is given by r. The particle diffusion coefficient D_p was adapted following Kruis et al. [115], and the description of the source term I and the monomer diameter $d_m = 0.4\,\mathrm{nm}$ was adapted from Wlokas et al. [247]. For mode 1, the volume- and surface-area concentration was obtained from the monomer diameter and particle number concentration.

Intramode- and intermode coagulation of particles from mode 1 and 2, as well as sintering by coalescence, is described by the transport equations for N_2, V_2, and A_2:

$$\frac{\partial N_2}{\partial t} + \nabla \cdot (uN_2) = \nabla \cdot (D_p \nabla N_2) - \frac{1}{2}\beta_{11} N_1^2 \left(\frac{1}{r-1}\right) - \frac{1}{2}\beta_{22} N_2^2 \tag{5.2}$$

$$\frac{\partial V_2}{\partial t} + \nabla \cdot (uV_2) = \nabla \cdot (D_p \nabla V_2) + \frac{1}{2}\beta_{11} N_1^2 \left(\frac{r}{r-1}\right) v_0 + \beta_{12} N_1 N_2 v_0 \tag{5.3}$$

$$\frac{\partial A_2}{\partial t} + \nabla \cdot (uA_2) = \nabla \cdot (D_p \nabla A_2) - \frac{1}{\tau}(A_2 - A_s) + \frac{1}{2}\beta_{11} N_1^2 \left(\frac{r}{r-1}\right) a_0 + \beta_{12} N_1 N_2 a_0 \tag{5.4}$$

The implementation of the model was validated against the artificial test case by Spicer et al. [218].

Simulation setup

The simulations of the flame and the probing were carried out on a two dimensional, rotationally symmetric computational domain as shown in Fig. 2. To consider the varying housing sizes, different simulation setups were applied. For the DFF configuration, an outlet boundary condition at 60 mm in radial direction were chosen, which ensure sufficient distance between burner and boundaries. The flames A and B from table 5.1.2 were simulated without probing (Unp.) and for different probing positions (40–50 mm). The smaller reactor housing for the upward burning flame in Duisburg was considered by isothermal walls at 50 mm in radial distance, and only the unperturbed flames A and B were simulated. For both UFF and DFF the inlet temperature was $T_{\text{in}} = 300\,\text{K}$. The thin walls of the probing nozzle allowed an assumption of adiabatic nozzle walls (instant heating). The pressure at the orifice was set to 1000 Pa, causing a critical flow into the nozzles tip. The pressure at the far field boundaries was set to 3000 Pa.

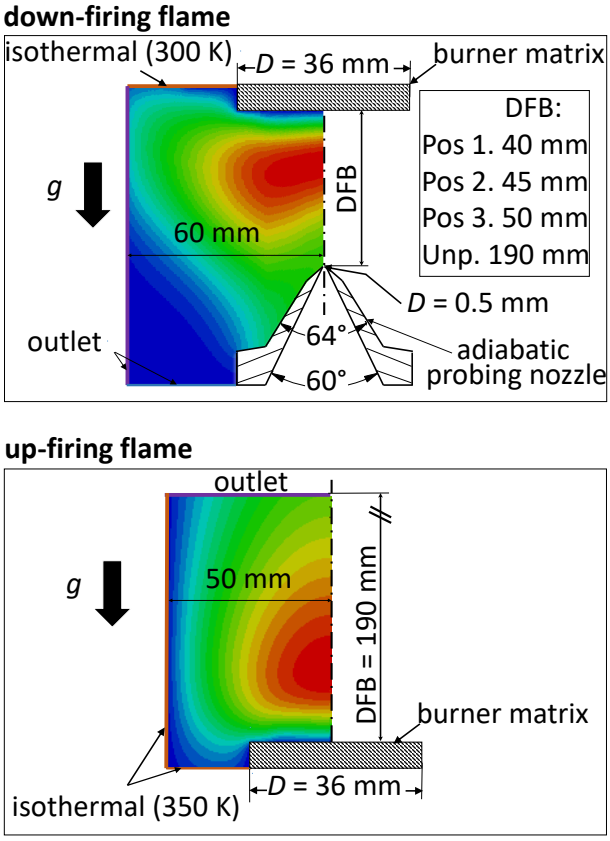

Figure 5.2: Simulation setup: Illustration of the temperature field and the extension of the computational domain.

5.1.4 Results and discussion

Impact of the reactor orientations

In order to examine the features associated with the down-firing flame, simulation results are compared against an up-firing flame in Fig. 5.3. In the DFF, strong density gradients in the flame caused buoyancy driven convection, leading to a deflection of the flow towards the sides and at some radial distance in the upward direction. On the centerline, this effect caused the formation of a stagnation point at 45 mm DFB for both flames A and B. The centre-line velocity showed similar behaviour as a flame burning against a stagnation plate, but at much higher temperature than in the stagnation point flame experiments, where the stagnation plate was

cooled. Interesting is the centerline of the flame, at which species and particle concentrations

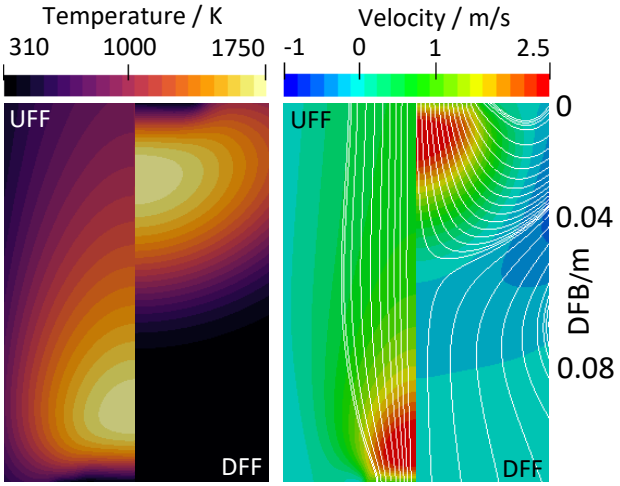

Figure 5.3: Contour plots of temperature (left) and velocity (right) of the up-firing flame (UFF, left) and down-firing flame (DFF, right). White lines indicate the flow stream lines.

were probed with a sampling nozzle. The temperatures and velocities of flame A in the DFF and UFF configuration, are shown in Fig. 5.4. Close to the burner (DFB $<$ 12 mm) the acceleration

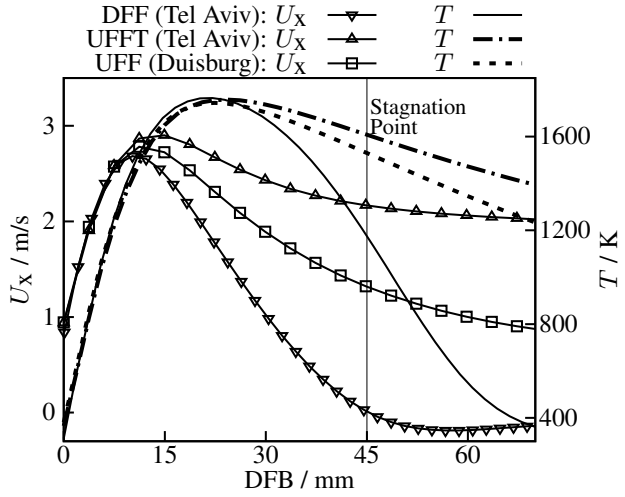

Figure 5.4: Axial profiles of the temperature (T) and the axial component of the velocity (U_x) profiles for flame A in DFF and UFF configuration.

of the flow due to buoyancy is negligible and the velocity for the DFF and UFF configuration is the same. The temperatures remain unaffected up to the reaction zone (DFB $<$ 15 mm). Beyond this point, the buoyant acceleration becomes significant, causing a detached stagnation point in the down-firing flame at DFB = 45 mm, while the up-firing flame is decelerated as a result from of the combustion products mixing with the cooler environment. The recombination zone of the down-firing flame, which is located at DFB $>$ 15 mm, shows stronger cooling, however, the temperatures remain high up to the stagnation point, at simultaneously increasing residence time.

To quantify the different velocity fields in the DFF and UFF cases, the residence time at the centre line was determined ($\Delta t = \Delta x/U$). Temperature and distance from the burner are shown in relation to the residence time in Fig. 5.5 for flame A in the DFF and UFF configuration. In terms of temperature and residence time, a fluid particle will experience the same history in the

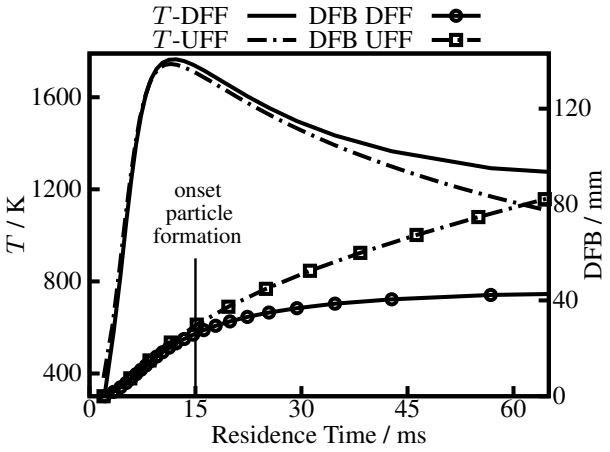

Figure 5.5: Temperatures and axial distance from the burner (DFB) as a function of residence time, for flame A in the DFF and UFF configuration.

up-firing flame and in the down-firing flame configuration for the first 12 ms. According to the simulations, the onset of iron oxide particle formation was observed after a residence time of 15 ms in both cases (DFF, UFF), but the conditions for the following process of particle growth were substantially different. The temporal evolution of the particles shows that particles in the DFF pass one third of the distance (25–42 mm DFB) and experience higher temperatures (1740–1290 K) compared to the UFF (29–85 mm DFB, 1703–1060 K). Thus, the variation of the reactor orientation seems to be a simple method to manipulate the particles' temperature–residence-time history without changing the initial flame conditions.

Investigation of the particle growth

Encouraged by the previously reported observations of condensed matter in the early flame [106], PMS measurements were conducted for the entire flame, beginning at the burner surface. Figure 5.6 (left side) shows the mass-averaged particle diameter and the mass-deposition rates measured in the up-firing flame via PMS and PMS-QCMB, respectively. Consistent with previous reports [106, 167], two particle formation zones were found: the first in the preheat zone of flame A at DFB of 7–10 mm with a particle diameter decreasing from 5.3 to 4.2 nm. (Measurements in flame B started at DFB = 10 mm missing the particle formation in this zone.) The late particle forming zone in flame A (and B) starts at 140 mm (100 mm) DFB with a diameter of 7.9 nm (7.3 nm) increasing up to a diameter of 8.6 nm (11.9 nm) at 170 mm (170 mm) DFB. The earlier and faster growth of particles in the late zone of flame B results from increased precursor concentrations. The particles found in the late zone are expected to be iron oxide [88, 167], which is the desired product of the synthesis. Simulations of iron oxide particle growth (occurring in the late zone) are in good agreement with the experiments. Figure 5.7 shows the mass-averaged diameter for the down-firing flame from experiments and simulations, and the mass deposition rate obtained in experiments for flame A and B. Like in the case of the up-firing flame, two particle formation zones were observed via PMS and PMS-QCMB. For flame A (and B) at 6.9–8.9 mm (7–10 mm) DFB in the preheat zone, particles with a diameter of 3.0–2.8 nm (4.4–3.7 nm) were found. As the early flame is not affected by buoyancy, the observed particle sizes in this regime should be identical. However, the up-firing flame operated in Duisburg using a much narrower housing than the down-firing flame operated in Tel Aviv. Thus, both configurations experienced different heat losses and slightly different flame temperatures, which is not captured in the simulations. The late particle-forming zone in the down-firing flame A (and B) was observed at 49–59 mm (43–59 mm) DFB with particle sizes of 2.9–3.6 nm (2.9–3.9 nm). At DFB $>$ 59 mm, no particles were sampled as the probe position shifted downstream of the detached stagnation point, which

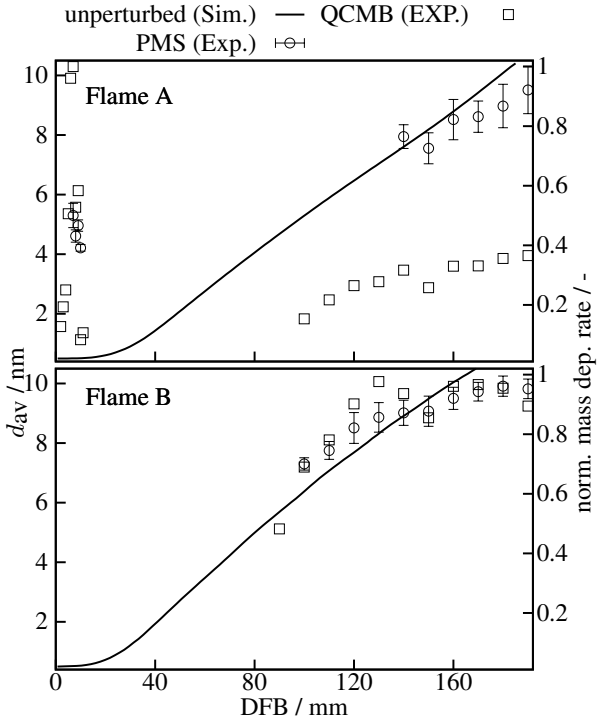

Figure 5.6: Mass-averaged particle diameter and normalized mass-deposition rate as a function of DFB, for flames A and B in UFF configuration. Simulated mass-averaged particle diameters are shown for the unperturbed flame.

was found at the same position for both flames. In the simulations, the stagnation point was predicted closer to the burner surface DFB = 46 mm than in the experiments DFB = 59 mm. The deviation can be attributed to the sensitivity of the flow situation to small (model) errors in the vicinity of the stagnation point, where small differences in the temperature (density) have a large impact. Nevertheless, the simulations were important to account for the probing effect, which was less dominant in the late zone of the up-firing flame [106]. Figure 5.7 shows that considering the probing effect, the simulation could reproduce the particle sizes and the shape of the axial particle-size profile, in particular for flame B. Comparisons of the predicted particle diameters with and without the probe show a systematic shift of the disturbed profile towards the burner and thus a faster growth of the particles in this region, presumably a deceleration of the flow due to the presence of the probe walls. However, the final aspirated product (which is compared against experiments) was underestimated, caused by the acceleration of the particle-laden gas into the probe and the rapid shortening of the residence time. While particles grow large near the stagnation point of the unperturbed flame, the sampling probe "removes" the stagnation point and reduces the temperature and residence time dramatically as shown in Fig. 5.8, due to acceleration to sonic state. Similar conclusions were made by Camacho et al. [21] for stagnation point probing from sooting flames [21].

Structure of the iron oxide forming flame

The composition of the particles formed in the first zone (preheat zone of the flame) remains uncertain. This work shows that relatively large particles with a size of 3–5 nm are formed. According to our current model assumption, these particles are formed from iron clusters and they "disappear" in the reaction zone. Fig. 5.9 illustrates the structure of the particle forming flame in case of down-firing flame A. The species concentrations (O, H, Fe-cluster, and Fe_2O_3) are not shown quantitatively but to scale in the axial direction showing the distinct particle formation zones as a special feature of the iron oxide forming flame. This can be naively explained by

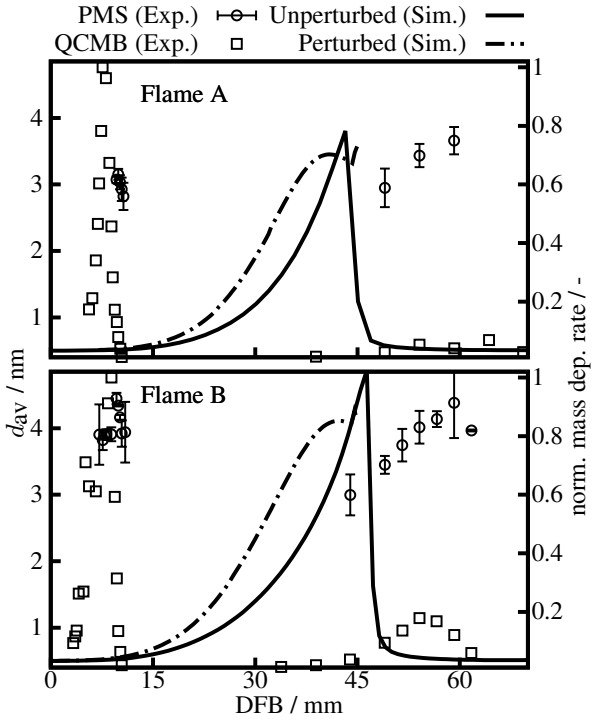

Figure 5.7: Spatial evolution of the mass-averaged particle diameter and normalised mass deposition, for flame A and B in DFF configuration. The mass-averaged particle diameters were simulated for the unperturbed flame (solid line) and the perturbed flame (dashed–dotted line) at a probing position DFB = 45 mm.

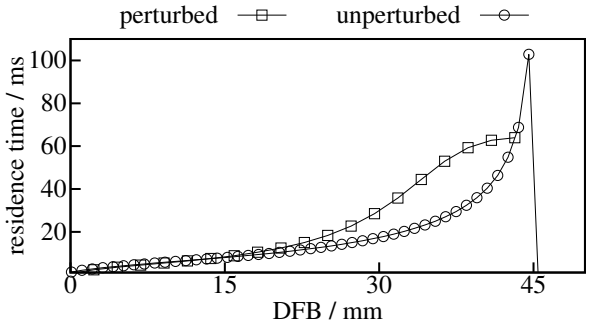

Figure 5.8: Residence time related to DFB for the perturbed and unperturbed flame A in the DFF with particle probing at Pos. 4 (DFB = 45 mm).

evaporation of the iron particles, which could be only a part of the truth as the tail of the particle signal resides already in a very reactive environment (indicated by O- and H-atom profiles) and a burning of particles cannot be excluded. The latter is supported by the strong broad-band radiation emitted from this region. Although we did not observe particles migrating through the reaction zone, this process cannot be excluded at high precursor concentrations and in turbulent flames. The uncertainty about the composition of early particles and the mechanisms of their decomposition was the main reason that the population dynamics of these intermediate products was left beyond the scope of the present work.

5.1.5 Conclusions

We demonstrated via PMS and PMS-QCMB that the iron oxide forming flame features two distinct particle forming zones. The corresponding reaction kinetics model reproduced this ob-

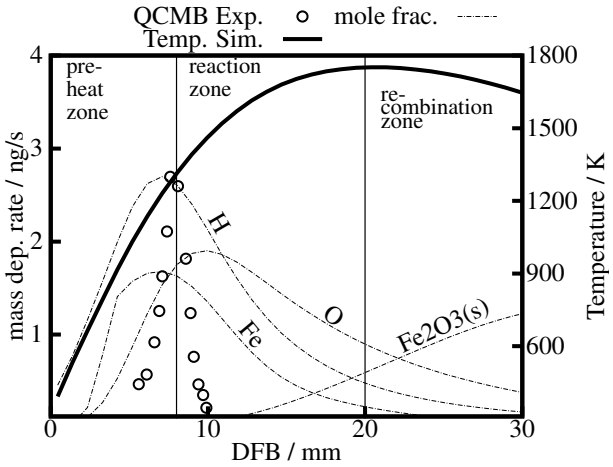

Figure 5.9: Temperature, mass-deposition rate, and mole fractions of H, Fe, and Fe_2O_3 in dependence on DFB for the DFF configuration A. The mole fractions are only qualitatively for Fe-cluster (Fe-Fe_8), Fe_2O_3, O, and H.

servation for the formation of iron clusters (in the preheat zone) and the formation of the (hypothetic) particle monomer species Fe_2O_3. The population balance model integrated within the simulation predicted the measured mean particle diameters of the iron oxide in the late regime (recombination zone) of the flame with better accuracy than the previously used monodisperse models. Furthermore, complementary simulations enabled the quantitative interpretation of the down-firing flame reactor setup. The down-firing flame has shown to be a promising tool for investigating the formation of particles in flames at large residence time and at elevated temperatures – a regime inaccessible in conventional up-firing burner setups. Finally, we would like to note that the existence of two particle-forming zones should be considered in future models for flame and process simulation as a possible source of unwanted products.

5.1.6 Acknowledgements

We gratefully acknowledge the financial support by the German Research Foundation (DFG, FOR 2284), The Open University of Israel Research Authority (Grant no 47324) and the Israel Ministry of National Infrastructures, Energy and Water Resources (Grant no. 21511034).

5.2 Influence of the sampling probe on flame temperature, species, residence of methane/oxygen flames in molecular beam mass spectrometry measurements [96] (Paper II)

The content of this chapter is the simulation part of the publication in Combustion and Flame 209, 111388 (2021), Y. Karakaya, J. Sellmann, I. Wlokas, T. Kasper, Influence of the sampling probe on flame temperature, species, residence times and on the interpretation of ion signals of methane/oxygen flames in molecular beam mass spectrometry measurements. It is reprinted with permission from Elsevier. The part presented in this thesis includes only the work in which the author was directly involved.
Y. Karakaya performed the experiments, evaluated and discussed the numerical and experimental data, and wrote the experimental part of the original manuscript draft. J. Sellmann performed the numerical simulations, interpretations of the results and wrote the numerics part of the original draft. I. Wlokas and T. Kasper provided discussions of the results and contributed to the manuscript.

5.2.1 Abstract

Laminar flames are widely used to analyze the fundamentals of combustion processes using molecular beam mass spectrometry. The extraction of a representative sample from a flame by an intrusive sampling technique is challenging because of two main issues. First, the sampling probe itself perturbs the flow and temperature field, affecting the species profiles. These effects need to be characterized by 2-D fluid dynamic simulations to reveal sources of perturbations that are in particular suction and flame cooling. Second, some intermediate species interact with the sampling probe and are removed from the gas sample before analysis. The concentrations of these intermediates in the flames are often low and close to the detection limit. Naturally occurring ions can also be extracted from the flame by molecular beam sampling. Coupled with modern ion optical devices for ion transfer to the mass analyzer very high sensitivity can be reached in the detection of ionic species in flames. Similarities in the shape of measured relative concentration profiles indicate a connection between neutrals and the corresponding protonated molecules by proton transfer reactions. A quantification method of neutral flame species based on signals of the flame-sampled ions is presented and evaluated for the intermediate methanol in methane/oxygen/argon flames. The proposed method is based on equilibrium calculations that depend on temperature. To characterize the sampling process and demonstrate the validity of the quantification approach for ion measurements, the influence of the sampling probe on flame temperature and mole fraction profiles of the main species and the intermediate methanol are investigated by a combined experimental and simulation study. A comparison of the methanol profiles measured by conventional molecular beam sampling and the novel ion sampling technique reveal acceptable agreement. This work shows that if all aspects of sampling are considered as well as possible, the ion sampling technique allows access to kinetic data of neutral intermediates.

5.2.2 Introduction

Low-pressure flames are particularly well suited for the investigation of the flame structure due to their axial one-dimensionality [44, 99, 223]. The information on as many interacting flame species as possible is needed to create a detailed kinetic reaction mechanisms for the combustion process. A large number of species can be detected by means of mass spectrometry and the flame structure can be spatially resolved in detail [99, 159, 160, 197, 223]. The operation of the flames at low pressure allows high spatial resolution of the preheating, reaction and recombination zones. But the introduction of a probe perturbs the temperature field and may block diffusion pathways in the flame [216]. Consequently, changes in the local composition of the flame are observed. The impact of the sampling probe on the flow, temperature and concentration fields of laminar

flames have been studied by various groups, e.g. by Hayhurst et al. [72, 74–78], Biordi et al. [12], Korobeinichev et al. [113, 213], Struckmeier et al. [223], Hartlieb et al. [71]. A complete overview of perturbation sources was given by Egolfopoulos et al. [44, 67], Deng et al. [40]. Recently, Hansen et al. [69, 70] investigated the flame perturbation and the drop in temperature due to the presence of the sampling probe in a $C_2H_4/O_2/Kr/Ar$ low pressure flame at 30 torr using x-ray fluorescence and highlighted the deformation of the temperature iso-lines. As confirmed by many studies, the temperature and velocity field deviate from the presumed flatness and the flames lose their one-dimensionality in the vicinity of the sampling probe [40, 44, 67, 69, 71, 72, 75, 78, 106, 113, 213, 223]. Still the ideal and steady, one-dimensional, laminar flame model is in general used for reaction mechanism development in the reaction kinetics community. In order to bridge the disparity of model and experiment, corrections have to be applied, as suggested in the past [71, 113, 223]. Unfortunately, the magnitude of the perturbation is difficult to determine experimentally and differs depending on the setup of the flame and the probing system. Since the reliability of kinetic models has increased and computational fluid dynamic simulations with detailed finite rate reaction kinetics mechanisms are affordable, these simulations are widely used for the quantification of probing effects and other sources of perturbation [21, 40, 106, 206, 239]. Multidimensional simulations of premixed flames were presented by Skovorodko et al. [213] and Faravelli et al. [163], and Sellmann et al. [206]. Gururajan et al. [67] investigated a 50 mbar rich propene/oxygen/argon flame and examined the influence of sampling, flange, non-adiabaticity, sampling point and compressibility during the suction through the probe on the flame by means of 2D-simulations. Deng et al. [40] have conducted 2D and 3D numerical studies of atmospheric laminar $CH_4/O_2/Ar$ and $H_2/O_2/N_2$ flames considering the burner structure and sampling probe, and were able to reproduce the measurements, previously inaccessible to one-dimensional simulations. As a coarse estimate, Deng et al. [40] proposed a spatial probe shift of 3 probe orifice diameters in the upstream direction. They could show that the temperature drop towards the probe inlet could be estimated by a simple one-dimensional energy balance presuming constant total enthalpy, as formerly stated by Hayhurst [73, 75]. The thermal perturbation of the flame's reaction zone cannot be estimated from a simplified rule as it strongly depends on the material and structure of the probe. The tools and work flow developed by Deng et al. [40] were applied since then in various fundamental studies complementary to the experiments [21, 106, 199, 206].

5.2.3 Experiment and flame conditions

Flame conditions

Methane flames with the same flame conditions were studied with three different sampling techniques. The burner feed was composed of a $CH_4/O_2/Ar$ mixture and the composition is shown in table 5.2.3. Flame conditions are chosen to be similar to the work of Alquaity et al. [2]. A McKenna-type burner is mounted in a vertical flow configuration on an axial-translation system, which allows sampling with a sampling probe at different heights above the burner (HAB) between HAB = 0 and 50 mm. The pressure in the burner chamber is measured by a capacitance manometer and held constant at 160 mbar by a throttle valve, which is connected to the vacuum pump. The burner and the mounting flange for the sampling probe are water-cooled. The gas flows are regulated by mass flow controllers and mixed before they enter the burner. The flame structure of flames A, B and C, are analysed, on the one hand with the aid of electron ionisation molecular beam mass spectrometry (EI-MBMS) and on the other hand with the aid of an ion sampling interface coupled to the same mass spectrometer (i-MBMS). Both systems have already been used in different studies. Identification and measurements of ions were performed in collaborative work with Alquaity et al. [2] and measurements with the aid of EI-MBMS are described by Karakaya et al. [94, 95], Janbazi et al. [86], and Gonchikzhapov [60]. A short summary of both systems is given below.

Table 5.2: Flame conditions in standard cubic centimeter per minute. Flame A is analysed with the aid of electron ionisation MBMS, flame B is analysed with the aid of electron ionisation expansion sampling, flame C is analysed by ion sampling. For flame B) and C) the same experimental setup is switched from expansion sampling with electron ionisation to ion sampling.

Flame	A	B	C
ψ		1	
p / mbar	160		
CH_4 / sccm	670		
O_2 / sccm	1330		
Ar / sccm	2000		
Orifice Diameter / μm	90	550	550
Sampling Probe Material	Quartz	Metal	Metal
Ionisation method	EI	EI	Ion sampling

Ion sampling (Flame C)

To analyse ions, the reactor chamber, which contains the burner with flame C is coupled to an orthogonal time-of-flight mass spectrometer (TOF) by three differentially pumped vacuum stages. In the first stage an operational pressure of 3 mbar, in the second stage 10^{-3} mbar and in the third stage $1{\cdot}10^{-6}$ mbar is maintained, while the TOF is kept at $1{\cdot}10^{-7}$ mbar. The charged species from the flame are sampled by a metallic sampling probe with an orifice diameter of 550 μm. A 300 V positive potential is applied to the probe and to the burner to avoid an inhomogeneous electric field between both. The transmission of the ions in the first stage is ensured by a low capacitance printed circuit board ion funnel to which a DC potential gradient is applied to transport the ions through the funnel. The second stage is equipped with a segmented octapole ion guide and in the third stage a quadrupole ion guide is used to reduce the kinetic energy of the ions. Subsequently, the ions pass through several apertures and beam forming Einzel lenses and are guided into the ionisation chamber of the TOF.

Electron ionisation TOF analysis with expansion sampling (Flame B) and with molecular beam sampling (Flame A)

To obtain the mole fractions of neutral species under identical sampling conditions as the ions, the ion optics of the ion interface can be grounded, so that the pumping stages serve as low efficiency molecular beam inlet. It is here referred to as expansion inlet. The neutral species are ionised by electron ionisation and analysed in the TOF. This analysis was performed for flame B. In addition, neutral species were measured using a dedicated molecular beam inlet in flame A. The probe in this experiment is made from quartz. Here, the probe diameter was reduced to 90 μm to allow expansion of the sample into a second vacuum stage kept at 10^{-3} mbar with acceptable gas load on the turbo molecular pump. The core of the molecular beam was extracted by a skimmer with an orifice diameter of 1.2 mm to the ionisation chamber of the TOF. The gas sample was ionised by electron ionisation (EI). The nominal kinetic energy of the electrons was chosen to be 14.5 eV to obtain a good compromise between signal-to-noise, short acquisition times and dissociative ionisation. For both sampling procedures, the ions pass between a repeller and extractor electrode and are accelerated into the flight tube of the TOF before they impact a multichannel plate. The orthogonal TOF mass analyser has a resolution of $m/\Delta m = 3000$, which is useful for a precise mass determination and separation of near mass overlaps, e.g. C_2H_4 and CO. The signals of the main and intermediate species obtained in the neutral mode using the ion transfer interface with expansion sampling, and the molecular beam system were converted to mole fractions using the procedures described in [99].

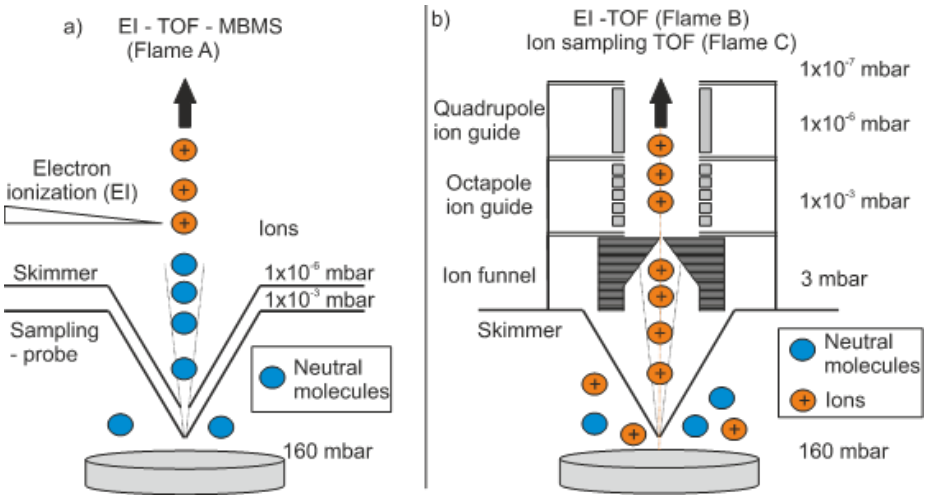

Figure 5.10: Schematics of the experimental setup for a) TOF-MBMS with electron ionisation (flame A) and b) TOF with electron ionisation and expansion sampling (flame B) and ion sampling TOF (flame C). For flame B) and C) the same experimental setup is used and can be switched from expansion sampling with electron ionisation to ion sampling. Reprinted from [96] with permission from Elsevier.

Temperature measurements

The temperature of the flames is measured with a type R thermocouple coated with SiO_2 with a diameter of 200 μm. The thermocouple is positioned one mm in front of the sampling probe. A radiation correction is performed following the procedure described in the study by Bahlawane et al. [6] to obtain the flame temperature. Additionally, the temperature dependence of the argon signal is evaluated to get a relative perturbed temperature profile as shown in the work of Struckmeier et al. [223]. The surface temperature of the metal sampling probe is estimated from a measurement with a thermocouple (type K) touching the inside of the sampling probe close to the tip. The surface temperature on the cold side of the probe was measured to avoid the influence of the thermocouple on the flame structure. The temperature of the molecular beam is measured with a thermocouple (type K) in a distance of one mm behind the orifice inlet. The temperature measurement of the molecular beam and sampling probe surface were carried out at 3 mbar without radiation correction. Temperature values were allowed to stabilise until thermal equilibrium between the gas phase and the thermometer was achieved. The error of the thermocouple measurements was within $\pm$ 0.75% (supplier's data sheet). Positioning errors are approximately 1 mm. Temperature measurements were performed independently from the species measurements and thermocouples were removed prior to species measurements.

5.2.4 Simulations

One-dimensional simulations are performed to gain insight into the flame structure. The flame perturbation in one-dimensional simulations is in general tentatively considered as input by the perturbed temperature profile. In order to get a deeper insight into the probe induced perturbation of the flame structure, two-dimensional simulations were performed, which include the sampling probe geometry and use specific experimentally accessible boundary conditions as input to describe the heat losses. The numerical setups of the simulations are briefly summarised.

One-dimensional simulation

ChemkinPro 19.2 [4] is used to simulate the flame structure for a 1D burner stabilised flame using a detailed chemical-kinetic reaction mechanism AramcoMech 2.0 [123] and a measured perturbed

temperature profile as input variables.

Two-dimensional simulation

The two-dimensional simulations of the flame sampling were carried out in a rotationally symmetric computational domain, sketched in Fig. 5.11. At the probe, the simulation domain ends

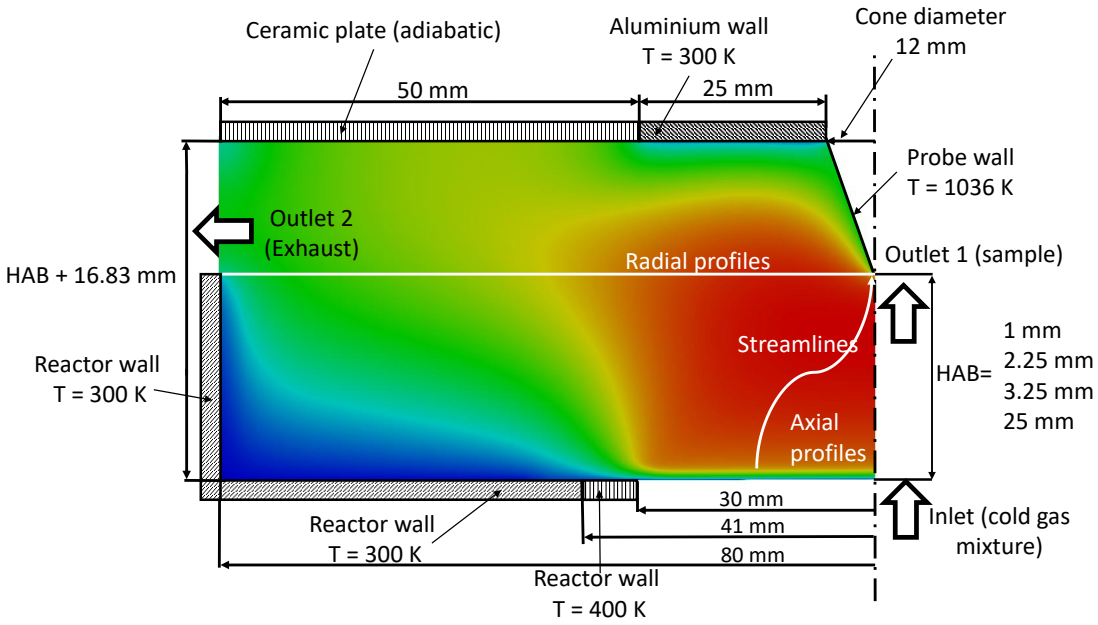

Figure 5.11: Computational two-dimensional domain and the boundary conditions for the simulation, exemplarily shown for flame B. White lines schematically show the profiles analysed in the post processing evaluation of the 2D-Simulation. The figure shows a schematic representation of the temperature

at the sampling probe inlet where the flow reaches a critical state. Simulation of the flow inside the sampling probe was beyond the scope of this study. Sampling probes with two different orifice diameters ($D = 90\mu$m, Flame A and $D = 550\mu$m, Flame B) were investigated, each at four different heights above burner (HAB = 1, 2.25, 3.25 and 25 mm). The chosen HAB are in particular locations relative to the flame front, which reflect the beginning, middle, end of flame front and the exhaust region. At least 12 cells were representing the diameter of the probe inlet. The flow through the sampling probe orifice is choked due to the large pressure ratio between the burner chamber and the sampling system, providing the critical pressure p^* as an outlet boundary condition. With an estimated, average specific heat ratio of the sampled gases $\kappa = 1.3$, the relation $p^* = p \cdot \left(\frac{2}{\kappa+1}\right)^{(\kappa/(\kappa-1))}$ results in an outlet pressure of $p = 85$ mbar [162]. The pressure at the far field boundaries was set to the chamber pressure $p = 160$ mbar. Due to a lack of detailed information on the thermal conductivity of the probe material, limiting boundary conditions were applied: adiabatic and isothermal probe walls, each. The temperature for the isothermal boundary condition for the metal sampling probe ($D = 550$ μm, $T = 1036$ K) was measured in the experiments and used for the quartz sampling probe ($D = 90$ μm) as well. A measurement of the surface temperature of the quartz sampling probe was not possible because the skimmer blocked access to the inside of the sampling probe. The burner inlet temperature is presumed to be fixed at $T = 400$ K. This configuration was chosen in order to keep both, 1D und 2D simulations consistent at the model level. To ensure this consistency is essential for the work-flow of mixed 1D and 2D simulations as it was introduced by Deng et al. [38]. This con-

figuration of boundary conditions is robust for water-cooled burners (like here) and sufficiently lifted flames. The simulation framework used for the investigation accounts for detailed molecular transport models, and corrects for the species diffusion at the inlet, consistent with the models implemented in the popular 1D kinetics tool-boxes ChemkinPro [4] and Cantera [62]. The Fickian diffusion was treated as mixture averaged. Detailed description of the model implementation in OpenFOAM [157] was provided by Deng et al. [40] and has been successfully used in previous studies [21, 106, 206]. The computational effort required a skeletal, reduced reaction scheme. In this work the DRM22 reaction mechanism was used [50]. All simulations were performed on a hexahedral mesh with 26580 to 47750 cells and the maximum runtime of the large setup was 120 hours on 48 cores (Intel E5-2650 v4 Broadwell CPUs). Axial, radial profiles, contour diagrams and isolated streamlines of fluid elements are analysed in more depth for a detailed investigation of the flame structure perturbation caused by the sampling probe.

5.2.5 Results and discussion

Influence of the sampling probe on flame temperature, species and residence times

Centerline flame temperature

Two-dimensional simulations of flames A and B were carried out to determine the impact of the probe on the temperature field at various heights above the burner (HAB = 1, 2.25, 3.25 and 25 mm). The measured and simulated flame temperature at the centerline of flame A and B with the presence of an isothermal sampling probe are shown in Fig. 5.12. The measurements with the thermocouple slightly upstream of the probe reveal that flame A reaches its maximum temperature of 1450 K at HAB = 3 mm and in the exhaust at HAB = 25 mm the temperature decreases to 1200 K. The 2D-simulations show higher temperatures in the undisturbed case compared to the measurements, but in the vicinity of the sampling probe, the temperature drops and agrees well with the measurements. In the reaction zone, the endpoints of the simulated values coincide with the measured temperature profile, while in the preheat zone at HAB = 1 mm deviations to the 2D-simulation are visible. The 2D-simulations reveal the strong decrease of the flame temperature caused by the sampling probe. With the presence of the probe at each sampling point, different intermediate temperature profiles upstream of the sampling probe are present.

In flame A, the intermediate temperature profile for a probe position of HAB = 1 mm, 2.25 mm, 3.25 mm increases less steeply compared to the unperturbed case with the probe at HAB = 25 mm.

As comparative data for the undisturbed flames the 2D-simulation with the sampling probe at HAB = 25 mm is used, as it represents the least perturbation near the burner surface. The temperature profiles for the probe at HAB close to the burner form intermediate maximum plateaus which subsequently decrease in temperature. Compared to the unperturbed profile (HAB = 25 mm) the temperatures at HAB = 1 mm, 2.25 mm, 3.25 mm perturbed by the sampling probe are significantly smaller. For flame A, this results in a flame front that is moving in downstream direction compared to the unperturbed profile (HAB = 25 mm).

The maximum measured temperature of flame B is 1500 K at HAB = 3 mm. In the exhaust gas at HAB = 25 mm the temperature decreases to 1250 K. For flame B, the effect of flame cooling by the probe at HAB = 25 mm is less pronounced, but also clearly visible in Fig. 5.12. The deviations in the preheat zone and exhaust are in on the same order as the experimental uncertainties. In addition, it should be mentioned that the measured temperature is compared to the centerline temperature, radial temperature gradients can increase the temperature of the sampled volume.

The temperatures at HAB = 1 mm, 2.25 mm, 3.25 mm are significantly smaller compared to the respective HAB in the unperturbed profile with the probe position at HAB = 25 mm. The ending point of the centerline temperature at HAB = 1 mm, 2.25 mm, 3.25 mm is reached further

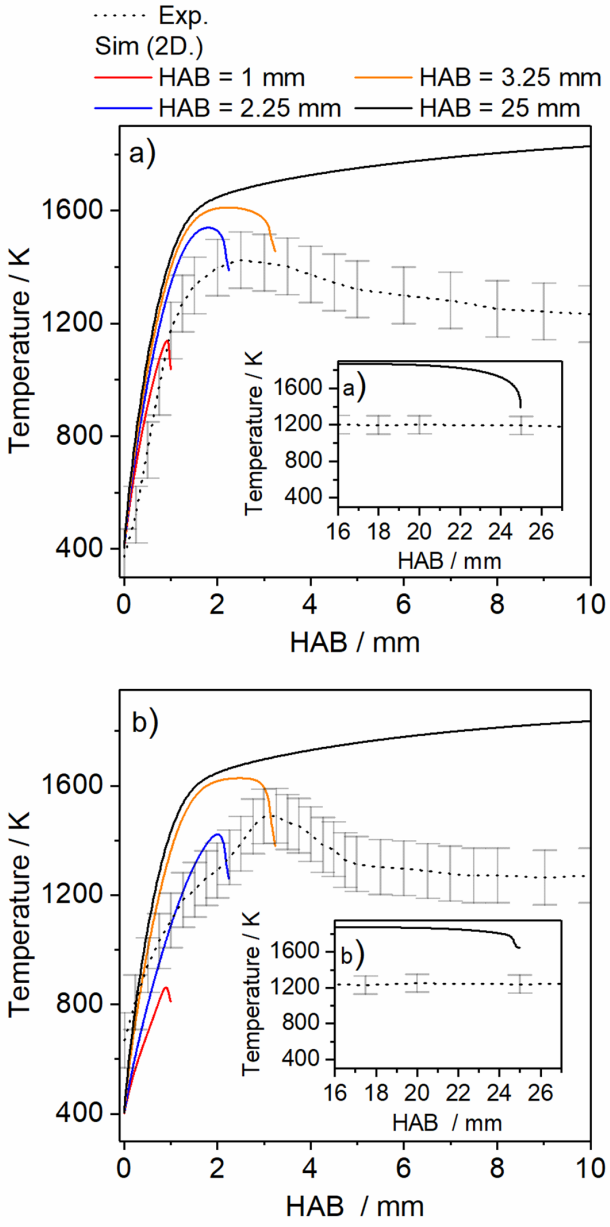

Figure 5.12: Measured (dotted lines) and simulated temperature profiles on the centerline (2D simulations, isothermal sampling probe, filled lines) in a) flame A, and b) flame B for various heights above the burner (HAB = 1, 2.25, 3.25, 25 mm).

downstream compared to the unperturbed case with the probe position HAB = 25 mm in flame B indicating the widening of the flame front of flame B in downstream direction.

Summarising, both experiments and simulation show plausible results with good agreement at the inlet of the sampling probe. This gives confidence in simulation and experiment. It is still to be emphasised how important the assumption of an isothermal probe is for the simulations. The simulations with an adiabatic sampling probe have shown significantly higher temperatures at the sample inlet and therefore not such a good agreement with the experiments. These simulations are not discussed further but are included in the supplementary material.

Two-dimensional temperature field

The two-dimensional temperature field helps to visualise the effect of flame perturbation by the sampling probe more clearly and can provide information about the differences between measurements and ideal 1D-simulations. The temperature fields are shown in Fig. 5.13 for flame A (Fig. 5.13 a-d) and flame B (Fig. 5.13 e-h). The sampling at HAB = 1 mm for flame A and B are shown in Fig. 5.13 a) and e). The probe is located in the centre of the reaction zone, which is characterised by a rapid temperature rise (strong gradient), but the maximum has not yet been reached. Since the body of the sampling probe is positioned upstream in the hot flame, an isothermal boundary condition for the probe wall is used for the 2D-simulation, and consequently the probe wall has a higher temperature compared to the gas at the tip of the probe. This assumption is based on the measured temperature of the metal probe that is approximately 1200 K at all positions in the flame (see Fig. 5.11). In principle, the probe causes the gas to heat up upstream of the inlet and the unperturbed 1D assumption is violated. This effect of gas heating (and cooling at larger HAB) by the probe was also reported by Deng et al. [40]. The second pronounced perturbation of the flame at this position is caused by the aspiration of the sample itself and is clearly visible in Fig. 5.13 a) and e). Perturbation of the one-dimensional temperature field of flame A is smaller than that of flame B. The reason can be traced to the orifice diameter of the probe. In flame A (D = 90 μm) the orifice is smaller than in flame B (D = 550 μm) and consequently a smaller sample volume is aspirated, including less cold gas from the preheat zone and more hot gas from the sampling point. The temperature field also reveals that gas fractions with various temperature history are sampled at the same time. The temperature and time histories of each fraction of sampled gas cannot be determined from the mass spectrometric measurements where an averaged signal of all fractions appears. Ideal one-dimensional models do not consider the various time and intermediate temperature histories of the sampled species, which may have an impact on the analysis of the flames. Further numerical investigations are needed at this point.

Near HAB = 2.25 mm, the gas has not reached the position of maximum flame temperature. Compared to the position HAB = 1 mm the temperature of the probe is lower than the gas temperature and has from this position on a cooling effect on the aspirated gas. A stretching of the flame structure towards the probe can be observed, which is stronger with increasing probe diameter (Fig. 5.13 b, f). The distortion results in less steep temperature gradients close to the burner surface than in the unperturbed flame. This effect is evident from the comparison of the simulated intermediate temperature profiles in Fig. 5.12 which are less steep than for the unperturbed case.

At HAB = 3.25 mm (see Fig. 5.13 c, g), close to the end of the flame front where the temperature gradients are less pronounced, stretching of the flame structure cannot be detected. Instead, the perturbation of the temperature field in front of the probe due to its cooling effect is now clearly visible.

At HAB = 25 mm the iso-lines show that the hot exhaust gas streams along the sample probe and cools down. At the tip of both probes (Flame A and B) it can be observed that the cooled gas is sucked in from the side and mixed with the hot exhaust gas on the centerline.

To quantify the extent of perturbation in radial direction in the sampling region, radial tem-

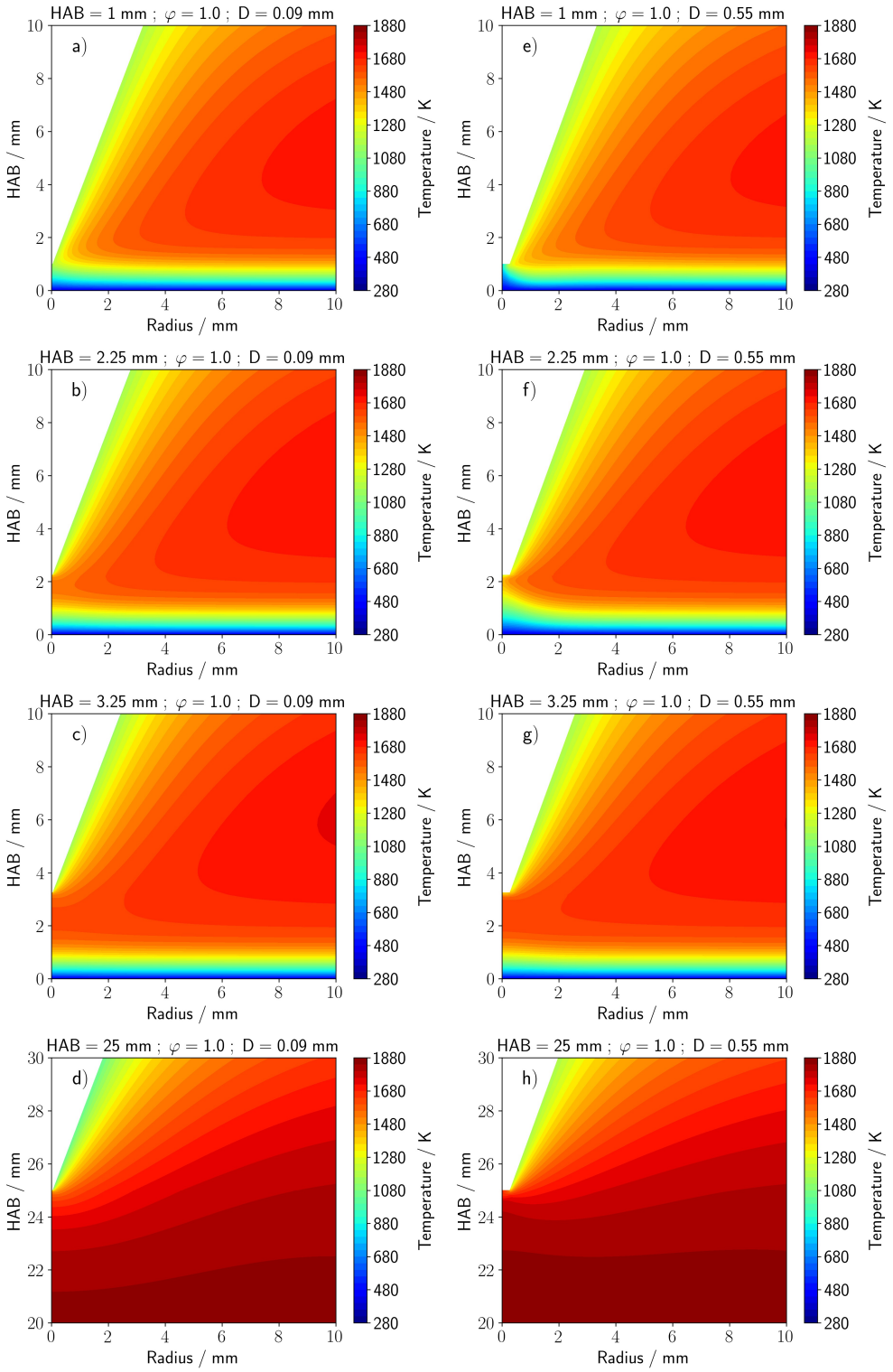

Figure 5.13: Two-dimensional simulation of the temperature field in flame A (4 a-d) and flame B (4 e-h) and isothermal probes for various heights above the burner (HAB = 1, 2.25, 3.25, 25 mm).

perature profiles are evaluated. Two regions must be distinguished. The first region is inside of the sampling probe in the cross section of the probe orifice. The second region is the flame beside and upstream of the probe. Radial temperature profiles inside of the probe inlet for the respective probe positions HAB = 1, 2.25, 3.25, 25 mm are shown in Fig. 5.14 a) for flame A using a probe with 90 μm orifice diameter and b) for flame B using a probe with 550 μm orifice diameter. Figure 5.14 c) explores how far upstream the radial temperatures are perturbed. It shows the radial temperature 0 mm, 1 mm, 2 mm, and 3 mm in front of the probe orifice when the probe is positioned at HAB = 25 mm.

The profiles at the probe cross section in Fig. 5.14 a) and b) show a temperature profile which is most pronounced for HAB = 1 mm with 810 K (1038 K) on the centerline to 1200 K (1134 K) near the probe wall for flame A (B). The temperature gradient towards the probe wall illustrates the heating effect of the probe on the gas for both probes. For flame B and the probe with the larger orifice, at HAB = 1 mm suction seems to be the dominating distorting effect on the temperature of the gas sample, because hot gas from the areas around the sampling point is mixed with cold gas from the centerline. The effect is still apparent in the exhaust gas but its influence on the temperature decreases with increasing HAB due to the decreasing temperature gradients. For probe positions larger than HAB = 1 mm the probe cools the gas. In Fig. 5.14 c) the cooling of the gas by the cold surface of the sampling probe is illustrated for a probe position of HAB = 25 mm. The closer the gas is to the probe, the more it is cooled down. The minimum temperatures are reached at the probe wall at R = 0.09 mm (R = 0.55 mm) for flame A (B). In the centre of the probe, however, a rise in temperature can be observed, as hot gas is drawn in from a hotter environment. The suction has two effects. Firstly, it accelerates the gas and reduces its residence time on the centerline. The second effect is still cooling but as an aerodynamic effect on the acceleration in its critical state.

Major species

In the following, the influence of the sampling probe on the major species in flame A and B is investigated. In the first part, each measurement is compared with a 1D-simulation, which was performed with the previously measured temperature profiles shown in Fig. 5.12. In the second part, the measurements are compared to 2D-simulations to capture the influence of the probe and the resulting deviation from the measured mole fraction profiles.

Measured and 1D-simulations of the species mole fraction profiles in flame A are shown in Fig. 5.15. Flame A has an equivalence ratio of $\varphi = 1$. The main species O_2, CO_2 and H_2O reach equilibrium mole fractions between HAB =2-3 mm. The dominant intermediate species is CO. It has a maximum mole fraction of 0.06 at HAB = 2.5 mm and decays until HAB = 5 mm to its equilibrium mole fraction with a value of 0.02. H2 has a maximum at HAB = 2 mm and reaches the baseline at HAB = 5 mm. The simulated mole fraction profile of CH_3OH peaks 1 mm earlier than the measured mole fraction profile. The deviation can be explained by suction of gas fractions from cold and hot regions at the same sampling point. The quantitative agreement of the simulated and measured CH_3OH mole fraction is very good. Overall, experiment and one-dimensional simulation show a good agreement.

2D-simulations of the species mole fraction profiles up to the sampling points at HAB = 1 mm, 2.25 mm, 3.25 mm and 25 mm in flame A are also shown in Fig. 5.15. The end points of the 2D-simulations coincide with the measured mole fractions with reasonable agreement. In the 2D simulation at HAB = 25 mm the reaction zone is almost unperturbed, while at the other HAB significant perturbation occurs. A comparison of these perturbed O_2 profiles of the 2D simulations to the almost unperturbed case reveals, that O_2 is consumed less rapidly and reaches a higher mole fraction in the reaction zone when the flame is perturbed (Fig. 5.15). This behaviour can also be observed for CH_4 decomposition. Consequently, the mole fraction profiles of the intermediate species CO, C_2H_4, H_2 and the main product species CO_2 and H_2O are less steep and the flame front widens by about 1 mm compared to the unperturbed case and it seems

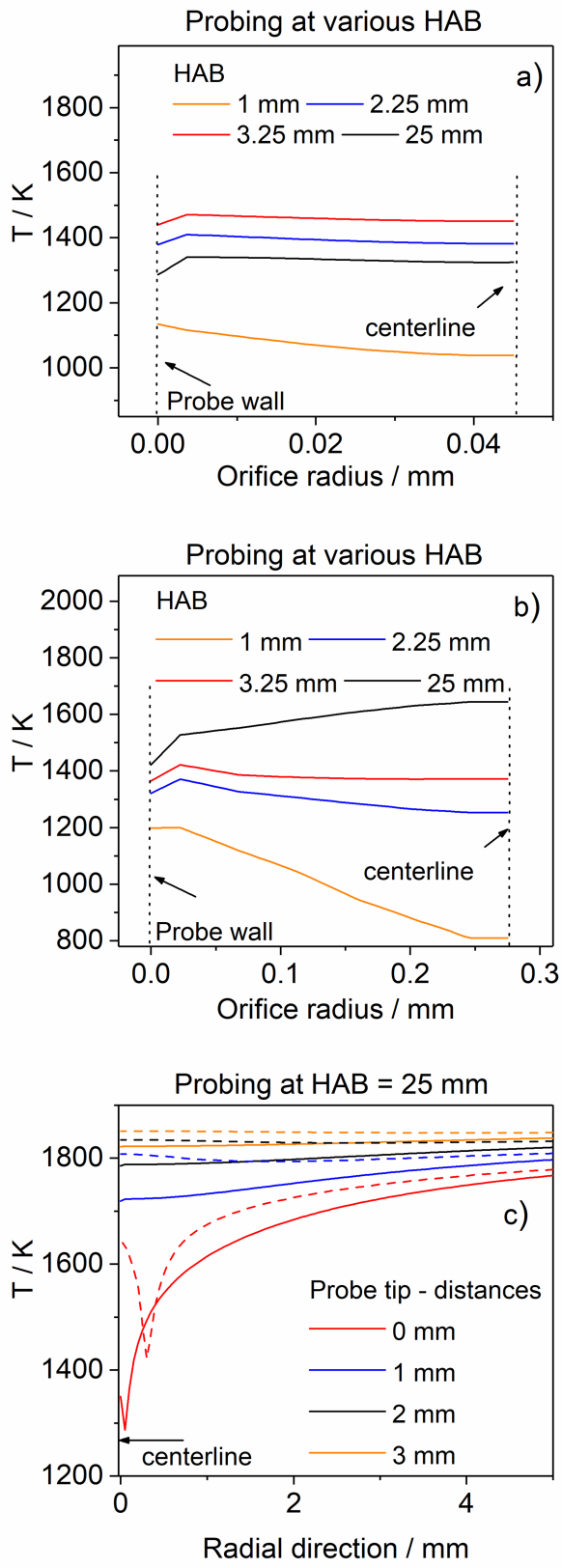

Figure 5.14: Two-dimensional simulation of the radial temperature profiles along the orifice diameter in a) flame A (probe diameter D = 90 μm), b) and flame B, C, (probe diameter D = 550 μm) at various HAB and c) at various distances parallel to the probe inlet with a distance of 0 mm, 1 mm, 2 mm, 3 mm (filled line for probe diameter D = 90 μm and dashed line for probe diameter D = 550 μm).

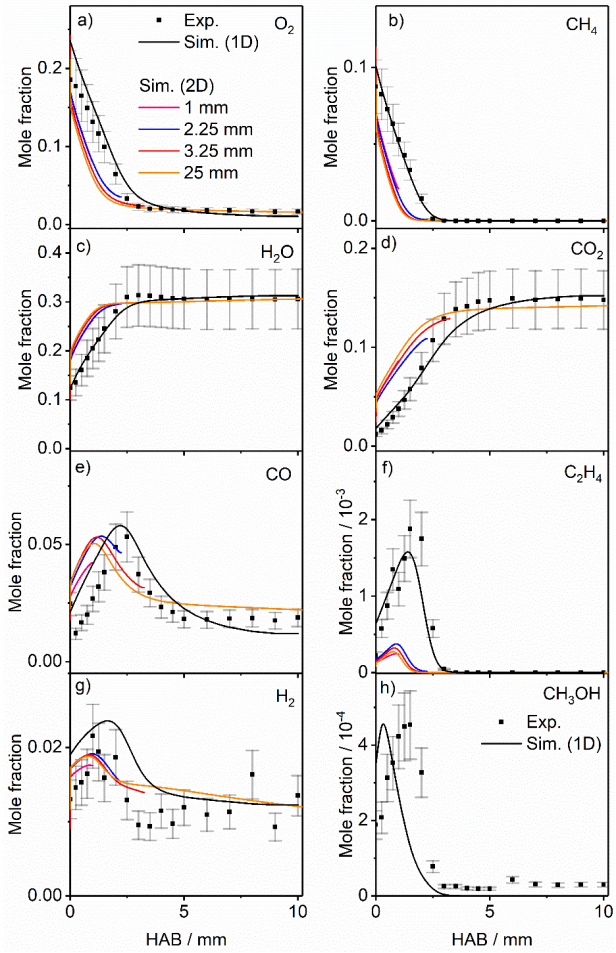

Figure 5.15: Measured (probe diameter D = 90 μm, symbols) and simulated (1D- and 2D-simulation, lines) mole fraction profiles of major species on the centerline in flame A. 2D-Simulations are done for an isothermal sampling probe and at various HAB = 1 mm, 2.25 mm, 3.25 mm, 25 mm.

as if the profiles are shifted in downstream flow direction.

Measured and 1D-simulations of the species mole fraction profiles in flame B are presented in Fig. 5.16. Flame B has an equivalence ratio of φ=1. Here, the main species reach equilibrium mole fractions between HAB = 3-4 mm. In this measurement CO does not exhibit a typical intermediate profile. From this observation it can be concluded that the flame is perturbed strongly by the sampling probe.

Despite the perturbation, experiment and the 1D-simulation show reasonable agreement in the exhaust gas. Close to the burner surface up to HAB = 2 mm larger deviations are observed for the 1D-Simulations. Only the 2D-simulations can capture the suction-effect at very close distances to the burner. The radial 2D effects cannot be captured accurately by the 1D-simulations, because only the perturbed temperature profile is used. The 2D-simulations show that for flame B the widening of the flame front is between HAB = 1 - 3 mm and is more pronounced than in flame A. The reason is the larger diameter of the probe orifice used in flame B that is associated with more suction and more mixing of gas fractions from different positions relative to the probe orifice. As discussed for the temperatures this ultimately results in an apparent widening of the flame front.

Overall, the measured temperature profile approximates the end of the temperature history of the sampled gas well and the 2D-simulation shows that a 1D flame simulation with a measured temperature profile as input is a suited method that achieves acceptable results and can give meaningful insight into the flame structure for small probe diameters.

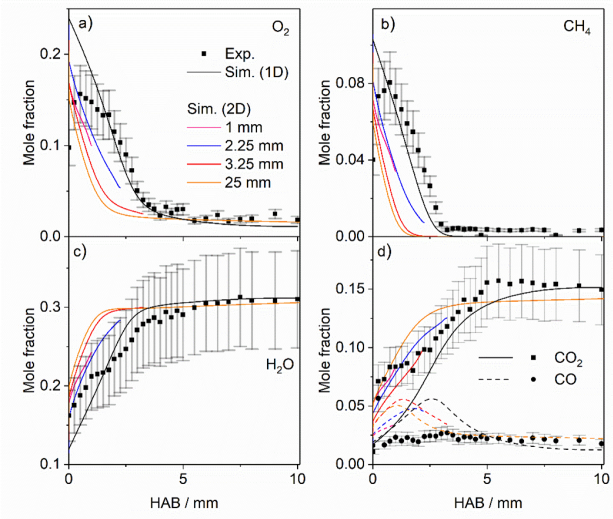

Figure 5.16: Measured (probe diameter D = 550 μm, symbols) and simulated (1D- and 2D-simulation, lines) mole fraction profiles of major species on the centerline in flame B. 2D-Simulations are done for an isothermal sampling probe and various HAB = 1 mm, 2.25 mm, 3.25 mm, 25 mm.

Radical species

CH_3 radicals were measured in flame A and are shown in Fig. 5.17. The reduced mechanism

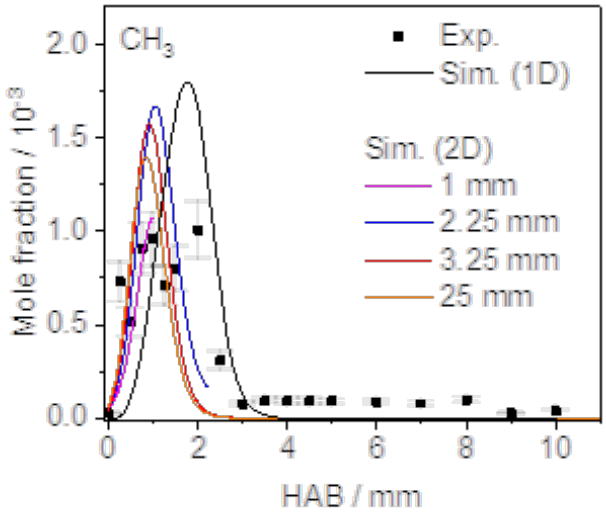

Figure 5.17: Measured (Flame A, Probe diameter D = 90 μm, symbols) and simulated (1D- and 2D-simulations, lines) mole fraction profiles of CH3 on the centerline in flame A. 2D-Simulations are done for an isothermal sampling probe and various HAB = 1 mm, 2.25 mm, 3.25 mm, 25 mm.

has already been used in previous work with promising results [40]. A comparison of the reduced mechanism with the full GRI mechanism [215] is shown in the supplementary material, which shows that it is capable to predict the flame species. The maximum CH_3 mole fraction of $1 \cdot 10^{-3}$ is reached at HAB = 1.5 mm and it is completely consumed at HAB = 3 mm. The CH_3 radical profile matches the 1D-simulation results. The ending points of the 2D-simulations are in reasonable agreement with the measured CH_3 radical profile. In the following, the intermediate maximum mole fraction profiles of CH_3 for the simulations with the presence of the sampling probe at HAB = 1 mm, 2.25 mm and 3.25 mm are compared to the CH3 mole fraction profile with the presence

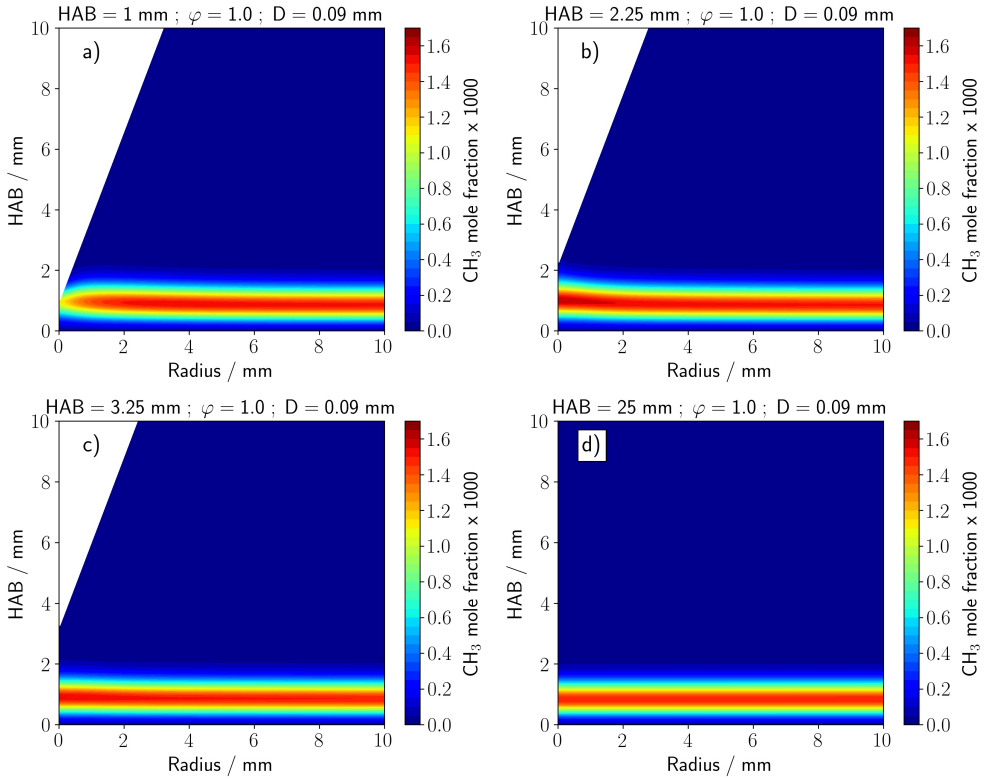

Figure 5.18: Two-dimensional simulations of the CH_3 mole fraction field in flame A) are done for an isothermal sampling probe and various HAB = 1 mm, 2.25 mm, 3.25 mm, 25 mm).

of the sampling probe at HAB = 25 mm. The maximum mole fraction of CH_3 in the simulation with the presence of the sampling probe at HAB = 25 mm is $x_{CH_3,max} = 1.4 \cdot 10^{-3}$. When the sampling probe is located at HAB = 1 mm, a lower maximum mole fraction of CH_3 is present ($x_{CH_3,max} = 1.1 \cdot 10^{-3}$), while for sampling positions at HAB = 2.25 mm ($x_{CH_3,max} = 1.7 \cdot 10^{-3}$) and 3.25 mm ($x_{CH_3,max} = 1.6 \cdot 10^{-3}$) the intermediate mole fractions of CH_3 exceed the value in the unperturbed flame. The higher maximum mole fraction of the CH_3 radical at probe position HAB = 2.25 mm can be explained by the presence of the probe which draws the precursors CH_4 and O_2 to higher temperatures and consequently changes the methyl concentration in comparison to the unperturbed flame. The 2D-simulation in Fig. 5.18, shows how the intermediate mole fractions of the methyl radicals are increased at the probe positions HAB = 2.25 mm and HAB = 3.25 mm compared to the simulation of the probe position at HAB = 25 mm which coincides with the unperturbed flame as can be seen in Fig. 5.18 d.

It should be mentioned that for each probe position the maximum mole fraction is different and also the position of the maximum varies slightly. The major source of error for methyl radical mole fractions typically reported in MBMS studies is the uncertainty in the ionisation cross section, which is quoted as 15 % [229]. The increase by probe perturbation is on the order of 10-20 % of the expected mole fraction and has a similar magnitude as the uncertainty of the cross section. It is also dependent on the probing position. At the maximum of the CH_3 peak the probe has a cooling effect on the flame and drastically reduces the CH3 mole fraction (here 30 %), but if the probe is positioned upstream of the maximum it leads to a moderate increase in the mole fraction (here 10-20 %). As a consequence, the methyl radical mole fraction is probably more uncertain than expected. In particular, the peak shape is affected: the increase in mole fraction is less steep, a lower maximum mole fraction is observed, and the decay of the mole fraction occurs at higher HAB and is also less steep. It is clear that the effect can be observed for other species too and will likely be even more pronounced for more reactive species than methyl

radicals, i.e. the naturally occurring flame ions.

Residence time profiles

The contour plots of the flame in Fig. 5.13 and Fig. 5.18 have shown, that the area of the flame that is affected by suction of the probe has a larger diameter than the probe itself. As a result the residence time (τ) of the gas fractions from different positions and the distance (z) that these gas fractions have traveled in the flame vary. The magnitude and effect of this difference is discussed below by comparing the distance (z) and the residence time (τ) of a gas sample on the centerline (shortest τ and z) and a gas sample at the outer edge of the intake area (longest z and τ). Residence time profiles of these two fluid elements on a streamline drawn from the centerline (r_1) and from the maximum radial point (r_2) are presented in Fig. 5.19. The maximum radial point describes the streamline that exits the burner at a radial distance from the centerline and is drawn in by the sampling probe.

For flame A, the values of radius r_{2A} from the centerline are r_{2A} = 0.89 / 0.81 / 0.79 / 0.79 mm for sampling at HAB = 1 / 2.25 / 3.25 / 25 mm, respectively. For flame B, the radii are r_{2B} = 5.4 / 5.21 / 5.13 / 5.1 mm for the same probing positions as in flame A. The radii are higher for smaller HAB (due to a compression of the flame front towards the burner surface) and decrease with increasing HAB. The higher radius at small HAB also indicates that a higher mass flow of fresh gas is sampled than at high HAB. Comparing the ratio of the two probe diameters of flame A and flame B (D_B/D_A = 6.1) to the diameter of the intake surface at the different positions (r_{2B}/r_{2A}= 6.1 / 6.4 / 6.5 / 6.5) the intake surface has increased roughly by the ratio of the probe diameter. The intake surface area is roughly a factor of 20 larger than the probe orifice, for each probe and for the flame conditions investigated here, so that it covers between 0.1 % and 3 % of the burner surface area.

Most of the gas flow in the experiment bypasses the sampling orifice and is pumped out of the chamber via 4 KF40-flanges. The outlets are outside of the simulation domain. The burner has a diameter of 6 cm, and only an area with a diameter of less than 6 mm interacts with the probe. The ratio of orifice/exhaust gas is roughly equal to the ratio of the areas (0.01). As consistency check we calculated the relative change in the ratio of the probe-burner interaction areas and compared them to the relative density change of the flame gases calculated based on simulated and measured temperatures.

In the contour plot in Fig. 5.19 a) and e) the radii r_1 and r_2 are illustrated for the probe position HAB = 1 mm by streamlines. For the small probe orifice used in flame A, all streamlines go from the burner directly to the probe. For flame B, some of the streamlines apparently pass behind the probe through a region of higher temperature than the temperatures downstream of the probe. As a result, the average temperature encountered by the gas sampled with the larger orifice can be expected to be substantially higher than the temperature encountered by the gas sampled with the smaller orifice at the same position in the flame, even though the cooling effect of the probe on the flame is comparable as can be seen in Fig. 5.13. This conclusion is true for all positions because the general form of the streamlines is similar at HAB = 25 mm as demonstrated in Fig. 5.19 a, b) and e, f). For both probes and larger HAB (Fig. 5.19 b and 5.19 f), the streamlines remain parallel to the centerline over a relatively long distance in the flame compared to small HAB. So, the gas samples experience a temperature history for a longer fraction of their residence time in the flame that resembles to a 1D assumption (direct streamline from the burner to the probe).

Even though the cooling effect of the probe on the flame and the effect of suction are convoluted in the flame, it helps to think of them as two separate effects to rationalise why 1D-simulations with the perturbed temperature profile match the experimental results better at larger HAB than at smaller HAB. At small HAB, the distortion of the streamlines by suction affects the gas sample during its entire residence time in the flame. At larger HAB, a significant distortion of the streamlines only occurs for a fraction of the residence time of the gas sample in the flame. The

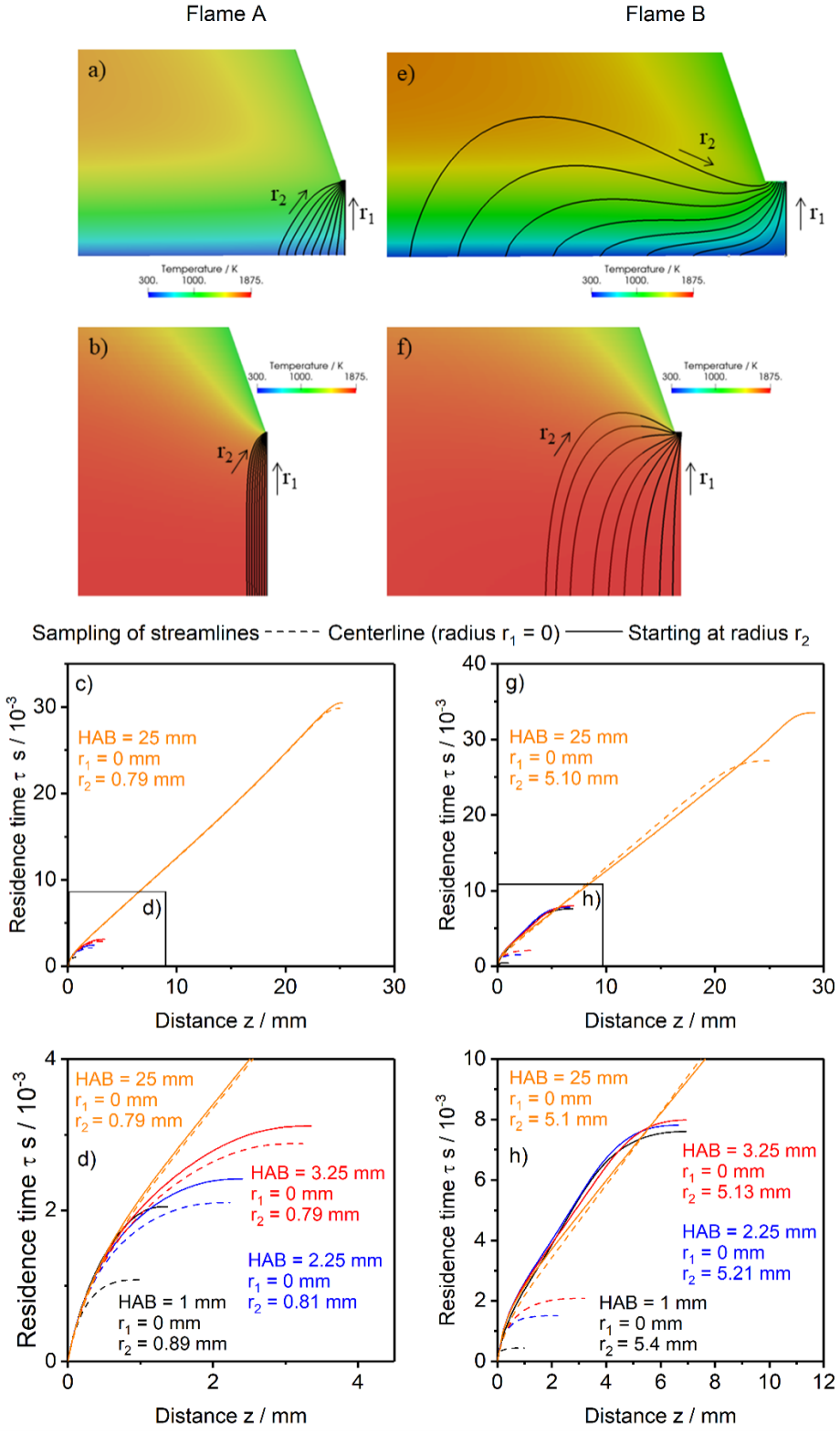

Figure 5.19: Two-dimensional simulation of the temperature field with a streamline pattern and a sampling probe position at HAB = 1 mm and HAB = 25 mm a,b) in flame A and e,f) in flame B. Residence time profiles of gas flows sampled at the centerline (dashed line) and on a streamline suctioned from a radial point of the burner by an isothermal sampling probe and various heights above the burner (HAB = 1, 2.25, 3.25, 25 mm) c,d) in flame A and g,h) in flame B. The distance z indicates the traveled length of the fluid element between burner exit and sampling probe inlet.

cooling effect of the probe on the flame is similar at all positions and in part taken into account in a 1D-simulation when using the perturbed temperature profile. Our results and also the results by [9, 10, 114, 118, 223] demonstrate that 1D-simulations with the perturbed temperature profile lead to very good agreement between experimental and simulation results except for the data points closest to the burner. Given our observations in this work, it seems likely that the concentration distortions induced by the sampling process are dominated by the effect of suction close to the burner and by the effect of cooling at larger HAB.

To substantiate this reasoning, Fig. 5.19 a-h compare the path length that a fluid element with a streamline with r_1 and r_2 experiences, and the respective residence times. Comparing the residence times in flame A for the two streamlines with radius r_1 and r_2, the following ratios of the residence times are found: τ_{2A}/τ_{1A} = 1.9 / 1.2 / 1.1 / 1.02 for a sampling position of HAB = 1 / 2.25 / 3.25 / 25 mm, respectively. The values for calculating the ratio can be found either in Fig. 5.19 or in the Table A.1 and Table A.2 in the supplementary material. The ratio of the two residence times shows how great the influence of the probe is, especially in the vicinity of the burner (probe located at HAB = 1 mm). Near the burner, the residence time of a fluid element on the centerline in the flame is about 2 times shorter than at the limiting radius r2. With larger distance to the burner, the ratio decreases as the area affected by suction remains comparable and the streamlines are parallel to the centerline for a substantial distance between probe and burner. For flame B, the ratio of the residence times is considerably larger τ_{2B}/τ_{1B} =17.23 / 5.2 / 3.8 / 1.13 and illustrates the immense influence of the larger probe orifice diameter on the individual time histories of the sampled gas.

It is conceivable that gas passing for a longer residence time along the streamline with r_2 will have also reacted for a longer time. Consequently, it can be expected for the larger probe diameter that the concentration of product species is higher in these fractions of the sampled gas. The effect will be enhanced if the gas sample passes through a region of higher temperature behind the probe. The analysed gas sample will consequently contain comparatively more product gases and less fuel and oxidiser. This effect is clearly visible in the main species profiles in Fig. 5.15 and Fig. 5.16. The measured oxygen and methane mole fractions at the first data point are approximately 20 % lower in flame B measured with the sampling probe with the larger orifice diameter ($x_{O_2,A}$ =0.19, $x_{CH_4,A}$ =0.09, $x_{O_2,B}$ =0.15, $x_{CH_4,B}$ =0.08), and the mole fractions of water and carbon dioxide are about 25 % smaller in flame A than in flame B ($x_{H_2O,A}$ =0.12, $x_{CO_2,A}$ =0.03, $x_{H_2O,B}$ =0.16, $x_{CO_2,B}$ =0.04). If compared to the 1D-simulation results, the experimental mole fraction values appear to be an average of the 1D simulated values at different HAB.

The effect on species profiles that are expected to show an intermediate profile with a mole fraction maximum at some distance from the burner is difficult to predict. On the one hand, the CO mole fraction profile in flame B measured with the probe with larger orifice diameter has become flat, which can be expected if the difference between the mole fraction at the maximum and the equilibrium mole fraction in the exhaust gas is small. Near the burner, gas fractions traveling along streamline r_2 have a 17 times longer residence (and probably reaction) time in the flame and reach the equilibrium value of 0.025. On the other hand, when sampling an intermediate species that is consumed completely in the exhaust gas with a probe with a large orifice diameter it may be expected that the intermediate profile shifts towards the burner because a fraction of the sampled gas has experienced a higher temperature and longer residence time than expected for a 1D flame. In addition, the profile will likely increase less steeply, and decay less rapidly as discussed for the methyl radical in flame A. In light of these insights, it is clear that a smaller sampling probe will lead to more accurate results because the effect of suction is less pronounced.

In summary, the path and the residence time that the sample passes prior to reaching the probe inlet can be different even for the same sampling location, as shown by the different residence time profiles for each HAB. The effect of suction is immense and increases with a larger orifice diameter of the probe. The previously described measured “perturbed” temperature profiles do not track the path the sample has passed accurately but they are able to lead to good 1D-simulation results

in areas of the flame where the cooling effect of the probe distorts the species concentrations in the gas sample more than the suction effect, e.g. at higher HAB. Because the influence of the different experienced paths on the sample cannot be assessed with the measured temperature profile, it can only tentatively describe the perturbation of the flame structure. The 2D simulations were performed because the use of a sampling probe with large orifice diameter caused a suction effect which perturbed the flame structure. By using small orifice diameters the suction effect is kept small and 1D simulations with the input of the perturbed temperature profile become sufficient to predict mole fraction profiles. However, it must be taken into account that even with small orifice diameters, slight deviations between experimental and 1D-simulated mole fraction profiles can still occur due to the suction effect, especially in the regions of high mole fraction gradients.

Gururajan et al. [67] have numerically investigated the influence of the boundary conditions of the numerical domain of the simulation of the temperature and species mole fraction profiles with the presence of the sampling probe. They have shown how important the boundary conditions are and that they can influence the simulated mole fractions. Deng et al. [40] omitted this question by a conjugate heat transfer computation including the heat transport within the probe. Within the scope of this work, the boundary conditions were experimentally determined from the molecular beam sampling TOF and ion sampling TOF.

Most recently, Hansen et al. [70] investigated the temperature drop due to the presence of the sampling probe experimentally. Under the one-dimensional model assumption, isotherms above the burner no longer run in horizontal order, but form a two-dimensional temperature field. As a result, the temperature curve in the area in front of the sampling probe changes in comparison to the unperturbed flame. Within this work, the 2D simulation reveal how the temperature is perturbed at various distances to the sampling probe and what the gradients are at the orifice of the sampling probe.

Skovorodko et al. [213] investigated the flow in the vicinity of the sampling probe and stated a significant effect of radial diffusion on the distribution of concentrations in the plane of the orifice. Deng et al. [40] studied the sampling probe effect on laminar flat flames and found that the suction effect is a dominant mechanism for the perturbation caused by the probe. In this work, 2D simulations show the suction-effect for two different sampling probe apertures under the same flame conditions at various distances from the burner. It could be shown for the first time in experiment and 2D simulation, that the suction effect decreases for smaller orifices and changes the shape of the species mole fraction profiles especially close to the burner surface.

5.2.6 Interpretation of ion signals

The section deals with the experimental evaluation of the measurement signals and was not performed by the author of this thesis and is therefore not part of the thesis. The title of this section is included here for completeness, while its content can be found in Karakaya et al. [96].

5.2.7 Conclusion

The work investigates the influence of the sampling probe on the temperature profiles, species profiles and species residence times and interprets ion signals of $CH_4/O_2/Ar$ laminar low-pressure flames in molecular beam measurements. In this study a quartz sampling probe and metal sampling probe were used to transfer a sample from a flat flame to the mass spectrometer. Most importantly, the quartz probe sucked the gas sample through a smaller orifice diameter (D = 90 μm) than the metal probe (D = 550 μm) into the vacuum system used to transfer a sample to the mass analyser.

Experimental mole fraction profiles of flame species, e.g. CH_4,O_2,H_2O,CO_2,CO,H_2,CH_3OH,C_2H_4, and CH_3 and flame temperature profiles were compared to 2D- and 1D-simulations.

For both sampling probes our results show, that three aspects must be considered when evaluating the effect of the sampling probe on the measured profiles. First, the sampling probe can reach

a higher temperature than the gas at the sampling point. As a result, it may heat the flame gases near the burner. Second, the probe sucks in gases from regions upstream and downstream of the probe orifice. As a result, fractions of gas with varying residence times are simultaneously analysed at each sampling position. These gases can also have higher or lower temperatures. Third, on the centerline in front of the probe suction pulls a gas sample towards the orifice, leading to deformed iso-lines of temperature and varying streamlines.
The results for both sampling probes demonstrate that especially suction is a governing type of perturbation of the flame structure. To get an insight into the suction the residence times of the gas samples along streamlines at various HAB are evaluated. At small HAB, the perturbation of the streamlines by suction affects the gas sample during almost its entire residence time in the flame and can increase the residence times of the sample fractions up to a factor of 2 and 17 for a sampling orifice diameter of D = 90 μm and D = 550 μm, respectively. At larger HAB, a significant distortion of the streamlines only occurs for a fraction of the residence time of the gas sample in the flame and the sampled fractions vary by a factor of 1 and 1.13 for a sampling orifice diameter of D = 90 μm and D = 550 μm, respectively. Our results show, that the magnitude of suction can be reduced by using a small orifice for the sampling probe aperture. This result can be generalised as a design rule for the sampling probe that helps to minimise the grade of perturbation on the 1D structure of flat flames during flame sampling at low-pressure.
The suction effect overlaps with the cooling effect by the sampling probe during flame-sampling. The perturbed temperature used as input for 1D-simulation takes the flame cooling by the sampling probe into account. The whole range of experienced path and residence times (reaction times) the sample has passed due to suction are not captured sufficiently by the perturbed temperature profile. This also explains why the 1D-simulation with the measured temperature profile as input often fits to experiments better for larger HAB than for the region at small HAB.

Chapter 6
Detailed simulation of turbulent flames

6.1 LES of nanoparticle synthesis in the SpraySyn burner: a comparison against experiments [208] (Paper III)

This section of Chapter 6 including all text, figures and tables is published in the journal Powder Technology 'Sellmann, J., Wollny, P., Baik, S.-J., Suleiman, S., Schneider, F., Schulz, C., Wiggers, H., Wlokas, I., Kempf, A. (2022). LES of nanoparticle synthesis in the SpraySyn burner: a comparison against experiments. Powder Technology, 404, 2022' [208] and is reprinted with permission from Elsevier.
Contributor Roles Taxonomy: J. Sellmann developed the code, ran the simulations and wrote the original manuscript draft. P. Wollny: developed the code and provided a discussion of the results. S. Suleiman performed experiments and wrote the experimental part of the manuscript. F. Schneider performed experiments. S.-J. Baik, C.Schulz, H. Wiggers, I. Wlokas, and A. M. Kempf provided discussions of the results and contributed to the manuscript.

Abstract

The synthesis of iron oxide nanoparticles from iron nitrate in the SpraySyn spray flame reactor was investigated by experiment and simulation. The focus was on the spray and flame structure, the particle growth by nucleation and coagulation, and the unresolved effects and their impact on the dispersed phase. The reacting flow was modelled in large eddy simulations with the premixed flamelet generated manifolds technique, including modifications for aerosol nucleation. Particle dynamics were described with a sectional model and a subgrid scale coagulation kernel. The particle size distributions at different distances from the burner surface were obtained using a particle mass spectrometer. The experiments and simulations are in good agreement for the flame centreline velocity and both size distribution and mean size of the particles (for particles larger 1 nm - the approximate detection limit of the experiment). Furthermore, simulations enabled to interpret the temporal evolution of the particle size distribution.

6.1.1 Introduction

Materials synthesis from the gas phase is an important route to produce powders with a large variety of composition and size properties. Among different existing processes, the flame-based synthesis has shown to be energy efficient, clean in terms of materials composition, continuous, and scalable. With the development of spray-flame synthesis (often also called flame spray pyrolysis, FSP), an enormous variety of available nanoparticle precursors and associated possible materials, became accessible [132, 230]. This process is far more complex than the gas-phase synthesis route based on homogeneously premixed gas mixtures and the development of a proper understanding requires support by sophisticated modelling and simulation. The development of the recently introduced SpraySyn burner [203] was inspired by the burner concept developed by Mädler et al. [132]. The development was motivated in order to enable close collaboration between simulation and experiment in academic research and to optimise the reproducibility of flow and synthesis conditions and materials. The main features distinguishing the SpraySyn burner from its conceptual predecessors are the precise control of the angular orientation of the spray nozzle and the sintered matrix providing almost homogeneous conditions for the pilot flame and the co-flow.

Early work on the numerical simulation of the FSP process was reported by Weise et al. [240], and Gröhn et al. [63, 64], and more recently by Meierhofer et al. [137] and Neto et al. [149], all of which used the the Reynolds-averaged Navier-Stokes (RANS) approach. The spray was described in the Lagrangian frame as discrete droplet parcels, while the gas phase and the dispersed particle phase were described as continuum in an Euler-Euler coupling. The aerosol dynamics of nanoparticle growth through coagulation and sintering in the work of Weise, Gröhn and Meierhofer [63, 64, 137, 240] were solved using a moment-based method, the so-called monodisperse model proposed by Kruis et al. [115], while Bianchi Netto used the improved direct quadrature method of moments (DQMoM) [134]. The results of these simulations of the spray-flame synthesis process were in a good agreement with experimental findings. The experimental data used in [63, 149, 240] was obtained from ex-situ analysis of the final product. Meierhofer et al. [137] compared their simulations to data obtained via TEM probing at different distances from burner. The use of RANS simulation reduces the computational effort enormously, but important information of the flow field and the flame is lost, and only ensemble-averaged statistics are available. Rittler et al. [191] overcame this drawback and performed the first large eddy simulation (LES) coupled with the monodisperse model of an spray-flame synthesis process. They found plausible results but could not make further comparisons due to a lack of experimental data. The highest possible resolution of the flow field was achieved by providing a full description of all the temporal and spatial scales in a direct numerical simulation (DNS) of the SpraySyn burner recently by Abdelsamie et al. [1]. The reacting flow simulation was coupled with the monodisperse model, the investigated material system was titania (TiO_2) and the influence of different pilot flames was investigated. Since DNS simulations are very expensive in solution and post-processing, the simulation domain only extends to $x = 18\,\mathrm{mm}$ above the burner. However, the main part of the particle growth takes place further downstream and only LES simulations offer the possibility to provide a reasonable resolution at moderate computational costs.

The monodisperse model [115] is extremely popular in conjunction with reacting flow simulations, since it is very efficient in terms of computational costs. But it usually does not provide direct access to the particle size distribution (PSD) and it is known to underestimate the growth of early particles, as Spicer et al. [218] have shown for titania. The extension of the model proposed by Jeong and Choi [90] allows to consider a nucleation mode of the PSD, but the model remains (bi-modal) monodisperse. If the shape of the PSD is in the focus of interest, only detailed models allow the direct comprehensive investigation of the particle size distribution and their interaction with turbulence. From the large variety of solution methods for the population balance equation [51, 135], the sectional method [55] is popular for linking the continuous gas and dispersed phases within the Eulerian frame. The direct discretisation of the particle volume (or radius/diameter) into bins does not require any strong presumptions about the PSD. It results from the solution of the population balance equation in its transport form and even though it is much more expensive, it offers access to the PSD and thus more detailed information on particle growth. In the work of Miller et al. [141] the sectional method was applied in a direct numerical simulation (DNS) to investigate the coagulation process in a turbulent jet. In the work of Garrick et al. [54], the sectional method coupled with a DNS was used to study particle growth by coagulation in a shear layer. The first work demonstrating the coupling of a LES with the sectional model was performed by Loeffler et al. [128]. The authors compared the LES with a DNS and found good agreement in particle concentration and mean diameter. However, they have already found that the coagulation rate is under-predicted due to the lack of sub-grid modelling in the LES. Most recently Cifuentes et al. [29] found similar results. They simulated nanoparticle growth in an isolated eddy using a DNS coupled with the sectional model and investigated a priori the coagulation rate for LES. The first attempt to address these deficits in the sectional model with a subfilter model was by Rodrigues et al. [192]. In the context of sooting flames, they used the intermittency model developed by Mueller et al. [144], and implemented it in the sectional model, finding a good agreement in comparison with experiments.

Summarising, it can be stated that currently only few detailed investigations of the spray-flame synthesis process were published. Also, only few high fidelity experimental data sets exist that could improve the model development. Models and simulations reported in the past were either coarse and artificial in terms of boundary and initial conditions, and in terms of chemistry modelling, or the simulation domain was small like in a DNS. Most of the reported simulations employed the monodisperse model. In this work, we present the combination of a high-resolution LES coupled with the sectional model, applied on the FSP under consideration of subgrid effects for the coagulation rate. To the best of our knowledge, such a simulation has not been carried out so far and is intended to show the necessity for this elaborate type of simulation. The simulations are validated by experimental data and the results were compared with in situ measurements on the nanoparticle synthesis [224]. In Section 6.1.2, the theoretical basics for models and numerical schemes are given. Section 6.1.4 explains the experimental setup of the SpraySyn burner and the measurement techniques employed in this work. The complete numerical framework is presented in Section 6.1.5. The results in Section 6.1.6 are structured in 2 parts as follows, general flame structure, and the comparison of the PSD with experiments and the analysis of individual information of the particle model. Final conclusions are presented in Section 6.1.7.

6.1.2 Modelling framework

Even though many processes in the spray flame run parallel to each other and interact with each other, the modelling of the spray-flame synthesis can be divided into four contributing parts: the description of the flow field, the combustion process including the gas-phase reactions of the precursor, the spray droplets and the description of the particle dynamic equations (PDE). All four parts are elaborated in the following.

6.1.3 Flow field modelling

The flow is modelled in the frame of a LES, via transport equations for the filtered mass and the momentum densities $\bar{\rho}$ and $\bar{\rho}\tilde{u}_i$.

$$\frac{\partial \bar{\rho}}{\partial t} + \frac{\partial \bar{\rho}\tilde{u}_i}{\partial x_i} = \dot{\Gamma}_{\bar{\rho}} \tag{6.1}$$

$$\frac{\partial \bar{\rho}\tilde{u}_i}{\partial t} + \frac{\partial \bar{\rho}\tilde{u}_i\tilde{u}_j}{\partial x_j} = -\frac{\partial \bar{p}}{\partial x_i} + \frac{\partial \bar{\tau}_{ij}}{\partial x_j} + \frac{\partial \tau_{ij}^{SGS}}{\partial x_j} + \dot{M}_{d,i} \tag{6.2}$$

The pressure and the stress tensor are denoted by p and τ_{ij}. The source terms for mass and momentum $\dot{\Gamma}_{\bar{\rho}}$ and $\dot{M}_{d,i}$ allow coupling of liquid phase evaporation effects. The subgrid scale effects are considered by Nicoud's sigma model [151].

Combustion modelling

Combustion modelling is performed following the Premixed Flamelet Generated Manifold (PFGM) approach for tabulated chemistry [231, 232]. In this approach, a series of one-dimensional freely propagating flames are calculated for multiple fuel and oxidiser compositions using a detailed mechanism. The computations were carried out with the software library Cantera [62] and the results are stored in low dimensional lookup-tables. These tables are accessed by the CFD solver using a small number of control variables. In the simulation of the SpraySyn burner, two combustion processes occur, the pilot combustion and the spray combustion. Hence, two mixture fractions and the reaction progress are chosen as control variables. The pilot mixture fraction is defined as: $Z_1 = Y_{\mathrm{CO_2}} + Y_{\mathrm{H_2O}} + Y_{\mathrm{O_2}} + Y_{\mathrm{CO}}$ assuming the pilot to be burned when it enters the simulation domain, with Y_α beeing the mass fraction of species α, the combustion products of methane/oxygen at the composition of the adiabatic flame. The spray mixture fraction is defined as $Z_2 = Y_{\mathrm{Ethanol}} + Y_{\mathrm{Fe_2O_3}} + Y_{\mathrm{H_2O}} + Y_{\mathrm{O}} + Y_{\mathrm{NO_2}}$ with a combination of evaporated ethanol and

the decomposed precursor (iron (III) nitrate in this work) mass fraction. It must be mentioned here, that the iron (III) nitrate decomposes already at low temperatures, below 140 °C. It was presumed that the decomposition product is iron oxide, (Fe_2O_3), such that the pyrolysis of the solution droplet yields an initial gas phase composition of Fe_2O_3, water, ethanol, oxygen, and NO according to the composition of the initial solution [103]. In the synthesis of iron oxide from iron (III) nitrate, ethylhexanoic acid (EHA) is added to the ethanol solution (up to 65%). It was found that the EHA addition promotes the microexplosions of droplets as an additional secondary breakup mechanism and is vital for the quality of the product [3, 222]. These microexplosions are not observed without the EHA addition. The experiments and simulations presented in this paper, however, did not rely on any EHA addition.

The progress variable is composed of a weighted linear combination of product and fuel species:

$$Y_\mathrm{p} = \sum a_1 Y_i + \sum a_2 (Y_{f,i} - Y_i) \tag{6.3}$$

where the first term right hand side represents the product species mass fractions Y_i with the weighting factor a_1 and the second term the fuel species mass fraction $Y_{f,i}$ with the weighting factor a_2. Here, the progress variable was chosen from the products CO and CO_2 with the weighting $a_1 = 1$ and the consumed species C_2H_5OH with the weighting $a_2 = 2$. The more familiar scaled progress variable c was then used for the tabulation $c = Y_\mathrm{p}/Y_\mathrm{p,max}$ [231]. For Z_1, Z_2 and Y_p, transport equations were solved following Peters [164]:

$$\frac{\partial \bar{\rho}\tilde{Z}_j}{\partial t} + \frac{\partial \bar{\rho}\tilde{u}_i\tilde{Z}_j}{\partial x_i} = \frac{\partial}{\partial x_i}\left(\left[FE\bar{\rho}D_\mathrm{p} + (1-\Omega)\frac{\mu_\mathrm{t}}{Sc_\mathrm{t}}\right]\frac{\partial \tilde{Z}_j}{\partial x_i}\right) + \dot{\Gamma}_{\tilde{Z}_j} \tag{6.4}$$

$$\frac{\partial \bar{\rho}\tilde{Y}_\mathrm{p}}{\partial t} + \frac{\partial \bar{\rho}\tilde{u}_i\tilde{Y}_\mathrm{p}}{\partial x_i} = \frac{E}{F}\dot{\omega}_s + \dot{\omega}_\mathrm{p,evp} + \frac{\partial}{\partial x_i}\left(\left[FE\bar{\rho}D_\mathrm{p} + (1-\Omega)\frac{\mu_\mathrm{t}}{Sc_\mathrm{t}}\right]\frac{\partial \tilde{Y}_\mathrm{p}}{\partial x_i}\right) \tag{6.5}$$

In Eq. (6.4) and Eq. (6.5), D_p represents the progress variable diffusion coefficient and $\dot{\omega}_s$ the progress variable reaction rate, both read from the FGM–table. The turbulent viscosity μ_t, is obtained by the sigma model [151], $\mathrm{Sc_t}$ is the turbulent Schmidt number, $\dot{\Gamma}_{\tilde{Z}_\alpha}$ the mixture fraction source term obtained from the evaporating spray droplets, and $\dot{\omega}_\mathrm{p,evp}$ represents the evaporating fresh fuel. Eq. (6.4) and Eq. (6.5) have been modified by the Artificially Thickened Flame (ATF) approach via the efficiency function E and thickening factor F [116].

A reaction scheme proposed by Feroughi et al. [46] was applied for the iron compounds within the iron pentacarbonyl doped flame. Though, the reaction pathways have been extended by reduction reactions for Fe_2O_3 with H_2 and CO as proposed by Oh and Noh [154]. The iron sub-mechanism was incorporated by the ethanol reaction scheme proposed by Olm et al. [156], while reactions of nitric oxides were neglected in our scheme. The final reaction scheme consists of 79 species and 251 reactions.

Without a direct coupling between the gas and particle phase, a conservation equation must be derived to ensure mass conservation [249], Eq. (6.5):

$$\frac{\partial \bar{\rho}\tilde{Y}_\mathrm{I}}{\partial t} + \frac{\partial \bar{\rho}\tilde{u}_i\tilde{Y}_\mathrm{I}}{\partial x_i} = \frac{\partial}{\partial x_i}\left[FED_\mathrm{p} + (1-\Omega)\frac{\mu_\mathrm{t}}{\mathrm{Sc_t}}\right]\frac{\partial \tilde{Y}_\mathrm{I}}{\partial x_i} + \frac{\mathrm{d}\bar{\rho}_\mathrm{I}}{\mathrm{d}t} \tag{6.6}$$

The last term on the right hand side is the averaged mass source at a certain combustion state. During the combustion process, spray droplets evaporate over large parts of the flame and continuously change the gas composition. In order to have control over the already nucleated particles and remaining condensable matter, the absolute change of the incepted particle mass per time step Φ_p was tabulated as suggested by Wollny et al. [249].

$$\frac{\partial \bar{\rho}_\mathrm{I}}{\partial t} = \frac{E}{F}\dot{\omega}_\mathrm{I}\bigg|_{x,t} \approx \frac{1}{\Delta t}\Delta\Phi_\mathrm{p}(Y_\mathrm{P}, Z_j) \tag{6.7}$$

The incepted particle mass Φ_p gives the mass per volume of the condensed matter for a certain condition (Y_p, Z_j). A special treatment has been made for the calculation of the nucleation source term. Conventionally, it is assumed for iron particles that the precursor decomposes and reacts with its environment until particle precursor molecules are formed that nucleate directly, i.e., the reaction rate is equal to the nucleation rate [29]. In this particular case, due to evaporation of the precursor solution, iron oxide already enters the system and decomposes, either entirely or partially, into a series of intermediates before forming stable nucleating species. Therefore, particle nucleation becomes a complex process, which may be captured by extending the PFGM table with the nucleation progress as a further dimension (control variables). This, however, would exceed the possible limit of a PFGM table, or lead to a poor resolution in all dimensions. Under simplification of the underlying, detailed kinetics, an alternative, mass-conserving calculation of the source term is proposed instead:

$$\Phi_\mathrm{p}(c, Z_j) = \frac{Y_F(c, Z_j) - Y_F(0, Z_j)}{1 - \gamma(Z_j)/Y_F(0, Z_j)} \rho(c, Z_j) \tag{6.8}$$

Here, $Y_F(0, Z_j)$ is the inlet mass fraction at the beginning of each flamelet, while $\gamma(Z_j)$ is an offset mass fraction. If Y_F does not decay completely, $\gamma(Z_j)$ represents the lowest value of Y_F within the flamelet. In case of a complete decomposition of Y_F, $\gamma(Z_j)$ is zero. As the decomposed and remaining iron oxide parts are assumed to form particle nuclei, the simplified transition from gas to particle phase respects mass conservation.

Liquid-phase modelling

The liquid phase is modelled using Lagrangian particles, where each particle represents a physical liquid droplet, as implemented by Rittler et al. [190, 191]. These numerical particles are characterised by position $x_{\mathrm{d},i}$, velocity $u_{\mathrm{d},i}$, mass m_d and temperature T_d determined from the following differential equations [38].

$$\frac{\mathrm{d}x_{\mathrm{d},i}}{\mathrm{d}t} = u_{\mathrm{d},i} \tag{6.9}$$

$$\frac{\mathrm{d}u_{\mathrm{d},i}}{\mathrm{d}t} = \frac{f_1}{\tau_\mathrm{d}}(\tilde{u}_i - u_{\mathrm{d},i}) + (1 - \frac{\bar{\rho}}{\rho_\mathrm{d}})g_i \tag{6.10}$$

$$\frac{\mathrm{d}m_\mathrm{d}}{\mathrm{d}t} = -\frac{Sh\ m_\mathrm{d}}{3Sc\ \tau_\mathrm{d}} ln(1 + B_m) \tag{6.11}$$

$$\frac{\mathrm{d}T_\mathrm{d}}{\mathrm{d}t} = \frac{Nu\ c_p}{3Pr\ c_{p,\mathrm{d}}} \frac{T - T_\mathrm{d}}{\tau_\mathrm{d}} \frac{ln(1 + B_h)}{B_h} + \frac{\mathrm{d}m_\mathrm{d}}{\mathrm{d}t} \frac{L_\mathrm{d}}{m_\mathrm{d} c_{p,\mathrm{d}}} \tag{6.12}$$

Where g_i, T, T_d, c_p, $c_{p,\mathrm{d}}$, and L_d denote the the gravitational acceleration, the gas and droplet temperature, the gas and droplet heat capacity, and the latent heat of vaporisation, respectively. The droplet relaxation time $\tau_\mathrm{d} = (\rho_\mathrm{d}/d_\mathrm{d}^2)/(18\mu)$ is determined from the droplet diameter d_d and effective gas viscosity μ. The drag coefficient f_1 is defined as a function of the droplet Reynolds number $f_1 = 1 + 0.15 Re_d^{0.687}$, with the droplet Reynolds number being $Re_\mathrm{d} = (\rho|\tilde{u}_i - u_{\mathrm{d},i}|d_\mathrm{d})/(\mu_\mathrm{d})$. Further the Schmidt-, the Sherwood-, the Nusselt-, the Prandtl-number, the Spalding number for mass and heat transfer are denoted as Sc, Sh, Nu, Pr, B_m, and B_h respecitvely.

Nanoparticle modelling

The dispersed nanoparticle phase and its particle size distribution (PSD) is described using the sectional model [14, 128, 141]. Within the model, the PSD is divided into individual sections k, where a particle number concentration Q_k is given for each section, representing a particle class of a particle volume v_k. Each section is described as a Eulerian field, transported by the following

equation:

$$\frac{\partial \overline{Q}_k}{\partial t}+\frac{\partial \overline{Q}_k \tilde{u}_j}{\partial x_j} = \frac{\partial}{\partial x_j}(D_Q + \frac{\nu_\mathrm{t}}{Sc_\mathrm{t}})\frac{\partial \overline{Q}_k}{\partial x_j} + \overline{R}_k^\mathrm{C} + \overline{I}\delta_{k1} \tag{6.13}$$

Here $D_Q = k_\mathrm{B}TC_c/(3\pi\mu d_\mathrm{k})$ is the particle diffusion coefficient, where k_B is the Boltzmann constant, C_c is the Cunningham slip correction factor, μ the dynamic viscosity, and d_k the particle diameter. The effect of the subgrid velocity contribution is considered via the turbulent viscosity approach [128] entering the diffusion coefficient, while the particle motion is assumed to follow the gas phase velocity.
The source term R^C represents the rate of particle formation and vanishing in a section due to coagulation, which corresponds to the collision of two solid particles resulting in a bigger nano particle. The coagulation is approximated by:

$$\overline{R}_k^\mathrm{C} \approx \frac{1}{2}\sum_{i,j=1}^{k} \chi_{ijk}\beta_{ij}\overline{Q}_i\overline{Q}_j - \sum_{i}^{N_s}\beta_{ik}\overline{Q}_i\overline{Q}_k \tag{6.14}$$

The first term, right hand side, represents the "birth" term (particle added to the section by coagulation), while the second term represents the death term (particle moves by coagulation into an another section). Here, χ_{ijk} is the size splitting operator, which interpolates the coagulation contributions of particle combinations, which fall between the defined sections, while N_s indicates the number of sections. The collision frequency β_{ij}, accounts for collisions between particle pairs i, j within the gas phase. It is described by the harmonic mean of the coagulation frequency in the free molecular range β_{ij}^f, and in the continuum regime β_{ij}^c [100, 173].

$$\beta_{ij} = \frac{\beta_{ij}^\mathrm{c}\beta_{ij}^\mathrm{f}}{\beta_{ij}^\mathrm{f} + \beta_{ij}^\mathrm{c}} \tag{6.15}$$

The collision frequency in the free molecular regime is:

$$\beta_{ij}^\mathrm{f} = \left(\frac{\pi k_\mathrm{B}T}{2}\right)^{1/2}\left[\frac{1}{m_{\mathrm{p},i}} + \frac{1}{m_{\mathrm{p},j}}\right]^{1/2}(d_{\mathrm{c},i} + d_{\mathrm{c},j})^2 \tag{6.16}$$

where the variables T, m_p and d_c stand for the gas phase temperature, the particle mass and the collision diameter of the particles [200]. The collision frequency in the continuum regime is:

$$\beta_{ij}^c = \frac{2k_\mathrm{B}T}{3\mu}\left[\frac{C_i}{d_{\mathrm{c},i}} + \frac{C_j}{d_{\mathrm{c},j}}\right](d_{\mathrm{c},i} + d_{\mathrm{c},j}) \tag{6.17}$$

The particle inception term $\overline{I}$ only occurs for the first section and is calculated by:

$$\bar{I} = \frac{\mathrm{d}\bar{\rho}_I}{\mathrm{d}t}\frac{N_\mathrm{A}}{\rho_p} \tag{6.18}$$

With $d\bar{\rho}_i/dt$ given by Eq. (6.7), the Avogadro constant N_A and the particle density for iron oxide particles $\rho_\mathrm{p} = 5242\ \mathrm{kg/m^3}$. To model the subfilter PDF of the nanoparticles, an approach assuming a double delta distribution was used, which was developed by Mueller and Pitsch [144] for the hybrid method of moments (HMOM) in the soot context and derived for the sectional model by Rodriguez et al. [192]. We have adapted it here for nanoparticles. In the model, the PDF is divided into two modes, described by two delta functions: A particle mode and a non-particle mode, which means that there are two regions within a CFD cell (or filter volume): the first without particles, the second with homogenous particles concentration:

$$P(Q_i) = \omega\delta(Q_i) + (1-\omega)\delta(Q_i - Q_i^*) \tag{6.19}$$

The subfilter intermittency factor ω represents the probability of finding at a random point inside the respective LES cell, i.e., the ratio of the empty volume to the cell or filter volume. The quantity Q^* is defined such that the convolution of the PDF reflects the filtered value of the nanoparticle scalar $\overline{Q}$:

$$\overline{Q}_i = \int Q_i P(Q_i) dQ_i = Q_i^*(1-\omega) \iff Q_i^* = \overline{Q}_i/(1-\omega) \tag{6.20}$$

The intermittency factor could be determined by each of the transported nano scalars, but Mueller [144] has shown that the total number concentration is most suitable. Thus, the subfilter intermittency can be calculated as follows:

$$\omega = 1 - \frac{\overline{Q}_{\mathrm{tot}}^2}{\overline{Q^2}_{\mathrm{tot}}} \tag{6.21}$$

In order to get the filtered values for Q_{tot} and Q_{tot}^2, the following filtered transport equations are solved [192]:

$$\frac{\partial \overline{Q_{\mathrm{tot}}^2}}{\partial t} + \frac{\partial \tilde{u}_i \overline{Q_{\mathrm{tot}}^2}}{\partial x_i} = 2\overline{Q_{\mathrm{tot}} \dot{m}_Q} - \overline{Q_{\mathrm{tot}}^2} \frac{\partial \tilde{u}_i}{\partial x_i} + \frac{\partial}{\partial x_i} \frac{\nu_{\mathrm{t}}}{Sc_{\mathrm{t}}} \frac{\partial \overline{Q_{\mathrm{tot}}^2}}{\partial x_i} \tag{6.22}$$

The first term on the right hand side is the particle number source term and $\dot{m}_Q$ considers nucleation and coagulation $\dot{m} = \overline{I} + \overline{R^C}$. Theoretically, the transport of Q_{tot} is not necessary, since it results from the transported individual sections Q_i, but to conserve the same numerical treatment between Q_{tot}^2 and Q_{tot}, especially for turbulent viscosity, Q_{tot} is transported as well [192]:

$$\frac{\partial \overline{Q}_{\mathrm{tot}}}{\partial t} + \frac{\partial \tilde{u}_i \overline{Q}_{\mathrm{tot}}}{\partial x_i} = \overline{\dot{m}}_Q + \frac{\partial}{\partial x_i} \frac{\nu_{\mathrm{t}}}{Sc_{\mathrm{t}}} \frac{\partial \overline{Q}_{\mathrm{tot}}}{\partial x_i} \tag{6.23}$$

6.1.4 Experimental setup

Burner setup

The SpraySyn burner consists of three concentrically arranged separate streams: spray, pilot flame, and co-flow, shown in Fig. 6.1. The spray is generated in a two-phase nozzle by passing the precursor solution (ethanol and 0.05 mol/$\mathrm{l_{spray}}$ iron nitrate nonahydrate, $\mathrm{Fe(NO_3)_3 \cdot {}_9H_2O}$), through a capillary ($D_{\mathrm{in/out}} = 0.4/0.7$ mm). The capillary is placed in a coaxial nozzle for the dispersion stream ($D = 1.5$ mm) of pure oxygen, which atomises the liquid by its high momentum. The spray is surrounded by a lean premixed methane/oxygen flame acting as a pilot flame with an equivalence ratio of $\phi = 0.125$, while the inert nitrogen ($\mathrm{N_2}$) co-flow shields the flame against the environment and stabilises the flow. (Note that $\mathrm{O_2}$ was used as co-flow gas in the simulations to limit the number of mixtures (i.e. transport equations and chemistry table dimensions) that needed tracking. The simplification is justified as mixing with the co-flow in the downstream regions of the flame does barely affect the chemistry due to the excess air from the lean pilot and the pure oxygen dispersion flow further upstream.)

Both flow through a sinter matrix, resulting in a laminar flow due to the high temperature and the low flow rate. The pilot flow and the co-flow are not separated within the porous burner matrix. The width of the pilot flame was determined from experiments. The procedure was described in [203]. The flow rates of the concentric inlets were set according to table 6.1.

Particle measurements

The particle-size distribution (PSD) was analysed applying particle mass spectrometry [224]. It is a well-established method for the online investigation of the formation and growth of nanoparticles in flames and is based on the deflection of charged particles in an electrical field as described

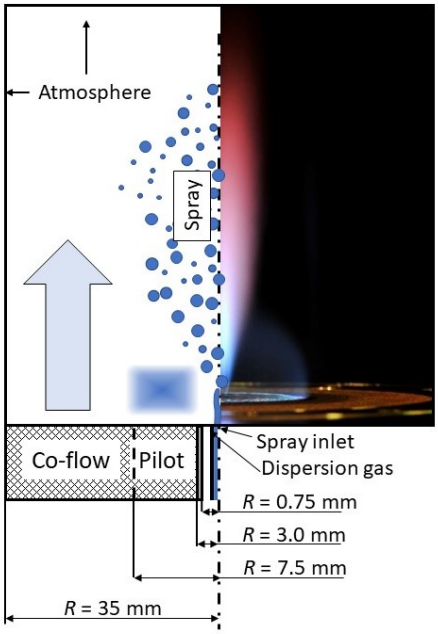

Figure 6.1: Sketch of the SpraySyn burner with inlets and dimensions.

Table 6.1: Geometric and mass flow parameters used within the experiment and simulation.

	r_{in} / mm	r_{out} / mm	mass flow	u / ms^{-1}
Spray	0	0.75	2 ml/min spray 10 slm O_2	103.6
Pilot $\phi = 0.125$	0.75	13.5	16 slm O_2 2 slm CH_4	4.6
Co-flow	13.5	35	120 slm O_2	0.621

by Roth and Hospital [195]. Particles were sampled with a water-cooled probe (orifice diameter of 0.8 mm) directly from the flame. The gas sampling is diluted and quenched immediately with 6 slm nitrogen and expanded into vacuum via a two-stage nozzle/skimmer system to generate a supersonic particle-laden molecular beam. The beam is guided through a deflecting capacitor, where particles are deflected depending on their charge, mass, and speed, and are detected by an off-axis Faraday cup. According to Fuchs' theory and from own experience it can be assumed that particles in the size regime of interest carry only one elementary charge [52]. With a known particle velocity u_{p}, the geometry constant of the particle mass spectrometer K_{PMS} considering the geometry of the deflector/detector setup, and a given deflection voltage U_{defl}, the determination of the particle mass m_{p} is possible as follows:

$$m_{\text{p}} = \frac{U_{\text{defl}}}{u_{\text{P}}^2} K_{\text{PMS}} \tag{6.24}$$

For a more detailed description of the setup and validation of the system, the reader is referred to the work of Suleiman et al. [224].

6.1.5 Numerical framework

The LES equations were solved with the in-house code 'PsiPhi' which has been used for many combustion simulations in the LES context [176, 187, 190, 249]. The code uses the finite volume method to solve the conservation equations on an equidistant Cartesian grid. The convective terms were discretised using a second order central difference method (CDS) for the momentum

and a total variation diminishing (TVD) scheme with the CHARM limiter [254] and (up to) second order accuracy for the scalars. The diffusive terms were discretised with a second order central difference method. The pressure–velocity coupling is achieved by a predictor–corrector projection method. The temporal discretisation is achieved by a low-storage Runge-Kutta method with third-order accuracy. The effect of subfilter fluxes on scalar and momentum fields is considered with the eddy-diffusivity and eddy-viscosity approach, respectively. The turbulent Schmidt-number was chosen as $Sc_t = 0.7$, and the turbulent viscosity was calculated with the σ–model of Nicoud et al. [151] with a model constant of $C_m = 1.5$. The PSD was discretised by twenty-four bins ($N_s = 24$). With the smallest volume being $v_1 = 0.0477\text{nm}^3$ and an equidistant spacing of $v_k = v_{k-1} * 1.8$, this allows the solution of particles covering a range of 6 orders of magnitude in volume. The simulation domain was chosen to start 3 mm above the burner, which has the

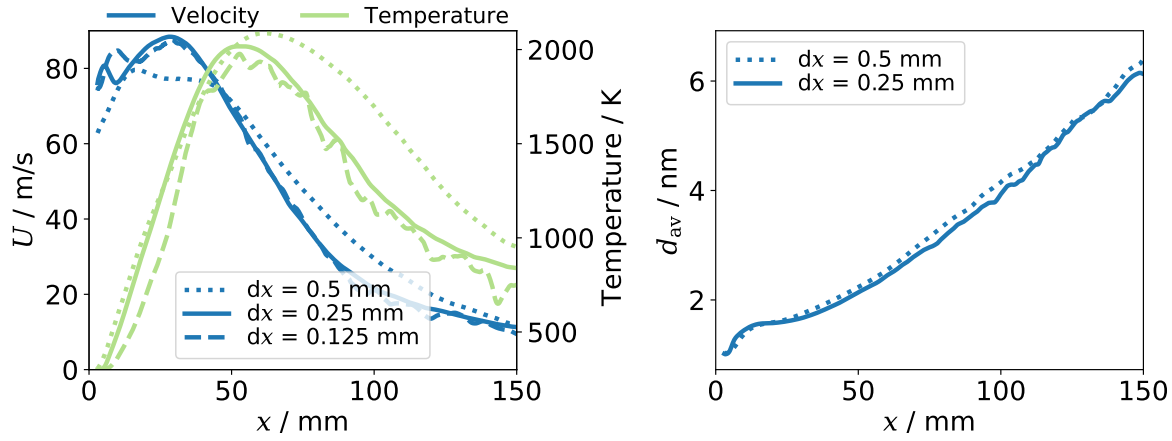

Figure 6.2: Axial mean profiles for velocity, temperature, and average diameter for different grid sizes $\Delta = 0.5$ mm (solid) and $\Delta = 0.25$ mm (dashed)

advantage that the primary and secondary break-up of the spray does not have to be simulated. To obtain realistic boundary conditions for the spray, droplet size distributions measured at this position were used [202]. The data was determined by a phase Doppler anemometry (PDA) measurement [202, 203] and provide axial and radial velocity as well as the droplet diameters at the respective radial positions. The measured samples are directly used instead of using an algorithm, to first construct the joint PDFs and then generate samples from it, using, for example, the Metropolis algorithm. Droplets are seeded with tuples of measured data. The average mass flow is preserved since the seeded mass is monitored, and the occurring misbalance caused by the discrete nature of the process is corrected over the next time step. Thus, the complexity of the algorithm is kept low, and the joint probability is fulfilled for the radial position, the droplet size, and the droplet velocity-vector from measurements. In order to obtain the best possible boundary conditions, simulations were carried out on a finer computational grid, starting at the edge of the burner to resolve the flow on the first 3 mm. Still, simplifications were necessary. The flow inside the burner and the resulting velocity profile is not resolved. The velocities on a slice at 3 mm height was then set as the boundary condition. The temperature boundary condition was set to the adiabatic flame temperature of the pilot since combustion is already complete at this height due to the high flame speed of an oxy-fuel flame. The final simulations were performed on a computational grid with cubic cells and a cell size of $\Delta = 0.25$ mm, which allows a resolution of the central jet with at least 6 cells across the diameter. The computational domain had a size of 150 mm $\times$ 52 mm $\times$ 52 mm, resulting in a total number of 26.7 million cells and a compute time of 162,000 CPU hours. A grid study was carried out, and the simulations converge for a grid size of $\Delta = 0.25$ mm. Figure 6.2 shows the results. While a refinement from $\Delta = 0.5$ mm to

$\Delta = 0.25\,\mathrm{mm}$ impacted the temperature and velocity distribution, further refinement towards a grid of $\Delta = 0.125\,\mathrm{mm}$ had a negligible impact and did not affect the overall simulation.

6.1.6 Results

In this section, the results of the simulation are shown and compared to the experimental data. First, the gas phase data is investigated, followed by the dispersed phase, where online and in situ measured PSDs are provided for comparison. Finally, the subfilter model is discussed at the end of this section.

Flow field

The selected variables (velocity, temperature, evaporation rate) shown in Fig. 6.3 indicate the general shape of the flame in the frame of instantaneous and averaged slices of the flow field. The

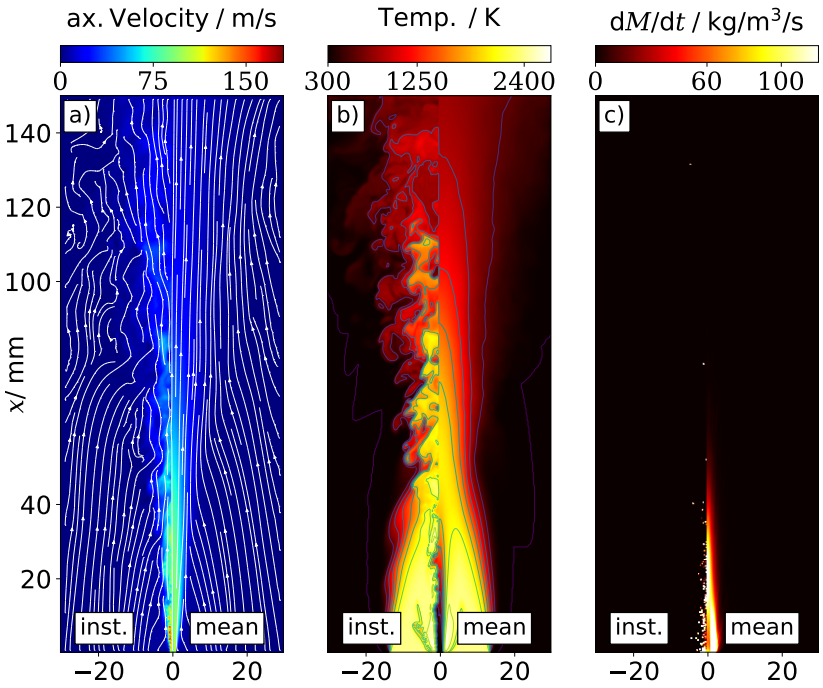

Figure 6.3: Instantaneous (left) and averaged (right) fields of (a) gas phase velocity u, (b) temperature, (c) evaporation rate $\mathrm{d}M$ on a 2D cross-section through the centre line.

region of the spray jet, which forms from spray droplets and dispersion gas, has the highest mean velocity ($u = 103\,\mathrm{m/s}$) compared to the pilot ($u = 8.3\,\mathrm{m/s}$) and the co-flow ($u = 0.62\,\mathrm{m/s}$), and can be clearly distinguished within the velocity field (Fig. 6.3 (a)). The mean velocity is 103 m/s, but the uneven velocity distribution across the nozzle, and turbulent fluctuations, leads to instantaneous velocity peaks of up to 150 m/s in the central jet close to the burner. Downstream, the jet decelerates, the turbulent structures become larger, the jet expands and mixes with the surrounding pilot and co-flow. The pilot stream is visible in the temperature field (b) due to its very high temperature. As described in Section 6.1.5, the simulation starts 3 mm above the burner matrix, where the combustion process of the pilot is already complete due to the high flame speed of an oxy-fuel flame [248]. The oxygen/methane pilot flame is modelled as completely burned in the inlet plane. The pilot flame gases are cooled at the outer radius by mixing with the co-flow. The interaction of the pilot with the spray (inside) provides the energy to evaporate the spray droplets, while small turbulent structures can be observed in this region. The co-flow is not

apparent from Fig. 6.3, but envelops the pilot and seals it off from external influences. Figure 6.3 (c) shows the evaporation rate of the spray droplets. Two regions of increased droplet evaporation can be identified: The first and stronger region is located within the shear layer between the hot pilot and the spray jet, where the pilot provides the necessary energy to evaporate the droplets. The second region is located further downstream, in the centre of the jet. Here, the jet has been heated due to ethanol combustion and mixing with the pilot at its interface. The spray heating led to the second droplet evaporation region, supported by convective evaporation driven by the high jet speeds.

The velocity profile was compared against experimental data along the centerline. The results are shown in Fig. 6.4. The velocity measurements were conducted by Martins et al. [136], who used the particle image velocimetry (PIV). From $x = 30 - 60\,\mathrm{mm}$, the experimental data

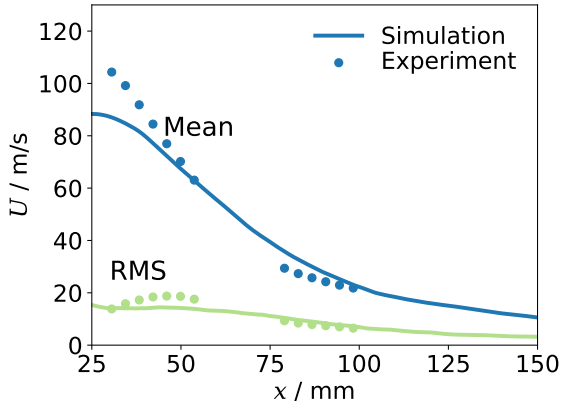

Figure 6.4: Axial profiles of mean and rms for velocity.

shows a constant decrease in velocity starting with a velocity of $u_\mathrm{E} = 110\,\mathrm{m/s}$. Closer to the burner, the spray density is too high, and no experimental data is available. The simulation shows a similar steep decrease, although, with $u_\mathrm{S} = 90\,\mathrm{m/s}$, it does not reach the experimentally observed peak value. This deviation might result from an insufficient boundary description of the simulation, which is described in Section 6.1.4. When comparing the RMS values, it is noticeable that in the experiments, a peak is measured around $x = 50\,\mathrm{mm}$, while simulations are showing a constantly decreasing RMS values consistent with the mean velocity profile. The measured peak might indicates the breakup of the jet which is not significantly visible in the mean velocity profile of the simulations, shown in Fig. 6.3 and 6.4. Nevertheless, the simulation satisfactorily reproduces the velocity field in general and allows the synthesis and growth of the nanoparticles to be observed more closely in the model.

Particle evolution

Figure 6.5 (a) and 6.5 (c) show instantaneous and mean profiles of the particle number density of the selected sections Q_1 and Q_{13}. The corresponding normalised coagulation rates were post-processed according to Eq. (6.14) and are shown as parts (b) and (d) within Fig. 6.5, while part (e) shows the volume averaged particle diameter. In each subplot of Fig. 6.5, the black iso-contours of the axial velocity u=3, 1.5, 0.6 m/s are chosen to represent different regimes of residence time, while the gold iso-contour in Fig. 6.5 (a) frames the high particle nucleation rate zones. The gold iso-contour in Fig. 6.5 (a) frames the zones of high particle nucleation-rate. The first section Q_1 represents freshly nucleated particles from the gas phase. Therefore, two particle-forming zones can be identified at the bottom of the flame. The first zone in the shear layer between the pilot and the spray coincides with a high droplet evaporation rate (Fig. 6.3 (c)). Here the temperature is high enough that the spray droplets evaporate very quickly and the

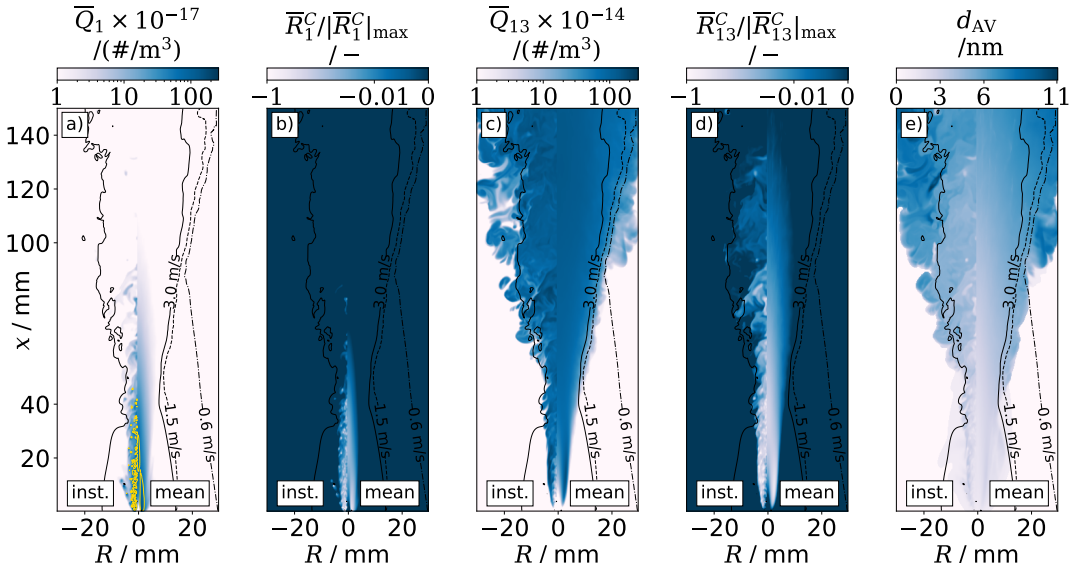

Figure 6.5: Instantaneous (left) and averaged (right) fields of: the number concentrations of section 1 (a) and 13 (c), coagulation rate R^{C} for sections 1 (b) and 13 (d), and the diameter of average volume (e), determined from Eq. (6.25). The sections 1 and 13 represent particles with diameters of $d_1 = 0.46\,\mathrm{nm}$ and $d_{13} = 3.0\,\mathrm{nm}$ respectively. The axial velocities u=3, 1.5, 0.6 m/s are shown by black iso-contours, while the gold iso-contour in Fig. (a) represents high nucleation rate areas.

reaction from reactants to products proceeds rapidly, thus also the nucleation of the nanoparticles. In comparison, the second zone is in the middle of the spray flame, slightly downstream of the zone of high evaporation rates (Fig. 6.3 (c)). The prevailing temperatures are lower here, the spray droplets evaporate and the nucleation process is slower. Away from this main particle-forming zone, however, high local particle concentrations can be detected. Here, large spray droplets have survived and evaporate away from the centre of the jet. Figure 6.5 (b) shows the coagulation rate (Eq. (6.14)) of the first section, because of the nature of the coagulation process (two particles form one bigger particle) the coagulation source term of the first section can only be negative throughout. The maximum is seen directly in the shear layer where the highest number of particles of the first section is located, which implies a rapid growth.

The section Q_{13} was chosen as representative of the global particle field, it shows the boundaries of the field, as particles of this section have originally formed very early and can be observed until the outlet. The particle cloud expands with the main gas flow which is consistent with the expansion of the jet in Fig. 6.3. The coagulation rate in Fig. 6.5 (d) shows negative values throughout, with a maximum near the burner. The highest coagulation rate is identified in the region of highest temperatures and number concentration, which both directly affect the coagulation rate in Eq. (6.14). The consistently negative values imply coagulation of the section with nanoparticles towards bigger sections. The particle diameter in Fig. 6.5 (e) shows continuous particle growth along with the height above the burner, while particles outside the centre grow more prominent due to lower velocities and thus longer residence times indicated by the axial velocity iso-lines.

Particle size distribution

The information from the sectional model allows us to observe the evolution of the PSD in the flame. In the following, these are validated for the first time for nanoparticle synthesis in spray flame with online and in situ measured data from experiments. In previous studies, only the end product could be analysed, which meant that the temporal history of the particles

was unknown. In Fig. 6.6, the PSDs at four different axial positions above the burner are compared against those obtained by the experiments. The PSDs in the simulation and the

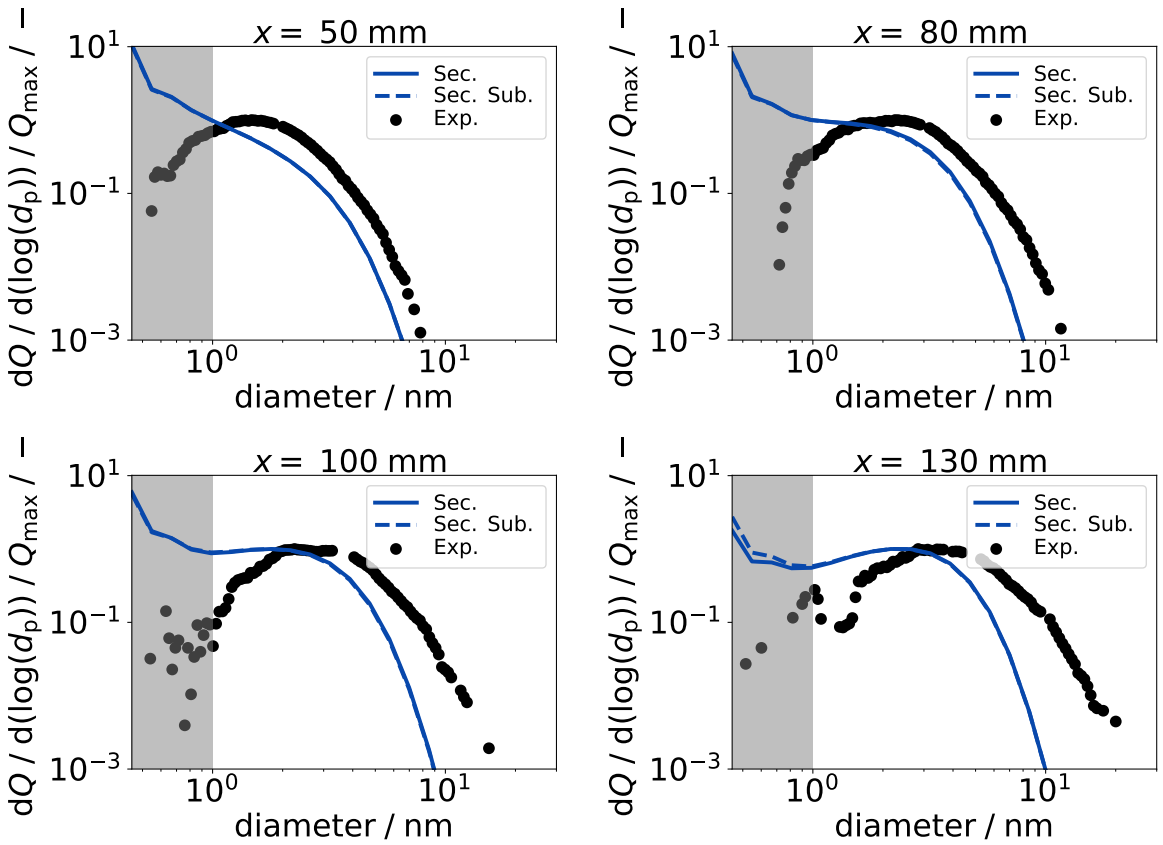

Figure 6.6: Particle size distribution at the centre line, for different heights above the burner. Comparison between experimental (symbols) and numerical results, with (blue-dashed) and without (blue-solid) subfilter model. The grey area marks the detection limit of the experiments. A meaningful comparison is not possible in the grey area.

experiment were normalised with their respective maximum value. While only one maximum can be observed in the experiments, there are two maxima in the simulations: the first represents a nucleation mode of freshly formed particles and the second corresponding to the mode of the self-preserving distribution of particles grown by coagulation [51]. The first maximum cannot be observed in the experiments because it lies below the detection limit (d_{AV} <1 nm) of the experiments. Thus, to compare both experiments and simulation, the value of the second smaller peak is used to normalise the simulation data. A grey zone indicates the detection limit in Fig. 6.6, and meaningful comparison is only possible outside this zone. When comparing the second maximum, good agreement between simulation and experiment can be observed at the low heights ($x \leq 80\,\mathrm{mm}$). Further downstream, a development of the PSD towards larger particles can be observed, which is slightly underpredicted when compared with the experiments. It is interesting to observe that the subfilter modelling has no noticeable influence on the simulations. In general, the agreement is satisfactory, deviations may occur due to the measurement procedure, which is intrusive and disturbs the flame structure. This requires further investigation but is beyond the scope of this work.

The advantage of a coupled LES with the sectional model is the unique information about the temporal development of the PSD. Figure 6.7 shows the PSD at the four different measurement points, where the PSD's have been collected over a duration of $t = 22\,\mathrm{ms}$ every $\Delta t = 0.5\,\mathrm{ms}$. The lines are transient, which indirectly results in a probability density function. Black regions correspond to the most probable value of the PSD, whereas slightly greyish regions correspond to

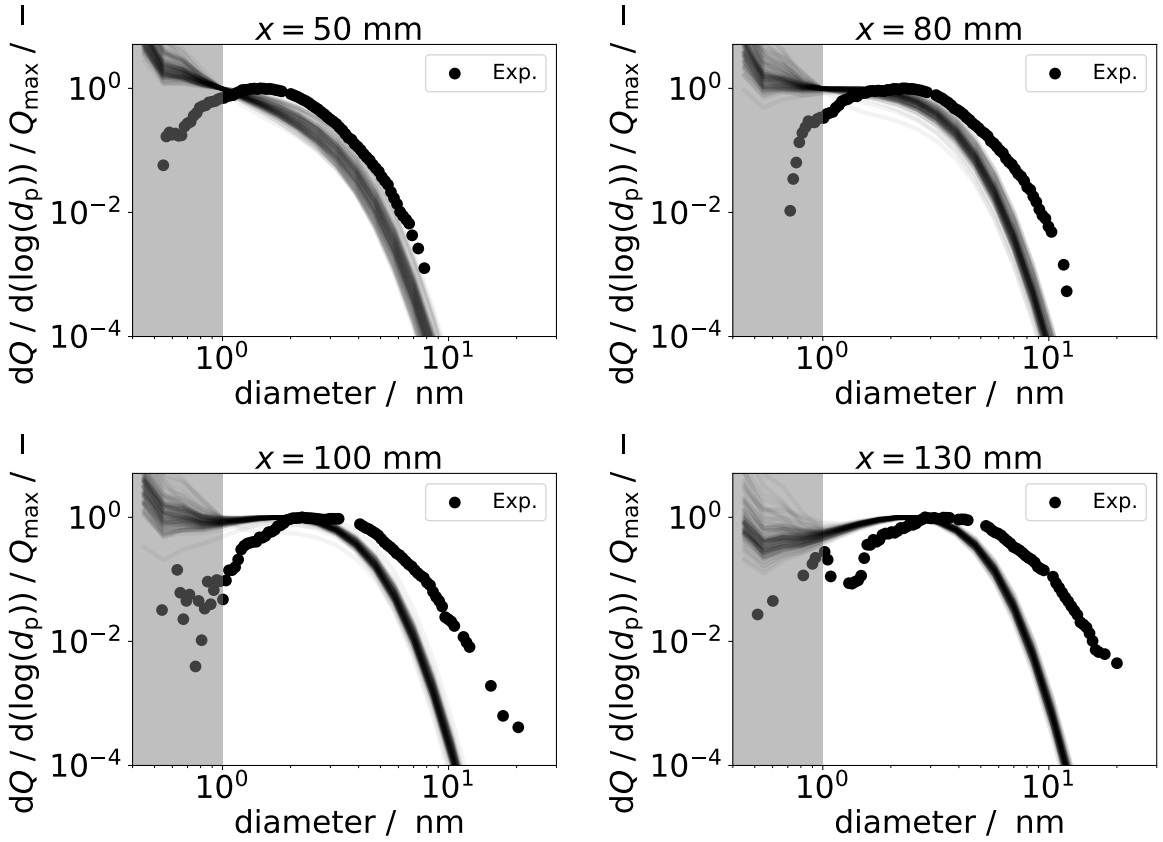

Figure 6.7: Probability density functions of the particle size distribution at the centre line, for different heights above the burner. The coloured area marks the detection limit of the experiments. A meaningful comparison is not possible in the grey area.

less probable values of the PSD. For $x = 50 - 80\,\mathrm{mm}$ strong fluctuations can be observed over the entire PSD. For $x = 50\,\mathrm{mm}$, it is consistently a two peak distribution. Moving downstream the synthesis flame, the nucleation mode becomes smaller and nearly vanishes at $x = 130$ mm. At the heights $x = 100 - 130\,\mathrm{mm}$, the velocity fluctuations have further decreased and also the variation of the PSD is smaller. Only fluctuations in the range of the detection limit can be observed.

The location of the distribution can be interpreted by its mean. Here, the mean diameter (d_{AV}) was calculated from the mean particle volume $\overline{v}_{\mathrm{m}}$, which provides a simple link between the total number and the total volume of the particle sample. The diameter is calculated from the representative volume of each section v_j as:

$$\overline{v}_{\mathrm{m}} = \frac{\sum_{j=1}^{N_{\mathrm{s}}} Q_j v_j}{\sum_{j=1}^{N_s} Q_j} \qquad \longrightarrow \qquad d_{\mathrm{AV}} = \left(\frac{6 \cdot \overline{v}_{\mathrm{m}}}{\pi} \right)^{1/3} \tag{6.25}$$

The corresponding field is shown in Fig. 6.5 (e) and the illustration agrees with the number concentration fields in Fig. 6.5 (a) and (c). A rapid growth is observed in the shear layer between pilot and spray-jet, and a more constant and slow growth in the centre of the jet. A comparison between experiments and simulations at the centre line is shown in Fig. 6.8 along with the nucleation rate. The diameter is post-processed from simulations, once neglecting sections below the detection limit of the experiments (black line, d^{DL}), and once considering all sections of the sectional model (blue lines, d^{S} without subfilter model, d^{SS} with subfilter model). At a height $x = 50\,\mathrm{mm}$, both experiments (d^{Exp}) and simulations (d^{DL}) predict the same diameter $d^{Exp} = d^{\mathrm{DL}} = 4.5\,\mathrm{nm}$. However, further downstream at $x = 130\,\mathrm{mm}$, the measured particle field ($d^{\mathrm{Exp}} = 9.8\,\mathrm{nm}$) shows faster growth than the simulations ($d^{\mathrm{DL}} = 7.4\,\mathrm{nm}$). The particles do

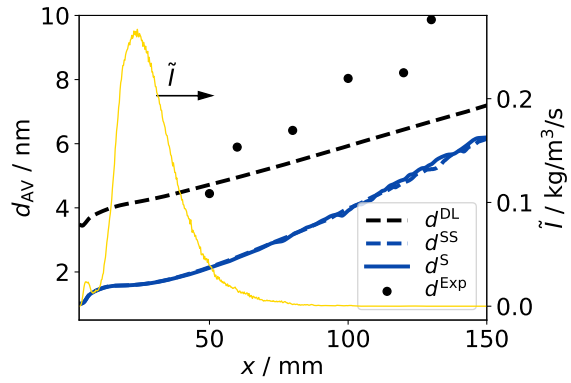

Figure 6.8: Comparison between the particle diameter of averaged volume, obtained by experiments (dots) and simulation (lines), along the centerline of the flame. Simulation results were performed with (d^{S}, blue-dashed) and without (d^{SS}, blue-solid) subfilter model and once neglecting small particles below the detection limit of the experiments ($d < 1\,\mathrm{nm}$) (d^{DL}, black-solid), further the nucleation rate is shown ($\tilde{I}$, yellow).

not grow at the same rate, but both growth rates are constant without any influence of the jet break-up or the pilot. For discussing the diameters d^{SS} and d^{S} considering particles below the detection limit, it should be stated that the driving process of increasing mean particle size here is coagulation. At the same time, nucleation is an inhibitory factor, as the inception of small particles reduces the mean particle size. In the region close to the burner, the mean particle size increase, despite the increasing nucleation rate, stating coagulation to be the dominating process. From the point where nucleation reaches its maximum, nuclei are added, and the average diameter stagnates. From $x = 35\,\mathrm{mm}$, the mean particle size increases again, and coagulation dominates over nucleation again. At $x = 50\,\mathrm{mm}$ simulations predict a diameter of $d^{\mathrm{S}} = 2.4\,\mathrm{nm}$ and at $x = 130\,\mathrm{mm}$ a diameter of $d^{\mathrm{S}} = 5.5\,\mathrm{nm}$. The direct comparison of the diameter d^{SS} and d^{S} against experiments shows overall smaller particles in the simulations while the growth rate looks similar. When considering particles below the detection limit, the mean diameter increases from position $x = 50\,\mathrm{mm}$ to position $x = 130\,\mathrm{mm}$ by a factor of 2.3, while in experiments, they grow by a factor of 2.2. To summarise, it can be stated that particles below the detection limit of the experiment reduce the average particle size. Near the burner the numerically obtained diameter shows particles in a similar size range when neglecting the particles below the detection limit in post-processing the number concentrations.

Subfilter modelling

One of the aims in this study was to apply a subfilter model, which is based on the intermittency of nanoparticles, as a closure for the coagulation source term. The intermittency model, initially developed by Mueller and Pitsch for sooting flames [144], computes an intermittency factor ω based on the first two moments of the PSD. The factor ω is directly correlated with the variance of the PSD. It becomes zero when particles are homogeneously distributed in the LES-cell and unity when the number concentration is highly intermittent and the probability of finding particles at a random point within an LES-cell approaches zero. In Fig. 6.9 on the left, the intermittence factor ω is shown in a vertical slice through the flame. The instantaneous image shows very fine structures in the vicinity of the burner, which decompose and diffuse further downstream. To be able to show the instantaneous image together with the averaged one, the scale was multiplied by 0.1. Local and instantaneous intermittency values of $\omega_{\mathrm{max}} = 0.5$ are found, but the average is a factor of 10 smaller, in the range up to $0 < \omega_{\mathrm{max}} < 0.05$. The intermittency shows the highest values near the burner nozzle and in the highest turbulence level region as a measure of

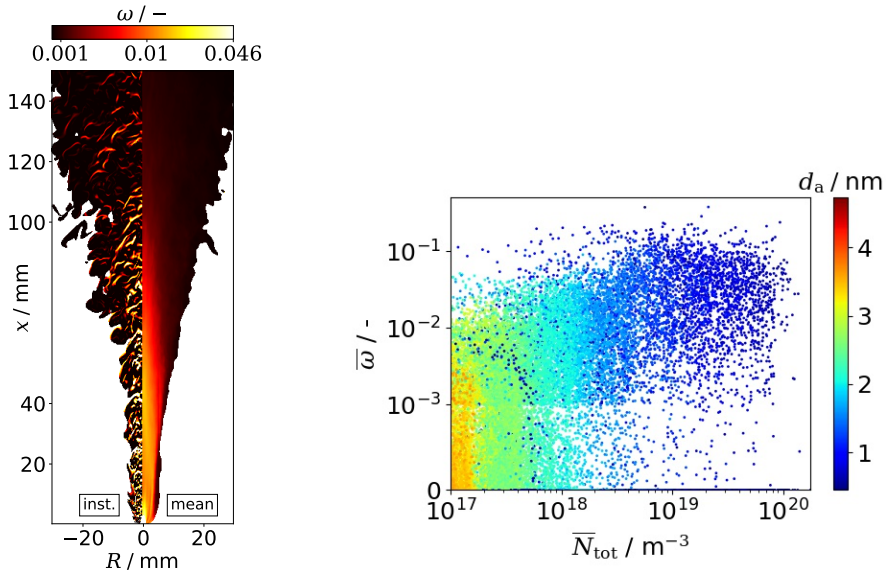

Figure 6.9: Left: Two-dimensional slice through the flame centre represents the intermittency factor, instantaneous (left, scaled by a factor of 0.1) and averaged (right). Right: PDF of the intermittency factor and the number concentration. Coloured with the particle diameter.

variance. Further downstream, the values decrease due to dissipation. The decreasing trend is also confirmed by the scatter plot on the right side of Fig. 6.9. The intermittence is plotted against the number of particle concentrations and coloured with the particle diameter. Consistent with the contour plot, the intermittence factor reaches the highest values at zones of high gradients in number concentrations and decreases at lower number concentrations gradients. High gradients in number concentrations and small particles are mainly found near the burner. Downstream, the particles grow, the turbulence decreases, and the particle number concentration decreases, as does the intermittence. Comparing the simulation with and without subfilter modelling in Fig. 6.8 and 6.6, the intermittence model has no significant influence on the results. Slightly larger particles in the burner-near region, whereas the particle diameter shows slower increase growth compared to the simulation without subfilter model far downstream. Nevertheless, the differences are marginal, which is somewhat surprising.

Summing up, the first particles are formed in the flame close to the burner in a highly turbulent region. Here, the turbulence model is required and shows the largest values. However, the main growth occurs further downstream in the exhaust gas of the flame, where the turbulent and intermittent structures are decaying due to dissipation. Further comparisons are necessary with a different material system to confirm measurements and simulations.

6.1.7 Conclusions

The spray-flame synthesis of Fe_2O_3 nanoparticles in the SpraySyn burner was investigated by numerical simulation and the results were compared to experimental data. For this purpose, existing experimental data was used [136, 202, 203] together with data from new measurements of the particle size distributions obtained using a particle mass spectrometer [224]. For the numerical investigation, a large eddy simulation was performed with a premixed flamelet generated manifolds model for the combustion. The droplets of the spray were individually resolved and described with a Lagrangian approach using droplet size distributions and velocities from experiments as initial values. The aerosol dynamics were considered using a sectional model, accounting for nucleation, coagulation, and an intermittency model to account for subfilter effects during coagulation. Three-dimensional simulations were carried out with and without a subfilter model to

determine its affect on the investigated case. First, the simulation was compared and validated with the velocity fields from the experiments. The comparison showed good agreement between experiments and simulations, while the area directly behind the burner could not be measured due to very strong fluctuations.

The simulations have been validated with online and in situ measured nanoparticle size distributions in a spray flame for the first time. The comparison shows good agreement between the simulation and the experiment for particle size distributions at different heights above the burner exit. The PSD obtained from simulations could be analysed and compared with measurements at different positions. A bimodal PSD is observed in simulations for $x < 100\,\mathrm{mm}$ although in measurements a monomodal PSD was measured. The missing first peak in the measurements is likely due to the detection limit of the experiments, as this peak represents the small fresh nuclei and particles with a diameter $d < 1\,\mathrm{nm}$. The second peak in the simulations represents the self-preserving distribution of particles grown by coagulation. In comparison with experiments, larger particles are measured further downstream, while the maxima of the particle size distributions agree with the simulations. Deviations and the stronger growth in experiments, may be due to various reasons in experiments as well as in simulations. For the experiments, the disturbance of the flame by the measurement probe needs to be further investigated. An intermittency model has been applied in order to investigate sub-filter effects on the particle field. It was shown that the model predicts regions of intermittent particle fields within the present case, while no significant influence on the particle field in the present case could be found. Nevertheless, for flames, which are characterised by a thin turbulent flame front (premixed, or high-pressure flames), the impact of the subfilter modelling might be more dominant.

6.1.8 Acknowledgments

The authors gratefully acknowledge the financial support from the German Research Foundation (DFG) within the priority program SPP 1980, "Nanoparticle Synthesis in Spray Flames, SpraySyn" (No. 375857243, 375857056, and 375220870) and the use of the MagnitUDE supercomputer system of the Center of Computational Sciences and Simulation (CCSS) and the Zentrum für Informations- und Mediendienste (ZIM) of the University of Duisburg-Essen. Further the authors gratefully acknowledge the Gauss Centre for Supercomputing e.V. (www.gauss-centre.eu) for funding this project by providing computing time on the GCS Supercomputer SuperMUC-NG at Leibniz Supercomputing Centre (www.lrz.de).

6.1.9 Additional comments as an outcome of the exam

During this work's disputation (exam), the subgrid model and its small influence on the particle size in the simulation were discussed. Remarkable are the low values of the intermittency factor, as shown in Fig. 6.9 (highest value ω =0.046). In future work, more careful attention should be paid to this parameter. It results from the total particle amount and the second moment of the total particle amount. However, these two depend on the intermittency factor used in calculating the coagulation source term. The coagulation source term is calculated from a coagulation frequency and the squared particle number concentration. From the square, it follows that even small changes are potentiated and have a significant effect or are potentiated and have a devastatingly small effect. As a potential source of error, the discussion is mentioned here, and greater attention should be paid to the source term in future before using this model.

Detailed investigation of subgrid effects on particle growth due to coagulation and its modelling

The influence of subfilter structures on the modelling of nanoparticle coagulation was investigated in more detail by an FDF method for the sectional model. This method was developed and implemented in the scope of this work. Therefore, the validation with the generic DNS case of Miller and Garrick [141] is shown in Appendix B. Subsequently, the FSD method was applied to the SpraySyn flame, and the results were published in the proceedings of the ECM [207].

6.2 Hybrid LES/Lagrange-FDF approach for the sub-grid modelling of nanoparticle synthesis in the SpraySyn burner [207] (Paper IV)

This section of Chapter 6 including all text, figures and tables is published in 'Proceedings of the European Combustion Meeting 'Sellmann, J., Wollny, P., Baik, S.-J., Suleiman, C., Wiggers, H., Wlokas, I., Kempf, A. (2021). Hybrid LES/Lagrange-FDF Approach for the Sub-grid Modelling of Turbulent Nanoparticle Synthesis.' [207].
Contributor Roles Taxonomy: J. Sellmann developed the code, ran the simulations and wrote the original manuscript draft. P. Wollny and S.-J. Baik, developed code, provided a discussion of the results and contributed to the manuscript. S. Suleiman performed experiments. H. Wiggers provided a discussion of the results. I. Wlokas and A. M. Kempf provided discussions of the results and contributed to the manuscript.

Abstract

The spray flame synthesis of Fe_2O_3 nanoparticles in the SpraySyn burner is simulated, and the influence of subfilter-effects on the accuracy of nanoparticle-dynamics modelling is investigated. For the numerical investigation, a large eddy simulation is performed with a premixed flamelet generated manifolds model for the combustion, and the spray-droplets are individually resolved and described with a Lagrangian approach. The nanoparticle dynamics were considered using a sectional model, solved conventionally in the Euler-field and also with an FDF-Lagrange approach to investigate the subfilter effects. Three dimensional simulations are carried out with both of the nanoparticle modelling approaches. The flame structure was analysed and the two main zones of spray evaporation were identified. From the investigation of the subfilter effects on the nanoparticle modelling, an increased coagulation rate can be detected for the calculation with the Euler method.

6.2.1 Introduction

In the numerical modelling of nanoparticles, the evolution of the particle properties as a particle size distribution (PSD) is described by the population balance equation (PBE) [51]. Popular solution approaches for the PBE are the sectional method [55], which discretises the PSD directly. Alternatively, the PBE is solved in the moment space of the PSD, e.g. presuming locally monodisperse particle size [115]. The sectional method does not require any presumptions about the PSD and if only a single particle property, the particle volume, is tracked, it is feasible for coupling with computational fluid dynamics simulation (CFD). In such coupled simulations, usually the steep gradients of the particle field cannot be resolved by the computational grid. Many past simulation approaches neglected the local fine structure of the particle field [141, 191]. In the context of soot, Mueller *et al.* introduced a method for modelling soot intermittency in a method of moments approach [144, 145]. Rodrigures *et al.* [192] applied this approach [144, 145] for the sectional model. Recently, Cifuentes *et al.* [29] investigated nanoparticle growth by nucleation and coagulation in a turbulent vortex using direct numerical simulation (DNS). In an a-priori

analysis, they were able to determine the deficiencies that occur by filtering of the particle field.

To account for the influence of the spatial gradients in a LES, the method of the transported filtered probability density function (FDF) is suitable [85]. In this method, the development of the FDF of an arbitrary scalar in the physical and the composition space is computed. The source terms appear in a closed form without neglecting the influence of the spatial gradients [53]. First pioneering work was presented by Sheikhi *et al.* [209] with the simulation of the Sandia Flame D and Raman et al. [181], who simulated the Sydney bluff-body flame. Both did not directly solve the transport of the FDF, but used a Monte-Carlo approach [171], where the FDF is represented by Lagrangian particles. These particles are transported with the flow and distorted by a dispersion model in physical space. On each particle, the composition space evolves and each particle represents a single part of the turbulent scalar field to be investigated. In our own preliminary work, this method was used and a hybrid combustion model was developed on the Lagrangian particles [188]. To the best of our knowledge, this method has not yet been used to describe nanoparticle synthesis.

In this study, we combine the FDF method with a LES simulation to obtain the transported FDF equation of particle number concentration in its closed form. For this purpose, a sectional model is solved on each numerical particle. The LES-FDF framework is applied to solve the spray flame synthesis of iron oxide (Fe_2O_3) nanoparticles in the SpraySyn [203] burner. The aim of the work is to compare the LES-FDF results with a conventional simulation, which solves the sectional model in Euler space and neglects the influence of the fine structure, its influence is then to be determined.

6.2.2 Modelling approach and experimental set up

Population balance modelling

The aerosol dynamics in the particle synthesis are modelled by the sectional approach [55]. The model provides access to the PSD, by a discretisation of the space of particle properties into k sections, each representing a number concentration Q_k of a particle volume v_k. Monomer particles are formed from the gas phase, which is considered by a nucleation source term affecting only the first section. Particles grow by coagulation with particles from the same section and with particles from all other sections. The rate of change $\dot{\omega}$ in each bin/section population depends on the local gas temperature and the particle number concentrations of colliding classes and is given as:

$$\frac{dQ_k}{dt} = \dot{\omega}_k^Q + I\delta_{(k=1)} \tag{6.26}$$

The Dirac measure δ ensures nucleation only in the first section. The source term $\dot{\omega}_k^Q$ is approximated by:

$$\dot{\omega}_k^Q \approx \frac{1}{2}\sum_{i,j=1}^{k} \chi_{ijk}\beta_{ij}Q_iQ_j - \sum_{i}^{Q_s} \beta_{ik}Q_iQ_k \tag{6.27}$$

Here, χ_{ijk} is the size splitting operator that interpolates the coagulation contributions of particle combinations between the defined sections. Detailed description of the model implementation can be found in the work by Wollny et al. [249]. To describe the interaction among gas phase and particles in a CFD simulation, Eq. (6.26) is reformulated in terms of a general transport equation. The transport equation is written in its filtered form as follows:

$$\frac{\partial \bar{Q}_k}{\partial t} + \frac{\partial \bar{Q}_k \bar{u}_j}{\partial x_j} = \frac{\partial}{\partial x_j}\left[\left(D_Q + \frac{\nu_t}{Sc_t}\right)\frac{\partial \bar{Q}_k}{\partial x_j}\right] + \bar{\dot{\omega}}_k^Q + \bar{I}\delta_{k1} \tag{6.28}$$

with the Favre-filtered gas phase velocity $\tilde{u}$, the particle diffusion coefficient D_Q, the turbulent viscosity ν_t and the turbulent Schmidt number Sc_t. The effect of the subfilter fluxes is modelled

using the eddy diffusivity approach [128]. The subfilter effects on the coagulation are not taken into account.

Transported filtered density function modelling

In order to determine the subfilter effects, the scalar filtered density function (SFMDF) [85] must be determined. In this work a transport equation for the SFMDF is used, where convective and diffusive subfilter fluxes are closed in the transport equation of the SFMDF, by the gradient-diffusion approach [32] and by the IEM mixing model [235]. The FDF evolves based on the Monte-Carlo method [171], and is represented by notional Lagrangian particles moving in physical and composition space. Each of the particles can be considered as a single representation of the turbulent scalar field [169] and its evolution in physical space can be described by the following governing equation:

$$dx_i^+ = \left(\tilde{u}_i + \frac{1}{\bar{\rho}} \frac{\partial \bar{\rho}(D_{sgs})}{\partial x_i} \right)^+ dt + (2D_{\text{sgs}}^+)^{1/2} dW_i^+ \tag{6.29}$$

Here the index + denotes particle quantities as opposed to Eulerian fields (e.g., ρ and $\tilde{u}_i$). The physical position x_i^+ of the particles depends on the local gas velocity $\tilde{u}$, the turbulent diffusivity D_{sgs} and the three-dimensional Wiener term dW_i^+. The turbulent diffusivity is determined under the assumption of a constant turbulent Schmidt number (Sc_{sgs}) and the Lewis number. The particle evolution in composition space is covered by the IEM mixing model:

$$d\psi_\alpha^+ = -\Omega_m^+(\psi_\alpha^+ - \bar{\phi}_\alpha^+)dt + \tilde{\Gamma}_\alpha^+ + S_\alpha(\psi^+)dt \tag{6.30}$$

where ψ_α^+ is the composition of the scalar α (here section Q_k), the mixing rate Ω_m^+ defined below (Eq. (6.32)). $\bar{\phi}_\alpha^+$ is the mean composition of the scalar α, the source term S_α, and with $\tilde{\Gamma}_\alpha^+$ being the transport term represented as a mean drift term [253]:

$$\tilde{\Gamma}_\alpha^+ \equiv \frac{1}{\bar{\rho}} \cdot (\bar{\rho} D_\alpha \nabla \tilde{\psi}_\alpha) \tag{6.31}$$

with the specific diffusivity D_α of each component α of the composition vector. In the current implementation of the IEM model, the particle composition ψ^+ relaxes to the mean composition $\tilde{\psi}^+$ interpolated onto the particle at the specific mixing rate:

$$\Omega_m = C_m \frac{\tilde{D} + \tilde{D}_{sgs}}{\Delta^2} \tag{6.32}$$

with a model constant $C_m = 12$ for all the components, where Δ is the filter width. The Favre averaged quantities $\tilde{q}$ are calculated by averaging over all particles in a LES cell:

$$\tilde{q} = \frac{\sum_{p=1}^{n_p} w_p q_p}{\sum_{p=1}^{n_p} w_p} \tag{6.33}$$

The mean values depend on a particle weight w_p assigned to a particle during generation.

Experimental setup

The SpraySyn burner [203] was developed within the framework of the DFG priority project SPP 1980 to provide benchmark conditions for experimental and numerical investigations. The geometry of the burner is shown in Fig. 6.10. The liquid precursor/solvent mixture is induced via a spray nozzle and atomised by an enveloping dispersion gas. A co-centric sinter matrix around the spray provides the pilot, a methane-oxygen flame (equivalence ratio of $\phi = 0.125$) which is shielded from the reactor walls by a nitrogen co-flow. Experimental measurements exist for temperature [221], droplet distribution [202], and particle size distribution. The validation of the simulations with this data is beyond the scope of this work but will be published eventually.

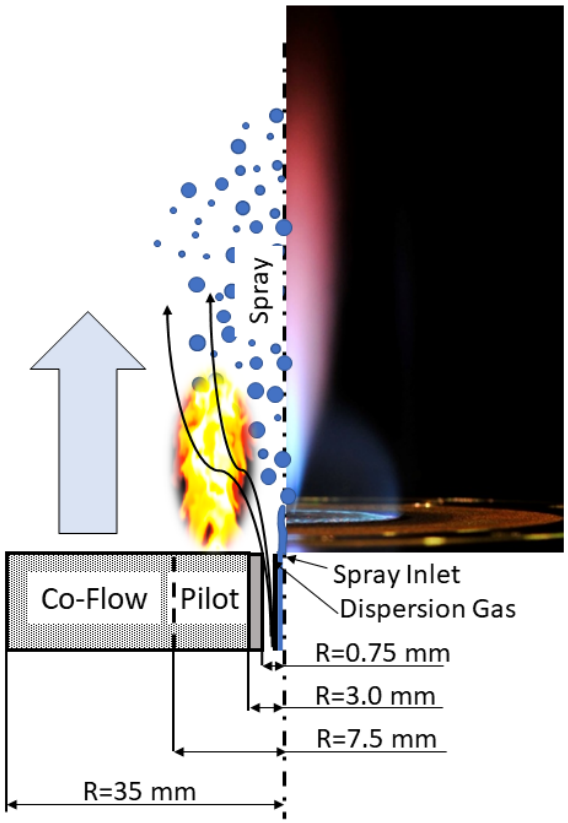

Figure 6.10: Sketch of the SpraySyn burner with inlets and dimensions.

Gas-, liquid-phase and combustion modelling

The flow field dynamics of the SpraySyn burner are calculated using LES by solving the filtered conservation equations for momentum and mass. A premixed flamelet generated manifold (PFGM) [231] model is used to model the combustion process. For this model, flames of different stoichiometries are pre-calculated in 1D and stored in tables. These tables can be accessed by providing three variables, (a) mixture fraction of the pilot flame Z_P, (b) mixture fraction of the spray compounds Z_S, and (c) a progress variable Y_P based on the combustion products. These variables require the solution of three additional transport equations to obtain detailed information about flame composition and progress. The primary and secondary spray break-up cannot be resolved in the LES. The computational inlet is thus positioned 3 mm above the burner exit, assuming a fully burnt pilot and a completed secondary break up of the spray. The spray droplet distribution is taken from experimental data [202] and each droplet is described by a numerical Lagrangian particle. Evaporation and transport of the droplets is described following the approach by De and Kim [38]. This setup has been published in previous works, and can be read in detail in the work by Wollny *et al.* [249] and Rittler *et al.* [191]. All models were implemented in the in-house code PsiPhi [176, 190] which is suitable for combustion simulations in the LES context.

6.2.3 Results

The flow pattern shown in Fig. 6.11, represents the transient and averaged velocity and the temperature fields of the simulated SpraySyn configuration. The two main streams of the burner, the spray-jet and the pilot, can be identified and distinguished by their very different states. The spray-jet in the centre of the burner, flows into the domain with a maximum velocity of $u_{jet} = 103\,\mathrm{m/s}$, the burnt pilot with a velocity of $u_{pilot} = 4.6\,\mathrm{m/s}$. In the velocity field, the spray-

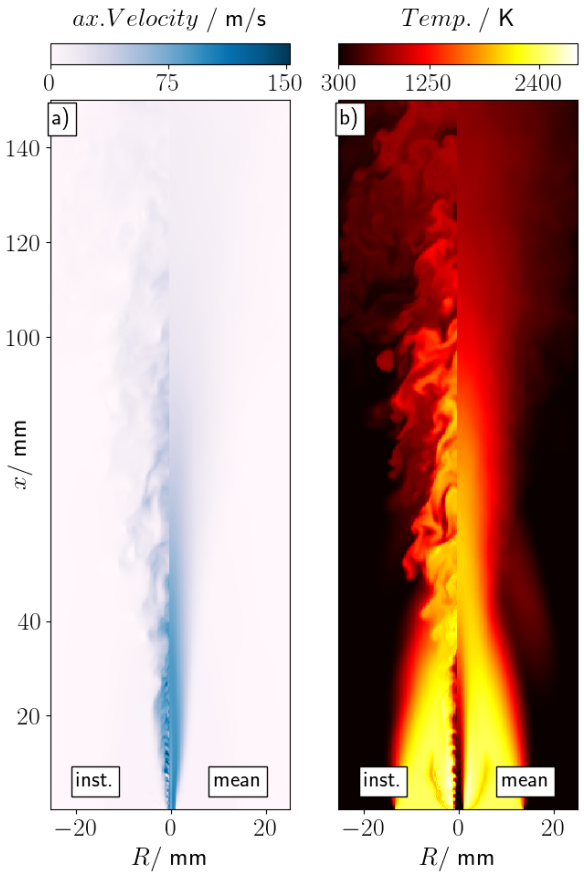

Figure 6.11: Instantaneous (left) and averaged (right) fields of (a) the gas phase velocity u, (b) temperature on a 2D cross-section through the centerline.

jet therefore stands out from the pilot. The simulation domain starts at $x = 3\,\text{mm}$ above the burner, and the pilot is assumed to be completely burnt and has a temperature of $T_{pilot} = 2390\,\text{K}$, compared to the spray-jet with $T_{jet} = 298\,\text{K}$. In the shear layer between pilot and spray, the two streams interact with each other. Due to the velocity difference, fine turbulent structures develop which lead to a break-up of the jet further downstream at $x = 45\,\text{mm}$. In addition, the pilot mixes completely at this position, leading to the ignition of the remaining vaporised spray/oxygen composition. Due to the decelerated flow after the jet break-up, the residence time for growing particles is enhanced.

The rates for the evaporation of the spray mass and the nucleating particle number concentration are shown in Fig. 6.12. Two regions of increased droplet evaporation can be identified: The first and stronger region is located within the shear layer between the hot pilot and the spray jet, where the pilot provides the necessary energy to evaporate the droplets. The second region occurs further downstream in the middle of the jet. Here, the jet has already been warmed up by mixing with the pilot and the droplets evaporate due to the warm up jet but also due to convective evaporation due to the high jet speeds. Nucleation takes place at the same two regions mentioned for the evaporation. The first is directly in the shear layer and coincides with the evaporation rate. The hot gas evaporates droplets immediately, while nanoparticles form. This does not apply to the region further downstream, as the temperatures here are not as high and the nucleation is slightly shifted downstream from the evaporation, as precursor decomposition is slower.

Due to the large computational effort required for the FDF method, only the region $x = 3-50\,\text{mm}$ above the burner is considered in the following discussion of the particle dynamics. This area is of certain interest due to the narrow spatial particle distribution and the resulting sharp gradients.

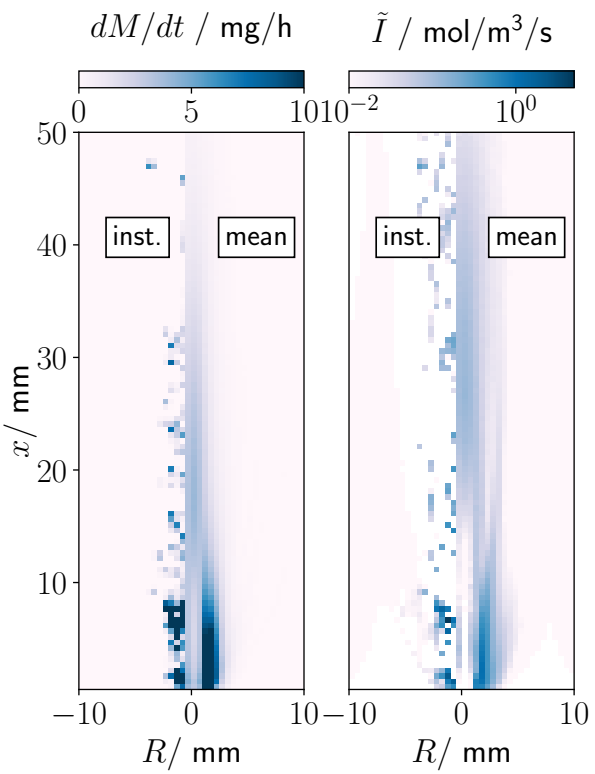

Figure 6.12: Instantaneous (left) and averaged (right) fields of (a) the spray evaporation rate dM, (b) Nucleation Source Term $\tilde{I}$ on a 2D cross-section through the centre line.

In Fig. 6.13 the nucleation rate is plotted along the centerline. It increases monotonically, due

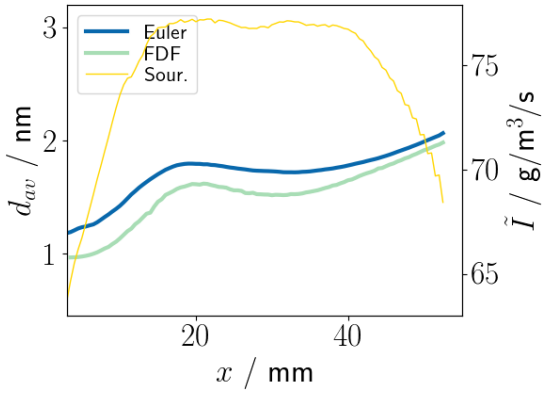

Figure 6.13: Number-averaged particle diameter along the centerline of the flame. The nucleation source term is plotted on the right axis and is the same for both models.

to the heating up of the jet and the associated evaporation of the droplets, reaching maximum plateau at $x = 15\,\text{mm}$. From $x = 40\,\text{mm}$ the nucleation rate drops again as most of the droplets are evaporated here. The mass-averaged diameter of the nanoparticles is approximated for the Lagrangian-FDF method and in the Euler field, and both show quantitatively the same particle growth. It should be stated that the driving process of particle growth here is coagulation, while nucleation is an inhibitory process in that context, as inception of small particles reduces the mean particle size. In the region close to the burner, the mean particle size increase, despite the increasing nucleation rate. From the point where nucleation reaches its maximum, a lot of mobile

mass is added and the average diameter stagnates or decreases due to the high number of small particles. From $x = 35\,\text{mm}$ the particles grow again and coagulation dominates over nucleation. The direct comparison of the diameter from both calculation methods shows weaker growth of the particles from the FDF method and increased coagulation using the euler method. Assuming that the FDF method gives the correct result, this means an overestimation of the coagulation rate by the Euler method. This needs to be investigated further, a smaller diameter would have been expected. Subfilter effects lead to a smearing of the results due to increased diffusion, which means lower local concentrations and thus lower coagulation and growth. However, downstream, the diameters converge and the subfilter effects appear negligible. A direct comparison of the PSD from the simulations with experimental data is shown in Fig. 6.14. Excellent agreement between

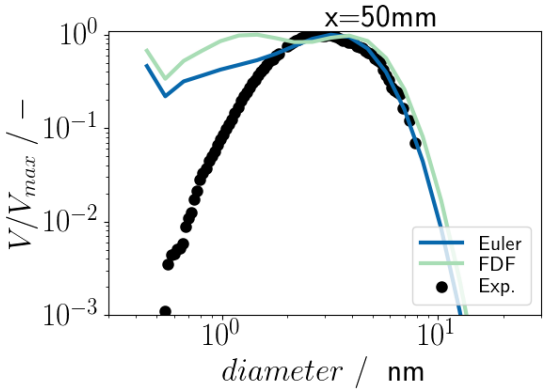

Figure 6.14: Particle size distribution compared to experimental data at $HAB = 50\,\text{mm}$

the two simulation methods is observed for larger particles. For smaller particles both methods show deviations from the experiments which is related to the measurement detection limit of the experiments but might also indicate an underestimation of the monomer diameter used in simulations, which is assumed to be one iron oxide molecule. Furthermore, a higher coagulation rate can be observed with the Euler method, which results in lower particle concentrations.

6.2.4 Conclusion

The spray flame synthesis of Fe_2O_3 nanoparticles in the SpraySyn burner was simulated, and the influence of subfilter-effects on the accuracy of nanoparticle-dynamics modelling investigated. For the numerical investigation, a large eddy simulation was performed with a premixed flamelet generated manifolds (PFGM) model for the combustion. The droplets of the spray were individually resolved and described with a Lagrangian approach, using droplet size distributions and velocities from experiments as initial values. The nanoparticle dynamics were considered using a sectional model, solved conventionally in the Euler-field and also with an FDF-Lagrange approach to investigate the subfilter effects. Three dimensional simulations were carried out with both of the nanoparticle modelling approaches. The flame structure was analysed and the two main zones of spray evaporation were identified. First in the shear layer between the pilot and the jet in the area close to the burner and the second further downstream in the centre of the spray jet. The main focus of the further investigation was then on particle modelling. The comparison with experimental data showed good agreement between experiment and simulation for the particle size distributions at $x = 50\,\text{mm}$. Especially the large sections describe the PSD very well. For smaller size classes $\approx 1\,\text{nm}$, significantly more particles can be observed in the simulations compared to the experiments. This may be due to the detection limit of the experiment, but also to the under-determination of the nucleated monomer size assumed for the simulations. From the investigation of the subfilter effects on the nanoparticle modelling, an increased coagulation

rate can be detected for the calculation with the Euler method. This leads to faster growth and a tendency towards larger particles in the Euler field calculation.

Acknowledgments

The authors gratefully acknowledge the financial support from the German Research Foundation (DFG, grant number KE-1751-11-1) and the use of the MagnitUDE supercomputer system of the Center of Computational Sciences and Simulation (CCSS) and the Zentrum für Informations- und Mediendienste (ZIM) of the University of Duisburg-Essen.

Additional comments

The disputation provided a noteworthy insight for upcoming simulations. While the definition of the mixing term in equation (3.105) agrees with existing literature, this term is predominantly influenced by turbulent diffusion. The diffusion of the nanoparticles is clearly limited due to the high Schmidt numbers ($D_\mathrm{t} > 1000D$), so that their correct mixing behaviour may not be properly represented. Subsequent investigations could benefit from the implementation of a revised mixing term:

$$\Omega_\mathrm{m}^+ = C_\mathrm{m} \frac{\tilde{D}^+}{\Delta^2} \tag{6.34}$$

Considering the complexity of the SpraySyn flame and the substantial modelling effort involved, it is advisable to choose a less complex reference flame for future simulations. This decision will facilitate the investigation of subfilter structures and their influence on the coagulation term. In this context, it would be useful to focus attention on flames characterised by a thin turbulent flame front, such as premixed flames or high-pressure flames.

Chapter 7
Summary

The work presented highly resolved simulations of laminar, iron oxide (Fe_2O_3) particle forming hydrogen/oxygen flames in a low-pressure environment (30 mbar). These flames were characterised by their orientations, one burning from top to bottom (down-firing) and the other burning regularly from bottom to top (up-firing). The simulations incorporated species-specific diffusion as well as finite rate chemistry and showed that the orientation of the flame affects the flow field. For the down-firing flame, it was observed that buoyancy forces lead to the formation of a stagnation point at which the hot flow is deflected. Furthermore, the simulation demonstrated that the down firing flame offers temperature-time profiles that cannot be realised in the conventional upward burning flame (higher temperatures over a longer period of time).

A bimodal particle model was implemented to approximate the particle dynamics, while particle formation was studied by experimentalists from Tel-Aviv University who used PMS and PMS-QCMB measurement techniques. The excellent agreement of the particle diameters confirms the two approaches (simulation and experiment) and shows the viability of the complementary approach. Moreover, experiments could identify a transient "pre"-particle forming zone. This particle zone is located in the preheating zone of the flame and vanishes at higher temperatures in the reaction zone. The modeled reaction kinetics could reproduce this observation for the formation of iron clusters. In addition, the systematic shift in the simulation results was attributed to the influence of the sampling probe.

In the subsequent study, a more detailed investigation of the impact of the sampling probe on the flame structure was performed. For this purpose, a methane-oxygen flame, operating at low pressure was investigated experimentally and numerically. While the experiments were carried out by colleagues at the University of Duisburg-Essen. Two different probing nozzles were studied, distinguished by their material (quartz/metal) and orifice diameter (90 μm/550 μm). The experiments used an EI-MBMS to detect the flame species and a thermocouple to measure the temperature. High-resolution simulations were performed using detailed chemistry and species-specific diffusion, and the two nozzles were simulated at four different probing positions above the burner.

The comparison between experiments and simulations showed satisfactory agreement, allowing the following three aspects to be deduced, which must be considered when estimating the probing effect. First, the sampling probe can reach higher temperatures than the probing point and thus heat up the flame. Second, the probe draws gases in, before and after the orifice, which results in varying residence times and temperatures of the simultaneously analyzed fractions in the probe. Third, the gas samples sucked into the probe lead to deformed isolines of the flow field temperature and streamlines. In this study, suction was detected as a governing type of perturbation and was further investigated by evaluating the residence times of single streamlines. The study shows that the impact on the flame caused by suction varies depending on the proximity to the burner. The closer the measurement is to the burner, the more prominent the suction effect. A minor suction impact was found for the smaller nozzle and is therefore recommended for the measurement.

The second part of this work is focused on the investigation of Fe_2O_3 particle formation in turbulent flames. Therefore, the SpraySyn flame, a spray flame operated at atmospheric conditions, was studied. The flame was fed with an ethanol/iron nitrate spray solution surrounded by a

methane/oxygen pilot for igniting the spray. High-resolution LES of the SpraySyn flame were performed, modelling the evolution of the spray and the evaporation with a Lagrangian approach, the combustion with an FGM approach and the particle synthesis with a sectional model. In addition, the intermittency model was implemented to investigate the influence of subfilter effects on particle growth. The researchers of other institutes at the University of Duisburg-Essen conducted experiments to measure the particle size distribution with a PMS, while the velocities and the distribution of the spray droplets could be found in publications. A comparison of the velocities from experiments and simulations showed deviations near the burner, while satisfactory agreement of the entire flow field were achieved in the LES.

Further the focus of the study was on the determination of particle growth, and the simulation results were validated for the first time (to our knowledge) with online and in-situ measured size distributions of nanoparticles in a turbulent spray flame. The predicted and experimentally determined PSD showed good agreement, while the resulting particle diameters downstream of the flame indicated a more pronounced growth in the experiments. This deficit was attributed to various reasons to both, experiments and simulations. As demonstrated for laminar flames, the disturbance of the flame by the measuring probe is of crucial importance and also needs to be investigated in detail for turbulent flames. The effects of the implemented subfilter model were evaluated by comparing it to a simulation without a subfilter model. The model determined strongly intermittent areas, although in the present case, it had no significant influence on particle growth.

In the last part of this thesis, a hybrid FDF-LES method was developed to investigate the unresolved subfilter motion and its effects on the coagulation source term in the sectional particle model. The implementation was validated by recalculating Miller and Garrick's generic two-dimensional DNS simulation. Subsequently, the FDF-LES approach was applied to the SpraySyn flame. The results were compared with an LES in which the nanoparticle growth was described conventionally in an Eulerian framework. The first results were published at the European Combustion Meeting.

Chapter 8
Conclusion & outlook

This thesis evaluated the ability to predict particle synthesis in laminar and turbulent flames using numerical simulations. Subsidiary, the understanding of the individual particle synthesis approaches and the interpretation of experimental data was improved.

The objectives were successfully pursued, and the following conclusions and recommendations for the future can be drawn based on the presented results. First, it has been shown that computational fluid dynamics is able to describe the synthesis of nanoparticles in laminar and turbulent flames. The approach of conducting experiments and simulations simultaneously has proven to be beneficial. In this way, both can complement and validate each other. This is important because nanoparticle synthesis research is still in its early days compared to other research areas. The numerical models and measurement systems are not yet sophisticated enough to be trusted unconditionally. In particular, experiments and measurements on turbulent flames are still limited, which is confirmed by the fact that in this work, for a turbulent spray flame, a PSD from simulations was compared with a in situ measured PSD for the first time.

In both, the laminar and the turbulent flames studied in this work, Fe_2O_3 particles were the desired material. For both flames, the assumption of collision-controlled nucleation as a modelling approach has proven to be a good practice. The assumption is justified on the basis that the critical diameter of Fe_2O_3 particles is smaller than their monomer diameter [251], and any gas-phase reaction from which Fe_2O_3 emerges will lead to the nucleation of particles. For other material systems, however, a detailed nucleation model such as the classical nucleation theory and an additional term that accounts for condensation should still be considered. This was recently shown by Wollny et al. [250] for SiO_2. For the laminar simulations, sintering was considered based on the work of Wlokas et al. [247]. Even though the results were very good at that time, it is recommended to use the new data from Rosenberger et al. [194] in the future. Furthermore, the investigations in the laminar down-burning flame have shown that a transient particle phase develops in the reaction zone for the Fe_2O_3 material system. These particles have not yet been found in the final product, but in order to ensure product purity for industrial production, this phase should be further investigated and identified. From an experimental point of view, it will be essential to determine the composition and fractal dimension of the particles. The particle models could be adapted based on the outcome and include a second particle phase.

The particle dynamics after nucleation from the gas phase were described for the laminar flame using the bi-modal model and for the turbulent flame using the sectional model. For the laminar flames, the bi-modal model is a suitable choice. It emerged from preliminary tests that it provides improved results with slightly higher computational effort than the simple monodisperse model, whereas the computational effort is still much lower than the sectional model. For the time being, however, this only applies to the flame type investigated in this study, which can be characterised as laminar, stationary and with a broad flame front without steep gradients in the species and particle number concentrations. However, investigations with this model in other configurations in the scope of this work have shown deficits in turbulent simulations, where it tends to be unstable.

In turbulent flames, the application of the sectional model could reproduce the experimental results. This model could predict the temporal evolution of the PSD at each point of the simulation and the mixing of PSD's with different temporal histories. These are essential information, especially if material with high purity and narrow size distribution is desired as a product. Even though the sectional model is the most computationally expensive model applied in this work,

with the increasing computational resources in the future, it should become standard, especially for the simulation of turbulent flames.

When investigating the influence of subfilter effects in the turbulent spray flame, no significant influence on the unclosed term for coagulation was observed. The reason for this may be related to the structure of the flame. It is to be expected that a considerable influence occurs in the area of high gradients of the particle number concentration or in the area of high turbulence [29]. Both were only present to a small extent in this flame structure. In retrospect, a simpler flame setup would be advantageous for such an investigation in the future. The flame setup was complex and required much modelling and computing. Parameter studies in the context of subfilter modelling took a lot of work. Potential future studies should choose a more straightforward setup, focusing on a thin flame front and high turbulence, such as premixed or high-turbulence flames. Due to the high computational effort of the particle models itself, future projects may aim to make these models more efficient. For example, using artificial intelligence to calculate the computationally intensive coagulation core would be conceivable. Further, the development of a hybrid model that can switch between the computationally "cheap" monodisperse and the computationally "expensive" sectional model depending on the required accuracy should also be considered. In addition, flames with higher particle loading may be examined for the future development of particle models relevant to industrial applications.

For the investigation and interpretation of experimental laminar flame setups, it has become clear how valuable CFD simulations are for identifying fluid mechanical effects (buoyancy) and sampling effects (perturbations). For most laminar experiments, the assumption of a one-dimensional flow pattern is applied, and the experiments are recalculated using high-resolution 1D simulations with detailed chemistry. However, as observed in this work, the flow perturbations lead to a deviation from this assumption. It further highlights the importance of 2D or 3D simulations for these experiments. The fluid mechanical effects should be investigated in advance and eliminated on a case-by-case basis. But the observed effects may not always be considered negative, as shown by the down-firing flame, which enables the realisation of different temperature-time profiles. The effects of the sampling nozzle remain crucial for the interpretation of measurements. The approach of using 2D simulations to provide the necessary data to correct them has proven to be very effective. Still, it is worth considering these effects in 1D simulations for future work. Even if the 3D suction effect cannot be fully accounted for, cooling due to flow acceleration might be implemented in the future as a function of nozzle diameter.

Appendix A

Influence of the sampling probe on flame temperature, species, residence times and on the interpretation of ion signals of methane/oxygen flames in molecular beam mass spectrometry measurements

A.1 Simulated residence times and distances of gas samples during flame sampling

Table A.1: Residence time τ and distances of gas samples starting at two radial points r_1 (=0) and r_2 in Flame A (pressure at the orifice $p = 85$ mbar)

HAB / mm	r / mm	Residence time τ_{1A} / s	Residence time τ_{2A} / s	Ratio residence time τ_{2A}/τ_{1A}	Ratio residence time τ_{1mm}/τ_{25mm}	Distance z_{1A} / mm	Distance z_{2A} / mm	Distance ratio r_{2A}/r_{1A}
1	0	$1.08\cdot10^{-3}$	-	-	1.94	1	-	-
1	0.89	-	$2.05\cdot10^{-3}$	1.9	-		1.3709	1.3709
2.25	0	$2.1\cdot10^{-3}$	-	-	1.74	2.25	-	-
2.25	0.81		$2.41\cdot10^{-3}$	1.15	-		2.40387	1.0684
3.25	0	$2.88\cdot10^{-3}$			1.67	3.25	-	-
3.25	0.79		$3.11\cdot10^{-3}$	1.08	-		3.35653	1.03
25	0	$2.985\cdot10^{-2}$			1	25	-	-
25	0.79		$3.048\cdot10^{-2}$	1.02	-	-	25.22987	1.01

Table A.2: Residence time τ and distances of gas samples starting at two radial points r_1 (=0) and r_2 in Flame A (pressure at the orifice $p = 85$ mbar)

HAB / mm	r / mm	Residence time τ_{1B} / s	Residence time τ_{2B} / s	Ratio residence time τ_{2B}/τ_{1B}	Ratio residence time τ_{1mm}/τ_{25mm}	Distance z_{1B} / mm	Distance z_{2B} / mm	Distance ratio r_{2B}/r_{1B}
1	0	$4.4109\cdot10^{-4}$	-	-	3.04	1	-	-
1	5.40	-	$7.6\cdot10^{-3}$	17.23	-	-	6.929	6.929
2.25	0	$1.51\cdot10^{-3}$	-	-	1.95	2.25	-	-
2.25	5.21	-	$7.81\cdot10^{-3}$	5.17	-	-	6.641	2.95
3.25	0	$2.09\cdot10^{-3}$	-	-	1.54	3.25	-	-
3.25	5.13	-	$7.99\cdot10^{-3}$	3.83	-	-	7.008	2.16
25	0	$2.717\cdot10^{-2}$	-	-	1	25	-	-
25	5.10	-	$3.35\cdot10^{-2}$	1.13	-	-	29.19	1.17

Appendix B

Hybrid LES/Lagrange-FDF approach for the sub-grid modelling of nanoparticle coagulation in a planar jet

The developed FDF method was first applied to Miller and Garrick's [141] generic DNS test case to validate the LES/FDF implementation. This planar jet flows into the domain loaded with monodisperse particles, which grow by coagulation only. The jet was resolved in two dimensions to allow for a DNS-like grid resolution. Hence, fully developed turbulence may not be expected. Nevertheless, the particle diffusion and the flow motion can be correlated with the coagulation process. Due to the simple setup and the isolated growth only by coagulation, this jet is well suited as a benchmark case.

B.1 Flow configuration and parameters

Miller and Garrick studied the coagulation of nanoparticles in DNS of a planar jet with a width of $D = 1\,\mathrm{mm}$ and an isothermal ($T = 300\,\mathrm{K}$), isobaric, and non-reactive fluid. The proposed geometry was two-dimensional in the x-y plane to keep the computational effort within limits, whereas in this work, an LES of the jet is performed, and the domain is extended to the third dimension to x-y-z with periodic boundary conditions in the z-direction, which are a common choice in the study of planar jets. The dimensions of the domain are shown in Fig. B.1. The

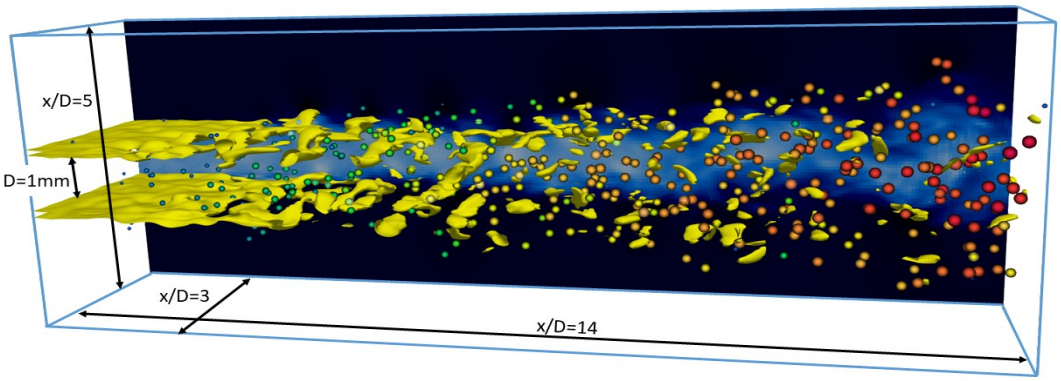

Figure B.1: Configuration of the planar jet

initial velocity for the jet is set to $U_{\mathrm{Jet}} = 95m$, and for the Co-flow, $U_{\mathrm{Cf}} = U_{\mathrm{Jet}} \cdot 0.55$. The Reynolds number of Re=4000 is obtained based on the jet velocity, which may be considered lower than typical LES studies, which commonly use Reynolds numbers up to 10000. Nevertheless, to support the evolution of the large-scale vortices, random perturbations of 3% of the jet velocity in the cross-stream direction were abandoned. Particles are inserted at the jet inlet $x/D = 0$ with a diameter of $D_p = 1\,\mathrm{nm}$ and a volume concentration of $V = 10^{-7}\,\mathrm{m}^3/\mathrm{m}^3$, corresponding to $N = 1.78 \cdot 10^{20}\#/\mathrm{m}^3$. A sectional method is applied to resolve the particle growth, and following Miller and Garrick, the PSD is divided into 10 sections with the smallest volume being $v_1 = 0.52\mathrm{nm}^3$ and an equidistant spacing of $v_k = v_{k-1} * 2$. The Schmidt number of the individual sections ranges from 5.47 - to 342, so only the free molecular coagulation kernel Eq. (2.56) was

used in this work. The density of the particles is not mentioned in the work of Miller and Garrick but is essential for calculating the coagulation rate. In order to determine the density, test runs with varying densities were carried out to match the average diameter of the DNS at $x/D = 2$, resulting in a theoretical density of $\rho_p = 25\,\mathrm{kg/m^3}$. The subgrid-stresses where obtained using the Sigma model by Nicoud et al. [150] with a model constant of $C_m = 1.5$ and a turbulent Schmidt number of $Sc_\mathrm{t} = 0.7$.

B.2 Results

The mean axial bulk velocity U across the jet radius is shown in Figure 2 for three different axial positions of the jet. Downstream, the velocity indicates an expansion of the jet and, at the same time, a reduction of the bulk velocity. Compared to the DNS data from Garrick and Miller, the agreement is very good for the axial positions $x/D = 2$ and 6. However, at the axial position $x/D = 10$ the jet in the LES simulation shows more widening towards the shear layer. The increased dimensionality of the LES justifies the more significant widening of the jet as energy is transferred to all three dimensions of the domain. Still, the DNS and LES/FDF velocities are in good agreement and allow further comparison of the particle dynamics. The particle diameter of

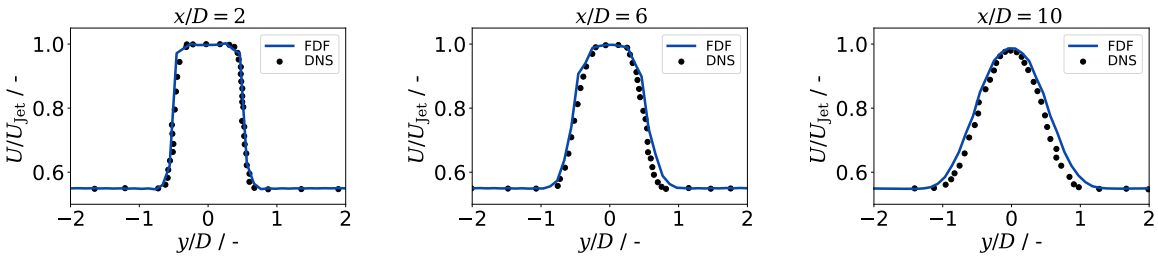

Figure B.2: Radial mean profiles for velocity, at different heights above the inlet (x/D=2,6,10). Comparison between DNS (symbols [141]) and LES/FDF (solid lines).

an averaged volume across the jet radius is shown in Fig. B.2 for three different axial positions of the jet. In general, due to coagulation, a growth of the particles along the jet can be observed. Further, the particle jet widens as it is transported with the fluid jet. Particles grow slightly larger at all three axial positions in the shear layer. While the particle concentration in this region is lower than in the bulk flow due to dilution with the particle-free co-flow, the growth may be attributed to the longer residence time. The jet decelerates in the shear layer due to a momentum loss towards the co-flow, increasing the residence time. At positions $x/D = 6$ and 10, there is a particle diameter peak, while at positions $x/D = 2$, the diameter remains constant. While the particle concentration towards the shear layer decreases due to a dilution with the co-flow, the particle concentration in the centre is relatively high, increasing the collision rate and leading to faster growth. At the position x/d=2, the dilution is moderately, and the bulk velocity field is located around the centre, as shown in Fig. B.2. Therefore, the diameter remains constant in the centre. In comparison to the DNS, both simulations show similar particles' growth, and the diameter at the centre of the jet coincides. Towards the shear layer, the LES/FDF shows a broader profile, and particles are transported further from the jet centre, which can be attributed to the underlying velocity field, as it also shows faster widening in the LES/FDF compared to the DNS.

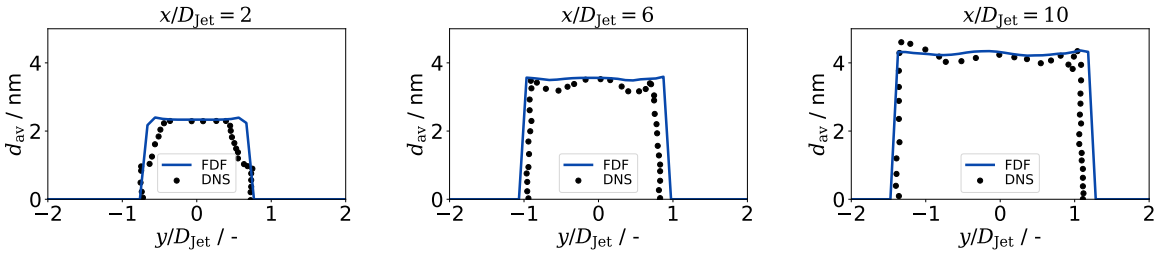

Figure B.3: Particle diameter of averaged volume at different heights above the inlet ($x/D = 2, 6, 10$). Comparison between DNS (symbols [141]) and LES/FDF (solid lines).

B.3 Conclusion

A planar particle-laden turbulent jet was simulated with the hybrid LES/FDF method, and the results are compared against DNS data by Miller and Garrick. The simulated flow agrees with the reference DNS data and exhibits a plausible flow pattern. Furthermore, the DNS and LES/FDF show good agreement in the simulation of particle growth and can reproduce the essential characteristics of the particle-size profile. The implementation of the hybrid LES/FDF is thus sufficiently validated and can be further applied to the investigation of sub-grid effects on the coagulation rate.

Appendix C
Additional Publications

This chapter provides an overview of author contributions to other published work. Presented are the paper abstracts of publications which are relevant to the topic of the present work together with a description about which parts the author of this thesis contributed.

C.1 Inline coating of silicon nanoparticles in a plasma reactor: Reactor design, simulation and experiment

Adrian Münzer, Johannes Sellmann, Paolo Fortugno, Andreas Kempf, Christof Schulz and Hartmut Wiggers

This paper was published in Materials Today: Proceedings 4, 118–127 (2017), [148] and the abstract is reprinted with permission from Elsevier.
The author J. Sellmann contributed CFD-simulation of the reactor system and developed the post-processing system of the plasma reactor, support, discussion, corrections and proof-readings.

Abstract

Gas-phase synthesis of nanoparticles (NPs) in hot plasmas is a promising approach to produce pure, highly specific, and complex nanomaterials at large production rates. Post-processing of the material by particle coating, embedding, or surface functionalization is often required to adjust the materials' properties with respect to their utilization in functional structures. Due to the high surface-to-volume ratio, the nanoparticles' surface properties strongly influence the processing and thus their applicability. We report on a scalable and continuous gas-phase synthesis process of silicon nanoparticles by a high-temperature single-step plasma process with subsequent inline coating. Our process requires a two-stage supply of process gases: First, silicon nanoparticles (Si-NPs) are formed from the gaseous precursor monosilane (SiH_4) after its decomposition in the plasma zone. Secondly, the coating agent ethylene (C_2H_4) is mixed with the hot, particle-laden gas flow downstream of the plasma zone via a specifically-designed coating nozzle. To facilitate a homogeneous intermixing of C_2H_4 and the nanoparticle-laden gas stream, fluid dynamics simulations were performed to design and optimize the geometry of the coating nozzle. The process conditions can be varied to tune the decomposition process of gaseous C_2H_4 in respect to coating the Si-NP surface. As a result, we are able to tune the composition of the nanoparticles. Product characterization by X-ray diffraction, Raman, FTIR and X-ray photoelectron spectroscopy revealed that either SiC, or silicon with a carbon-like or a polyethylene-like shell is produced respectively, with increasing distance of the coating nozzle from the plasma. For all process conditions, spherical, coated particles with a highly-crystalline silicon core were observed as indicated by TEM measurements.

C.2 The role of phase transition by nucleation, condensation, and evaporation for the synthesis of silicon nanoparticles in a microwave plasma reactor — Simulation and experiment

Patrick Wollny, Jan Menser, Linus Engelmann, Johannes Sellmann, Christof Schulz, Hartmut Wiggers, Andreas Kempf and Irenäus Wlokas

The paper was published in 'Chemical Engineering Journal: Volume 453, 139695 (2023), [250], and the abstract is reprinted with permission from Elsevier.
The author J. Sellmann contributed the basic simulation setup, first approximations of the flow field, support and discussions.

Abstract

A novel particle model is presented to simulate the synthesis of silicon nanoparticles from monosilane in a laboratory sized microwave plasma reactor. The simulations contribute essentially to the understanding of the particle formation process and the spatial and size distribution of particles observed in the experiment. The model approach features phase transition and explains the observed, tube-shaped particle formation zones by a competing nucleation, condensation, and evaporation process coupled with complex transport phenomena. The simulation results are in excellent agreement with experimental data from Rayleigh scattering and line-ofsight optical absorption with onion-peeling reconstruction (LOSA) measurements of the particle front, as well as with multiline SiO laser-induced fluorescence (LIF) temperature measurements. Particle size distributions determined from transmission electron microscopy (TEM) on thermophoretically sampled particles are in good agreement with the simulation results. Average diameters of 25.8 nm calculated in the simulation compare well to 27.6 nm measured in the experiment. It was found that thermophoresis has a crucial impact on particle trajectories, as it extends the particle residence time within the reactor by about 20% and provides the determining force for particles to escape zones of high temperature in which particles evaporate otherwise. The sectional model features two-way coupled phase transition formulations for the condensing matter, which is formed through the decomposition of monosilane diluted in argon/hydrogen mixtures. The process is investigated by the combination of two simulations with different grid resolutions, which show differences for the high Schmidt number particle phase only. The simulations feature a global monosilane decomposition reaction, while the microwave plasma source is simplified by a local heat source.

C.3 Determining the sintering kinetics of Fe and FexOy-Nanoparticles in a well-defined model flow reactor

Thore Rosenberger, Ivan Skenderović, Johannes Sellmann, Patrick Wollny, Alexander Levish, Irenäus Wlokas, Andreas Kempf, Markus Winterer and Einar Kruis

The paper was published in Aerosol Science and Technology, 1-18, (2022), [194], and the abstract and the publication is reprinted with permission from Taylor & Francis.
The author J. Sellmann contributed simulations, which were used during the design phase of the reactor for its optimization, simulations for the calculation of the presented sintering mechanics, support, discussion, corrections and proof-readings.

Abstract

A model flow reactor provides a narrow particle temperature-residence time distribution with well-defined conditions and is mandatory to measure changes of the particle structure precisely. The experimental data of iron and iron oxide agglomerates are used to determine the sintering kinetics considering the temperature-time history of the particles. Thousand particle trajectories are tracked in a validated CFD model at three different furnace temperatures each. Strongly agglomerated particles with a small primary particle size ($\approx$ 4 nm) are synthesized by spark discharge and are size-selected (25–250 nm) before sintering. The structure development is measured simultaneously with different online instrumentations and the structure calculated by means of structure models. A simple sintering model, based on the reduction of surface energy, is numerically quantified with the experimental results. The surface of the particles is strongly dependent on the primary particle size and the agglomerate structure. The chemical phase is analyzed using the offline techniques XANES, XRD, and EELS. It is observed that the addition of hydrogen led to a reduction of iron oxide to iron nanoparticles and to changes of the sintering kinetics. The sintering exponent $m = 1$ was found to be optimal. For Fe, an activation energy E_a of 59.15 kJ/mol and a pre-exponential factor A_s of 1.57 10^4 s/m were found, for Fe_3O_4 an activation energy E_a of 55.22 kJ/mol and a pre-exponential factor A_s of 2.54 10^4 s/m.

C.4 Direct numerical simulations of nanoparticle formation in premixed and non-premixed flame–vortex interactions

Luis Cifuentes, Johannes Sellmann, Irenäus Wlokas, Andreas Kempf

The paper was published in Physics of Fluids, 32, 093605 (2022), [29], and the abstract and the publication is reprinted with permission from AIP Publishing.
The author J. Sellmann contributed the development of the simulation setup, 1D simulations to validate the simulation, support, discussion, corrections and proofreading.

Abstract

Direct numerical simulations (DNSs) of nanoparticle formation in reactive flows are challenging, and only greatly simplified DNS test-cases are possible, which help clarify the turbulence–particle–dynamics interaction and guide the necessary modeling efforts. As a basis for such studies, a new DNS database is introduced, which resolves the smallest relevant scales of the nanoparticle concentration field to obtain insights into the statistics of nanoparticle formation in reactive flows. Formation and evolution of iron oxide nanoparticles in premixed and nonpremixed flames wrapped-up by a vortex have been investigated using the sectional model and direct chemistry. The DNSs capture the "engulfing" and local dilution of the particle fields. Different zones of high particle number concentration have been found in every flame, and it was shown that the thickness of these zones decreases with increasing Schmidt number, which confirms that in simulations of nanoparticleforming turbulent reacting flows, the grid resolution has to be very fine to resolve the characteristic scale for high sections. The contributions to the change in particle concentration due to diffusion, coagulation, and nucleation have been analyzed in detail, and dominant contributions across the particle number concentration layers and across the flames have been identified. This analysis has also been carried out in terms of flat, concave, and convex iso-surface geometries, induced by the flame–vortex interaction and characterized by the curvature of the particle number concentration fields and also by the flame curvature. The results demonstrate that the flame curvature effects cannot be ignored in modeling strategies. The probability density functions for the particle number concentrations have been analyzed and quantified in terms of Shannon information entropy, which illustrates the effect of fast diffusion (and entropy production) of the smaller particles and slow diffusion (and entropy production) of the largest particles with high Schmidt numbers. In addition, the unclosed filtered or averaged agglomeration term was evaluated as a basis for future modeling efforts, showing that agglomeration rates will be underestimated by orders of magnitude unless suitable models are developed.

C.5 Insights into the Mechanism of Combustion Synthesis of Iron Oxide Nanoparticles Gained by Laser Diagnostics, Mass Spectrometry, and Numerical Simulations: A Mini-Review

Igor Rahinov, Johannes Sellmann, Matthieu Lalanne, Monika Nanjaiah, Thomas Dreier, Sergey Cheskis, and Irenäus Wlokas

The paper was published in Energy & Fluids, 35.1, 137-16032 (2020), [179], and the abstract and the publication is reprinted with permission from ACS Publications.
The author J. Sellmann contributed to this review a new analysis of the data from the publication 'Detailed simulation of iron oxide nanoparticle forming flames: Buoyancy and probe effects', as well as discussions and support.

Abstract

To fully master a scaled-up combustion synthesis of nanoparticles toward a wide library of materials with tailored functionalities, a detailed understanding of the underlying kinetic mechanism is required. In this respect, flame synthesis of iron oxide nanoparticles is a model case, being one of the better understood systems and guiding the way how other material synthesis systems could be advanced. In this mini-review, we highlight, on the example of an iron oxide system, an approach combining laser spectroscopy and mass spectrometry with detailed simulations. The experiments deliver information on time-temperature history and concentration field data for gas-phase species and condensable matter under well-defined conditions. The simulations, which can be considered as *in silico* experiments, combining detailed kinetic modeling with computational fluid dynamics, serve both for mechanism validation via comparison to experimental observables as well as for shedding light on quantities inaccessible by experiments. This approach shed light on precursor decomposition, initial stages of iron oxide particle formation, and precursor role in flame inhibition and provided insights into the effect of temperature-residence time history on nanoparticle formation, properties, and flame structure.

C.6 Flame surface density based modelling of head-on quenching of turbulent premixed flames

Johannes Sellmann, Jiawei Lai, Andreas Kempf, Nilanjan Chakraborty

The paper was published in Proceedings of the Combustion Institute, 36, 1817-1825 (2017), [205], and the abstract and the publication is reprinted with permission from Elsevier.
The author J. Sellmann developed the presented FSD models and wrote the original manuscript.

Abstract

The near-wall behaviour of the generalised flame surface density (FSD) transport in the context of Reynolds Averaged Navier–Stokes (RANS) simulations has been analysed for different values of global Lewis number using three-dimensional Direct Numerical Simulation (DNS) data of head-on quenching of statistically planar turbulent premixed flames by an isothermal inert wall. It has been found that the statistical behaviour of the FSD based reaction rate closure and the terms of the FSD transport equation are significantly affected by the presence of the wall and by the global Lewis number. The near-wall predictions of the standard FSD based mean reaction rate closure and existing sub-models for the unclosed terms of the FSD transport equation have been found to be inadequate based on a-priori DNS assessment, and modifications to these models have been suggested so that the predictions of modified models for reaction rate closure and FSD transport remain satisfactory, both close to the wall and away from it over a wide range of global Lewis number.

Bibliography

[1] A. Abdelsamie, F. E. Kruis, H. Wiggers, and D. Thévenin. Nanoparticle formation and behavior in turbulent spray flames investigated by DNS. *Flow, Turbulence and Combustion*, 105(2):497–516, 2020. doi: 10.1007/s10494-020-00144-y.

[2] A. B. Alquaity, B. Chen, J. Han, H. Selim, M. Belhi, Y. Karakaya, T. Kasper, S. M. Sarathy, F. Bisetti, and A. Farooq. New insights into methane-oxygen ion chemistry. *Proceedings of the Combustion Institute*, 36(1):1213–1221, 2017. doi: 10.1016/j.proci.2016.05.053.

[3] S. Angel, J. Neises, M. Dreyer, K. F. Ortega, M. Behrens, Y. Wang, H. Arandiyan, C. Schulz, and H. Wiggers. Spray-flame synthesis of La(Fe, CO)O_3 nano-perovskites from metal nitrates. *AIChE Journal*, 66(1), 2019. doi: 10.1002/aic.16748.

[4] Ansys Chemkin-Pro(19.2). Reaction design, San Diego, 2011.

[5] N. Ashgriz. *Handbook of Atomization and Sprays*. Springer US, 2011. doi: 10.1007/978-1-4419-7264-4.

[6] N. Bahlawane, U. Struckmeier, T. S. Kasper, and P. Oßwald. Noncatalytic thermocouple coatings produced with chemical vapor deposition for flame temperature measurements. *Review of Scientific Instruments*, 78(1):013905, 2007. doi: 10.1063/1.2426876.

[7] C. Baumgarten. *Mixture formation in internal combustion engines*. Springer Science & Business Media, 2006. doi: 10.1007/3-540-30836-9.

[8] M. Bieber, R. Tischendorf, H.-J. Schmid, M. A. Reddemann, and R. Kneer. *Influence of precursor concentration on spray and particle formation in flame spray pyrolysis*. Universitätsbibliothek der RWTH Aachen, 2019.

[9] T. Bierkandt, T. Kasper, E. Akyildiz, A. Lucassen, P. Oßwald, M. Köhler, and P. Hemberger. Flame structure of a low-pressure laminar premixed and lightly sooting acetylene flame and the effect of ethanol addition. *Proceedings of the Combustion Institute*, 35(1): 803–811, 2015. doi: 10.1016/j.proci.2014.05.094.

[10] T. Bierkandt, P. Hemberger, P. Oßwald, M. Köhler, and T. Kasper. Insights in m-xylene decomposition under fuel-rich conditions by imaging photoelectron photoion coincidence spectroscopy. *Proceedings of the Combustion Institute*, 36(1):1223–1232, 2017. doi: 10.1016/j.proci.2016.06.143.

[11] R. W. Bilger, S. Stårner, and R. Kee. On reduced mechanisms for methane-air combustion in nonpremixed flames. *Combustion and Flame*, 80(2):135–149, 1990. doi: 10.1016/0010-2180(90)90122-8.

[12] J. C. Biordi, C. P. Lazzara, and J. F. Papp. Molecular beam mass spectrometry applied to determining the kinetics of reactions in flames. I. empirical characterization of flame perturbation by molecular beam sampling probes. *Combustion and Flame*, 23(1):73–82, 1974. doi: 10.1016/s0010-2180(74)80028-3.

[13] P. Biswas and C.-Y. Wu. Nanoparticles and the environment. *Journal of the Air & Waste Management Association*, 55(6):708–746, 2005. doi: 10.1080/10473289.2005.10464656.

[14] P. Biswas, C. Y. Wu, M. R. Zachariah, and B. McMillin. Characterization of iron oxide-silica nanocomposites in flames: Part II. comparison of discrete-sectional model predictions to experimental data. *Journal of Materials Research*, 12(3):714–723, 1997. doi: 10.1557/jmr.1997.0106.

[15] M. Boger, D. Veynante, H. Boughanem, and A. Trouvé. Direct numerical simulation analysis of flame surface density concept for large eddy simulation of turbulent premixed combustion. *Symposium (International) on Combustion*, 27(1):917–925, 1998. doi: 10.1016/s0082-0784(98)80489-x.

[16] S. Bonacchi, D. Genovese, R. Juris, M. Montalti, L. Prodi, E. Rampazzo, and N. Zaccheroni. Luminescent silica nanoparticles: Extending the frontiers of brightness. *Angewandte Chemie International Edition*, 50(18):4056–4066, 2011. doi: 10.1002/anie.201004996.

[17] J. V. Boussinesq. Essai sur la théorie des eaux courantes. *Mémoires présentés par divers savant à l'Académie des Sciences de l'Institut de France*, 23:1 – 680, 1877.

[18] C. E. Brennen. *Fundamentals of Multiphase Flow*. Cambridge University Press, 2005. doi: 10.1017/CBO9780511807169.

[19] B. Buesser and S. E. Pratsinis. Design of gas-phase synthesis of core-shell particles by computational fluid-aerosol dynamics. *AIChE Journal*, 57(11):3132–3142, 2011. doi: 10.1002/aic.12512.

[20] T. Butler and P. O'Rourke. A numerical method for two dimensional unsteady reacting flows. *Symposium (International) on Combustion*, 16(1):1503–1515, 1977. doi: 10.1016/S0082-0784(77)80432-3.

[21] J. Camacho, C. Liu, C. Gu, H. Lin, Z. Huang, Q. Tang, X. You, C. Saggese, Y. Li, H. Jung, L. Deng, I. Wlokas, and H. Wang. Mobility size and mass of nascent soot particles in a benchmark premixed ethylene flame. *Combustion and Flame*, 162(10):3810–3822, 2015. doi: 10.1016/j.combustflame.2015.07.018.

[22] R. K. Chakrabarty, I. V. Novosselov, N. D. Beres, H. Moosmüller, C. M. Sorensen, and C. B. Stipe. Trapping and aerogelation of nanoparticles in negative gravity hydrocarbon flames. *Applied Physics Letters*, 104(24):243103, 2014. doi: 10.1063/1.4884057.

[23] N. Chakraborty and S. Cant. Effects of lewis number on flame surface density transport in turbulent premixed combustion. *Combustion and Flame*, 158(9):1768–1787, 2011. doi: 10.1016/j.combustflame.2011.01.011.

[24] F. Charlette, A. Trouvé, M. Boger, and D. Veynante. A flame surface density model for large eddy simulations of turbulent premixed flames. In *Proceedings of the Joint Meeting of the British, German and French Sections of the Combustion Institute*. The Combustion Institute Pittsburgh, PA, 1999.

[25] F. Charlette, C. Meneveau, and D. Veynante. A power-law flame wrinkling model for LES of premixed turbulent combustion part I: non-dynamic formulation and initial tests. *Combustion and Flame*, 131(1-2):159–180, 2002. doi: 10.1016/s0010-2180(02)00400-5.

[26] F. Charlette, C. Meneveau, and D. Veynante. A power-law flame wrinkling model for LES of premixed turbulent combustion part II: dynamic formulation. *Combustion and Flame*, 131(1-2):181–197, 2002. doi: 10.1016/s0010-2180(02)00401-7.

[27] D.-H. Chen and X.-R. He. Synthesis of nickel ferrite nanoparticles by sol-gel method. *Materials Research Bulletin*, 36(7–8):1369 – 1377, 2001. doi: 10.1016/s0025-5408(01)00620-1.

[28] M. Chrigui, J. Gounder, A. Sadiki, A. R. Masri, and J. Janicka. Partially premixed reacting acetone spray using LES and FGM tabulated chemistry. *Combustion and Flame*, 159(8): 2718–2741, 2012. doi: 10.1016/j.combustflame.2012.03.009.

[29] L. Cifuentes, J. Sellmann, I. Wlokas, and A. Kempf. Direct numerical simulations of nanoparticle formation in premixed and non-premixed flame–vortex interactions. *Physics of Fluids*, 32(9):093605, 2020. doi: 10.1063/5.0020979.

[30] R. A. Clark, J. H. Ferziger, and W. C. Reynolds. Evaluation of subgrid-scale models using an accurately simulated turbulent flow. *Journal of Fluid Mechanics*, 91(01):1, 1979. doi: 10.1017/s002211207900001x.

[31] O. Colin, F. Ducros, D. Veynante, and T. Poinsot. A thickened flame model for large eddy simulations of turbulent premixed combustion. *Physics of Fluids*, 12(7):1843–1863, 2000. doi: 10.1063/1.870436.

[32] P. J. Colucci, F. A. Jaberi, P. Givi, and S. B. Pope. Filtered density function for large eddy simulation of turbulent reacting flows. *Physics of Fluids*, 10(2):499–515, 1998. doi: 10.1063/1.869537.

[33] J. Crank and P. Nicolson. A practical method for numerical evaluation of solutions of partial differential equations of the heat-conduction type. volume 43, pages 50–67. Cambridge University Press (CUP), 1947. doi: 10.1017/s0305004100023197.

[34] C. T. Crowe, J. D. Schwarzkopf, M. Sommerfeld, and Y. Tsuji. *Multiphase Flows with Droplets and Particles*. CRC Press, 2011. doi: 10.1201/b11103.

[35] R. L. Curl. Dispersed phase mixing: I. theory and effects in simple reactors. *AIChE Journal*, 9(2):175–181, mar 1963. doi: 10.1002/aic.690090207.

[36] Y. Dahman, N. Ignatius, A. Poblete, A. Krunic, P. Ma, N. Gosalia, and T. Ali. Nanotechnology: application and potentials for heterogeneous catalysis. In *Nanotechnology in Paper and Wood Engineering*, pages 231–263. Elsevier, 2022. doi: 10.1016/b978-0-323-85835-9.00013-1.

[37] C. J. Dasch and D. M. Heffelfinger. Planar imaging of soot formation in turbulent ethylene diffusion flames: Fluctuations and integral scales. *Combustion and Flame*, 85(3-4):389–402, jun 1991. doi: 10.1016/0010-2180(91)90142-x.

[38] S. De and S. H. Kim. Large eddy simulation of dilute reacting sprays: Droplet evaporation and scalar mixing. *Combustion and Flame*, 160(10):2048 – 2066, 2013. doi: 10.1016/j.combustflame.2013.04.024.

[39] L. Deng. *Numerical investigation of uncertainties in experiments for flame structure analysis and particle synthesis*. PhD thesis, University of Duisburg-Essen, Apr 2017.

[40] L. Deng, A. Kempf, O. Hasemann, O. P. Korobeinichev, and I. Wlokas. Investigation of the sampling nozzle effect on laminar flat flames. *Combustion and Flame*, 162(5):1737–1747, 2015. doi: 10.1016/j.combustflame.2014.11.035.

[41] C. Dopazo. Functional formulation of nonisothermal turbulent reactive flows. *Physics of Fluids*, 17(11):1968, 1974. doi: 10.1063/1.1694652.

[42] T. Dreier and C. Schulz. Laser-based diagnostics in the gas-phase synthesis of inorganic nanoparticles. *Powder Technology*, 287:226–238, 2016. doi: 10.1016/j.powtec.2015.10.015.

[43] A. C. Eckbreth. *Laser diagnostics for combustion temperature and species*, volume 3. CRC press, 1996. doi: 10.1201/9781003077251.

[44] F. Egolfopoulos, N. Hansen, Y. Ju, K. Kohse-Höinghaus, C. Law, and F. Qi. Advances and challenges in laminar flame experiments and implications for combustion chemistry. *Progress in Energy and Combustion Science*, 43:36–67, 2014. doi: 10.1016/j.pecs.2014.04.004.

[45] A. Faccinetto, B. Tribalet, H. Orthner, H. Wiggers, and C. Schulz. Investigation of iron oxide nanoparticle growth with respect to flame equivalence ratio. In *European Combustion Meeting. Cardi*, 2011.

[46] O. M. Feroughi, L. Deng, S. Kluge, T. Dreier, H. Wiggers, I. Wlokas, and C. Schulz. Experimental and numerical study of a HMDSO-seeded premixed laminar low-pressure flame for SiO_2 nanoparticle synthesis. *Proceedings of the Combustion Institute*, 36(1):1045–1053, 2017. doi: 10.1016/j.proci.2016.07.131.

[47] A. Fomin, M. Poliak, I. Rahinov, V. Tsionsky, and S. Cheskis. Combined particle mass spectrometer – quartz crystal microbalance apparatus for in situ nanoparticle monitoring during flame assisted synthesis. *Combustion and Flame*, 160(10):2131–2140, 2013. doi: 10.1016/j.combustflame.2013.04.011.

[48] R. O. Fox. *Computational Models for Turbulent Reacting Flows*. Cambridge Series in Chemical Engineering. Cambridge University Press, 2003. doi: 10.1017/CBO9780511610103.

[49] I. Freestone, N. Meeks, M. Sax, and C. Higgitt. The lycurgus cup-a roman nanotechnology. *Gold Bulletin*, 40:270–277, 12 2007. doi: 10.1007/BF03215599.

[50] M. Frenklach and A. Kazakov. http://www.me.berkeley.edu/drm/, 2000.

[51] S. K. Friedlander. *Smoke, Dust and Haze. Fundamentals of Aerosol Dynamics*. Oxford University Press, Inc., 2000.

[52] N. A. Fuchs. *The mechanics of aerosols*. Pagamon, New York, 1964.

[53] F. Gao and E. E. O'Brien. A large-eddy simulation scheme for turbulent reacting flows. *Physics of Fluids A: Fluid Dynamics*, 5(6):1282–1284, 1993. doi: 10.1063/1.858617.

[54] S. Garrick, K. Lehtinen, and M. Zachariah. Nanoparticle coagulation via a navier–stokes/nodal methodology: Evolution of the particle field. *Journal of Aerosol Science*, 37(5):555–576, 2006. doi: 10.1016/j.jaerosci.2005.04.010.

[55] F. Gelbard, Y. Tambour, and J. H. Seinfeld. Sectional representations for simulating aerosol dynamics. *Journal of Colloid and Interface Science*, 76(2):541–556, aug 1980. doi: 10.1016/0021-9797(80)90394-x.

[56] M. Germano, U. Piomelli, P. Moin, and W. H. Cabot. A dynamic subgrid-scale eddy viscosity model. *Physics of Fluids A: Fluid Dynamics*, 3(7):1760–1765, jul 1991. doi: 10.1063/1.857955.

[57] O. Gicquel, N. Darabiha, and D. Thévenin. Liminar premixed hydrogen/air counterflow flame simulations using flame prolongation of ILDM with differential diffusion. *Proceedings of the Combustion Institute*, 28(2):1901–1908, 2000. doi: 10.1016/s0082-0784(00)80594-9.

[58] A. Giesen, J. Herzler, and P. Roth. Kinetics of the fe-atom condensation based on fe-concentration measurements. *The Journal of Physical Chemistry A*, 107(26):5202–5207, jun 2003. doi: 10.1021/jp022392x.

[59] P. Givi. Model-free simulations of turbulent reactive flows. *Progress in Energy and Combustion Science*, 15(1):1–107, 1989. doi: 10.1016/0360-1285(89)90006-3.

[60] M. Gonchikzhapov and T. Kasper. Decomposition reactions of $Fe(CO)_5$, $Fe(C_5H_5)_2$, and TTIP as precursors for the spray-flame synthesis of nanoparticles in partial spray evaporation at low temperatures. *Industrial & Engineering Chemistry Research*, 59(18):8551–8561, 2020. doi: 10.1021/acs.iecr.9b06667.

[61] M. Goodson and M. Kraft. An efficient stochastic algorithm for simulating nano-particle dynamics. *Journal of Computational Physics*, 183(1):210–232, 2002. doi: 10.1006/jcph.2002.7192.

[62] D. G. Goodwin. Cantera. http://code.google.com/p/cantera, 2009.

[63] A. J. Gröhn, S. E. Pratsinis, and K. Wegner. Fluid-particle dynamics during combustion spray aerosol synthesis of ZrO_2. *Chemical Engineering Journal*, 191:491–502, may 2012. doi: 10.1016/j.cej.2012.02.093.

[64] A. J. Gröhn, S. E. Pratsinis, A. Sánchez-Ferrer, R. Mezzenga, and K. Wegner. Scale-up of nanoparticle synthesis by flame spray pyrolysis: The high-temperature particle residence time. *Industrial &amp Engineering Chemistry Research*, 53(26):10734–10742, 2014. doi: 10.1021/ie501709s.

[65] P. Gruhlke, H. Janbazi, I. Wlokas, C. Beck, and A. M. Kempf. Investigation of a high Karlovitz, high pressure premixed jet flame with heat losses by LES. *Combustion Science and Technology*, 192(11):2138–2170, 2020. doi: 10.1080/00102202.2020.1781101.

[66] S. R. Gunakala, V. M. Job, S. Sakhamuri, P. Murthy, and B. Chowdary. Numerical study of blood perfusion and nanoparticle transport in prostate and muscle tumours during intravenous magnetic hyperthermia. *Alexandria Engineering Journal*, 60(1):859–876, 2021. doi: 10.1016/j.aej.2020.10.015.

[67] V. Gururajan, F. N. Egolfopoulos, and K. Kohse-Höinghaus. Direct numerical simulations of probe effects in low-pressure flame sampling. *Proceedings of the Combustion Institute*, 35(1):821–829, 2015. doi: 10.1016/j.proci.2014.06.046.

[68] E. Gutheil and W. A. Sirignano. Counterflow spray combustion modeling with detailed transport and detailed chemistry. *Combustion and Flame*, 113(1–2):92 – 105, 1998. doi: 10.1016/s0010-2180(97)00192-2.

[69] N. Hansen, R. S. Tranter, K. Moshammer, J. B. Randazzo, J. P. Lockhart, P. G. Fugazzi, T. Tao, and A. L. Kastengren. 2D-imaging of sampling-probe perturbations in laminar premixed flames using Kr X-ray fluorescence. *Combustion and Flame*, 181:214–224, 2017. doi: 10.1016/j.combustflame.2017.03.024.

[70] N. Hansen, R. Tranter, J. Randazzo, J. Lockhart, and A. Kastengren. Investigation of sampling-probe distorted temperature fields with x-ray fluorescence spectroscopy. *Proceedings of the Combustion Institute*, 37(2):1401–1408, 2019. doi: 10.1016/j.proci.2018.05.034.

[71] A. Hartlieb, B. Atakan, and K. Kohse-Höinghaus. Effects of a sampling quartz nozzle on the flame structure of a fuel-rich low-pressure propene flame. *Combustion and Flame*, 121 (4):610–624, jun 2000. doi: 10.1016/s0010-2180(99)00176-5.

[72] A. Hayhurst and D. Kittelson. Mass spectrometric sampling of ions from atmospheric pressure flames—III: Boundary layer and other cooling of the sample. *Combustion and Flame*, 28:137–143, 1977. doi: 10.1016/0010-2180(77)90019-0.

[73] A. Hayhurst and N. Telford. The occurrence of chemical reactions in supersonic expansions of a gas into a vacuum and its relation to mass spectrometric sampling. *Proceedings of the Royal Society of London. A. Mathematical and Physical Sciences*, 322(1551):483–507, 1971. doi: 10.1098/rspa.1971.0080.

[74] A. Hayhurst, D. Kittelson, and N. Telford. Mass spectrometric sampling of ions from atmospheric pressure flames—II: Aerodynamic disturbance of a flame by the sampling system. *Combustion and Flame*, 28:123–135, 1977. doi: 10.1016/0010-2180(77)90018-9.

[75] A. N. Hayhurst. Mass spectrometric sampling of a flame. *Combustion, Explosion, and Shock Waves*, 48(5):516–525, 2012. doi: 10.1134/s0010508212050036.

[76] A. N. Hayhurst and S. G. Taylor. The ions in fuel-rich hydrogen flames with added ammonia: measurements of the proton affinity of NH_3 and the enthalpy of monohydration of NH_4^+. *Physical Chemistry Chemical Physics*, 4(4):561–570, 2002. doi: 10.1039/b108247g.

[77] A. N. Hayhurst and S. G. Taylor. The stabilities of the gas-phase ions $Li^+{\cdot}H_2O$, $Li^+{\cdot}(H_2O)_2$ and $Li^+{\cdot}CO$ as measured by mass-spectrometric sampling of fuel-rich flames of C_2H_2+O_2. *Physical Chemistry Chemical Physics*, 5(8):1610–1618, 2003. doi: 10.1039/b300860f.

[78] A. N. Hayhurst, J. M. Goodings, and S. G. Taylor. The effects of applying electric fields on the mass spectrometric sampling of positive and negative ions from a flame at atmospheric pressure. *Combustion and Flame*, 161(12):3249–3262, 2014. doi: 10.1016/j.combustflame.2014.06.012.

[79] J. O. Hirschfelder, C. F. Curtiss, R. B. Bird, and M. G. Mayer. *Molecular theory of gases and liquids*, volume 165. Wiley New York, 1964.

[80] C. Hirt and B. Nichols. Volume of fluid (VOF) method for the dynamics of free boundaries. *Journal of Computational Physics*, 39(1):201–225, 1981. doi: 10.1016/0021-9991(81)90145-5.

[81] P. Holister, J.-W. Weener, C. Roman, and T. Harper. Nanoparticles. *Technology white papers*, 3:1–11, 2003.

[82] R. Hong, Z. Ren, J. Ding, and H. Li. Experimental investigation and particle dynamic simulation for synthesizing titania nanoparticles using diffusion flame. *Chemical Engineering Journal*, 108(3):203–212, 2005. doi: 10.1016/j.cej.2005.02.011.

[83] M. Ihme, L. Shunn, and J. Zhang. Regularization of reaction progress variable for application to flamelet-based combustion models. *Journal of Computational Physics*, 231(23):7715–7721, 2012. doi: 10.1016/j.jcp.2012.06.029.

[84] R. Issa. Solution of the implicitly discretised fluid flow equations by operator-splitting. *Journal of Computational Physics*, 62(1):40–65, jan 1986. doi: 10.1016/0021-9991(86)90099-9.

[85] F. A. Jaberi, P. J. Colucci, S. JAMES, P. Givi, and S. B. Pope. Filtered mass density function for large-eddy simulation of turbulent reacting flows. *Journal of Fluid Mechanics*, 401:85–121, 1999. doi: 10.1017/s0022112099006643.

[86] H. Janbazi, Y. Karakaya, T. Kasper, C. Schulz, I. Wlokas, and S. Peukert. Development and evaluation of a chemical kinetics reaction mechanism for tetramethylsilane-doped flames. *Chemical Engineering Science*, 209:115209, 2019. doi: 10.1016/j.ces.2019.115209.

[87] J. Janicka, W. Kolbe, and W. Kollmann. Closure of the transport equation for the probability density funcfion of turbulent scalar fields. *Journal of Non-Equilibrium Thermodynamics*, 4(1), 1979. doi: 10.1515/jnet.1979.4.1.47.

[88] C. Janzen and P. Roth. Formation and characteristics of Fe_2O_3 nano-particles in doped low pressure H_2/O_2/Ar flames. *Combustion and Flame*, 125(3):1150–1161, may 2001. doi: 10.1016/s0010-2180(01)00235-8.

[89] H. Jasak. *Error analysis and estimation for the finite volume method with applications to fluid flows.* PhD thesis, Imperial College London (University of London), 1996.

[90] J. I. Jeong and M. Choi. A simple bimodal model for the evolution of non-spherical particles undergoing nucleation, coagulation and coalescence. *Journal of Aerosol Science*, 34(8):965 – 976, 2003. doi: 10.1016/s0021-8502(03)00067-3.

[91] X. Ji, Q. Li, H. Song, and C. Fan. Protein-mimicking nanoparticles in biosystems. *Advanced Materials*, 34(37):2201562, 2022. doi: 10.1002/adma.202201562.

[92] W. P. Jones and B. E. Launder. The prediction of laminarization with a two-equation model of turbulence. *International Journal of Heat and Mass Transfer*, 15(2):301 – 314, 1972. doi: 10.1016/0017-9310(72)90076-2.

[93] H. K. Kammler, R. Mueller, O. Senn, and S. E. Pratsinis. Synthesis of silica-carbon particles in a turbulent H_2-air flame aerosol reactor. *AIChE Journal*, 47(7):1533–1543, 2001. doi: 10.1002/aic.690470707.

[94] Y. Karakaya, S. Peukert, and T. Kasper. Mass spectrometric study on the combustion of tetramethylsilane and the formation of silicon oxide clusters in premixed laminar low-pressure synthesis flames. *The Journal of Physical Chemistry A*, 122(36):7131–7141, 2018. doi: 10.1021/acs.jpca.8b06510.

[95] Y. Karakaya, H. Janbazi, I. Wlokas, A. Levish, M. Winterer, and T. Kasper. Experimental and numerical study on the influence of equivalence ratio on key intermediates and silica nanoparticles in flame synthesis. *Proceedings of the Combustion Institute*, 38(1):1375–1383, 2021. doi: 10.1016/j.proci.2020.06.096.

[96] Y. Karakaya, J. Sellmann, I. Wlokas, and T. Kasper. Influence of the sampling probe on flame temperature, species, residence times and on the interpretation of ion signals of methane/oxygen flames in molecular beam mass spectrometry measurements. *Combustion and Flame*, 229:111388, 2021. doi: 10.1016/j.combustflame.2021.02.034.

[97] Y. H. Karakaya. *Mass spectrometric gas phase diagnostics in particle forming flames.* PhD thesis, Dissertation, Duisburg, Essen, Universität Duisburg-Essen, 2021, 2021.

[98] D. Kashchiev and G. M. van Rosmalen. Review: Nucleation in solutions revisited. *Crystal Research and Technology*, 38(78):555–574, 2003. doi: 10.1002/crat.200310070.

[99] T. Kasper, P. Oßwald, U. Struckmeier, K. Kohse-Höinghaus, C. Taatjes, J. Wang, T. Cool, M. Law, A. Morel, and P. Westmoreland. Combustion chemistry of the propanol isomers — investigated by electron ionization and VUV-photoionization molecular-beam mass spectrometry. *Combustion and Flame*, 156(6):1181–1201, 2009. doi: 10.1016/j.combustflame.2009.01.023.

[100] A. Kazakov and M. Frenklach. Dynamic modeling of soot particle coagulation and aggregation: Implementation with the method of moments and application to high-pressure laminar premixed flames. *Combustion and Flame*, 114(3):484–501, 1998. doi: 10.1016/S0010-2180(97)00322-2.

[101] R. Kee, F. Rupley, and J. Miller. The chemkin thermodynamic data base. Technical report, mar 1990.

[102] G. A. Kelesidis, E. Goudeli, and S. E. Pratsinis. Flame synthesis of functional nanostructured materials and devices: surface growth and aggregation. *Proceedings of the Combustion Institute*, 36(1):29–50, 2017. doi: 10.1016/j.proci.2016.08.078.

[103] A. Keller, I. Wlokas, M. Kohns, and H. Hasse. Thermophysical properties of solutions of iron (III) nitrate-nonahydrate in mixtures of ethanol and water. *Journal of Chemical & Engineering Data*, 2021. doi: 10.31224/osf.io/9esd5.

[104] A. M. Kempf. *Large-Eddy Simulation of Non-Premixed Turbulent Flames*. PhD thesis, Darmstadt University of Technology, Germany, 2003.

[105] W. D. Kingery. *Introduction to ceramics*. John Wiley & Sons, 1960.

[106] S. Kluge, L. Deng, O. Feroughi, F. Schneider, M. Poliak, A. Fomin, V. Tsionsky, S. Cheskis, I. Wlokas, I. Rahinov, T. Dreier, A. Kempf, H. Wiggers, and C. Schulz. Initial reaction steps during flame synthesis of iron-oxide nanoparticles. *CrystEngComm*, 17(36):6930–6939, 2015. doi: 10.1039/c5ce00456j.

[107] R. Knikker, D. Veynante, and C. Meneveau. A priori testing of a similarity model for large eddy simulations of turbulent premixed combustion. *Proceedings of the Combustion Institute*, 29(2):2105–2111, 2002. doi: 10.1016/s1540-7489(02)80256-5.

[108] R. Knikker, D. Veynante, and C. Meneveau. A dynamic flame surface density model for large eddy simulation of turbulent premixed combustion. *Physics of Fluids*, 16(11):L91–L94, 2004. doi: 10.1063/1.1780549.

[109] A. Kobata, K. Kusakabe, and S. Morooka. Growth and transformation of TiO_2 crystallites in aerosol reactor. *AIChE Journal*, 37(3):347–359, 1991. doi: 10.1002/aic.690370305.

[110] T. T. Kodas and M. Hampden-Smith. *Aerosol processing of materials*. Wiley-Vch, 1999.

[111] A. N. Kolmogorov. The local structure of turbulence in incompressible viscous fluid for very large reynolds numbers. In *Dokl. Akad. Nauk SSSR*, volume 30, pages 301–305. JSTOR, 1941.

[112] S.-C. Kong and R. D. Reitz. Application of detailed chemistry and CFD for predicting direct injection HCCI engine combustion and emissions. *Proceedings of the Combustion Institute*, 29(1):663–669, 2002. doi: 10.1016/s1540-7489(02)80085-2.

[113] O. P. Korobeinichev, A. G. Tereshchenko, I. D. Emel'yanov, A. L. Rudnitskii, S. Y. Fedorov, L. V. Kuibida, and V. V. Lotov. Substantiation of the probe mass-spectrometric method for studying the structure of flames with narrow combustion zones. *Combustion, Explosion, and Shock Waves*, 21(5):524–530, 1985. doi: 10.1007/bf01463575.

[114] D. Krüger, P. Oßwald, M. Köhler, P. Hemberger, T. Bierkandt, Y. Karakaya, and T. Kasper. Hydrogen abstraction ratios: A systematic ipepico spectroscopic investigation in laminar flames. *Combustion and Flame*, 191:343–352, 2018. doi: 10.1016/j.combustflame.2017.12.025.

[115] F. E. Kruis, K. A. Kusters, S. E. Pratsinis, and B. Scarlett. A simple model for the evolution of the characteristics of aggregate particles undergoing coagulation and sintering. *Aerosol Science and Technology*, 19(4):514–526, 1993. doi: 10.1080/02786829308959656.

[116] G. Kuenne, A. Ketelheun, and J. Janicka. Les modeling of premixed combustion using a thickened flame approach coupled with fgm tabulated chemistry. *Combustion and Flame*, 158(9):1750 – 1767, 2011. doi: 10.1016/j.combustflame.2011.01.005.

[117] K. K. Kuo. *Principles of combustion*. Elsevier Science Pub. Co. Inc., New York, NY, 1986.

[118] N. J. Labbe, V. Seshadri, T. Kasper, N. Hansen, P. Oßwald, and P. R. Westmoreland. Flame chemistry of tetrahydropyran as a model heteroatomic biofuel. *Proceedings of the Combustion Institute*, 34(1):259–267, 2013. doi: 10.1016/j.proci.2012.07.027.

[119] J.-P. Legier, T. Poinsot, and D. Veynante. Dynamically thickened flame LES model for premixed and non-premixed turbulent combustion. In *Proceedings of the summer program*, volume 12, pages 157–168. Citeseer, 2000.

[120] R. J. LeVeque et al. *Finite volume methods for hyperbolic problems*, volume 31. Cambridge university press, 2002.

[121] D. Li, W. Y. Teoh, C. Selomulya, R. C. Woodward, P. Munroe, and R. Amal. Insight into microstructural and magnetic properties of flame-made γ-Fe_2O_3 nanoparticles. *Journal of Materials Chemistry*, 17(46):4876, 2007. doi: 10.1039/b711705a.

[122] S. Li, Y. Ren, P. Biswas, and S. D. Tse. Flame aerosol synthesis of nanostructured materials and functional devices: Processing, modeling, and diagnostics. *Progress in Energy and Combustion Science*, 55:1–59, 2016. doi: 10.1016/j.pecs.2016.04.002.

[123] Y. Li, C.-W. Zhou, K. P. Somers, K. Zhang, and H. J. Curran. The oxidation of 2-butene: A high pressure ignition delay, kinetic modeling study and reactivity comparison with isobutene and 1-butene. *Proceedings of the Combustion Institute*, 36(1):403–411, 2017. doi: 10.1016/j.proci.2016.05.052.

[124] D. K. Lilly. A proposed modification of the Germano subgrid-scale closure method. *Physics of Fluids A*, 4(3):633–635, 1992. doi: 10.1063/1.858280.

[125] S. Lindsay. *Introduction to nanoscience*. OUP Oxford, 2009.

[126] J. T. Lipkowicz, I. Wlokas, and A. M. Kempf. Analysis of mild ignition in a shock tube using a highly resolved 3D-LES and high-order shock-capturing schemes. *Shock Waves*, 29 (4):511–521, 2018. doi: 10.1007/s00193-018-0867-4.

[127] A. B. Liu, D. Mather, and R. D. Reitz. Modeling the effects of drop drag and breakup on fuel sprays. In *SAE Technical Paper Series*. SAE International, 1993. doi: 10.4271/930072.

[128] J. Loeffler, S. Das, and S. C. Garrick. Large eddy simulation of titanium dioxide nanoparticle formation and growth in turbulent jets. *Aerosol Science and Technology*, 45(5):616–628, 2011. doi: 10.1080/02786826.2010.551147.

[129] T. Ma, Y. Gao, A. M. Kempf, and N. Chakraborty. Validation and implementation of algebraic les modelling of scalar dissipation rate for reaction rate closure in turbulent premixed combustion. *Combustion and Flame*, 161(12):3134 – 3153, 2014. doi: 10.1016/j.combustflame.2014.05.023.

[130] U. Maas and S. Pope. Implementation of simplified chemical kinetics based on intrinsic low-dimensional manifolds. volume 24, pages 103–112. Elsevier BV, 1992. doi: 10.1016/s0082-0784(06)80017-2.

[131] U. Maas and S. B. Pope. Simplifying chemical kinetics: Intrinsic low-dimensional manifolds in composition space. *Combustion and Flame*, 88(3–4):239 – 264, 1992. doi: 10.1016/0010-2180(92)90034-m.

[132] L. Mädler, H. K. Kammler, S. E. Pratsinis, and R. Mueller. Controlled synthesis of nanostructured particles by flame spray pyrolysis. *Journal of Aerosol Science*, 33(2):369–389, 2002. doi: 10.1016/s0021-8502(01)00159-8.

[133] L. Mädler, W. J. Stark, and S. E. Pratsinis. Flame-made Ceria nanoparticles. *Journal of Materials Research*, 17:1356–1362, 2002. doi: 10.1557/jmr.2002.0202.

[134] D. L. Marchisio and R. O. Fox. Solution of population balance equations using the direct quadrature method of moments. *Journal of Aerosol Science*, 36(1):43–73, 2005. doi: 10.1016/j.jaerosci.2004.07.009.

[135] D. L. Marchisio and R. O. Fox. *Computational models for polydisperse particulate and multiphase systems*. Cambridge University Press, 2013.

[136] F. J. Martins, J. Kirchmann, A. Kronenburg, and F. Beyrau. Experimental investigation of axisymmetric, turbulent, annular jets discharged through the nozzle of the SPP1980 SpraySyn burner under isothermal and reacting conditions. *Experimental Thermal and Fluid Science*, 114:110052, 2020. doi: 10.1016/j.expthermflusci.2020.110052.

[137] F. Meierhofer, L. Mädler, and U. Fritsching. Nanoparticle evolution in flame spray pyrolysis—process design via experimental and computational analysis. *AIChE Journal*, 66(2): e16885, 2020. doi: 10.1002/aic.16885.

[138] S. Menon, P.-K. Yeung, and W.-W. Kim. Effect of subgrid models on the computed interscale energy transfer in isotropic turbulence. In *Fluid Dynamics Conference*. American Institute of Aeronautics and Astronautics, 1994. doi: 10.2514/6.1994-2387.

[139] F. R. Menter. Two-equation eddy-viscosity turbulence models for engineering applications. *AIAA Journal*, 32(8):1598–1605, 1994. doi: 10.2514/3.12149.

[140] W. J. Menz and M. Kraft. A new model for silicon nanoparticle synthesis. *Combustion and Flame*, 160(5):947–958, 2013. doi: 10.1016/j.combustflame.2013.01.014.

[141] S. E. Miller and S. C. Garrick. Nanoparticle coagulation in a planar jet. *Aerosol Science and Technology*, 38(1):79–89, 2004. doi: 10.1080/02786820490247669.

[142] A. Mittasch. Über Eisencarbonyl und Carbonyleisen. *Angewandte Chemie*, 41(30):827–833, 1928. doi: 10.1002/ange.19280413002.

[143] P. Moin, K. Squires, W. Cabot, and S. Lee. A dynamic subgrid-scale model for compressible turbulence and scalar transport. *Physics of Fluids A*, 3(11):2746–2757, 1991. doi: 10.1063/1.858164.

[144] M. E. Mueller and H. Pitsch. Large eddy simulation subfilter modeling of soot-turbulence interactions. *Physics of Fluids*, 23(11):115104, 2011. doi: 10.1063/1.3657826.

[145] M. E. Mueller and H. Pitsch. LES model for sooting turbulent nonpremixed flames. *Combustion and Flame*, 159(6):2166–2180, 2012. doi: 10.1016/j.combustflame.2012.02.001.

[146] M. E. Mueller and H. Pitsch. Large eddy simulation of soot evolution in an aircraft combustor. *Physics of Fluids*, 25(11):110812, 2013. doi: 10.1063/1.4819347.

[147] J. W. Mullin. *Crystallization*. Elsevier, 2001.

[148] A. Münzer, J. Sellmann, P. Fortugno, A. Kempf, C. Schulz, and H. Wiggers. Inline coating of silicon nanoparticles in a plasma reactor: Reactor design, simulation and experiment. *Materials Today: Proceedings*, 4:S118–S127, 2017. doi: 10.1016/j.matpr.2017.09.176.

[149] P. B. Neto, F. Meierhofer, H. F. Meier, U. Fritsching, and D. Noriler. Modelling polydisperse nanoparticle size distributions as produced via flame spray pyrolysis. *Powder Technology*, 370:116–128, 2020. doi: 10.1016/j.powtec.2020.05.019.

[150] F. Nicoud and F. Ducros. Subgrid-scale stress modelling based on the square of the velocity gradient tensor. *Flow, turbulence and Combustion*, 62(3):183–200, 1999. doi: 10.1023/A:1009995426001.

[151] F. Nicoud, H. B. Toda, O. Cabrit, S. Bose, and J. Lee. Using singular values to build a subgrid-scale model for large eddy simulations. *Physics of Fluids*, 23(8):085106, 2011. doi: 10.1063/1.3623274.

[152] F. Nicoud, H. B. Toda, O. Cabrit, S. Bose, and J. Lee. Using singular values to build a subgrid-scale model for large eddy simulations. *Physics of Fluids*, 23(8):085106, 2011. doi: 10.1063/1.3623274.

[153] E. E. O'Brien. The probability density function (pdf) approach to reacting turbulent flows. In *Topics in Applied Physics*, pages 185–218. Springer Berlin Heidelberg, 1980. doi: 10.1007/3540101926_11.

[154] J. Oh and D. Noh. The reduction kinetics of hematite particles in H_2 and CO atmospheres. *Fuel*, 196:144–153, 2017. doi: 10.1016/j.fuel.2016.10.125.

[155] M. M. Olaimat, L. Yousefi, and O. M. Ramahi. Using plasmonics and nanoparticles to enhance the efficiency of solar cells: review of latest technologies. *Journal of the Optical Society of America B*, 38(2):638, 2021. doi: 10.1364/josab.411712.

[156] C. Olm, T. Varga, É. Valkó, S. Hartl, C. Hasse, and T. Turányi. Development of an ethanol combustion mechanism based on a hierarchical optimization approach. *International Journal of Chemical Kinetics*, 48(8):423–441, 2016. doi: 10.1002/kin.20998.

[157] O. R. OpenFOAM. Version 2.1, 2012. URL `https://openfoam.org/release/2-1-0/`.

[158] H. Orthner and P. Roth. Formation of iron oxide powder in a hot-wall flow reactor. *Materials Chemistry and Physics*, 78(2):453–458, 2003. doi: 10.1016/s0254-0584(02)00228-6.

[159] P. Oßwald, U. Struckmeier, T. Kasper, K. Kohse-Höinghaus, J. Wang, T. A. Cool, N. Hansen, and P. R. Westmoreland. Isomer-specific fuel destruction pathways in rich flames of methyl acetate and ethyl formate and consequences for the combustion chemistry of esters. *The Journal of Physical Chemistry A*, 111(19):4093–4101, 2007. doi: 10.1021/jp068337w.

[160] P. Oßwald, K. Kohse-Höinghaus, U. Struckmeier, T. Zeuch, L. Seidel, L. Leon, and F. Mauss. Combustion chemistry of the butane isomers in premixed low-pressure flames. *Zeitschrift fuer physikalische Chemie*, 225(9-10):1029–1054, 2011. doi: 10.1524/zpch.2011.0148.

[161] S. Panda and S. E. Pratsinis. Modeling the synthesis of aluminum particles by evaporation-condensation in an aerosol flow reactor. *Nanostructured Materials*, 5(7–8):755 – 767, 1995. doi: 10.1016/0965-9773(95)00292-m.

[162] H. Pauly. *Atom, Molecule, and Cluster Beams I: Basic Theory, Production and Detection of Thermal Energy Beams*, volume 1. Springer Science & Business Media, 2000.

[163] W. Pejpichestakul, A. Cuoci, A. Frassoldati, M. Pelucchi, A. Parente, and T. Faravelli. Buoyancy effect in sooting laminar premixed ethylene flame. *Combustion and Flame*, 205:135–146, 2019. doi: 10.1016/j.combustflame.2019.04.001.

[164] N. Peters. *Turbulent Combustion*. Cambridge University Press, 2000.

[165] U. Piomelli and J. Liu. Large-eddy simulation of rotating channel flows using a localized dynamic model. *Physics of Fluids*, 7(4):839–848, 1995. doi: 10.1063/1.868607.

[166] T. J. Poinsot and D. Veynante. *Theoretical and Numerical Combustion*. Aquaprint, Bordeaux, France, 3rd edition, 2012.

[167] M. Poliak, A. Fomin, V. Tsionsky, S. Cheskis, I. Wlokas, and I. Rahinov. On the mechanism of nanoparticle formation in a flame doped by iron pentacarbonyl. *Physical Chemistry Chemical Physics*, 17(1):680–685, 2015.

[168] S. Pope. The probability approach to the modelling of turbulent reacting flows. *Combustion and Flame*, 27:299–312, 1976. doi: 10.1016/0010-2180(76)90035-3.

[169] S. Pope. Computations of turbulent combustion: Progress and challenges. volume 23, pages 591–612. Elsevier BV, 1991. doi: 10.1016/s0082-0784(06)80307-3.

[170] S. B. Pope. Transport equation for the joint probability density function of velocity and scalars in turbulent flow. *Physics of Fluids*, 24(4):588, 1981. doi: 10.1063/1.863425.

[171] S. B. Pope. Pdf methods for turbulent reactive flows. *Progress in energy and combustion science*, 11(2):119–192, 1985.

[172] S. B. Pope. *Turbulent Flows*. Cambridge University Press, 2000. imp-import.

[173] S. E. Pratsinis. Simultaneous nucleation, condensation, and coagulation in aerosol reactors. *Journal of Colloid and Interface Science*, 124(2):416–427, 1988. doi: 10.1016/0021-9797(88)90180-4.

[174] S. E. Pratsinis and P. T. Spicer. Competition between gas phase and surface oxidation of ticl4 during synthesis of tio2 particles. *Chemical Engineering Science*, 53(10):1861 – 1868, 1998. doi: 10.1016/s0009-2509(98)00026-8.

[175] F. Proch. *Highly-resolved numerical simulation of turbulent premixed and stratified combustion under adiabatic and non-adiabatic conditions with tabulated chemistry*. PhD thesis, University of Duisburg-Essen, Nov. 2016.

[176] F. Proch and A. M. Kempf. Numerical analysis of the cambridge stratified flame series using artificial thickened flame LES with tabulated premixed flame chemistry. *Combustion and Flame*, 161(10):2627 – 2646, 2014. doi: 10.1016/j.combustflame.2014.04.010.

[177] F. Proch, M. W. A. Pettit, T. Ma, M. Rieth, and A. M. Kempf. *Direct and Large-Eddy Simulation IX*, chapter Investigations on the Effect of Different Subgrid Models on the Quality of LES Results, pages 141–147. Springer International Publishing, Cham, 2015. doi: 10.1007/978-3-319-14448-1_19.

[178] N. Qamar, Z. Alwahabi, Q. Chan, G. Nathan, D. Roekaerts, and K. King. Soot volume fraction in a piloted turbulent jet non-premixed flame of natural gas. *Combustion and Flame*, 156(7):1339–1347, 2009. doi: 10.1016/j.combustflame.2009.02.011.

[179] I. Rahinov, J. Sellmann, M. R. Lalanne, M. Nanjaiah, T. Dreier, S. Cheskis, and I. Wlokas. Insights into the mechanism of combustion synthesis of iron oxide nanoparticles gained by laser diagnostics, mass spectrometry, and numerical simulations: A mini-review. *Energy &amp Fuels*, 35(1):137–160, 2020. doi: 10.1021/acs.energyfuels.0c03561.

[180] V. Raman and H. Pitsch. A consistent les/filtered-density function formulation for the simulation of turbulent flames with detailed chemistry. *Proceedings of the Combustion Institute*, 31(2):1711 – 1719, 2007. doi: 10.1016/j.proci.2006.07.152.

[181] V. Raman, H. Pitsch, and R. O. Fox. Hybrid large-eddy simulation/lagrangian filtered-density-function approach for simulating turbulent combustion. *Combustion and Flame*, 143(1-2):56–78, 2005. doi: 10.1016/j.combustflame.2005.05.002.

[182] D. Ramkrishna. *Population balances: Theory and applications to particulate systems in engineering*. Elsevier, 2000.

[183] W. E. Ranz and W. R. Marshall. Evaporation from drops—I–II. *Chemical Engineering Progress*, 48(22):141–146, 1952.

[184] E. Ranzi, A. Frassoldati, R. Grana, A. Cuoci, T. Faravelli, A. Kelley, and C. Law. Hierarchical and comparative kinetic modeling of laminar flame speeds of hydrocarbon and oxygenated fuels. *Progress in Energy and Combustion Science*, 38(4):468–501, 2012. doi: 10.1016/j.pecs.2012.03.004.

[185] L. F. Richardson. *Weather prediction by numerical process*. Cambridge university press, 2007.

[186] M. Rieth, F. Proch, M. Rabaçal, B. Franchetti, F. C. Marincola, and A. Kempf. Flamelet LES of a semi-industrial pulverized coal furnace. *Combustion and Flame*, 173:39–56, 2016. doi: 10.1016/j.combustflame.2016.07.013.

[187] M. Rieth, A. Clements, M. Rabaçal, F. Proch, O. Stein, and A. Kempf. Flamelet LES modeling of coal combustion with detailed devolatilization by directly coupled CPD. *Proc. Combust. Inst.*, 36(2):2181 – 2189, 2017. doi: 10.1016/j.proci.2016.06.077.

[188] M. Rieth, J.-Y. Chen, S. Menon, and A. M. Kempf. A hybrid flamelet finite-rate chemistry approach for efficient les with a transported fdf. *Combustion and Flame*, 199:183–193, 2019.

[189] A. Rittler. *Large eddy simulation of nanoparticle synthesis from spray*. PhD thesis, Universität Duisburg-Essen, Fakultät für Ingenieurwissenschaften, 2018.

[190] A. Rittler, F. Proch, and A. M. Kempf. LES of the sydney piloted spray flame series with the PFGM/ATF approach and different sub-filter models. *Combustion and Flame*, 162(4): 1575 – 1598, 2015. doi: 10.1016/j.combustflame.2014.11.025.

[191] A. Rittler, L. Deng, I. Wlokas, and A. Kempf. Large eddy simulations of nanoparticle synthesis from flame spray pyrolysis. *Proceedings of the Combustion Institute*, 36(1):1077–1087, 2017. doi: 10.1016/j.proci.2016.08.005.

[192] P. Rodrigues, B. Franzelli, R. Vicquelin, O. Gicquel, and N. Darabiha. Coupling an LES approach and a soot sectional model for the study of sooting turbulent non-premixed flames. *Combustion and Flame*, 190:477–499, 2018. doi: 10.1016/j.combustflame.2017.12.009.

[193] T. Rosenberger, J. Sellmann, I. Wlokas, and F. E. Kruis. A model flow reactor design for the study of nanoparticle structure formation under well-defined conditions. *Review of Scientific Instruments*, 91(9):095114, 2020. doi: 10.1063/5.0018880.

[194] T. Rosenberger, I. Skenderović, J. Sellmann, P. Wollny, A. Levish, I. Wlokas, A. Kempf, M. Winterer, and F. E. Kruis. Determining the sintering kinetics of fe and Fe_xO_y-nanoparticles in a well-defined model flow reactor. *Aerosol Science and Technology*, 56 (9):833–846, 2022. doi: 10.1080/02786826.2022.2089011.

[195] P. Roth and A. Hospital. Design and test of a particle mass spectrometer (PMS). *Journal of Aerosol Science*, 25(1):61–73, 1994. doi: 10.1016/0021-8502(94)90182-1.

[196] M. Rumminger, D. Reinelt, V. Babushok, and G. T. Linteris. Numerical study of the inhibition of premixed and diffusion flames by iron pentacarbonyl. *Combustion and flame*, 116(1-2):207–219, 1999. doi: 10.1016/s0010-2180(98)00033-9.

[197] L. Ruwe, L. Cai, J. Wullenkord, S. C. Schmitt, D. Felsmann, M. Baroncelli, B. Chen, K. Moshammer, N. Hansen, H. Pitsch, and K. Kohse-Höinghaus. Low- and high-temperature study of n-heptane combustion chemistry. *Proceedings of the Combustion Institute*, 38(1):405–413, 2021. doi: 10.1016/j.proci.2020.07.007.

[198] C. Saggese, S. Ferrario, J. Camacho, A. Cuoci, A. Frassoldati, E. Ranzi, H. Wang, and T. Faravelli. Kinetic modeling of particle size distribution of soot in a premixed burner-stabilized stagnation ethylene flame. *Combustion and Flame*, 162(9):3356–3369, 2015. doi: 10.1016/j.combustflame.2015.06.002.

[199] C. Saggese, A. Cuoci, A. Frassoldati, S. Ferrario, J. Camacho, H. Wang, and T. Faravelli. Probe effects in soot sampling from a burner-stabilized stagnation flame. *Combustion and Flame*, 167:184–197, 2016. doi: 10.1016/j.combustflame.2016.02.013.

[200] M. Sander, R. H. West, M. S. Celnik, and M. Kraft. A detailed model for the sintering of polydispersed nanoparticle agglomerates. *Aerosol Science and Technology*, 43(10):978–989, 2009. doi: 10.1080/02786820903092416.

[201] F. G. Schmitt. About boussinesq's turbulent viscosity hypothesis: historical remarks and a direct evaluation of its validity. *Comptes Rendus Mécanique*, 335(9-10):617–627, 2007. doi: 10.1016/j.crme.2007.08.004.

[202] F. Schneider, T. Dreier, and C. Schulz. SpraySyn – standard burner for the collaborative investigation of spray-flame synthesis of nanoparticles: Droplet velocity and size of the non-reactive ethanol spray. *Proceedings of the European Combustion Meeting*, 9, 2019.

[203] F. Schneider, S. Suleiman, J. Menser, E. Borukhovich, I. Wlokas, A. Kempf, H. Wiggers, and C. Schulz. SpraySyn— a standardized burner configuration for nanoparticle synthesis in spray flames. *Rev. Sci. Instrum.*, 90:085108, 08 2019. doi: 10.1063/1.5090232.

[204] J. Seinfeld and S. Pandis. *Atmospheric Chemistry and Physics: From Air Pollution to Climate Change*. Wiley New York, 1998.

[205] J. Sellmann, J. Lai, A. M. Kempf, and N. Chakraborty. Flame surface density based modelling of head-on quenching of turbulent premixed flames. *Proceedings of the Combustion Institute*, 36(2):1817–1825, 2017. doi: 10.1016/j.proci.2016.07.114.

[206] J. Sellmann, I. Rahinov, S. Kluge, H. Jünger, A. Fomin, S. Cheskis, C. Schulz, H. Wiggers, A. Kempf, and I. Wlokas. Detailed simulation of iron oxide nanoparticle forming flames: Buoyancy and probe effects. *Proceedings of the Combustion Institute*, 37(1):1241–1248, 2019. doi: 10.1016/j.proci.2018.06.041.

[207] J. Sellmann, P. Wollny, S.-J. Baik, S. Suleiman, H. Wiggers, I. Wlokas, and A. Kempf. Hybrid LES/Lagrange-FDF approach for the sub-grid modelling of turbulent nanoparticle synthesis. *Proceedings of the European Combustion Meeting*, 10, 2021.

[208] J. Sellmann, P. Wollny, S.-J. Baik, S. Suleiman, F. Schneider, C. Schulz, H. Wiggers, I. Wlokas, and A. Kempf. LES of nanoparticle synthesis in the spraysyn burner: A comparison against experiments. *Powder Technology*, 404:117466, 2022. doi: 10.1016/j.powtec.2022.117466.

[209] M. Sheikhi, T. Drozda, P. Givi, F. Jaberi, and S. Pope. Large eddy simulation of a turbulent nonpremixed piloted methane jet flame (Sandia flame D). *Proceedings of the Combustion Institute*, 30(1):549–556, 2005. doi: 10.1016/j.proci.2004.08.028.

[210] S. Shekar, M. Sander, R. C. Riehl, A. J. Smith, A. Braumann, and M. Kraft. Modelling the flame synthesis of silica nanoparticles from tetraethoxysilane. *Chemical Engineering Science*, 70:54–66, 2012. doi: 10.1016/j.ces.2011.06.010.

[211] T.-H. Shih, W. W. Liou, A. Shabbir, Z. Yang, and J. Zhu. A new k-ϵ eddy viscosity model for high reynolds number turbulent flows. *Computers & Fluids*, 24(3):227–238, 1995. doi: 10.1016/0045-7930(94)00032-t.

[212] N. Sikalo, O. Hasemann, C. Schulz, A. Kempf, and I. Wlokas. A genetic algorithm-based method for the automatic reduction of reaction mechanisms. *International Journal of Chemical Kinetics*, 46(1):41–59, 2013. doi: 10.1002/kin.20826.

[213] P. Skovorodko, A. Tereshchenko, O. Korobeinichev, D. Knyazkov, and A. Shmakov. Experimental and numerical study of probe-induced perturbations of the flame structure. *Combustion Theory and Modelling*, 17(1):1–24, 2013. doi: 10.1080/13647830.2012.715674.

[214] J. Smagorinsky. General circulation experiments with the primitive equations, 1, the basic experiment. *Monthly Weather Review*, 91(3):99–164, 1963. doi: 10.1175/1520-0493(1963)091⟨0099:gcewtp⟩2.3.co;2.

[215] G. P. Smith, D. M. Golden, M. Frenklach, N. W. Moriarty, B. Eiteneer, M. Goldenberg, C. T. Bowman, R. K. Hanson, S. Song, W. C. Gardiner, Jr., V. V. Lissianski, and Z. Qin. http://www.me.berkeley.edu/gri_mech, 2000.

[216] O. I. Smith and D. W. Chandler. An experimental study of probe distortions to the structure of one-dimensional flames. *Combustion and Flame*, 63(1-2):19–29, 1986. doi: 10.1016/0010-2180(86)90108-2.

[217] P. Spalart and S. Allmaras. A one-equation turbulence model for aerodynamic flows. In *30th aerospace sciences meeting and exhibit*, page 439, 1992. doi: 10.2514/6.1992-439.

[218] P. T. Spicer, O. Chaoul, S. Tsantilis, and S. E. Pratsinis. Titania formation by $TiCl_4$ gas phase oxidation, surface growth and coagulation. *Journal of Aerosol Science*, 33(1):17–34, 2002. doi: 10.1016/s0021-8502(01)00069-6.

[219] S. Staude, C. Hecht, I. Wlokas, C. Schulz, and B. Atakan. Experimental and numerical investigation of $Fe(CO)_5$ addition to a laminar premixed hydrogen/oxygen/argon flame. *Zeitschrift für Physikalische Chemie*, 223(4-5):639–649, 2009. doi: 10.1524/zpch.2009.6048.

[220] O. T. Stein. *Large Eddy Simulation of Combustion in Swirling and Opposed Jet Flows*. PhD thesis, Imperial College London, 2009.

[221] M. F. Stodt, C. Liu, S. Li, L. Mädler, U. Fritsching, and J. Kiefer. Phase-selective laser–induced breakdown spectroscopy in flame spray pyrolysis for iron oxide nanoparticle synthesis. *Proceedings of the Combustion Institute*, 38(1):1711–1718, 2021. doi: 10.1016/j.proci.2020.06.092.

[222] M. F. B. Stodt, J. Kiefer, and U. Fritsching. Drop dynamics in heterogeneous spray flames for nanoparticle synthesis. *Atomization and Sprays*, 30(11):779–797, 2020. doi: 10.1615/atomizspr.2020034819.

[223] U. Struckmeier, P. Oßwald, T. Kasper, L. Böhling, M. Heusing, M. Köhler, A. Brockhinke, and K. Kohse-Höinghaus. Sampling probe influences on temperature and species concentrations in molecular beam mass spectroscopic investigations of flat premixed low-pressure flames. *Zeitschrift für Physikalische Chemie*, 223(4-5):503–537, 2009. doi: 10.1524/zpch.2009.6049.

[224] S. Suleiman, M. Nanjaiah, I. Skenderovic, T. Rosenberger, F. Kunze, I. Wlokas, F. E. Kruis, H. Wiggers, and C. Schulz. Atmospheric-pressure particle mass spectrometer for investigating particle growth in spray flames. *Journal of Aerosol Science*, 158:105827, 2021. doi: 10.1016/j.jaerosci.2021.105827.

[225] Y. Sung, V. Raman, and R. O. Fox. Large-eddy-simulation-based multiscale modeling of TiO_2 nanoparticle synthesis in a turbulent flame reactor using detailed nucleation chemistry. *Chemical Engineering Science*, 66(19):4370–4381, 2011. doi: 10.1016/j.ces.2011.04.024.

[226] Y. Sung, V. Raman, H. Koo, M. Mehta, and R. O. Fox. Large-eddy simulation modeling of turbulent flame synthesis of titania nanoparticles using a bivariate particle description. *AIChE Journal*, 60(2):459–472, 2014. doi: 10.1002/aic.14279.

[227] P. K. Sweby. High resolution schemes using flux limiters for hyperbolic conservation laws. *SIAM Journal on Numerical Analysis*, 21(5):995–1011, 1984. doi: 10.1137/0721062.

[228] M. T. Swihart. Vapor-phase synthesis of nanoparticles. *Current Opinion in Colloid & Interface Science*, 8(1):127 – 133, 2003. doi: 10.1016/s1359-0294(03)00007-4.

[229] V. Tarnovsky, A. Levin, H. Deutsch, and K. Becker. Electron impact ionization of (x= 1-4). *Journal of Physics B: Atomic, Molecular and Optical Physics*, 29(1):139–152, 1996. doi: 10.1088/0953-4075/29/1/017.

[230] W. Y. Teoh, R. Amal, and L. Mädler. Flame spray pyrolysis: An enabling technology for nanoparticles design and fabrication. *Nanoscale*, 2(8):1324, 2010. doi: 10.1039/c0nr00017e.

[231] J. A. van Oijen and L. P. H. de Goey. Modelling of premixed laminar flames using flamelet-generated manifolds. *Combust. Sci. Technol.*, 161(1):113–137, 2000. doi: 10.1080/00102200008935814.

[232] J. A. van Oijen, F. A. Lammers, and L. P. H. de Goey. Modeling of complex premixed burner systems by using flamelet-generated manifolds. *Combustion and Flame*, 127(3):2124 – 2134, 2001. doi: 10.1016/s0010-2180(01)00316-9.

[233] J. A. van Oijen, R. J. M. Bastiaans, and L. P. H. de Goey. Low-dimensional manifolds in direct numerical simulations of premixed turbulent flames. *Proc. Combust. Inst.*, 31(1): 1377–1384, 2007. doi: 10.1016/j.proci.2006.07.076.

[234] H. K. Versteeg and W. Malalasekera. *An Introduction to Computational Fluid Dynamics - The Finite Volume Method*. Pearson Prentice Hall, 2007.

[235] J. Villermaux and L. Falk. A generalized mixing model for initial contacting of reactive fluids. *Chemical Engineering Science*, 49(24):5127–5140, 1994. doi: 10.1016/0009-2509(94) 00303-3.

[236] A. W. Vreman. An eddy-viscosity subgrid-scale model for turbulent shear flow: Algebraic theory and applications. *Physics of Fluids*, 16(10):3670–3681, 2004. doi: 10.1063/1.1785131.

[237] G. Wang, M. Boileau, and D. Veynante. Implementation of a dynamic thickened flame model for large eddy simulations of turbulent premixed combustion. *Combustion and Flame*, 158 (11):2199 – 2213, 2011. doi: 10.1016/j.combustflame.2011.04.008.

[238] C. Weise. *Towards the modelling of a spray flame process for nanoparticle synthesis*. PhD thesis, University of Duisburg-Essen, Nov. 2015.

[239] C. Weise, A. Faccinetto, S. Kluge, T. Kasper, H. Wiggers, C. Schulz, I. Wlokas, and A. Kempf. Buoyancy induced limits for nanoparticle synthesis experiments in horizontal premixed low-pressure flat-flame reactors. *Combustion Theory and Modelling*, 17(3): 504–521, jun 2013. doi: 10.1080/13647830.2013.781224.

[240] C. Weise, J. Menser, S. A. Kaiser, A. M. Kempf, and I. Wlokas. Numerical investigation of the process steps in a spray flame reactor for nanoparticle synthesis. *Proceedings of the Combustion Institute*, 35(2):2259 – 2266, 2015. doi: 10.1016/j.proci.2014.05.037.

[241] H. Weller, G. Tabor, A. Gosman, and C. Fureby. Application of a flame-wrinkling LES combustion model to a turbulent mixing layer. *Symposium (International) on Combustion*, 27(1):899–907, 1998. doi: 10.1016/s0082-0784(98)80487-6.

[242] J. Z. Wen, C. F. Goldsmith, R. W. Ashcraft, and W. H. Green. Detailed kinetic modeling of iron nanoparticle synthesis from the decomposition of $Fe(CO)_5$. *The Journal of Physical Chemistry C*, 111(15):5677–5688, 2007. doi: 10.1021/jp066579q.

[243] D. C. Wilcox. Reassessment of the scale-determining equation for advanced turbulence models. *AIAA Journal*, 26(11):1299–1310, 1988. doi: 10.2514/3.10041.

[244] D. C. Wilcox et al. *Turbulence modeling for CFD*, volume 2. DCW industries La Canada, CA, 1998.

[245] C. E. Willert and M. Gharib. Digital particle image velocimetry. *Experiments in Fluids*, 10(4):181–193, 1991. doi: 10.1007/bf00190388.

[246] J. Williamson. Low-storage runge-kutta schemes. *Journal of Computational Physics*, 35 (1):48–56, 1980. doi: 10.1016/0021-9991(80)90033-9.

[247] I. Wlokas, A. Faccinetto, B. Tribalet, C. Schulz, and A. Kempf. Mechanism of iron oxide formation from iron pentacarbonyl-doped low-pressure hydrogen/oxygen flames. *International Journal of Chemical Kinetics*, 45(8):487–498, 2013. doi: 10.1002/kin.20786.

[248] P. Wollny, B. Rogg, and A. Kempf. Modelling heat loss effects in high temperature oxy-fuel flames with an efficient and robust non-premixed flamelet approach. *Fuel*, 216:44–52, 2018. doi: 10.1016/j.fuel.2017.11.127.

[249] P. Wollny, S. Angel, H. Wiggers, A. M. Kempf, and I. Wlokas. Multiscale simulation of the formation of platinum-particles on alumina nanoparticles in a spray flame experiment. *Fluids*, 5(4):201, 2020. doi: 10.3390/fluids5040201.

[250] P. Wollny, J. Menser, L. Engelmann, J. Sellmann, C. Schulz, H. Wiggers, A. Kempf, and I. Wlokas. The role of phase transition by nucleation, condensation, and evaporation for the synthesis of silicon nanoparticles in a microwave plasma reactor — simulation and experiment. *Chemical Engineering Journal*, 453:139695, 2023. doi: https://doi.org/10.1016/j.cej.2022.139695.

[251] Y. Xiong and S. E. Pratsinis. Gas phase production of particles in reactive turbulent flows. *Journal of Aerosol Science*, 22(5):637 – 655, 1991. doi: 10.1016/0021-8502(91)90017-c.

[252] V. Yakhot, S. A. Orszag, S. Thangam, T. B. Gatski, and C. G. Speziale. Development of turbulence models for shear flows by a double expansion technique. *Physics of Fluids A: Fluid Dynamics*, 4(7):1510–1520, 1992. doi: 10.1063/1.858424.

[253] J. You, Y. Yang, and S. B. Pope. Effects of molecular transport in LES/PDF of piloted turbulent dimethyl ether/air jet flames. *Combustion and Flame*, 176:451–461, 2017. doi: 10.1016/j.combustflame.2016.11.007.

[254] G. Zhou. *Numerical simulations of physical discontinuities in single and multi-fluid flows for arbitrary Mach numbers*. PhD thesis, Chalmers University of Technology, Goteborg, Sweden, 1995.

DOI: 10.17185/duepublico/79243
URN: urn:nbn:de:hbz:465-20231115-111813-3